中国科学技术大学

博士学位论文

RHIC-STAR 200GeV 金核-金核碰撞中极低横动量 J/ψ 的产生

作者姓名：　李子阳

学科专业：　粒子物理与原子核物理

导师姓名：　唐泽波教授　查王妹副教授

完成时间：　二〇二四年五月二十一日

University of Science and Technology of China

A dissertation for doctor's degree

Study of very low p_{T} J/ψ production in Au+Au collisions at $\sqrt{s_{\mathrm{NN}}}$ = 200 GeV with STAR experiment

Author: Ziyang Li

Speciality: Particle and Nuclear Physics

Supervisors: Prof. Zebo Tang, Prof. Wangmei Zha

Finished time: May 21, 2024

中国科学技术大学学位论文原创性声明

本人声明所呈交的学位论文，是本人在导师指导下进行研究工作所取得的成果。除已特别加以标注和致谢的地方外，论文中不包含任何他人已经发表或撰写过的研究成果。与我一同工作的同志对本研究所做的贡献均已在论文中作了明确的说明。

作者签名：李子明　　签字日期：2024.5.24

中国科学技术大学学位论文授权使用声明

作为申请学位的条件之一，学位论文著作权拥有者授权中国科学技术大学拥有学位论文的部分使用权，即：学校有权按有关规定向国家有关部门或机构送交论文的复印件和电子版，允许论文被查阅和借阅，可以将学位论文编入《中国学位论文全文数据库》等有关数据库进行检索，可以采用影印、缩印或扫描等复制手段保存、汇编学位论文。本人提交的电子文档的内容和纸质论文的内容相一致。

控阅的学位论文在解密后也遵守此规定。

☑公开　□控阅（　　年）

作者签名：李子明　　导师签名：[illegible]

签字日期：2024.5.24　　签字日期：2024.5.24

摘　要

量子色动力学（QCD）是研究夸克和胶子之间强相互作用的标准动力学理论，也是粒子物理标准模型的重要组成部分。格点量子色动力学（Lattice QCD）的计算表明，夸克和胶子在高温或高密的极端条件下，会发生从普通强子物质到夸克胶子等离子体（Quark-Gloun Plasma, QGP）的相变。QGP 被认为存在于宇宙大爆炸之后的很短时间内，对 QGP 的研究有助于理解宇宙的早期演化，是高能核物理领域的前沿热点之一。产生 QGP 的极端条件在实验室中可以通过相对论重离子对撞实验实现，位于布鲁克海文国家实验室的相对论重离子对撞机（RHIC）是专门用来寻找 QGP 并研究其性质的重要大科学装置之一。

在相对论重离子对撞中，高速运动的重离子会激发出极强的电磁场。由于洛伦兹收缩，这个电磁场几乎完全垂直于重离子的运动方向，也就是横平面，且电场和磁场的幅度几乎相同，彼此相互垂直。这与光子的电磁场非常类似，基于等效光子近似（EPA），可以用一束准实光子来等效这个电磁场。在相对论重离子对撞中，两个接近光速运动的原子核相互接近，其中一个核发出的光子可以与另一个核通过交换玻密子进行相互作用，称为光-核子过程，这个过程会产生矢量介子，包括粲夸克偶素 J/ψ。如果在作用前后，靶核保持完整，既为相干光核作用过程。相干光核作用一个重要特性是这个过程产生的矢量介子横动量（p_{T}）很小，因此在实验中可以与强相互作用来源的矢量介子做出很好的区分。由于光-核作用过程涉及到一个原子核发射的光子和另一个原子核发射的玻密子，因此测量相干光致产生过程的粲夸克偶素为研究电磁场的性质以及原子核中的胶子分布提供了一种手段。此前，在 RHIC 上的螺线管径迹探测器（STAR）上通过双电子衰变道在偏心碰撞中测量到了极低横动量的 J/ψ 产额增强，与相干光致产生过程的预期一致。与双电子衰变道相比，缪子有更低的韧致辐射，以及较少的在探测器材料中多次散射，其测量具有额外的优势。此外，在理解光-核作用过程的机制上，双缪子衰变道的结果会是对双电子衰变道结果的补充。

在 2014 年，RHIC-STAR 完成了缪子望远镜探测器（MTD）的安装，首次具备了中高横动量缪子的鉴别能力，可以用来重建 J/ψ。本论文分析了 RHIC-STAR 在 2014 和 2016 年双缪子触发采集到的 200 GeV 金核-金核对撞数据，通过联合时间投影室（TPC）和 MTD 完成了缪子的鉴别，通过拟合双缪子不变质量谱提取了极低横动量 J/ψ 的信号，测量了偏心碰撞中相干光核作用过程产生的 J/ψ。这是首次在 RHIC-STAR 上通过双缪子衰变道在偏心碰撞中测量极低横动量的 J/ψ。

本论文展示了 J/ψ 不变产额的横动量谱，结果显示在极低横动量区间（p_{T}

< 0.2 GeV/c），J/ψ 产额相比其强产生外推在偏心碰撞中有明显的反常增强。基于 J/ψ 的横动量谱，我们计算了 J/ψ 在 200 GeV 金核-金核碰撞中的核修正因子 R_{AA}，发现在 $p_{\mathrm{T}} > 0.2$ GeV/c 区间，R_{AA} 的测量结果低于 1，与强产生加上热核和冷核效应的预期相符；而在 $p_{\mathrm{T}} < 0.2$ GeV/c 区间，R_{AA} 的测量结果显著大于 1，且有很强的中心度依赖，预示着在该横动量区间可能存在着新的产生机制。

为探索该反常增强，我们将总 J/ψ 产额扣除强产生贡献，得到反常增强的产额，进一步测量了 40-80% 中心度下增强产额的 p_{T}^2 谱。该谱的形状与极度偏心碰撞中（Ultra-Peripheral Collisions, UPCs）相干光致产物的 p_{T}^2 谱极为相似，预示着该额外增强源自相干光致产生。此外，p_{T}^2 谱的第一个数据点有明显的压低，与重离子碰撞中相干光致产生的干涉效应预期一致。本论文还测量了增强产额与中心度的关系。如果增强源自强产生，其产额应有强烈的中心度依赖性，而对于相干光致产生，理论计算表明其产额有相对较弱的依赖性。实验结果显示增强产额在误差范围内没有显示出中心度依赖，且可以被基于 EPA 的光致产生模型很好的描述，证明了该增强源自相干光致产生。

本论文中还将双缪子衰变道与 STAR 合作组已发表的双电子衰变道的结果进行了比较，结果显示来自不同衰变道的测量结果在误差范围内一致。

本论文的工作为理解相干光子-核子作用过程的机制，研究相对论重离子碰撞中夸克胶子等离子和初始电磁场的性质提供了重要的实验依据。

关键词：粲夸克偶素　相对论重离子对撞　夸克胶子等离子体　等效光子近似　相干光子-核子作用过程　缪子望远镜探测器

ABSTRACT

Quantum chromodynamics (QCD) describes the strong interaction between quarks mediated by gluons, forming an integral part of the Standard Model for particle physics. Calculations based on lattice QCD suggest that at high temperature or density, hadronic matter undergoes a phase transition to a deconfined state of quarks and gluons, called the Quark-Gluon Plasma (QGP). The QGP is believed to have existed for a brief moment after the Big Bang, and studying its properties will shed light on understanding the early evolution of the Universe. The extreme conditions for generating the QGP can be reached in the laboratory through ultra-relativistic heavy-ion collisions. The Relativistic Heavy Ion Collider (RHIC) at Brookhaven National Laboratory is dedicated to creating the QGP and studying its properties.

In these collisions, the high-speed movement of heavy ions generates a strong electromagnetic field, which due to Lorentz contraction, is almost entirely transverse with the electric and magnetic fields being perpendicular to ion's travel direction and of almost equal magnitude. This closely resembles the electromagnetic field of a photon, and, therefore, this transverse electromagnetic field can be considered as a beam of quasi-real photons, based on the Equivalent Photon Approximation (EPA). Consequently, the photon emitted by one nucleus can interact with the nucleus coherently through Pomeron exchange, referred to as the coherent photon-nucleus process, producing vector mesons such as the J/ψ meson (a bound state made of a charm quark and an anticharm quark). A distinctive feature of this process is that the produced vector mesons are dominantly concentrated at very low transverse momentum (p_{T}), allowing for a clear differentiation from vector mesons produced through other processes, such as hadronic interactions. Since the photon-nucleus process involves photons emitted by one nucleus and Pomerons emitted by the other nucleus, measurement of coherent J/ψ production provides a means to study the nature of the electromagnetic field as well as the gluon distribution in the nucleus. Recently, a enhancement of J/ψ yield at very low p_{T} in peripheral collisions was observed by the Solenoidal Tracker at RHIC (STAR), which is consistent with the expectation of photon-nucleus process. Compared to the dielectron decay channel, muons exhibit lower bremsstrahlung radiation and undergo fewer multiple scatterings in detector material, facilitating the J/ψ signal extraction. Furthermore, the dimuon analysis is complementary to the dielectron result in understanding the dynamics of photon-nuclear interactions.

In 2014, the Solenoidal Tracker at RHIC (STAR) enhanced its capability for muon triggering and identification with the installation of the Muon Telescope Detector (MTD). In this thesis, 200 GeV Au+Au collision data collected by RHIC-STAR with a dimuon trigger in 2014 and 2016 are analyzed. Muons are identified through a combination of the Time Projection Chamber (TPC) and MTD, and the signals of very low p_{T} J/ψ are extracted by fitting the invariant mass spectrum of dimuon pairs. This marks the first measurement of very low p_{T} J/ψ in peripheral collisions through the dimuon channel at RHIC-STAR.

In this thesis, we present invariant yield of J/ψ as a function of p_{T}, showing a significant enhancement compared to hadronic contribution at very low p_{T} ($p_{\mathrm{T}} < 0.2$ GeV/c) across different centrality classes. Based on the measured invariant yields, nuclear modification factors R_{AA} for J/ψ in 200 GeV Au+Au collisions are calculated. For $p_{\mathrm{T}} > 0.2$ GeV/c, the measured R_{AA} is below 1, consistent with expectation of combined cold and hot medium effects. Remarkably, at $p_{\mathrm{T}} < 0.2$ GeV/c, R_{AA} rises significantly above 1 and shows a strong centrality dependence, indicating that the enhanced yield originates from the coherent photon-nucleus interaction.

Subsequently, the coherent J/ψ yield, also referred to as the excess yield, is obtained by subtracting the contribution from hadronic interactions from the total J/ψ yield. The p_{T}^2 spectrum of the excess yield for 40-80% centrality, which is closely related to the distribution of interaction sites and can be used to infer the gluon distribution in the nucleus. The shape of the measured spectrum is consistent with expectations from the coherent photon-nucleus process, and the slope parameter is extracted. The first data point in the p_{T}^2 spectrum shows a notable suppression, probably arising from interference effects. We also measure the collision centrality dependence of the excess yield. For the coherent photon-nucleus process, its cross section is directly related to the photon flux which is proportional to nucleus charge squared, but depends weakly on centrality. Experimental results indeed show that within the uncertainties the excess yield does not exhibit a strong centrality dependence within the measured centrality range. Comparison to a theoretical model calculation, that is based on EPA and considers the entire nucleus as the photon-emitting source and the spectator nucleons in the target nucleus as the Pomeron emitter, reveals good consistency.

In this thesis, the results from the dimuon decay channel are compared with those from the dielectron decay channel published by the STAR collaboration. The results show that the measurements from different decay channels are consistent within uncertainty.

The work presented in this thesis provides crucial experimental insights for understanding the mechanism of coherent photon-nucleus interactions and studying the nature of the initial electromagnetic field in relativistic heavy-ion collisions. In the future, the RHIC running of 2023 and 2025 promises significantly larger datasets than what's currently available, and will improve the analysis of coherent J/ψ production.

Key Words: Charmonium, Relativistic Heavy-Ion Collisions, Quark-Gluon Plasma, Equivalent Photon Approximation, Coherent Photon-nucleus Process, Muon Telescope Detector

Contents

List of Figures

List of Tables

Chapter 1 Introduction

1.1 The Standard Model

The cumulative efforts of countless physicists have revealed that the Universe is constituted from a limited set of basic building blocks, known as fundamental particles, and governed by four fundamental forces. The Standard Model encapsulates our understanding of how these particles interact through three of the four fundamental forces, excluding gravity[1]. Formulated in the early 1970s, the Standard Model has accounted for almost all experimental outcomes and accurately predicted a multitude of phenomena. As such, it is viewed as a thoroughly tested and verified theory framework for particle physics.

The Standard Model is built upon a $SU(3) \times SU(2) \times U(1)$ gauge symmetry, providing a quantum field theory framework that elucidates the properties and interactions of fundamental particles. As depicted in Fig. 1.1, this theory categorizes elementary particles into two primary sectors: fermions and bosons, details their properties such as mass, charge, and spin.

Incorporating twelve elementary fermions, each with spin-$\frac{1}{2}$ and obeying the Pauli exclusion principle, the Standard Model pairs each fermion with a corresponding antiparticle, mirroring the particle's properties but with opposite charge. These fermions are bifurcated into quarks and leptons across three generations, each with increasing mass. Quarks, denoted as up (u), down (d), charm (c), strange (s), top (t), and bottom (b), are unique in carrying the color charge, and engaging in strong interactions, alongside participating in electromagnetic and weak interactions thanks to their electric charge and weak isospin. u, c, and t quark have a fractional electric charge of $+\frac{2}{3}$, while d, s, and b quark have $-\frac{1}{3}$. The lepton sector comprises the electron (e^-), electron neutrino (ν_e), muon (μ^-), muon neutrino (ν_μ), tau (τ^-), and tau neutrino (ν_τ). Leptons are not subject to strong interactions since they do not carry any color charges. The main leptons carry an electric charge of -1, while the three neutrinos carry zero electric charge. Thus, the neutrinos' motion are only influenced by weak interaction and gravity, making them difficult to detect.

The gauge bosons, entities of spin-1, alongside the scalar Higgs boson with spin-0, are the force carriers within the Standard Model. The electromagnetic force is mediated by photons, with quantum electrodynamics (QED) providing the theoretical description. Gluons, mediating the strong force as described by the quantum chromodynamics

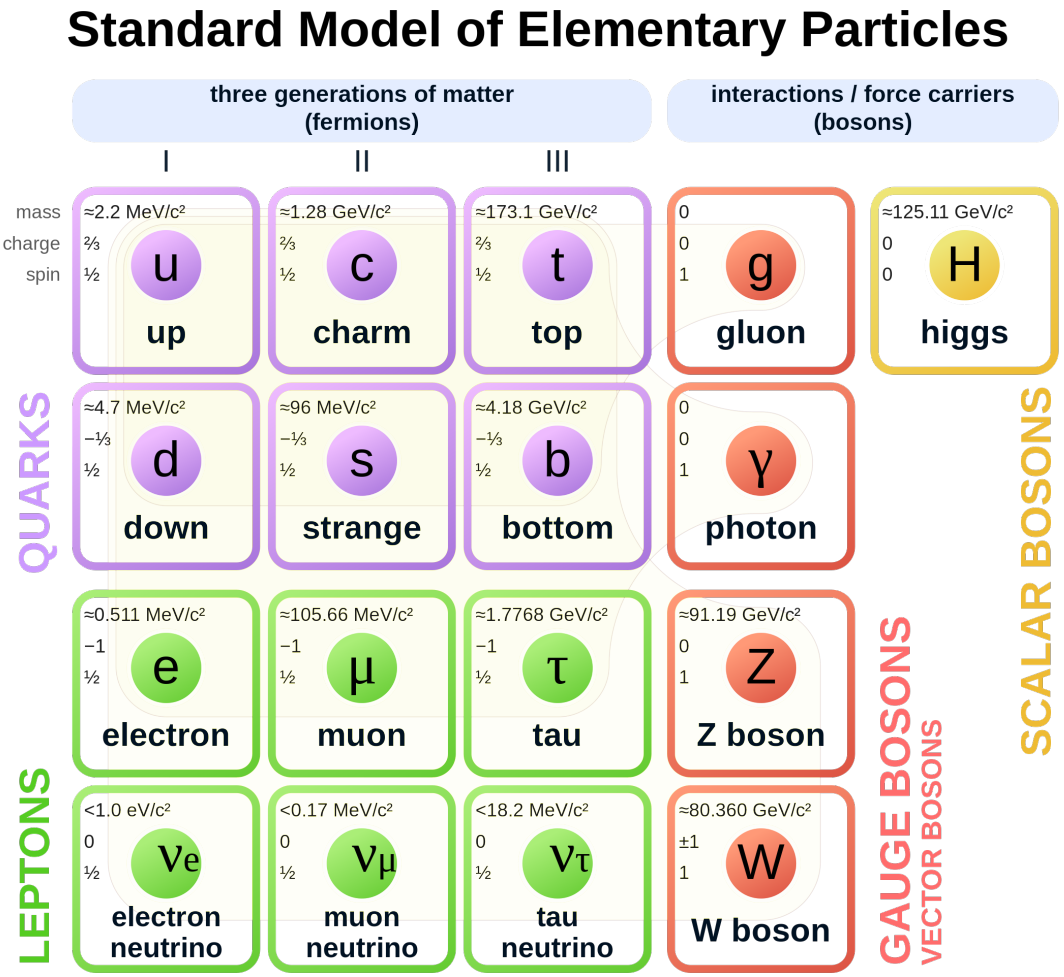

Figure 1.1 The Standard Model of elementary particles. Figure is taken from[2].

(QCD), bind quarks together. In particular, they are capable of self-interaction due to their inherent color charges. The weak force, responsible for radioactive decays, is carried by $W^{\pm}$ and Z bosons, impacting all fermions and distinguishing between particle chirality. The unification of electromagnetic and weak interactions is described through the electroweak theory. Gravity remains the outlier of the four fundamental forces with the hypothesized graviton still unobserved. The Higgs boson is a massive scalar particle with zero spin, which is important for understanding the origin of particle mass[3].

1.2 Quantum Chromodynamics

Quantum Chromodynamics (QCD) describes the strong force interactions among colored quarks and gluons, and represents the SU(3) component of the $SU(3)\times SU(2)\times$

$U(1)$ Standard Model[4-6]. The Lagrangian of QCD is given by[7]:

$$\mathcal{L} = \sum_q \bar{\psi}_{q,a} \left(i\gamma^\mu \partial_\mu \delta_{ab} - g_s \gamma^\mu t^C_{ab} \mathcal{A}^C_\mu - m_q \delta_{ab} \right) \psi_{q,b} - \frac{1}{4} F^A_{\mu\nu} F^{A\mu\nu}, \tag{1.1}$$

where repeated indices are summed over. The γ^μ are the Dirac γ-matrices. $\psi_{q,a}$ are quark-field spinors for a quark of flavor q and mass m_q, with a color-index a that runs from 1 to $N_c = 3$, *i.e.*, quarks come in three colors. The $\mathcal{A}^C_\mu$ correspond to the gluon fields, with C running from 1 to N_c^2-1 = 8, *i.e.*, there are eight types of gluons. Gluons transform under the adjoint representation of the SU(3) color group. The matrices t^C_{ab}, which number eight and are 3×3 in dimension, serve as the generators for the SU(3) group. They encapsulate the concept that the interaction between a gluon and a quark results in the rotation of the quark's color within the framework of SU(3) space. The quantity g_s (or $\alpha_s = \frac{g_s^2}{4\pi}$) is the QCD coupling constant. Besides quark masses, which have electroweak origin, g_s is the only fundamental parameter in QCD. Finally, the field tensor $F^A_{\mu\nu}$ is given by

$$\begin{aligned} F^A_{\mu\nu} &= \partial_\mu \mathcal{A}^A_\nu - \partial_v \mathcal{A}^A_\mu - g_s f_{ABC} \mathcal{A}^B_\mu \mathcal{A}^C_\nu, \\ \left[t^A, t^B \right] &= i f_{ABC} t^C. \end{aligned} \tag{1.2}$$

A distinctive feature of QCD is the color confinement. It posits that quarks and gluons are never found in isolation but always in bound states known as hadrons, which are color-neutral. Despite extensive theoretical and experimental investigations, an analytic proof of color confinement within non-abelian gauge theories remains elusive. However, the qualitative understanding of this phenomenon draws significantly from the unique properties of gluons, the force carrier in QCD. Gluons possess color charge, unlike the photons in QED, which results in remarkably different behavior of the strong force from the electromagnetic force. In QED, the electric field between electric charges diminishes rapidly with increasing separation. Conversely, in QCD, the gluon field between color charges generates a narrow flux tube or string, maintaining a constant force regardless of the distance between the color charges. This distinctive behavior implies that, as color charges are pulled apart, energy accumulates in the flux tube, eventually leading to the creation of a new quark-antiquark pair rather than extending the tube indefinitely. This process effectively ensures that quarks and gluons remain confined within hadrons. The phenomenon of color confinement is further elucidated through deep inelastic scattering experiments, which reveal that quarks behave almost freely within hadrons under conditions of high momentum transfer. This observation is con-

sistent with the static QCD potential, described by the equation:

$$V_s = -\frac{4}{3} \times \frac{\alpha_s}{r} + k \times r \tag{1.3}$$

where α_s is the coupling constant in strong interactions, k denotes the QCD string tension, and r represents the distance between color charges. This potential captures the dual nature of the strong force: at short distances, it resembles the Coulomb potential between electric charges, as captured by the first term, while at larger distances, the linear term $k \times r$ prevails, manifesting quark and gluon confinement within hadrons.

The phenomenon of the strong force diminishing at closer distances between quarks leads to another unique aspect of the QCD, known as the asymptotic freedom. Asymptotic freedom concerns the variation of the strong coupling constant, α_s, with the energy scale, or renormalization scale. This effect can be qualitatively understood by considering the influence of the quantum field on virtual particle pairs that carry the relevant charge. Again, let's start with QED. The phenomenon known as the Landau pole states that the effect of virtual charged particle–antiparticle pairs, such as electron–positron pairs, screens the electric charge in the vacuum. Nearing a charge, the vacuum becomes polarized: virtual particles with opposite charges are attracted, and like charges are repelled, leading to a partial cancellation of the electric field at finite distances, and thus effectively reducing the charge[7]. QCD exhibits a similar behavior with virtual quark-antiquark pairs screening the color charge. However, QCD introduces a unique mechanism through its force-carrying gluons, which themselves possess color charge. Each gluon carries a color charge and an anti-color magnetic moment, leading to a net effect in the vacuum polarization that does not only screen the color field but augments and modifies it through a process known as antiscreening. As a result, approaching a quark reduces the antiscreening effect of virtual gluons, thereby diminishing the effective color charge with decreasing distance. Thus, the effective QCD coupling constant α_s at the leading order can be written as:

$$\alpha_s\left(Q^2\right) \approx \frac{1}{4\pi\beta_0 \ln\left(Q^2/\Lambda^2_{QCD}\right)}, \tag{1.4}$$

where $\beta_0 = \frac{1}{(4\pi)^2}\left(11 - \frac{2}{3}N_f\right)$ is a constant dependent on the number of active quark flavors N_f (with $N_f = 6$). Q is the energy scale and Λ_{QCD} is the QCD scale determined experimentally ($\Lambda_{QCD} \approx 200$ MeV). Experimental data on α_s as a function of Q, depicted in Fig. 1.2, demonstrates a good agreement with the QCD predicted values, confirming that the coupling constant weakens at higher energies or shorter distances.

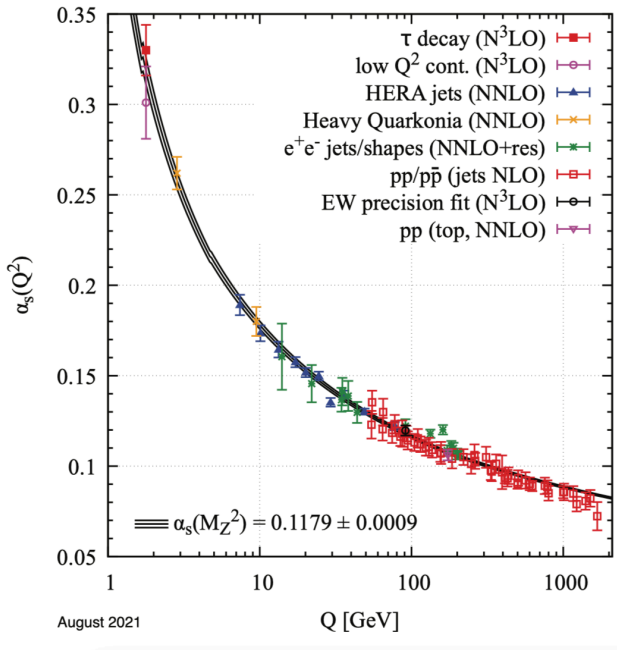

Figure 1.2 The measured running coupling constant α_s as a function of the energy scale Q. Figure is taken from [7].

This behavior lays the foundation for the framework of perturbative QCD (pQCD), which allows for reliable calculations of process cross sections involving quarks and gluons with systematically improvable precision through series expansions in α_s when α_s is small [8]. In contrast, at low energies or larger distances where α_s increases, perturbative methods become ineffective, and lattice QCD, discretizing spacetime to simulate QCD from first principles, provides a way for exploring the strong force in this non-perturbative regime [9]. This domain is essential for understanding phenomena such as quark confinement and the mass spectra of hadrons.

1.3 Quark-Gluon Plasma and Phase Transition

Incorporating the concept of asymptotic freedom, predictions from QCD indicate that at sufficiently high temperatures and/or densities, the strength of the strong force diminishes. This reduction permits quarks and gluons to escape their confinement within hadrons, potentially creating a distinct state of matter known as the quark-gluon plasma (QGP) [10-11]. The transition to this novel phase is underpinned by comprehensive theoretical work, notably including calculations from lattice QCD [12]. It is theorized that QGP was prevalent during the early Universe, approximately 10^{-5} to 10^{-6} seconds after the Big Bang, in an environment characterized by extreme temperatures and densities, before it cooled and transitioned into the hadrons that comprise the Universe as of today. Figure 1.3 sketches the evolution of the Universe starting from the Big Bang. The pro-

cess and implications of this phase transition, particularly in the context of high energy densities and temperatures, remain an area of active investigation, with potential ramifications for our understanding of astrophysical phenomena, such as the internal structure of neutron stars. Being a complex system, the QGP also offers an invaluable means to probe many-body dynamics of the QCD.

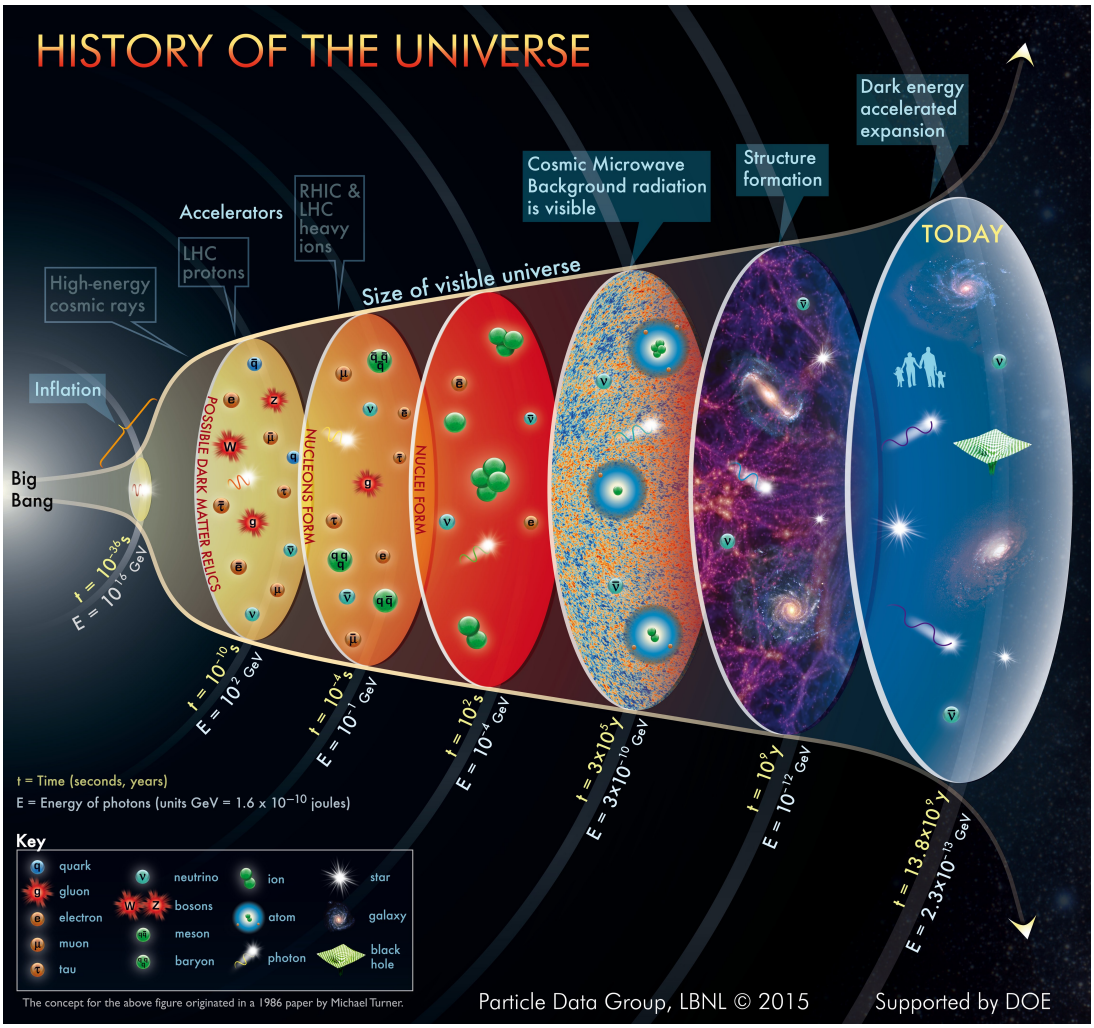

Figure 1.3 History of the Universe. Figure is taken from Particle Data Group at Lawrence Berkeley National Lab[7].

While lattice QCD calculations suggest that the transition at vanishing netbaryon density is a smooth crossover, the hypothesis of a first-order phase transition accompanied by a critical point at large net-baryon densities has gained widespread attraction. The quest to locate the critical point and delineate the first phase transition boundary is at the forefront of global research efforts, both theoretically and experimentally. Figure 1.4 shows a sketch of the QCD phase diagram plotted in the temperature (T) versus chemical baryon potential (μ_B) plane[13]. The expected ranges in μ_B of the heavy-ion facilities are indicated at the top of the figure. The diagram positions the QGP phase

predominantly in the upper part, where temperature or baryon density is elevated. Ordinary nuclear matter is situated at nearly zero temperature and a μ_B of approximately 940 MeV, marked on the diagram along the x-axis. As forementioned, at $\mu_B = 0$, it's anticipated that the QCD phase transition from hadron gas to the QPG will occur via a smooth crossover. With an increase in μ_B, a first-order phase transition is expected to occur, and ends at the critical point[14]. Recent findings suggest that the location of the critial point is disfavored for $\mu_B \leq 2T$[15].

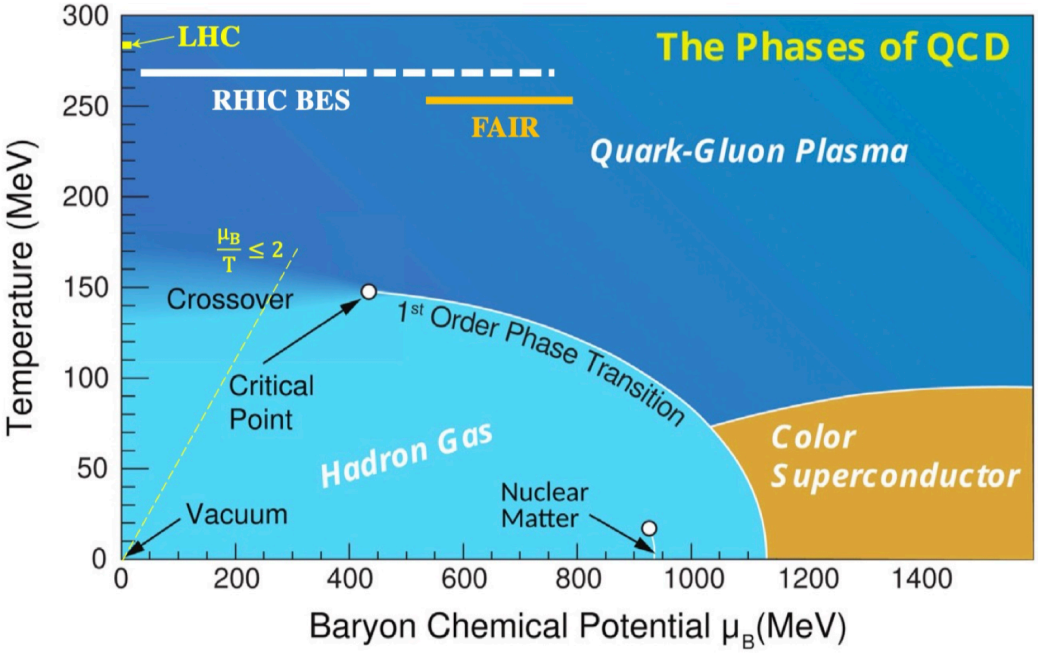

Figure 1.4 A schematic view of the QCD phase diagram, plotted in T vs. μ_B. Figure is taken from[13].

1.4 Relativistic Heavy-ion Collisions

Although one can not travel back in time to study Universe in its infancy, physicists can recreate early Universe conditions locally and momentarily through relativistic heavy-ion collisions. Proposed by Nobel Prize-winning physicist Tsung-Dao Lee in the 1970s, this method involves accelerating heavy nuclei to near speed of light and smash them head-on to create QGP in the laboratory[16]. This novel field, blending particle and nuclear physics, has garnered significant interest since then. Experimentally, heavy ions (like gold or lead nuclei) are accelerated to high speeds in large collider rings, and their enormous kinetic energies are released through collisions within a small volume, creating conditions similar to those after the Big Bang. And hence heavy-ion collisions are sometimes referred to as "Little Bang".

1.4.1 Evolution of Relativistic Heavy-ion Collisions

Figure 1.5 presents a diagrammatic representation of the space-time evolution in relativistic heavy-ion collisions. Initially, two nuclei, accelerated to velocities approaching the speed of light, can be treated as slim disks due to Lorentz contraction along the beam direction. The moment of their intersection, defined as $t = 0$ fm/c, marks the potential onset of the QGP formation, contingent upon surpassing critical temperature and energy density thresholds. Absent these conditions, the collision evolves hydrodynamically (depicted on the left side of the figure), transitioning through a pre-hadronic phase where, despite increased pressure and temperature, parton deconfinement remains unattained. The system evolves very differently in the case of QGP formation, detailed on the right side of the figure:

- Pre-equilibrium ($t \lesssim 1$ fm/c): partons scatter among each other, leading to an abundant production of deconfined quarks and gluons. High transverse momentum particles ($p_{\mathrm{T}} \gg 1$ GeV/c) and high mass particles (m $\gg 1$ GeV/c^2) are produced at this stage.
- Thermalization: partonic interactions within the QGP facilitate a transition to thermal equilibrium, with inelastic collisions potentially altering particle flavor composition. The system, driven by internal pressure, undergoes rapid expansion and cools down, transitioning into a hadron gas during the mixed phase.
- Hadronization ($t \sim$ 5-10 fm/c): when the system reaches the critical energy density once more, the hadronization begins, leading to the condensation of quarks and gluons from the QGP into new hadrons. This process unfolds through two mechanisms: fragmentation, where a high p_{T} parton fragments into lower p_{T} hadrons, and coalescence, where partons with lower p_{T} combining to form larger p_{T} hadrons. During hadronization, the energy density of the system significantly decreases, and the interaction region expands, yet the temperature remains stable at T_C. Hadrons continue to interact among themselves until the rate of interaction is insufficient to sustain the expansion, marking a stage where the composition of particle species no longer changes, which is called the chemical freeze-out.
- Kinetic freeze-out: when the mean distance between hadrons grows larger than the radius of strong interaction (at T $\sim$ 120 MeV). At this point, elastic scatterings between hadrons cease, and the kinematic spectra of the system is fixed.

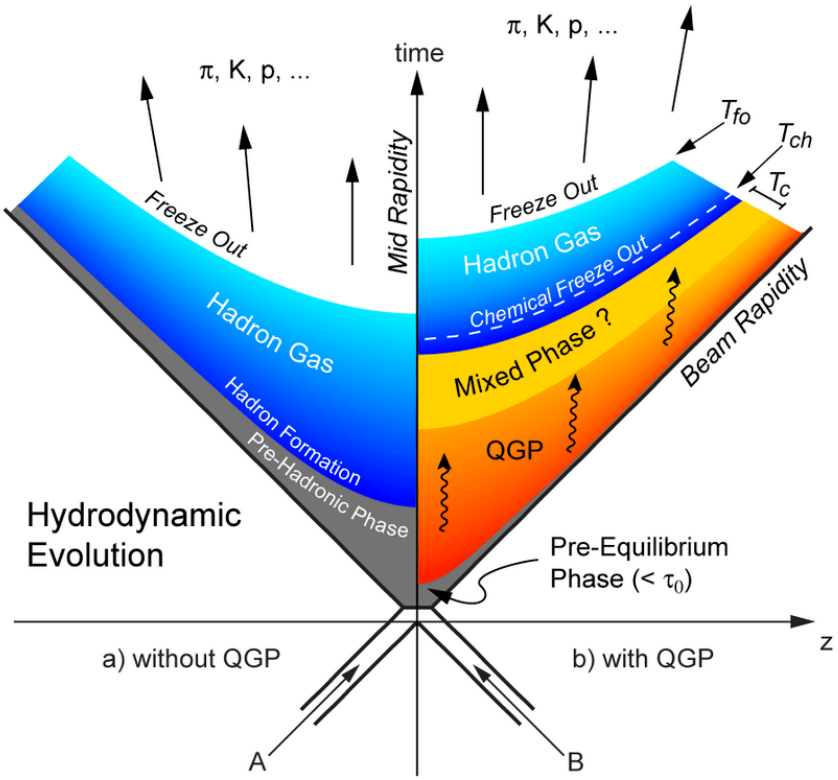

Figure 1.5 A description of different stages in a heavy-ion collision, shows both with or without QGP. Figure is taken from[17].

1.4.2 Collision Geometry

The geometry of relativistic heavy-ion collisions plays a significant role in the dynamics of these collisions. Since the de Broglie wavelength of nucleons is much smaller than the size of the nucleus, it is appropriate to use the impact parameter (b) for describing these collisions. Figure 1.6 schematically shows the collision geometry of a heavy-ion collision.

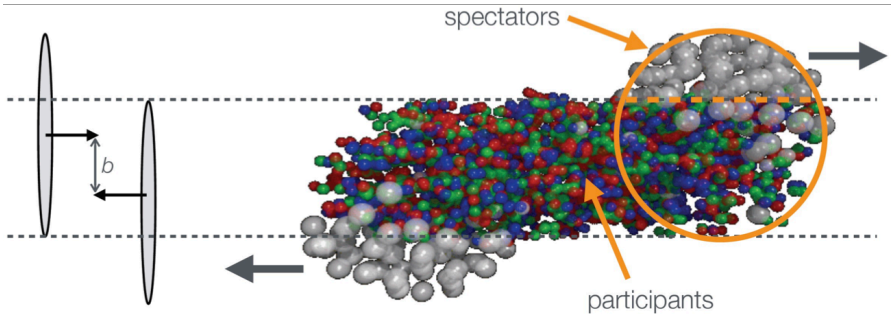

Figure 1.6 A schematic view of the geometry of two nuclei before and after their collision. Figure is taken from[18].

Nucleons in the nuclei are divided into two categories: participants, as shown in color in Fig. 1.6, and spectators, as shown in gray. This geometric approach, known as the participant-spectator model, has successfully described many characteristics of

heavy-ion collisions observed experimentally. As illustrated in Fig. 1.6, the number of participants (N_{part}) and the number of spectators (N_{spec}) are closely related to the impact parameter b. For most heavy-ion collision experiments, information on collision geometry is inferred from N_{part}, which can be obtained through a combination of semi-classical Glauber model[19] introduced below and data, since direct measurements of b or N_{part} is not possible experimentally.

The Glauber model has been successfully applied to describe high-energy nuclear collisions and is widely used to estimate a collision's N_{part} and the number of binary nucleon-nucleon collisions (N_{coll}). This semi-classical model treats nuclear collisions as a superposition of interactions between nucleons in the incident nucleus and nucleons in the target nucleus. It assumes that nucleons move in straight lines, and there is no deflection in their direction of movement after a collision (a good approximation in the high-energy regime). Moreover, the model assumes that the inelastic nucleon-nucleon scattering cross section is consistent with that in vacuum, *i.e.*, it does not account for the generation of secondary particles or possible nucleon excitations.

Moreover, the charged-particle multiplicity (N_{ch}), which is defined as the total number of charged particles produced in an event, has a linear relationship with b. It can be measured experimentally and compared against Glauber model in determining event centrality[19]. Usually, central (peripheral) events refer to those with small (large) impact parameters. Figure 1.7 shows the correlation between N_{ch}, $\langle b \rangle$, $\langle N_{\text{part}} \rangle$, and centrality percentages for Au+Au collisions at $\sqrt{s_{\text{NN}}} = 200$ GeV. As one can see, more central collisions produce larger N_{ch} values.

1.5 Quarkonium

Quarkonium is a flavorless meson whose constituents are a heavy quark and its own antiquark, making it both a neutral particle and its own antiparticle. It serves as a crucial instrument in the exploration of QCD. The quarkonium states include charmonium ($c\bar{c}$) and bottomonium ($b\bar{b}$), which consist of charm-anticharm and bottom-antibottom quark pairs, respectively. The existence of toponium ($t\bar{t}$) is precluded by the rapid decay of the top quark through electroweak interactions before a bound state has the opportunity to form. This section provides a general introduction to quarkonia.

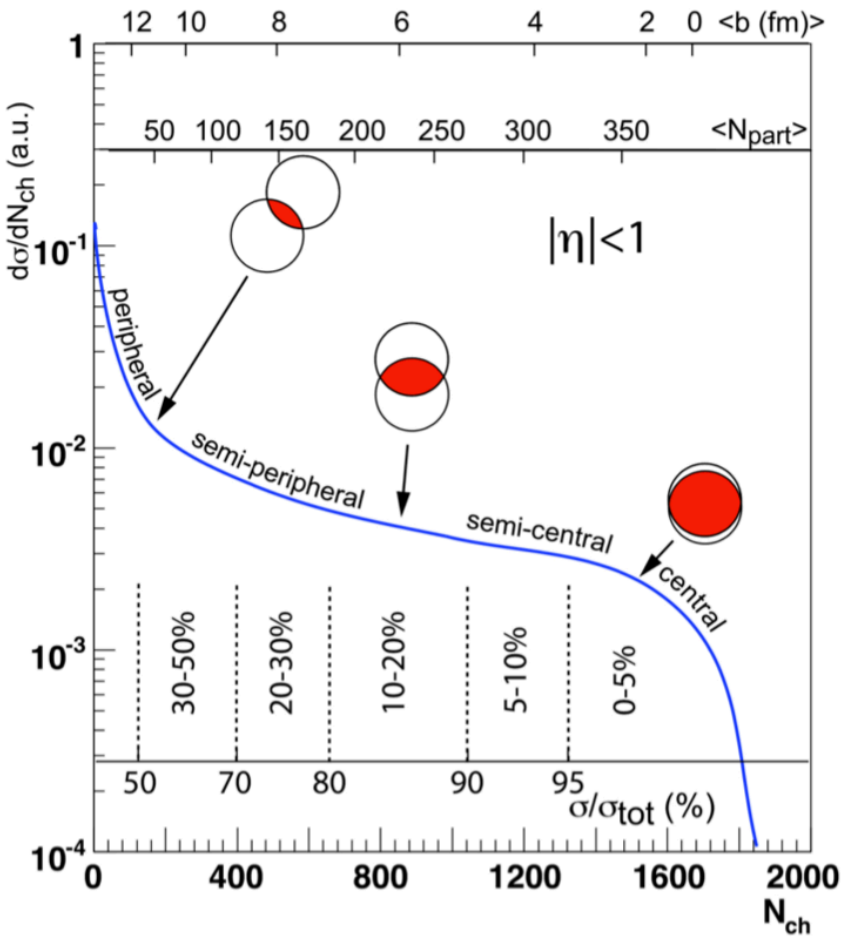

Figure 1.7 An example of the correlation between experimentally measurable charged-particle multiplicity N_{ch} and quantities calculated through the Glauber model (b and N_{part}). Figure is taken from [19]

.

1.5.1 The discovery of quarkonium

The J/ψ meson is the first particle known to contain a charm quark. Its discovery in 1974 marked a pivotal moment in the history of particle physics, leading to widespread acceptance of the quark model for hadron structure and providing the first clear evidence for the existence of the charm quark. It was also referred to as the ”November Revolution”. This discovery was simultaneously made by two independent research groups: one led by Burton Richter at the Stanford Linear Accelerator Center (SLAC) in California [20], and the other by Samuel Ting at the Brookhaven National Laboratory in New York [21].

Richter's group at SLAC observed the particle in electron-positron collisions using the Stanford Positron-Electron Asymmetric Ring (SPEAR), naming it the “ψ” meson. Almost concurrently, Ting's group detected the same particle in proton-proton collisions using the Alternating Gradient Synchrotron (AGS) at Brookhaven, calling it the “J”

meson, which is similar with his last-name written in Chinese "丁". Given these parallel discoveries, the particle became known as the J/ψ meson. Ten days later, Richeter's group at SLAC discovered another state of charmonium at higher mass, called ψ' (or $\psi(2S)$)[22].

The subsequent discovery of open charm, specifically within the D meson family[23], along with the revelation of the Λ_c baryon in 1976[24] provided concrete evidence for the charm quark. In 1977, a Fermilab team led by Leon Lederman discovered the lowest mass bottomonium state, the $\Upsilon(1S)$ resonance[25], in proton-nucleus collisions. The excited states, $\Upsilon(2S)$[26] and $\Upsilon(3S)$[27], were discovered shortly after. The open bottom (the B meson family)[28] and Λ_b baryon[29] followed in 1981. The top quark's discovery in 1994 at Fermilab marked the observation of all three generations of quarks[30]. However, as previously noted, the top quark's extremely brief lifetime precludes the formation of toponium.

1.5.2 J/ψ in charmonium family

The focus of this thesis is on the J/ψ meson, a state within the charmonium family. In the figure referred to as Fig. 1.8, a schematic representation is displayed, illustrating both the recognized charmonium states and those seemingly related to charmonium. The quantum numbers and fundamental properties of charmonium states are well described by the picture of a nonrelativistic quark-antiquark pair $c\bar{c}$. This picture categorizes the charmonium states based on their orbital angular momentum L, the quark pair's total spin S, and the total angular momentum J. The J determined as: $\vec{J} = \vec{L} + \vec{S}$, which is the vector sum of orbital and spin momenta, and similarly, S is determined as: $\vec{S} = \vec{S}_c + \vec{S}_{\bar{c}}$, which is the vector sum of the quark and antiquark spins. Clearly, the spin S values can be 0 or 1, dividing the spin states of the pair into a singlet and a triplet. Additionally, radial motion excitation of the $c\bar{c}$ pair generates a spectrum of states with identical L, S, and J values but varying radial quantum excitation numbers (n_r), with $n_r = 0$ denoting the spectrum's lowest state. These quantum numbers are typically represented using the notation $(n_r + 1)^{2S+1}L_J$. The $2S + 1$ component indicates the spin multiplicity, and the L values are denoted as S, P, D, F, etc., following atomic physics tradition. For instance, the lowest state with $L = 0$, $S = 0$, and consequently $J = 0$ is denoted as 1^1S_0 (η_c resonance).

The parity (P) of each state is determined by L as $P = (-1)^{L+1}$, and the charge conjugation parity (C) is influenced by both L and S, resulting in $C = (-1)^{L+S}$. Thus, the mentioned $^1S_0$ states possess quantum numbers $J^{PC} = 0^{-+}$, while the $^3S_1$ states,

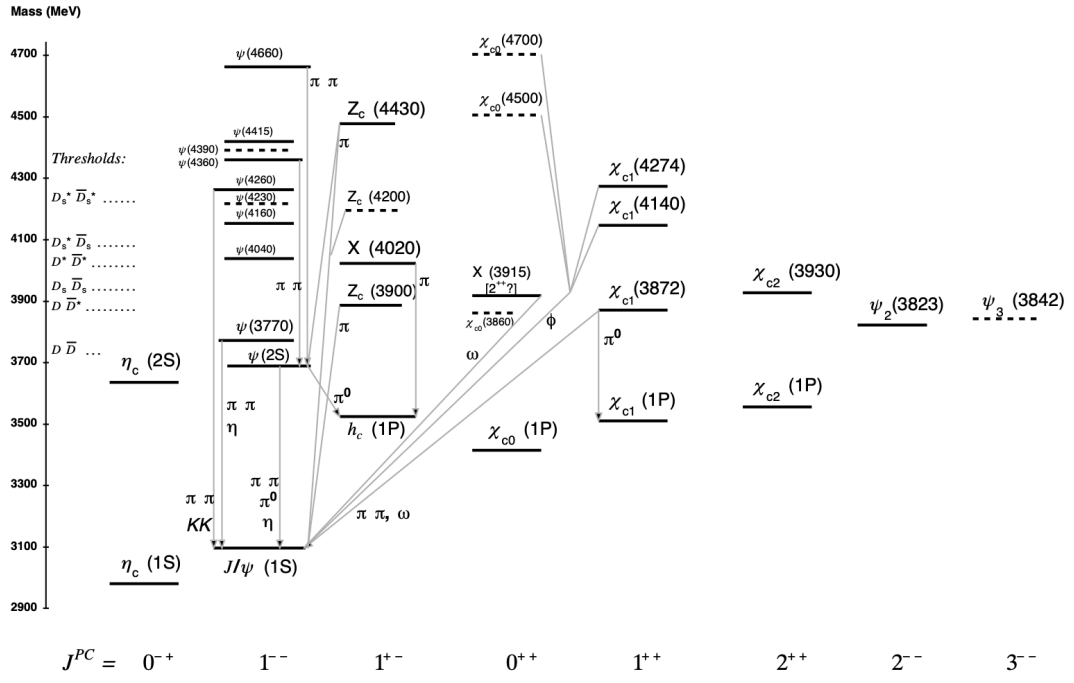

Figure 1.8 A schematic view of the charmonium family. Figure is taken from[31].

analogous to the electromagnetic current, have $J^{PC} = 1^{--}$, enabling their production as resonances in e^+e^- annihilation. J/ψ is a 1^3S_1 state, has $J^{PC} = 1^{--}$.

As illustrated in Fig. 1.8, excited charmonium states can decay to lower states. Therefore, the inclusive J/ψ meson sample measured experimentally includes contributions from both direct production and feed-down of excited charmonium states[32], termed prompt J/ψ, as well as from B hadron decays, known as non-prompt J/ψ. Experimentally, non-prompt contributions can be distinguished from prompt production by identifying the secondary decay vertices of B hadrons, achievable with high-precision spatial resolution provided by silicon detectors.

1.5.3 Quarkonium Production Mechanisms

Understanding the production mechanism of quarkonium states remains a significant challenge due to the intricate interplay between perturbative and nonperturbative physics. Quarkonium production is usually separated into two steps. The initial production of a heavy-quark pair $Q\bar{Q}$ occurs through a hard-scattering process, which is perturbative, given that the momentum transfer is at least as large as the heavy-quark mass m_Q, and $m_Q \gg \Lambda_{QCD}$, where Λ_{QCD} is the QCD scale parameter and the strong coupling constant α_s is small ($\alpha_s \ll 1$). However, the subsequent evolution of the $Q\bar{Q}$ pair into a bound quarkonium state involves dynamics at smaller momentum scales. This transition from the $Q\bar{Q}$ pair to a physical quarkonium state is nonperturbative, making

it the subject of various theoretical models. Below, we provide a brief overview of the most prominent models addressing quarkonium production:

1. The Color Evaporation Model

The Color Evaporation Model (CEM)[33-35] is assumed that any $Q\bar{Q}$ pair with an invariant mass below the open-charm (or open-bottom) threshold has a probability of evolving into a specific quarkonium state H. The probability is given by a constant F_H which is independent of momentum and process. Within the CEM, the production cross section for a quarkonium state H is given by:

$$\sigma_H = F_H \int_{2m_Q}^{2m_D} \frac{d\sigma_{Q\bar{Q}}}{dm_{Q\bar{Q}}} dm_{Q\bar{Q}}, \tag{1.5}$$

where $2m_D$ denotes the open-charm/bottom threshold. where $2m_D$ is the open-charm/bottom threshold. The model introduces a single free parameter F_H for each quarkonium state, encapsulating the model's simplicity and intuitive appeal. Despite its success in describing J/ψ production across various experiments, the CEM faces scrutiny for its prediction that the production ratios of different charmonium states are constant across processes and kinematic conditions. This prediction stands in contrast to experimental data, such as the observed p_{T} dependency of the $\psi(2S)$ to J/ψ production cross section ratio in proton-proton collisions[36-37]. To address these discrepancies, an Improved Color Evaporation Model (ICEM) has been proposed, incorporating a momentum scaling factor $\frac{m_{Q\bar{Q}}}{m_H}$ to account for the momentum discrepancy between the $Q\bar{Q}$ pair and the resultant quarkonium. In the ICEM, the lower limit of the above integral is replaced by m_H, allowing the model to describe the charmonium yields as well as the ratio of $\psi(2S)$ over J/ψ[38]. The ICEM was also combined with k_T-factorization to describe quarkonium polarization[39].

2. The Color-Singlet Model

In the Color-Singlet Model (CSM), the $Q\bar{Q}$ pair evolving into a quarkonium state is assumed to mirror the quarkonium's color, spin, and orbital-angular-momentum quantum numbers, specifically being in a color-singlet state. This model posits that the production cross section for each quarkonium state H is related to the wave function of H at the origin (or its derivatives), which can be deduced from the decay process of H or calculated through potential models or lattice QCD. Consequently, the CSM essentially introduces no free parameters. At relatively low energies, Leading Order (LO) predictions of the CSM for quarkonium production agree with the experimental data. However, at high energies, the LO CSM predictions significantly underestimate the experimental data on direct J/ψ and $\psi(2S)$ production in $\sqrt{s_{\mathrm{NN}}} = 1.8$ TeV $p+p$ collisions[40], which

is known as the $\psi(2S)$ surplus puzzle. Over the last decade, it has been observed that NLO and NNLO corrections to the CSM are significantly larger than the LO contributions[41-43], mitigating the disparity between LO CSM predictions and experimental data. Nevertheless, fully accounting for the experimental observations remains challenging. Moreover, the pronounced magnitude of NLO and NNLO corrections raises doubts about the convergence of the perturbative expansion in α_s. Additionally, for P-wave production and decay, the CSM encounters unresolved infrared divergences, a flaw effectively addressed within the broader framework of Non-Relativistic QCD (NRQCD) factorization theory.

3. The NRQCD Factorization Approach

NRQCD is an effective theory of QCD. NRQCD can reproduce the dynamics of full QCD at momentum scales of order $m_Q v$ and smaller. In NRQCD, the production cross section of a heavy quarkonium H can be represented by the factorization formula:

$$\sigma_H = \sum_n \sigma_n \left(\mu_\Lambda\right) \left\langle \mathcal{O}_n^H \left(\mu_\Lambda\right) \right\rangle, \tag{1.6}$$

where μ_Λ is the NRQCD factorization scale, representing the ultraviolet (UV) cutoff of the NRQCD effective theory. σ_n denotes the short-distance coefficient (SDC) which accounts for the production of a $Q\bar{Q}$ pair with quantum number n in the hard scattering, and $\left\langle \mathcal{O}_n^H \left(\mu_\Lambda\right) \right\rangle$ is the NRQCD long-distance matrix elements (LDMEs). The LDMEs are defined as the vacuum expectation value of a four-fermion operator in NRQCD, each scaled distinctively in powers of v. The LDMEs describe the hadronization of the $Q\bar{Q}$ pair in state n into heavy quarkonium H. The summation over n allows organization in powers of v, rendering Eq. 1.6 a double expansion in α_s and v. For specific accuracy, the summation is truncated, keeping only a few LDMEs for each H production. The effectiveness of the NRQCD factorization approach hinges on the convergence of this velocity expansion and the universality of LDMEs.

Notably, Eq. 1.6 incorporates contributions from both color-singlet (CS) and color-octet (CO) channels. Nullifying CO contributions reverts to the CSM for S-wave heavy quarkonium production. The inclusion of CO channels addresses the infrared divergence issue found in the CSM[44]. While a comprehensive proof of NRQCD factorization for quarkonium production is pending, evidence suggests that factorization is valid up to next-to-next-to-leading order (NNLO) in α_s, if the LDMEs are modified to ensure gauge completeness[45-46].

4. The Soft Gluon Factorization Approach

The Soft Gluon Factorization (SGF) approach was proposed to address certain challenges in describing inclusive quarkonium production data, where NRQCD shows limitations in its convergence in velocity expansion[47], alongside facing the universality problem and the polarization puzzle[48]. The SGF aims to offer a framework with enhanced convergence[49]. The differential cross section for the production of quarkonium H within SGF is factorized as follows:

$$(2\pi)^3 2P_H^0 \frac{d\sigma_H}{d^3P_H} \approx \sum_n \int \frac{d^4P}{(2\pi)^4} H_n(P) F_{n\longrightarrow H}\left(P, P_H\right), \tag{1.7}$$

where P represents the momentum of the intermediate $Q\bar{Q}$ pair, P_H is the momentum of H, and $F_{n\to H}\left(P, P_H\right)$ denotes the soft gluon distribution function (SGD), which also describes the hadronization of H but through soft hadron emission. Diverging from the NRQCD's approach, the SGF maintains a distinction between the momentum of the intermediate state P and the observed quarkonium momentum P_H, to incorporate the influence of soft hadron emission. The SGD is defined by QCD fields in a small loop momentum region. By precisely delineating this region and taking advantage of equations of motion, the SGF demonstrates equivalence to NRQCD factorization[50]. Yet, compared to NRQCD, SGF accumulates a series of relativistic corrections derived from kinematic effects, leading to a more convergent velocity expansion. Consequently, SGF is anticipated to align more closely with experimental data.

1.5.4 J/ψ in medium

Quarkonia also serve as important probes for the study of the QGP formed in ultra-relativistic heavy-ion collisions. Due to the significantly larger masses of the constituent heavy quarks ($m_c \sim 1.3$ GeV/c^2, $m_b \sim 4.8$ GeV/c^2) compared to light quarks and the QCD energy scale (Λ_{QCD})[51], quarkonia are produced predominantly through initial hard processes at the early stage of heavy-ion collisions, and their thermal production is negligible. Thus, quarkonia experience the entire evolution of the QGP, making them an ideal probe.

In a QED medium, Debye screening reduces the interaction between electric charges. Similarly, in the QGP, a color-screened Coulombic potential, akin to the Yukawa potential, is anticipated:

$$V_s = -\frac{4}{3} \times \frac{\alpha_s}{r} e^{-r/\lambda_D} \tag{1.8}$$

where λ_D represents the Debye screening radius, and r is the distance between interacting partons. If λ_D is smaller than the radius of the $Q\bar{Q}$ bound state, the confining

potential fails to maintain the quark-antiquark pair together, leading to dissociation of the quarkonium state. Experimentally, this manifests as a suppression of the quarkonium yields compared to the case of no QGP effects, and therefore the J/ψ suppression due to the color screening was proposed as a direct evidence of the QGP formation[52]. Since the Debye screen radius is inversely proportional to the medium temperature, the dissociation temperature (T_d), at which a particular quarkonium state breaks up, relates to its radius and consequently its binding energy. This implies that quarkonium states with a more lax binding exhibit lower T_d values. Within both the charmonium and bottomonium families, T_d diminishes as the mass of the quarkonium increases. Furthermore, excited states have a lower T_d compared to their respective ground states, as shown in Table 1.1[51,53]. Furthermore, inelastic collisions between quarkonia and constituents of the QGP can result in the dynamic dissociation of the bound states. This process can also contribute to the breakup of quarkonia, with its effects intensifying at higher medium temperatures and for quarkonia with larger sizes[54-55].

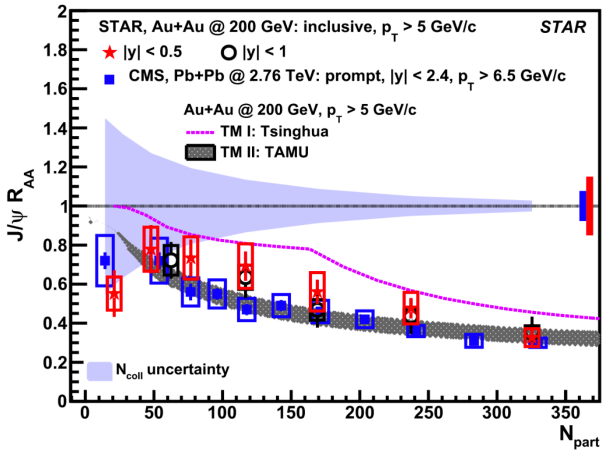

Figure 1.9 The J/ψ R_{AA} as a function of N_{part} in high p_{T} region in Au+Au collisions at $\sqrt{s_{\mathrm{NN}}}$ = 200 GeV measured by the RHIC-STAR experiment[56] and in Pb+Pb collisions at $\sqrt{s_{\mathrm{NN}}}$ = 2.76 TeV measured by the LHC-CMS experiment[57]. Figure is taken from[56].

Table 1.1 The mass, binding energy, radius, and dissociation temperature T_d/T_c of charmonium and bottomonium states. Table is taken from[53].

State	Charmonium			Bottomonium				
	J/ψ	χ_c	$\psi(2S)$	$\Upsilon(1S)$	χ_b	$\Upsilon(2S)$	χ_b'	$\Upsilon(3S)$
Mass (GeV/c^2)	3.10	3.53	3.68	9.46	9.99	10.02	10.26	10.36
Radium (fm)	0.25	0.36	0.45	0.14	0.22	0.28	0.34	0.39
ΔE (GeV/c^2)	0.64	0.20	0.05	1.10	0.67	0.54	0.31	0.20
T_d/T_c	2.1	1.16	1.12	≤ 4.0	1.76	1.6	1.19	1.17

Opposing the dissociation process, the yield of quarkonium production might be enhanced via the recombination of heavy quarks and their antiquarks throughout the

evolution of the QGP and/or during hadronization. This recombination mechanism suggests that a heavy quark and a heavy antiquark, even if not originally generated as a bound state or from the dissociation of a quarkonium, can form a bound state like J/ψ when they come into close proximity in terms of both space and momentum. The recombination probability scales with the square of the quantity of charm and anti-charm quark pairs generated in a singular event, which could reach up to 10 in central Au+Au collisions at top RHIC energy. The significant rise in the production cross section of charm and anticharm quark pairs with increasing collision energy can further enhance the importance of the recombination mechanism at the LHC.

To quantify quarkonium production modifications in heavy-ion collisions compared to that in p+p collisions, the nuclear modification factor, R_{AA}, is utilized, defined as:

$$R_{\mathrm{AA}} = \frac{1}{N_{\mathrm{coll}}} \times \frac{\left(dN/dp_{\mathrm{T}}\right)_{\mathrm{N+N}}}{\left(dN/dp_{\mathrm{T}}\right)_{p+p}}, \tag{1.9}$$

where N_{coll} is the average nucleon-nucleon binary collisions, $\left(dN/dp_{\mathrm{T}}\right)_{\mathrm{N+N}}$ is the yield in nucleus-nucleus collisions and $\left(dN/dp_{\mathrm{T}}\right)_{p+p}$ is the yield in p+p collisions. An $R_{\mathrm{AA}}<1$ indicates net suppression, while $R_{\mathrm{AA}}>1$ suggests net enhancement. Figure 1.9 shows the J/ψ R_{AA} as a function of N_{part} in high p_{T} region in 200 GeV Au+Au collisions measured by the RHIC-STAR experiment[56] and in 2.76 TeV Pb+Pb collisions measured by the LHC-CMS experiment[57]. For high p_{T} J/ψ, the expected regeneration contribution is minimal, and the Cold Nuclear Matter effects, which are discussed later, are also anticipated to be limited. The suppression of J/ψ production in 0-10% central collisions at STAR by a factor of 3.1, with 8.5σ significance, strongly supports the color-screening effect in the deconfined medium. Additionally, a systematic higher J/ψ R_{AA} at RHIC for semi-central bins hints at a higher medium temperature at the LHC than at RHIC, leading to an increased dissociation rate.

1.5.5 Cold nuclear matter effects

Besides the hot nuclear matter effects, the production of quarkonium in heavy-ion collisions is also influenced by the so-called cold nuclear matter (CNM) effects. These effects are attributed to the modifications in the properties and interactions of partons when they are embedded in a nuclear environment, independent of QGP creation. CNM effects can be experimentally explored through collisions between protons or light nuclei and heavy nuclei, where hot medium effects are expected to be minimal, if not absent. There are two primary categories of CNM effects: initial- and final-state effects.

Most of the initial-state effects caused by the nuclear parton distribution functions (nPDFs) are modified compared to those in a free nucleon, with modifications varying with the momentum fraction x and the square of the momentum transfer Q^2. For example, Fig. 1.10 illustrates the nuclear modification from EPPS21 as a function of x[58], showing nuclear shadowing (suppression at $x <\sim 0.05$) and anti-shadowing (enhancement around $x = 0.1$). Such altered nPDFs lead to modified hard partonic scatterings cross sections. Additionally, an energetic parton may undergo multiple scatterings before hard interactions, which will broad the transverse momentum distribution of quarkonium(the Cronin effect[59-61]). Furthermore, the gluon formation (radiation) time scale is comparable to the parton's traversal time through the nucleus, the fast parton may suffer energy loss in the cold nuclear target at the initial state[62-63].

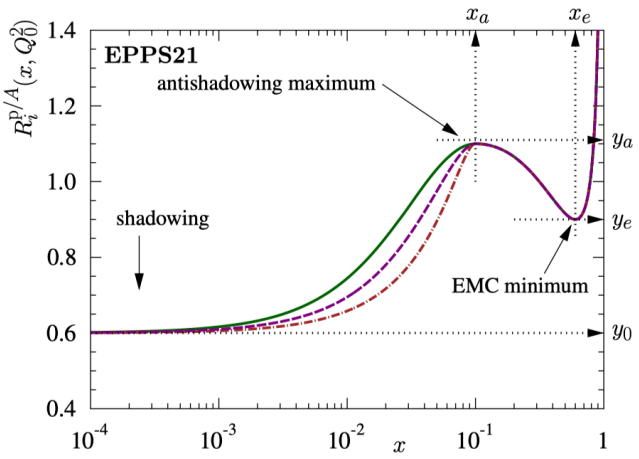

Figure 1.10 EPPS21 parameterization of nPDF modification relative to p+p. Figure is taken from[58].

Final-state effects encompass two main effects. Firstly, nuclear absorption, where a $Q\bar{Q}$ pair interacts with remnants of the heavy nucleus, potentially disrupting the pair and reducing the survival probability of quarkonia in a nuclear environment[64]. Secondly, nucleus-nucleus collisions often involve multiple nucleon-nucleon interactions per event, leading to a higher production rate of hadrons compared to that in p+p collisions. This increases the likelihood of produced quarkonia interacting with co-moving final-state hadrons, potentially leading to quarkonium breakup—a process referred to as co-mover absorption[65-66].

Figure 1.11 presents the inclusive J/ψ R_{AA} in 0-20% collisions as a function of $\sqrt{s_{\mathrm{NN}}}$[67]. The R_{AA} remains approximately constant at ~ 0.4 from $\sqrt{s_{\mathrm{NN}}} = 17.3$ GeV to 200 GeV, then dramatically increases to exceed 0.6 at LHC energies. Theoretical calculations from a transport model[68], which incorporates Cold Nuclear Matter (CNM)

effects, Quark-Gluon Plasma (QGP) melting, and recombination mechanisms, are depicted in the figure. The dashed curve represents the R_{AA} for primordially produced J/ψ, which is influenced by both QGP melting and CNM effects. This curve presents a relatively stable pattern from $\sqrt{s_{\mathrm{NN}}}$ = 17.3 GeV to 62 GeV, before it starts to diminish as the energy increase. This behavior stems from the interplay between the effects of CNM and the disintegration due to QGP; as energy escalates, the nuclear absorption cross-section declines, causing an upward shift in R_{AA} with energy. In contrast, the melting of QGP brings about a downward trend due to increased energy density, marking a significant influence at the highest RHIC energies. Exclusively attributing to CNM effects, the R_{AA} is projected to be approximately 0.6 in central Au+Au collisions at $\sqrt{s_{\mathrm{NN}}}$ = 200 GeV, according to[68]. The melting effect of QGP lowers the R_{AA} from 0.6 to 0.2. Illustrated by a dotted line, the R_{AA} for J/ψ through recombination is trivial from the SPS energy up to the RHIC BES energy level, gaining importance at elevated energies. At the pinnacle of RHIC energy, recombination's contribution to J/ψ parallels that of the primordial J/ψ that survives, taking a predominant stance at the LHC. The complete scenario, depicted by a solid line, accurately captures the inclusive J/ψ R_{AA} across central heavy-ion collisions from the SPS, dominated by CNM effects, to the LHC, where recombination takes precedence, within uncertainties.

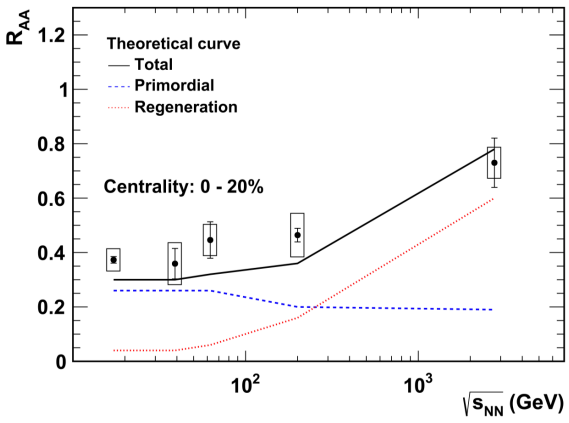

Figure 1.11 The results of J/ψ R_{AA} as a function of collision energy for centrality $0-20\%$, in comparison with model calculations[68]. Figure is taken from[67].

In summary, the mechanisms of dissociation, recombination, feed-down, and CNM effects have been briefly introduced. The complex interplay among these effects can qualitatively account for the observed modifications of J/ψ mesons in heavy-ion collisions. Additionally, the relativistic heavy ions generate strong electromagnetic fields, leading to the production of J/ψ mesons through coherent photon-nucleus interactions. This process is the main focus of this thesis work, and will be described in the following

sections.

1.6 Strong EM Fields in Heavy Ion collisions

Relativistic heavy-ion collisions generate strong electromagnetic (EM) fields, providing a unique environment for studying the QCD under the influence of strong EM fields. The basis for the production of these fields can be understood by considering the movement of a single nucleus at ultra-relativistic speeds, as shown in Fig. 1.12, which can be described by Maxwell's equations. When such a positively charged nucleus moves through space, it creates an electric current, inducing a magnetic field that encircles the current. Due to Lorentz contraction, the electric fields of the moving nucleus are compressed into the transverse plane perpendicular to its direction of motion, alongside the induced magnetic fields, allowing the fields to be effectively approximated as a transverse electromagnetic wave. This framework sets the stage for understanding EM field generation in the context of heavy-ion collisions. In the scenario where two nuclei collide head-on at a non-zero impact parameter b, Fig. 1.13 provides a geometrical depiction of a non-central heavy-ion collision[69]. In the given plot, R_A symbolizes the radius of the nucleus. The impact parameter is parallel to the x-axis, while the z-axis runs along the beam direction. The span of the x and z axes defines the reaction plane. Due to the symmetry of the collision geometry on the left and right, the magnetic field at the center of the overlap area is anticipated to be perpendicular to the reaction plane, specifically in the -$\hat{y}$ direction. To estimate the strength of the magnetic field, we consider a Au+Au collision at a fixed impact parameter b = 10 fm at the center-of-mass energy per nucleon-nucleon pair ($\sqrt{s_{\rm NN}}$) of 200 GeV. Using the Biot-Savart law, a simple estimation yields:

$$-eB_y \sim 2Z_{\rm Au}\gamma\frac{e^2}{4\pi}v_z\left(\frac{2}{b}\right)^2 \approx 10m_\pi^2 \approx 10^{19}\ \text{Gauss}\ , \tag{1.10}$$

where $v_z = \sqrt{1-\left(2m_N/\sqrt{s}\right)^2} \approx 0.99995$ (with m_N being the nucleon mass) is the velocity of the nucleus, $\gamma = 1/\sqrt{1-v_z^2} \approx 100$ is the Lorentz gamma factor, and Z_{Au} = 79 is the charge number of the gold nucleus.

This estimated magnetic field strength is among the strongest known in the Universe, surpassing even the magnetic fields of magnetars ($\sim 10^{14} - 10^{15}$ Gauss[70-71]). However, this simplified estimation needs refinement to accurately simulate EM fields in heavy-ion collisions, considering factors such as the Woods-Saxon distribution for protons and neutrons within nuclei, event-by-event fluctuations due to varying proton

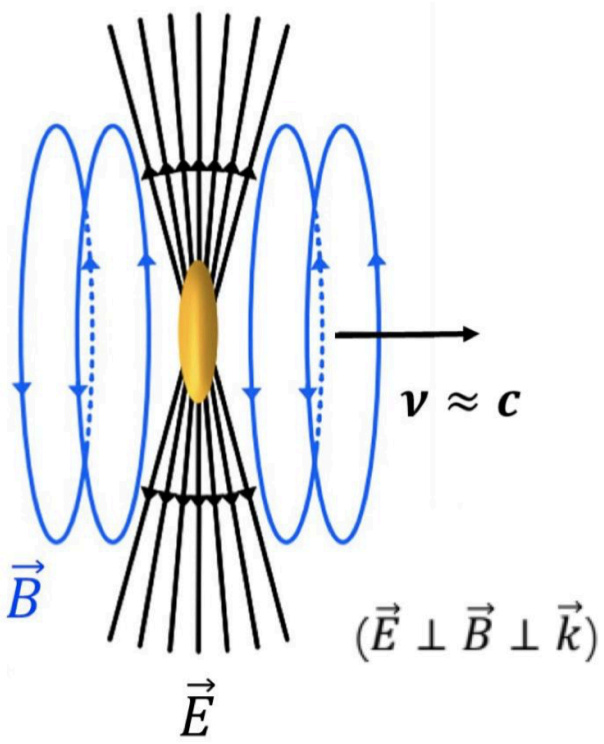

Figure 1.12 A schematic view of the electromagnetic field from a boosted nucleus.

.

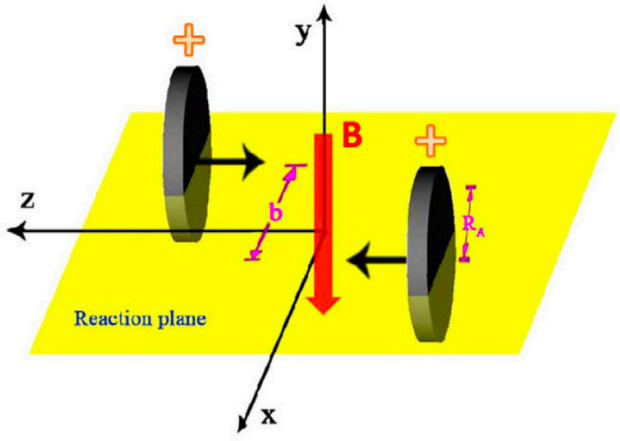

Figure 1.13 A geometrical representation of the magnetic field in a non-central heavy-ion collision. Here R_A signifies the radius of the nucleus, and b is the impact parameter. Due to the left-right symmetry inherent in the collision geometry, the magnetic field B is perpendicular to the reaction plane. Figure is taken from [69].

distributions[72-74], and the replacement of the Biot-Savart law with the full relativistic Liénard-Wiechert potentials to account for retardation effects. Figure 1.14 shows the impact parameter dependence of EM fields at the relative position of the field point $r = 0$ and $t = 0$, with the time $t = 0$ defined as the moment of complete overlap between the colliding nuclei. The y-component of the event-averaged EM fields is represented by black curves, while the absolute values for the x- and y-components of magnetic fields for individual events are depicted by blue and red curves, respectively. The x- and y-components of electric fields for each event are shown in violet and orange. Results for Au+Au collisions at RHIC energy of $\sqrt{s_{\rm NN}}$ = 200 GeV and Pb+Pb collisions at LHC energy of $\sqrt{s_{\rm NN}}$ = 2.76 TeV are indicated by full and open symbols, respectively, with the latter scaled by a factor of 13.8 = 2760/200. The close similarity between RHIC and scaled LHC results suggest a linear dependency of EM field magnitude on collision energy. The event averaged EM fields predominantly exhibit a nonzero $\langle B_y \rangle$ component, with all other components ($\langle B_x \rangle$, $\langle B_z \rangle$, $\langle E \rangle$) averaging to zero. Nonetheless, due to fluctuations in proton positions within the nuclei, their magnitudes can be significant in an individual event (except for the z-components, which remain minimal).

The EM field's time evolution in the early stages of a heavy-ion collision is mainly driven by spectators. They exit the collision region swiftly, with the magnetic field's lifetime due to spectators estimated by $t_B \approx R_A/\left(\gamma v_z\right) \approx \frac{2m_{\rm N}}{\sqrt{s}} R_A$, reflecting a brief existence for large $\sqrt{s_{\rm NN}}$ values. For Au+Au collisions at 200 GeV, t_B is approximately 0.065 fm, and for Pb+Pb collisions at 2.76 TeV, t_B is around 0.005 fm. Figure 1.15 presents the numerical results for the early-stage time evolutions of EM fields at the center point (r = 0) in collisions with an impact parameter b of 10 fm, for 200 GeV Au+Au and 2.76 TeV Pb+Pb collisions. The transverse fields diminish rapidly following the collision, illustrating the rapid departure of the spectators from the collision zone. However, the formation of QGP alters the EM field's temporal evolution. QGP, as indicated by theoretical and lattice QCD studies[75-76], exhibits properties of a good conductor. This characteristic leads to the occurrence of Faraday induction within the QGP. In this phenomenon, a rapidly diminishing external magnetic field induces a circular electric current within the medium. This induced current subsequently produces a magnetic field that acts to counter the decay of the external field. Still, precise calculation of magnetic field evolution during the QGP stage remains challenging due to the complexity of the system.

There are numerous quantum phenomena are expected through the strong EM fields produced in heavy-ion collisions, drawing considerable interests from both

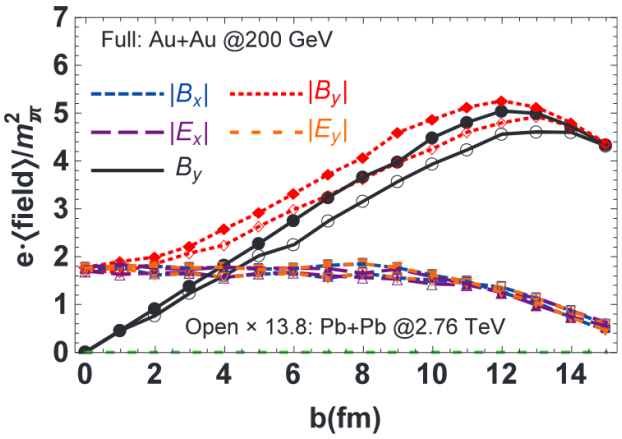

Figure 1.14 Different components of EM fields at the point in time $t = 0$ and at the relative position of the field point $r = 0$ are depicted as a functions of the impact parameter b. Figure is taken from [69,73].

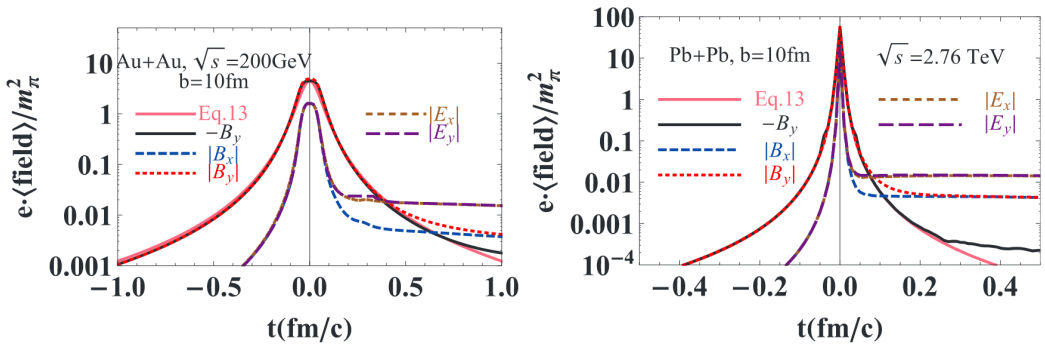

Figure 1.15 Early-stage evolution of the EM fields at $r = 0$ with $b = 10$ for 200 GeV Au + Au collisions and 2.76 TeV Pb + Pb collisions. Figure is taken from [73].

high-energy and nuclear physics communities, such as the Chiral Magnetic Effect (CME)[69,77-82], the magnetic field effect on charmonium production[83], the magnetic field effect on the polarization of quarks[84-85], etc. Efforts to explore QCD matter under strong EM fields have led to the development of theoretical models and experimental approaches. These phenomena predominantly occur in the presence of the strong EM field within the QGP. However, the initial conditions of these EM fields, including their initial strength, spatial distribution, and the relationship between the EM fields and the nuclear charge distribution, are yet to be fully understood. These factors play a pivotal role in understanding the time evolution of EM fields within the QGP. Photon induced interactions, which are intrinsically related to the initial EM fields, offer additional insights into these initial conditions.

1.7 Photoproduced J/ψ

1.7.1 Equivalent photon approximation

As discussed earlier, the boosted nuclei are capable of generating intense EM fields in relativistic heavy-ion collisions. As a consequence of Lorentz contraction, the electromagnetic fields undergo compression into the transverse plane, perpendicular to the direction of particle motion. This configuration permits the approximation of these fields as a transverse electromagnetic wave. In such a setup, the electric and magnetic fields, nearly equal in absolute value, are perpendicular to each other, resembling the electromagnetic fields of photons, as illustrated in Fig. 1.12. In 1924, Fermi introduced a technique known as the equivalent (or virtual) photon method, replacing the electromagnetic fields from a fast charged particle with an equivalent flux of virtual photons[86]. This approach was later expanded by Weizsäcker and Williams in the 1930s to encompass ultra-relativistic particles, thereby establishing what is often referred to as the Weizsäcker-Williams method[87-88]. Within this framework, the Equivalent Photon Approximation (EPA) posits that in a specific phase space, the energy flux of a moving nucleus's transverse electromagnetic field can be described by the Poynting vector ($\vec{S} = \frac{1}{\mu_0}\vec{E} \times \vec{B}$). The number of equivalent photons is determined by the energy flux and is proportional to the Z^2, where Z is the charge of the nucleus.

The presence of strong EM fields enables the photon-induced processes during the collision of two fast moving nuclei, leading to two primary types of electromagnetic interactions: photon-nucleus and photon-photon processes[89-91]. As shown in Fig. 1.16, in the photon-nucleus process, a photon from one nucleus impacts the other, while in the photon-photon process, photons from each nucleus collide. The coherent photon-photon process can generate dilepton pairs ($\gamma + \gamma \rightarrow l^+ + l^-$, where $l = e, \mu, \tau$) through the Breit-Wheeler process[92] . On the other hand, the photon-nucleus process can produce vector mesons ($\gamma + A \rightarrow V + A$), such as J/ψ, ρ, ω, etc., occurring either coherently, leaving the target nucleus intact, or incoherently, where the target nucleus has been excited or dissociated.

1.7.2 Coherent photon-nucleus interaction

Coherent photon-nucleus process is constrained by the requirement of color neutrality, necessitating the exchange of at least two gluons. At high energies, such exchanges are dominated by a pomeron exchange, a theoretical construct with vacuum-like quantum numbers $J^{PC} = 0^{++}$[90]. This exchange effectively represents the absorptive

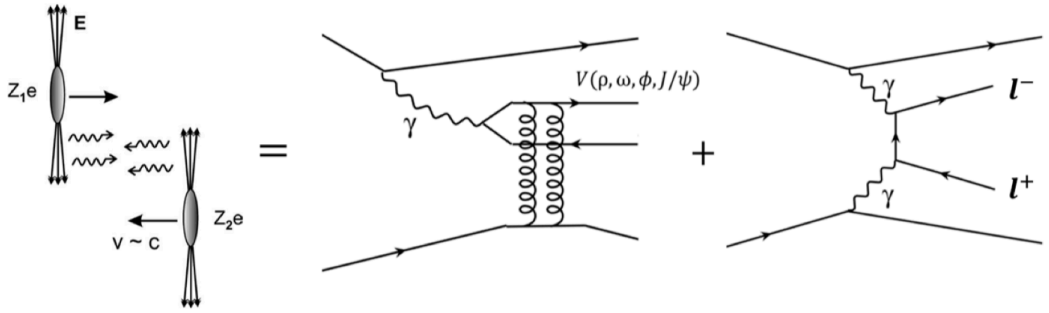

Figure 1.16 The schematic view of two possible photon-induced processes.

.

component of the cross section, facilitating interactions without color exchange. Beyond the dominant photon-Pomeron fusion mechanism, coherent J/ψ production in heavy-ion collisions may also proceed via three-photon (3γ) fusion and Pomeron-odderon processes. However, calculations by Bertulani and Navarra for both RHIC and LHC energies have demonstrated that the cross section for J/ψ production through three-photon fusion is negligible compared to photon-Pomeron fusion[93-94]. Furthermore, in the context of heavy-ion collisions, the photon-Pomeron process is expected to overshadow Pomeron-odderon contributions, given the amplification of the coherent photon flux by a factor of Z^2, in contrast to the $A^{1/3}$ scaling of the odderon[95]. The photon-Pomeron fusion allows for the fluctuation of virtual photons emitted by one nucleus into $c\bar{c}$ pairs, which can then scatter off the opposing nucleus, resulting in the production of J/ψ. This process's coherent nature is characterized by a distinct signature: the emergence of two intact nuclei and a singular J/ψ possessing very low transverse momentum ($p_{\mathrm{T}} < 0.1$ GeV/c) as the sole product of the interaction.

Traditionally, such coherent photon-nucleus interactions are studied primarily in Ultra-Peripheral Collisions (UPCs), where no hadronic interactions, since the impact parameter (b) is larger than twice the nuclear radius (R_A)[96-98]. Recent experimental findings in hadronic heavy-ion collisions (HHICs), however, suggest the presence of such coherent photon-nucleus interactions[99-101], presenting significant challenges to existing models, particularly concerning how disrupted nuclei maintain their coherence. The energetic hadronic interactions in HHICs occur on a significantly reduced timescale compared to the coherent process, potentially exerting a profound influence on coherent photoproduction. To adapt theoretical frameworks to HHICs, one can address potential disruptive effects on two specific subprocesses: photon emission and coherent scattering[102]. Consequently, four different scenarios emerge for the coherent J/ψ production: (1) nucleus (photon emitter) + nucleus (target), short for "N+N" here; (2) nucleus + spectator ("N+S"); (3) spectator + nucleus ("S+N"), and (4) spectator

+ spectator ("S+S"). Furthermore, for J/ψ with $p_{\mathrm{T}} < \hbar/b$, distinguishing between the photon-emitting nucleus and the target nucleus becomes infeasible. The inherent negative parity of the J/ψ meson leads to opposing signs between the two interaction amplitudes, resulting in destructive interference. This phenomenon, known as the INT2N effect, has been analyzed by Klein and Nystrand in their work of vector meson production in UPCs[103] and subsequently verified by the STAR measurement of coherent ρ^0 production[104]. Contrary to UPCs, the impact parameters in HHICs are correlatable with the collision centrality. Such a correlation enables a direct comparison between the measured p_{T} spectra of coherent J/ψ production across various centrality classes and the theoretical predictions for varying impact parameters. Such comparisons facilitate a differential examination of the INT2N effect, providing insights into the detailed dynamics of photon-induced interactions in a heavy-ion collision environment.

In recent years, numerous experiments have focused on investigating the coherent photoproduction within the nuclear overlap region. Key questions under exploration include: How does the coherence condition persist in photon-nucleus interactions even when the nucleus may be disrupted during hadronic collisions? How to identify the roles of spectators and participants as photon sources and targets in the coherent process? To what extent does the photon-nucleus cross section undergo modifications by target nucleons that engage in hadronic interactions and consequently lose energy prior to photoproduction? Additionally, how does the interaction with the rapidly expanding QGP medium influence the yield of photoproduced J/ψ mesons? Moreover, the coherent photoproduction mechanism, wherein a photon interacts with an entire nucleus, offers insights into the initial electromagnetic fields, the parton distribution, and enables studies on interference. These investigations not only enhance our understanding of the QGP properties but also contribute to our knowledge of nuclear structure.

1.7.3 Previous experimental results

The coherent photoproduction of J/ψ in hadronic heavy-ion collisions has been explored through experiments at RHIC and the LHC. This section presents a brief overview of these findings.

1. ALICE measurements

ALICE (A Large Ion Collider Experiment) is a detector dedicated to heavy-ion physics at the LHC. In 2016 ALICE first reported significant excesses of J/ψ yield at very low p_{T} (< 0.3 GeV) in peripheral Pb+Pb collisions at $\sqrt{s_{\mathrm{NN}}} = 2.76$ TeV[99]. Figure 1.17 shows the J/ψ R_{AA} as a function of $\langle N_{\mathrm{part}} \rangle$ for three p_{T} ranges at forward rapidity

(2.5 < y < 4). The J/ψ R_{AA} demonstrates a marked increase in the p_{T} range 0-0.3 GeV for the most peripheral Pb+Pb collisions, a pattern not predicted by transport models at LHC energies. Coherent photoproduction of J/ψ in overlapping Pb–Pb collisions was proposed as a plausible explanation for these observations.

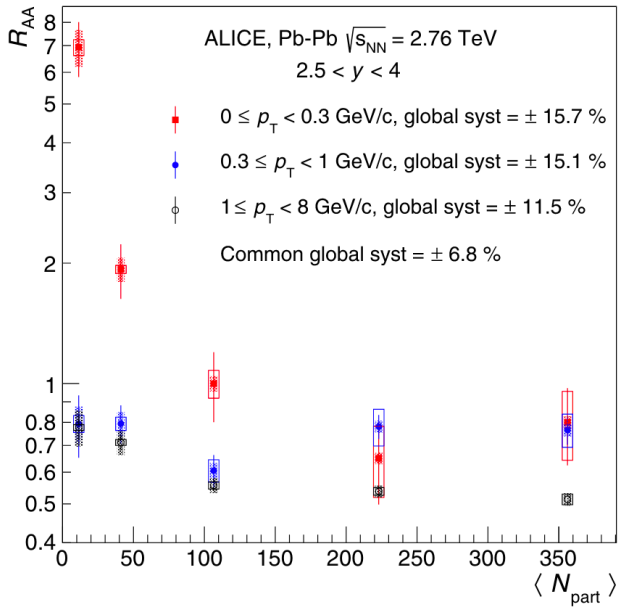

Figure 1.17 J/ψ R_{AA} **as a function of** $\langle N_{\mathrm{part}} \rangle$ **for three** p_{T} **ranges in Pb+Pb collisions at** $\sqrt{s_{\mathrm{NN}}}$ **= 2.76 TeV. Figure is taken from** [99].

Further, in 2023, ALICE reported on the measurement of J/ψ production at very low p_{T} in hadronic Pb+Pb collisions at $\sqrt{s_{\mathrm{NN}}} = 5.02$ TeV at forward rapidity [105]. Figure 1.18 depicts J/ψ R_{AA} as a function of $\langle N_{\mathrm{part}} \rangle$, as in Fig. 1.17. The R_{AA} at $p_{\mathrm{T}} < 0.3$ GeV/c, a region expected to contain the largest coherent photoproduction, and $0.3 < p_{\mathrm{T}} < 1.0$ GeV/c, where incoherent photoproduction might contribute, are contrasted with that for $1.0 < p_{\mathrm{T}} < 2.0$ GeV/c, dominated by hadroproduction. Notably, the R_{AA} for the p_{T} interval $0-0.3$ GeV/c is significantly higher than the R_{AA} at larger transverse momenta, with the exception of the most central events. This data set is compared against a model encompassing initial J/ψ production, J/ψ regeneration, and a J/ψ photoproduction component specifically for $p_{\mathrm{T}} < 0.3$ GeV/c [106]. Additionally, this model accounts for modifications of both shadowing effect and QGP suppressions on photoproduced J/ψ. The theoretical predictions are found to be in good agreement with the observed data across the considered p_{T} and centrality ranges.

This measurement also quantified the excess relative to the expected hadronic production, revealing an enhancement with great significance at very low p_{T} ($p_{\mathrm{T}} < 0.3$ GeV/c): 24σ in the 70–90% centrality class, 16σ in 50–70%, and 5.6σ in the 30–50%

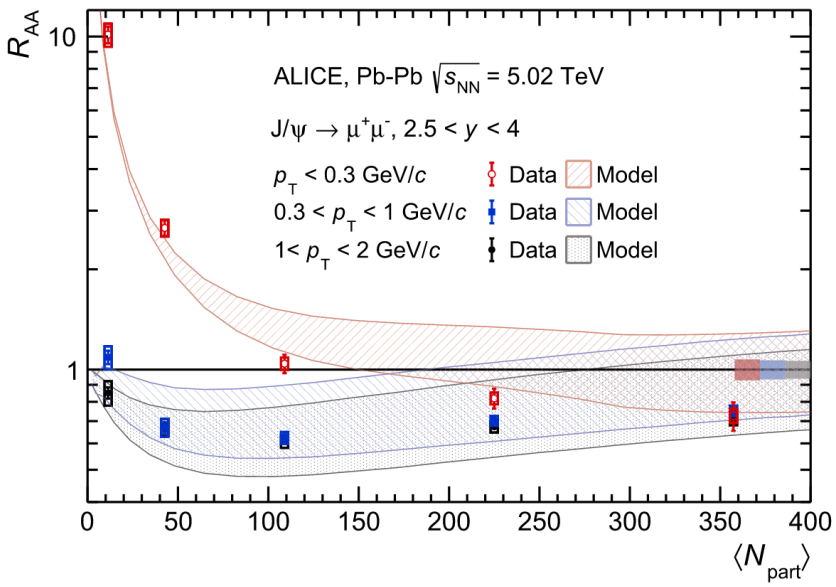

Figure 1.18 J/ψ R_{AA} **as a function of** $\langle N_{part} \rangle$ **measured in the rapidity range of** $2.5 < y < 4$ **for three transverse momentum intervals. Data are compared with predictions from**[106]**, shown as bands. Figure is taken from**[105]**.**

centrality class. Figure 1.19 presents the coherent J/ψ photoproduction cross section at $\sqrt{s_{NN}}$ = 5.02 TeV as a function of $\langle N_{part} \rangle$, compared with several theoretical calculations. Among these models are:

- A model representing subnucleonic degrees of freedom as hot spots, extended from protonic to nuclear targets via the Glauber–Gribov (GG-hs) approach[107], applicable predominantly to the most peripheral centrality interval (70-90%), where it aligns well with the data.
- A vector dominance model (VDM)[108], predicting a mild cross section increase in peripheral events, a stable evolution in semi-central events, and a decrease in the most central events, displaying reasonable agreement with the observed data.
- Models based on the GBW and IIM calculations, offering two scenarios[109]. The GBW model utilizes the light cone color dipole formalism, while the IIM model adopts the Color Glass Condensate approach (IIM S2 and S3, and GBW S2 and S3). The S2 scenario of the GBW model tends to overestimate the data across all centrality intervals, whereas the IIM model remains consistent with the data in the initial two centrality intervals but diverges by 2.1σ in the 30–50% centrality class. Conversely, the S3 version of both GBW and IIM models exhibits compatibility with the data across the entire range of centralities, albeit within the bounds of current uncertainties.

Figure 1.20 presents the ratio of the coherent J/ψ cross section at $\sqrt{s_{NN}}$ = 5.02 TeV and $\sqrt{s_{NN}}$ = 2.76 TeV. This ratio reveals that the hot-spot model tends to underestimate

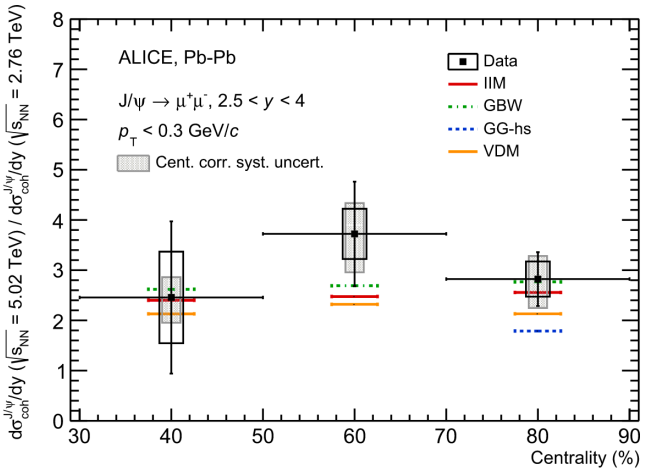

Figure 1.19 J/ψ **coherent photoproduction cross section as a function of** $\langle N_{\text{part}} \rangle$ **in 5.02 TeV Pb+Pb collisions at forward rapidity. Figure is taken from** [105].

the increase in the cross section with the center-of-mass energy in peripheral hadronic interactions. Conversely, the other models, including the IIM and GBW, demonstrate a reasonable agreement with the observed ratio across all centrality ranges, albeit within significant uncertainties. Notably, in this comparison, no distinction is made between the IIM and GBW model scenarios with or without modification of the photon-nucleus cross section, as their energy dependence is identically the same. In summary, a set of theoretical calculations successfully used to describe coherent photoproduction in UPC, and modified to account for geometrical constraints on the photon flux in the selected centrality classes, is compared with the measurement. The cross section as a function of centrality is well described by two models, one implementing a modification of the photon flux only, and the other requiring an additional modification of the photon-nucleus cross section.

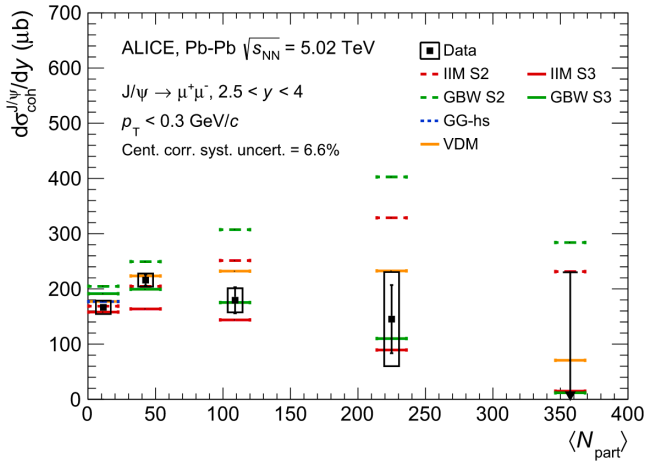

Figure 1.20 J/ψ **coherent photoproduction cross section ratio for two different energies** $\left(\sqrt{s_{\text{NN}}} = 5.02\text{TeV}\right.$ **over** $\left.\sqrt{s_{\text{NN}}} = 2.76\text{TeV}\right)$ **as a function of centrality. Figure is taken from** [105].

Most recently, ALICE measured the coherent J/ψ photoproduction cross section at midrapidity in peripheral to semi-central Pb+Pb collisions at $\sqrt{s_{\rm NN}} = 5.02$ TeV. Figure 1.21 shows the double-differential cross section $\mathrm{d}^2\sigma/\mathrm{d}y\,\mathrm{d}p_{\rm T}$ extracted for the $50-70$ and $70-90\%$ centrality classes. Theoretical calculations[102,110] can well describe the measurements in both $p_{\rm T}$ shape and magnitude within the large experimental uncertainties.

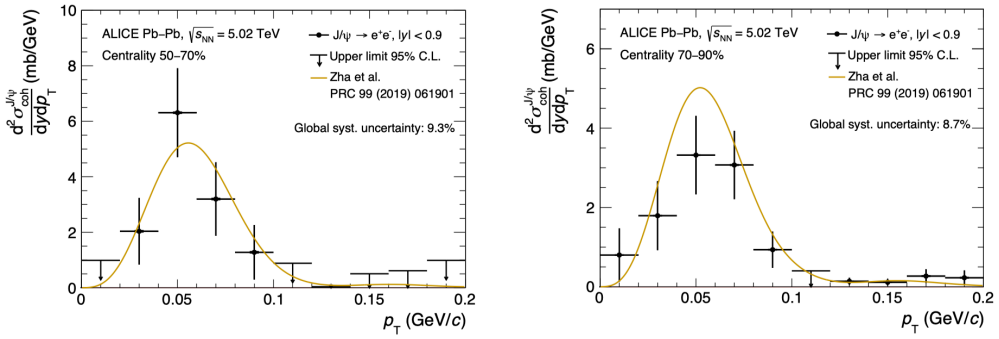

Figure 1.21 Coherent J/ψ cross section as a function of $p_{\rm T}$ in Pb+Pb collisions at $\sqrt{s_{\rm NN}} = 5.02$ TeV in midrapidity measured in the 50-70% and 70-90% centrality classes.

The left panel of Fig. 1.22 shows the coherent J/ψ photoproduction cross section $\mathrm{d}\sigma/\mathrm{d}y$, extracted at midrapidity ($|y| < 0.9$), as a function of $\langle N_{\rm part} \rangle$, for the centrality classes 70-90, 50-70 and 40-50%. Experimental results are compared with theoretical calculations, showing qualitative agreement, although the absolute cross section values for the two most peripheral intervals are overestimated by all models. Specifically, the GBW and the IIM calculations[109] for scenario S3, which account for suppression in the overlap zone, most closely match the data with statistical significance of differences averaged over the three centrality intervals of less than 2σ.

Experimental data has yet to reveal evidence of any final-state QGP influence on photoproduced charmonia. In the naive expectation, there will be more obvious effects at midrapidity due to higher medium temperatures and radial velocities. To investigate potential QGP effects, a comparison of the centrality dependence of photoproduced J/ψ yield at mid- and forward-rapidity has been conducted, normalizing measurements to coherent J/ψ production cross sections in UPC within the same rapidity intervals. The right panel of Fig. 1.22 shows this ratio, corrected for centrality interval widths ΔC, as a function of $\langle N_{\rm part} \rangle$, for both rapidity ranges. Despite large uncertainties, ratios at two rapidities are statistically compatible, displaying a nearly flat trend with $\langle N_{\rm part} \rangle$. Precise measurements for the most peripheral collisions, $70-90\%$, are in excellent agreement. The measured cross sections do not indicate QGP effects, though

the limited centrality range and significant uncertainties may obscure medium-induced suppressions. The upcoming LHC Runs 3 and 4, with increased luminosity, are expected to broaden this measurement to central collisions and clarify these phenomenological aspects.

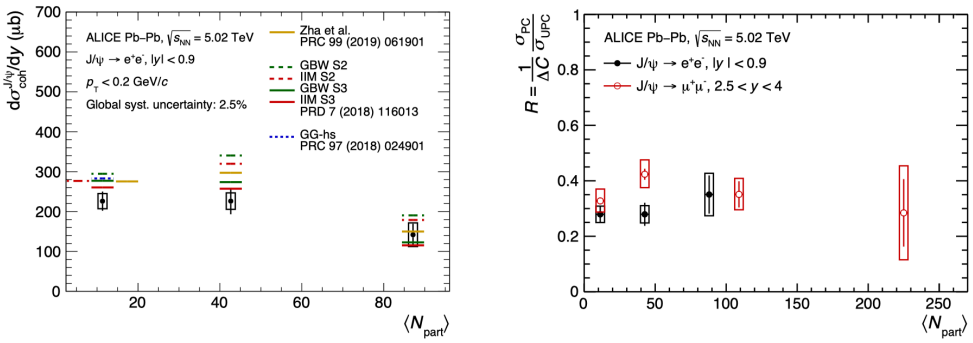

Figure 1.22 Left: Coherent J/ψ cross section as a function of N_{part} in Pb+Pb collisions at $\sqrt{s_{NN}}$ = 5.02 TeV. Right: Coherent J/ψ cross section measured at midrapidity (black markers) and forward rapidity (red markers)[105] normalized to the corresponding cross section measured in the same rapidity range in UPC.

2. STAR measurements

The Solenoidal Tracker at RHIC (STAR) is an experiment constructed at RHIC to investigating the formation and characteristics of QGP. STAR has reported measurements of J/ψ production yields at very low p_T in Au+Au collisions at $\sqrt{s_{NN}}$ = 200 GeV and U+U collisions at $\sqrt{s_{NN}}$ = 193 GeV at mid-rapidity via the dielectron decay channel[101]. Figure 1.23 illustrates the J/ψ R_{AA} as a function of p_T across different centrality classes for both collision systems. A suppression of J/ψ production for p_T > 0.2 GeV/c aligns with prior observations and fits within predictions from transport models considering both cold and hot medium effects[68,111]. Remarkably, an enhancement of R_{AA} above unity in the p_T < 0.2 GeV/c range for peripheral collisions (40-80%) suggests an additional production mechanism beyond dissociation (suppression), CNM effects (suppression), and regeneration (enhancement but negligible) in peripheral collisions. The overall impact would result in a value of R_{AA} less than 1 for hadronic production, markedly below what is currently observed in measurements. For p_T < 0.05 GeV/c in the 60-80% centrality class, the R_{AA} is 24 ± 5 (stat.) ±9 (syst.) for Au+Au collisions and 52 ± 18 (stat.) ±16 (syst.) for U+U collisions. These values show a significant deviation from the expectations based on the hadronic p+p reference scaled by the number of binary nucleon-nucleon collisions (N_{coll}).

Assuming that the coherent photoproduction is the mechanism to the observed excess, STAR has also reported on the differential cross section $d\sigma/dt$, where t represents

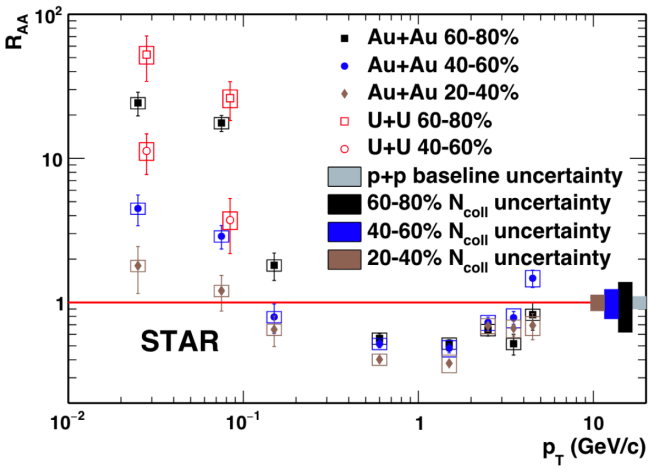

Figure 1.23 The p_T dependence of J/ψ R_{AA} in 200 GeV Au + Au collisions and 193 GeV U + U collisions. Figure is taken from[101].

the negative momentum transfer squared ($-t \sim p_T^2$). The $d\sigma/dt$ measurement is closely related to the parton distribution and sheds light on the distribution of interaction sites within the nucleus. Figure 1.24 displays the J/ψ yield, after subtracting the expected hadronic contribution, plotted against $-t$ for the 40-80% centrality class in both Au+Au and U+U collisions. The shape of the dN/dt distribution shows a coherent peak and an incoherent tail, which is very similar to that seen for the ρ^0 meson in UPC[112]. An exponential fit has been applied to the Au+Au collision data over the $-t$ range of 0.001-0.015 GeV/c^2, with the slope parameter indicative of the interaction sites' positioning within the target. This parameter, measured as 177 $\pm$ 23 GeV/c^2, aligns within uncertainties with expectations for an Au nucleus (199 GeV/c^2)[103]. Notably, the data point at -t < 0.001 GeV/c^2 falls significantly lower (3.0σ) than the exponential fit's extrapolation, suggesting potential interference as aforementioned, which is corroborated by ρ^0 meson results previously measured by STAR[112]. An theoretical calculation incorporating interference, depicted as the blue curve, describes the Au+Au data (χ^2/ndf = 4.8/4) for -t < 0.015 GeV/c^2 quite well.

Figure 1.25 presents the N_{part} dependence of the p_T-integrated J/ψ excess yields for p_T < 0.1 GeV/c for 30-80% Au+Au and 40-80% U+U collisions. The expected hadronic contributions are subtracted and also plotted for comparison in Au+Au collisions. It is evident that hadronic production is subdominate in the low p_T range for the measured centrality classes. Moreover, the observed excess exhibits no significant centrality dependency within the uncertainties while hadronic contributions markedly increase towards more central collisions. For coherent photoproduction, the yield in U+U collisions would be expected to surpass that in Au+Au collisions due to the larger electric charge of the Uranium nucleus and thus larger photon flux. As expected, the

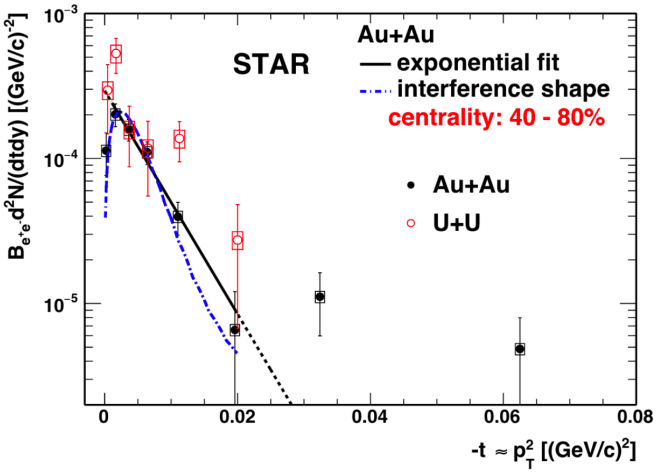

Figure 1.24 The J/ψ yield as a function of the negative momentum transfer squared $-t$ ($-t \sim p_T^2$) for the $40-80\%$ centrality class in $\mathrm{Au}+\mathrm{Au}$ and $\mathrm{U}+\mathrm{U}$ collisions. Figure is taken from [101].

measured central values in U+U collisions are larger than those in Au+Au collisions, although the observed discrepancy (2.0σ) is not significant. Model calculations for coherent J/ψ photoproduction in Au+Au collisions, using four aforementioned scenarios for photon and Pomeron emitters are also shown for comparison[102]. Each scenario is capable of describing the data in the most peripheral centrality classes (60-80%). On the other hand, the N+N configuration substantially overestimates the yields the 30-40% centrality class, suggesting a disruption of coherent production due to the concurrent hadronic interactions in the overlapping region. Semi-central collision data appear to align more closely with the N+S or S+N scenarios. However, potential modifications to coherently produced J/ψ by hot medium effects, such as dissociation in the QGP, is not included in this model.

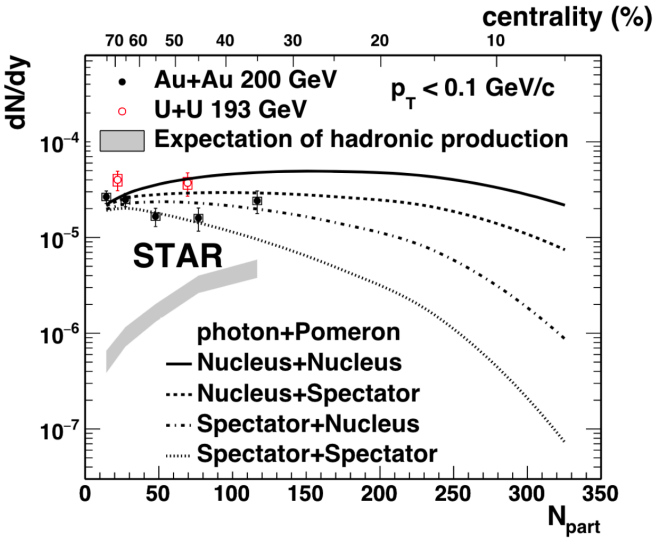

Figure 1.25 The p_T-integrated J/ψ yields (p_T < 0.1 GeV/c) as a function of N_{part} for 30-80% Au+Au collisions and 40-80% U+U collisions. Figure is taken from [101].

3. LHCb measurements

The Large Hadron Collider beauty (LHCb) experiment has also reported precise measurements of prompt J/ψ production at very low p_{T} in Pb+Pb collisions at $\sqrt{s_{\mathrm{NN}}} = 5$ TeV [113] in forward rapidity ($2.0 < y < 4.5$). Figure 1.26, top panel, shows the differential yield of photoproduced J/ψ as a function of rapidity for events with $\langle N_{\mathrm{part}} \rangle = 19.7 \pm 9.2$, while the middle panel exhibits the differential yield as a function of $\langle N_{\mathrm{part}} \rangle$. Additionally, the bottom panel showcases the double-differential J/ψ photoproduction yield as a function of p_{T}. The mean p_{T} of the coherent J/ψ is found to be $\langle p_T \rangle = 64.9 \pm 2.4$ MeV/c. The results indicates that the yield of coherently produced J/ψ is higher at lower rapidity and remains consistent with respect to $\langle N_{\mathrm{part}} \rangle$ within the analyzed region. The results are compared to the theoretical calculations [102,110], which include two scenarios regarding the coherence of J/ψ production: one accounting for interactions within the overlap region of the colliding nuclei (overlap effect) and another excluding such interactions (no overlap effect). Calculations reveal a minimal difference between these two scenarios. There is a mild trend that the difference grows towards central collisions, which could be attributed to the augmented photon flux with reduced impact parameter for the scenario without taking into account the overlap effect. For the scenario accounting for the overlap effect, this enhancement in photon flux is mitigated by excluding the overlapping region from the interaction domain. The theoretical calculations can qualitatively describe the shape observed in the results, though a normalization discrepancy is noted, which might be a hint of the presence of an additional contribution.

1.8 Scope of this thesis

In relativistic heavy-ion collisions, ultra-strong electromagnetic (EM) fields are induced by incoming ions at the very early stages of the collision and can generate various QED and QCD related phenomena. The strong EM field can be represented by a flux of quasi-real photons leading to photon-induced interactions. Traditionally, such interactions are studied in ultraperipheral collisions (UPCs) without nuclear overlap. However, experimental observations have shown a significant enhancement of J/ψ production at very low transverse momentum ($p_{\mathrm{T}} < 0.2$ GeV/c) beyond the expected yields from hadronic interactions in non-UPC events. This raises several questions, such as the persistence of coherence in photon-nucleus interactions amidst nuclear disruption during hadronic collisions, the roles of spectator and participant nucleons as photon sources and targets in the coherent process, modifications of the photon-nucleus cross section

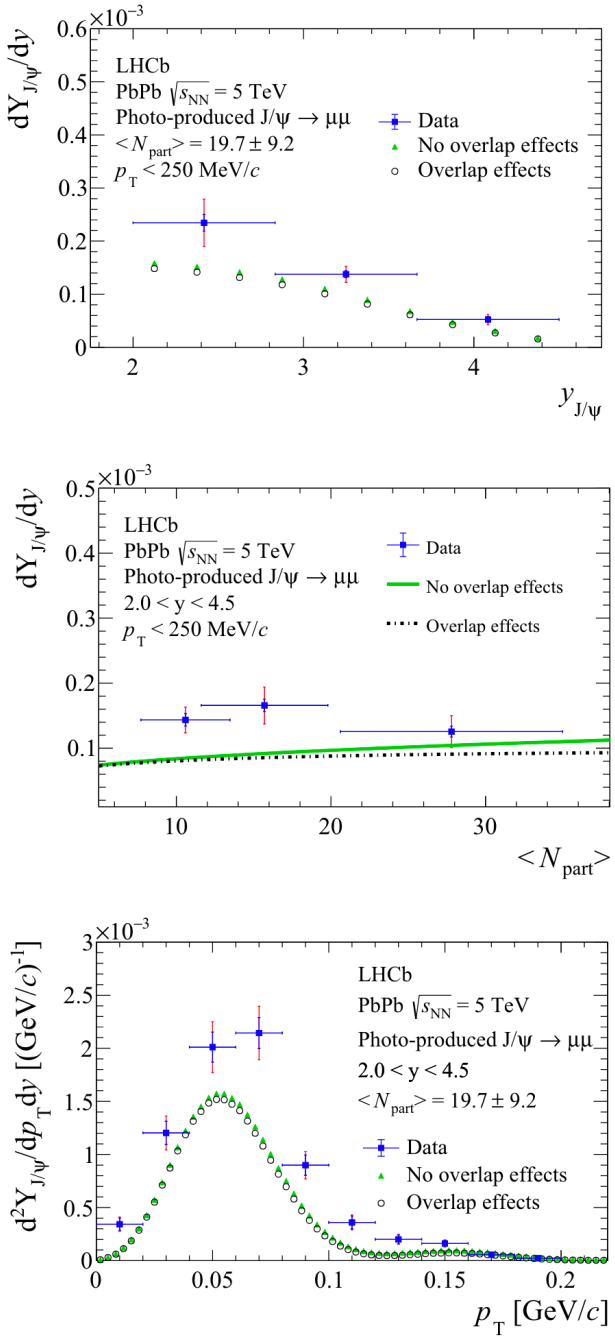

Figure 1.26 Differential yields of photoproduced J/ψ as a function of rapidity (top) and $\langle N_{\text{part}} \rangle$ (middle) . Bottom: double differential yield as a function of p_T. The vertical inner blue bars represent the statistical uncertainties and the outer red bars show the total systematic uncertainties. The horizontal bars in the middle panel correspond to the standard deviations of the N_{part} distributions in each centrality class. The yields are compared to theoretical calculations[102,110] that take (black) or do not take (green) into account the effect from the overlap region of the collision.

due to nucleons undergoing hadronic interactions, and the impact of interactions with the QGP medium on photoproduced J/ψ yields. Moreover, the coherent photoproduction mechanism, wherein the productions at different sites add up coherently, offers insights into the initial electromagnetic fields, the parton distribution, and enables studies on interference. The RHIC and LHC have measured coherent photoproduction of J/ψ in several collision systems, comparing the results with various theoretical models. These measurements indicate that the yields of photo-induced J/ψ align with predictions, highlighting the necessity of more precise measurements to effectively constrain these models, including understanding the roles of spectators and participants and the potential influence of the hot partonic medium. The STAR experiment has reported on J/ψ photoproduction via the dielectron channel. Measurements via the dimuon channel in peripheral collisions can provide complementary information to study photoproduction in heavy-ion collisions with well-defined and relatively smaller impact parameters compared to UPCs. The dimuon channel is expected to offer similar physics insights as the dielectron channel but can improve measurement precision and feature different analysis methodologies due to diminished bremsstrahlung, decreased multiple scattering in the detector material, and reduced internal radiation. Additionally, dimuon channel measurement can use different subsystems to identify muons. STAR can also provide different PID detector for dimuon channel. These features highlight the importance of conducting measurements via the dimuon channel, which is crucial for a comprehensive understanding of photoproduction in heavy-ion collisions.

In 2014, the Muon Telescope Detector (MTD) was fully integrated into the STAR experiment, significantly augmenting its capabilities in muon identification crucial for J/ψ measurement through the dimuon channel. This advancement also introduced the capability to trigger on muon pairs from quarkonium decays and sample the full luminosity delivered by RHIC. Utilization of the dimuon trigger enabled the collection of a large dataset of Au+Au collisions at $\sqrt{s_{\mathrm{NN}}}$ = 200 GeV in 2014 and 2016. This thesis focuses on the measurements of very low p_{T} J/ψ production in peripheral Au+Au collisions via the dimuon channel, using combined datasets from 2014 and 2016.

Chapter 2 Experimental setup

The quest to understand the fundamental properties of matter under extreme conditions has led to the creation of facilities capable of simulating the earliest moments of the universe. Among these, the Relativistic Heavy-Ion Collider (RHIC) at Brookhaven National Laboratory (BNL) is distinguished as a leading venue for investigating the Quark-Gluon Plasma (QGP). RHIC achieves this by colliding heavy ions at ultra-relativistic speeds, generating extreme temperatures and energy densities. These conditions are enough to transition hadronic matter into a deconfined phase, where quarks and gluons are free from their hadronic bounds. RHIC aims to investigate the QCD phase diagram, understand the properties and behavior of the QGP, and explore the spin structure of protons[114]. The Solenoidal Tracker At RHIC (STAR) is one of the key experiments at RHIC, designed with a large acceptance and comprehensive detection capabilities to measure a wide range of particles produced in heavy-ion collisions. This chapter will introduce the RHIC facility and the STAR detector. The key components of the STAR detector, including the Time Projection Chamber (TPC) and the Muon Telescope Detector (MTD), will be discussed in detail.

2.1 The Relativistic Heavy Ion Collider

The RHIC at BNL in Upton, New York, illustrated in Fig. 2.1, is one of the world's two high-energy heavy-ion colliders. Operational since 2000, it has been at the forefront of high-energy nuclear physics research. Its mission is to accelerate a broad range of nuclei, from protons to uranium, to velocities approaching the speed of light, facilitating collisions that enable scientists to study the formation and properties of QGP[115]. The collider achieves top energies of 100 GeV/u for gold ions and 250 GeV for protons. Uniquely, RHIC is the only collider capable of conducting experiments with polarized proton beams, providing invaluable insights into the nucleon spin structure[116].

The collider features two quasi-circular concentric rings, designated for clockwise and counter-clockwise beam circulation, labeled as the "Blue Ring" and "Yellow Ring," respectively. These rings intersect at six points along their 3.8 km circumference, with each intersection hosting an interaction point for experiments. Initially, RHIC supported four major detectors: STAR, PHENIX, PHOBOS, and BRAHMS.

Presently, STAR and the newly operational sPHENIX, which commenced data col-

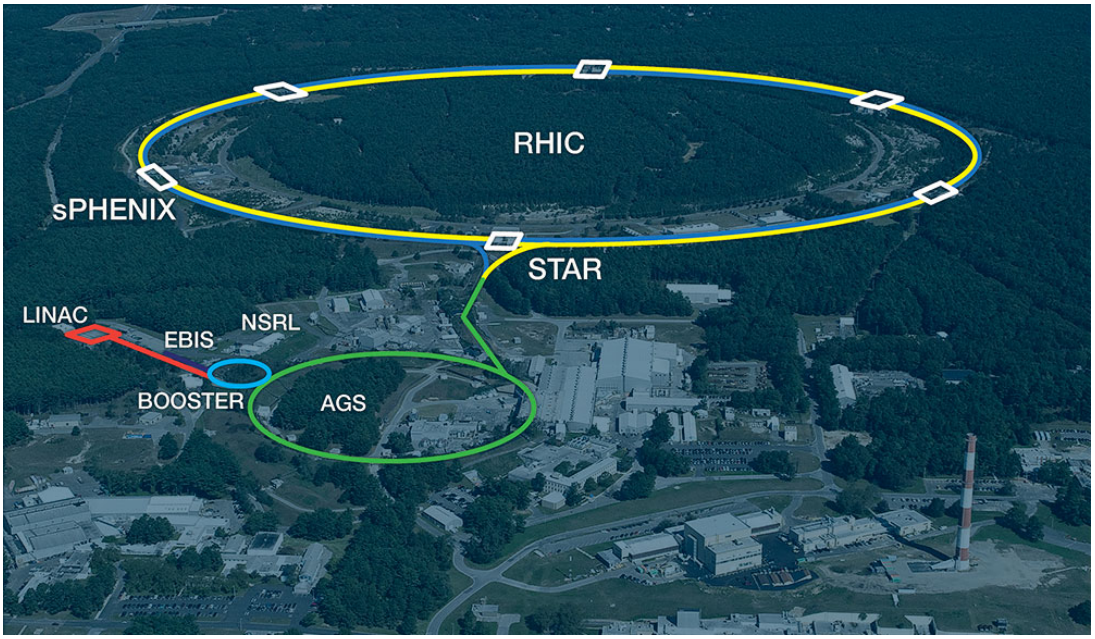

Figure 2.1 The bird's eye view of the RHIC facility.

lection in 2023, are the active detectors at RHIC. The sPHENIX detector is particularly focused on the study of strongly interacting particles, as indicated by the "s" in its acronym[117].

The ion injection chain for RHIC includes the Tandem Van de Graaff, a Linear Proton Accelerator, the Booster Synchrotron, and the Alternating Gradient Synchrotron (AGS)[118]. The acceleration sequence for gold ions is depicted in Fig. 2.2. In the initial, gold ions carrying a negative charge (Q = -1) undergo processing within the Tandem Van de Graaff, where they lose some electrons and gain acceleration up to an energy level of 1 MeV/u. After leaving the Tandem possessing an increased charge (Q = +32), these ions are directed towards the Booster Synchrotron. Here, their acceleration increases to 95 MeV/u, and they are further stripped until they reach a charge state of Q = +77, subsequently being forwarded to the Alternating Gradient Synchrotron (AGS). Once at the AGS, the ions undergo four Booster cycles, filling up with 24 bunches. Within the AGS, the processes of de-bunching and re-bunching condense them into four bunches, achieving an energy plateau of 10.8 GeV/u. As the gold ions exit the AGS with a fully realized charge state of Q = +79, through the AGS-to-RHIC beam transfer line, they are sequentially injected into the RHIC ring. Here, their acceleration is enhanced to reach up to 100 GeV/u. Since 2012, the Electron Beam Ion Source (EBIS), showcased in Fig. 2.1, has replaced the Tandem Van de Graaff as the pulsed sputter ion source. The proton acceleration process differs slightly, starting with an acceleration to 200 MeV in

a linear accelerator (Linac). Following this, the protons advance through the Booster and AGS, culminating in their entry into the RHIC ring.

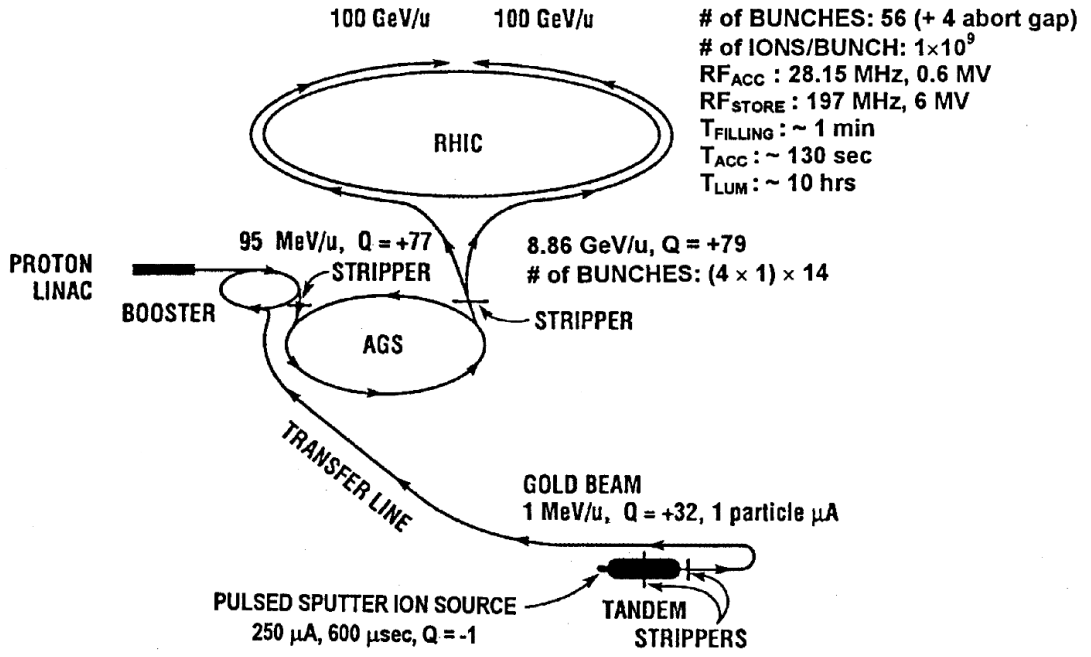

Figure 2.2 Acceleration scenario for Au beam. Figure is taken from[118].

Since beginning operations in 2000, RHIC has successfully collided different particle species of collisions such as U + U, Au + Au, Cu + Au, Cu + Cu, ^{3}He + Au, d + Au, p + Au, p + Al, and $p + p$, covering a wide range of energies. The top collision energies achieved are 200 GeV per nucleon pair for Au+Au and 510 GeV for p+p collisions. Over the past decade, in order to search for the QCD critical point and map out the first-order phase transition boundary, RHIC has undertaken the Beam Energy Scan (BES) program. The BES phase I program examined Au+Au collisions from 7.7 GeV to 62.4 GeV in 2010, 2011, and 2014. The BES phase II program, conducted from 2019 to 2021, investigated collision energies form 7.7 GeV to 19.6 GeV to enhance the statistical significance within the energy range where the QCD critical point is postulated to exist.

In January 2020, the U.S. Department of Energy announced the plan to transform RHIC into the Electron Ion Collider (EIC), known as eRHIC, within the next decade. The EIC is poised to perform 3D imaging of the internal structure of nucleons and nuclei via high-energy electron beams, to unravel the emergent properties of mass and spin from the quark and gluon interactions and probe the phenomenon of gluon saturation.

2.2 STAR detector system

The STAR was designed with the initial physics task of studying the formation and characteristics of the QGP[119-120]. STAR is equipped to measure a broad array of observables simultaneously, in order to draw strong conclusions about the properties of the QGP. For this purpose, STAR incorporates complex detector systems designed for precise tracking, momentum analysis, and particle identification at the mid-rapidity region.

The STAR detector is schematically shown in Fig. 2.3. The coordinate system of STAR is anchored at its center, which acts as the origin point. The x-axis is oriented towards the south, and the y-axis extends upwards. The z-axis aligns with the beam pipe, with the positive direction defined towards the west. The main tracking device, the Time Projection Chamber (TPC), is cylindrical, spanning 4.2 meters in length and 2 meters in radius, and envelops the full azimuthal range. It offers pseudo-rapidity coverage of $|\eta| < 1.0$ and measurements of ionization energy loss in the TPC gas to identify particles[121-122].

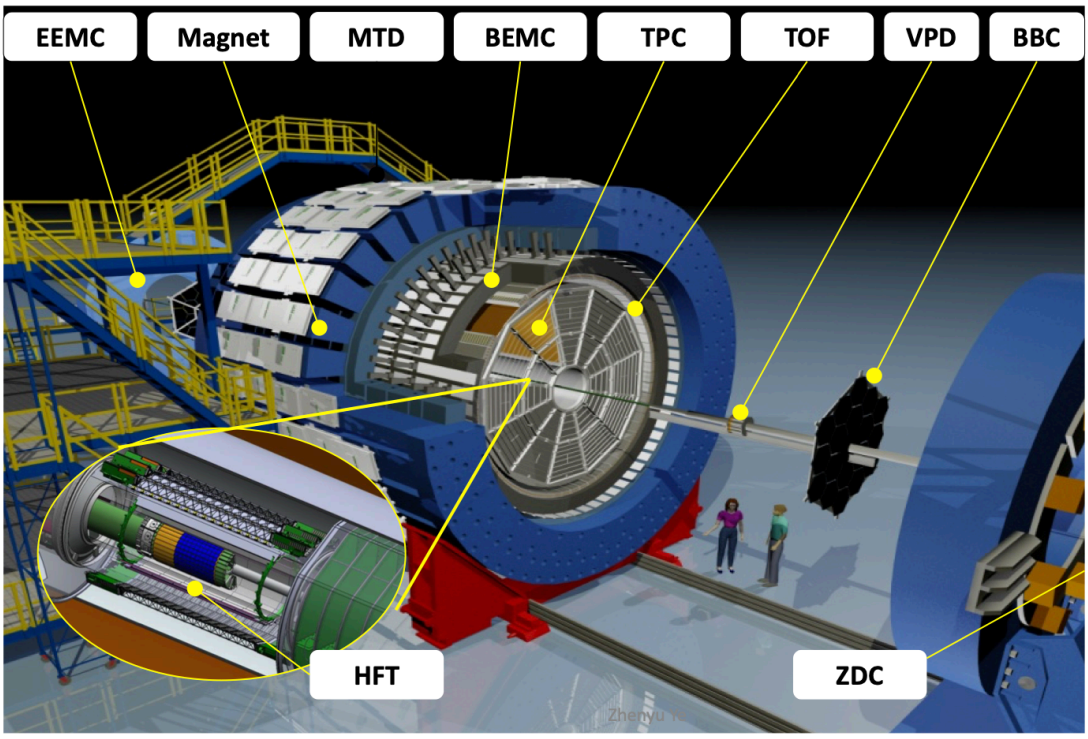

Figure 2.3 The schematic view of the STAR detector system.

The Heavy Flavor Tracker (HFT)[123], operational from 2014 to 2016, was located inside the TPC and possessed the capability to reconstruct secondary vertices from charm and bottom hadron decays, owing to its high-resolution tracking. Encircling

the TPC, the Time-of-Flight (TOF) detector extends over $|\eta| < 0.9$[124], fully covering the azimuthal angle, and measures the velocity of charged particles for identification purposes. Beyond the TOF lies the Barrel Electromagnetic Calorimeter (BEMC)[125], which spans $|\eta| < 1$ and the full azimuthal range. The BEMC is responsible for measuring the energy deposition and spatial distribution of particle-induced showers, discerning between electrons, photons, and hadrons. The magnet system of the STAR surrounds the BEMC, generating a nearly uniform magnetic field parallel to the beam pipe, which is 0.5 Tesla in this analysis.

In 2014, the Muon Telescope Detector (MTD) was added to the outermost layer of the STAR detector system[126], offering around 45% azimuthal coverage within $|\eta| < 0.5$. Its primary role is to trigger on and identify muons from quarkonium decays. The MTD's placement ensures that most hadrons are absorbed before detection, thus enhancing muon identification capabilities, especially for high p_{T} ($p_{\mathrm{T}} \leq 1.3$ GeV/c) particles.

STAR utilizes three fast trigger detectors, including the Zero Degree Calorimeter (ZDC)[127], the Beam Beam Counter (BBC)[128], and the Vertex Position Detector (VPD)[129]. They are positioned in the direction of the beam. The BBC detector is a set of scintillator annuli installed around the beam pipe on the EAST and WEST pole tips of the STAR magnet. Both BBC EAST and BBC WEST are placed at 3.75 meters from the center of interaction region and cover a pseudo-rapidity range of $3.4 < |\eta| < 5$. The BBC is essential for providing the p+p minimum bias trigger through the coincidence of hits on BBC EAST and BBC WEST. The VPD consists of two identical assemblies, each with 19 channels, located symmetrically on either side of the STAR detector. Situated in close proximity to the beam pipe and positioned at a distance of 5.7 meters from the center of STAR, the VPD spans a pseudo-rapidity range of $4.24 \leq |\eta| \leq 5.1$. In each assembly, the readout channels come equipped with a Pb converter, succeeded by a fast plastic scintillator and a fine-mesh dynode PMT. Fully integrated into the STAR trigger system, the VPD furnishes the principal input for the minimum-bias trigger in nucleus-nucleus collisions. In addition to its triggering capabilities, the VPD offers high-precision event start-time information for TOF and MTD. The ZDC, consisting of two identical assemblies located 18 meters from the interaction region on both sides of the STAR detector, specializes in detecting forward neutrons. The centrality of collisions influences the survival rate of these neutrons: more central collisions lead to a higher degree of ion overlap, fewer surviving neutrons, and consequently, a lower signal in the ZDCs. This distinctive behavior renders the ZDC particularly responsive to

variations in collision centrality, providing information for triggering and luminosity monitoring. The ZDC complements the VPD by exhibiting higher trigger efficiency in peripheral collisions, while the VPD is more efficient in central collisions, together ensuring comprehensive trigger coverage in nucleus-nucleus collisions.

The TPC and MTD are the main sub-detectors used in this analysis. Subsequent sections will provide detailed descriptions of these systems.

2.3 Time Projection Chamber

Conceived by David Nygren in 1974, the Time Projection Chamber (TPC) is a gas-filled cylindrical chamber that can operate under various pressure conditions, including atmospheric, pressurized, or even in a liquid state. Its design typically features one or two endplates and allows for a considerable drift distance, often extending to several meters. This innovative detector system has been instrumental in numerous particle and heavy ion physics experiments due to its ability to furnish a comprehensive 3D picture of the ionization deposited in the chamber. Central to the STAR, the STAR TPC excels as the primary tracking detector, recording particle tracks and determining their momenta. The measurement of ionization energy loss (dE/dx) can be used to identify particles. The capability to distinguish particles across a momentum spectrum from 100 MeV/c to beyond 1 GeV/c, and to measure momenta within a range of 100 MeV/c to 30 GeV/c.

The STAR TPC depicted in Fig. 2.4. It measures 4.2 meters in length and has a radius of 2 meters, encompassed by an inner field cage at a radius of 0.5 meters and an outer field cage at 2 meters. It operates within the solenoidal magnet that provides a 0.5 T magnetic field when at full strength. The chamber is filled with P10 gas—a mixture of 10% methane and 90% argon, maintained at 2 mbar above atmospheric pressure, to create an environment conducive to tracking ionization trails of particles with high precision. The uniform electric field within the TPC, approximately 135 V/cm, guides the secondary electrons liberated by ionizing particles to the readout end caps at the ends of the chamber. This configuration facilitates the reconstruction of particle paths through the gas volume. The choice of P10 gas is attributed to its optimal drift velocity at relatively low electric fields, enhancing the stability of drift measurements against minor fluctuations in environmental conditions. The transverse and longitudinal diffusion coefficients in P10 are 230 μm/$\sqrt{\text{cm}}$ at 0.5 T and $\sigma_T = 3.3$ mm for a 10 cm drift, and $\sigma_L = 5.2$ mm for the full length of the TPC, respectively. These diffusion properties dictate the resolution capabilities of the TPC's wire chamber readout system

in both the X, Y plane and longitudinal (Z) dimensions, with the drift velocity of 5.45 cm/μs leading to a longitudinal spread in drift time of approximately 230 ns FWHM.

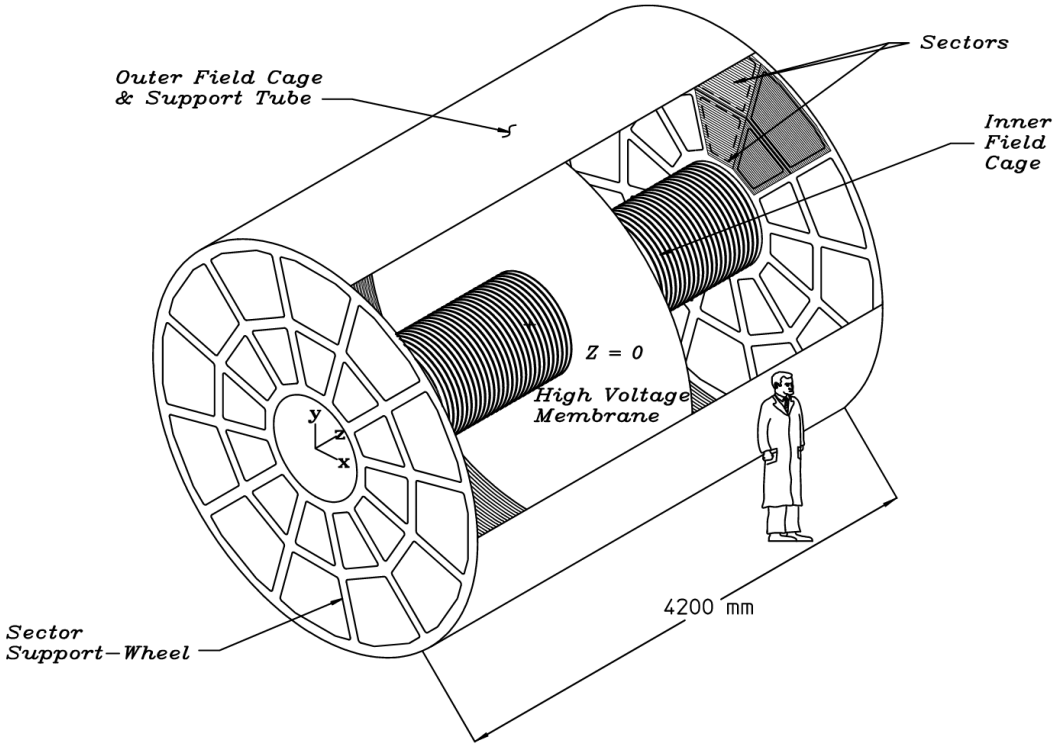

Figure 2.4 The schematic view of the STAR TPC. Figure is taken from[122].

The uniform electric field in the TPC is meticulously engineered through the precise arrangement of its components, including the central membrane (CM), end caps, and field cage cylinders. The CM is held at a potential of 28 kV, while the end caps are grounded, establishing the fundamental electric gradient necessary for particle detection. Surrounding the central volume, the field cage cylinders are designed with a sequence of equipotential rings. These rings partition the space between the CM and the anode planes into 182 segments, equally spaced to ensure uniform field distribution across the chamber. A pivotal ring positioned at the center serves both ends of the TPC and is directly connected to the CM.

The Multi-Wire Proportional Chambers (MWPC) coupled with readout pads constitue the TPC readout system, which is organized into modular units supported by aluminum wheels. These modules, or sectors, are distributed evenly in a circular arrangement akin to a clock face, with 12 sectors completing the circle. The design ensures minimal spacing between sectors, limited to 3 mm, facilitating a compact and efficient readout array. A schematic view of one sector is shown in Fig. 2.5. Each sector is divided into an inner subsector and an outer subsector, housing 13 and 32 pads re-

spectively, allowing for a maximum of 45 hits per track. The outer subsectors boast continuous pad coverage, eliminating gaps between pad rows to maximize the resolution of ionization energy loss (dE/dx) measurements. This configuration ensures the comprehensive collection of ionization signals, enhancing dE/dx statistics. Additionally, the layout contributes to improved tracking resolution through the anti-correlation of measurement errors across pad rows. Pads in these subsectors are organized on a rectangular grid. They feature a pitch of 6.7 mm parallel to the wire's direction and 20.0 mm perpendicularly, closely aligned with the anode wires to optimize signal collection. Conversely, the inner subsectors, situated in areas of dense track distribution, feature smaller pads (3.35 mm by 12 mm) to achieve superior two-hit resolution. This adjustment in pad size and spacing, down to 2 mm between the pad plane and the anode wire plane, tailors the induced signal's width to match the diffusion profile over approximately three pads. Despite the increased resolution in track separation, the discrete pad rows in the inner subsectors slightly limit their contribution to overall dE/dx resolution. These sectors are instrumental in extending precise positional measurements to smaller radii. This advancement not only improves momentum resolution but also improves the matching to inner tracking systems. This is particularly beneficial for detecting lower momentum particles. Significant improvements to the TPC were made with the completion of the iTPC upgrade in 2019[130]. This upgrade refined the segmentation of the inner pad plane and revitalized the wire chambers within the inner sector, leading to marked enhancements in tracking precision, especially for trajectories at acute angles relative to the beamline. The upgrade expanded the TPC's acceptance to a pseudorapidity of $|\eta| < 1.5$ and improved the resolution and acceptance for tracks across the momentum spectrum, with notable benefits for low-momentum track detection.

The MWPC chambers consist of a pad plane and three wire planes: anode, shield (ground), and gating, as depicted in Fig. 2.6. The layer responsible for amplification and readout includes the anode wire plane, which consists of small, 20 μm wires. This plane is sandwiched between the pad plane on one side and the ground wire plane on the opposite side. Unlike traditional TPC designs, the STAR TPC's anode plane utilizes a singular layer of 20 μm wires set at a 4 mm pitch, notably omitting intermediate field wires. This configuration enhances the chamber's stability and essentially eliminates initial voltage conditioning time. A notable aspect of the anode design is the inclusion of unusually large capacitors (1 nF) grounded on each wire, effectively minimizing the negative crosstalk induced on the pads by charge avalanches along the wire. Furthermore, the anode wire voltage governs the gas gain, allowing for precise control over

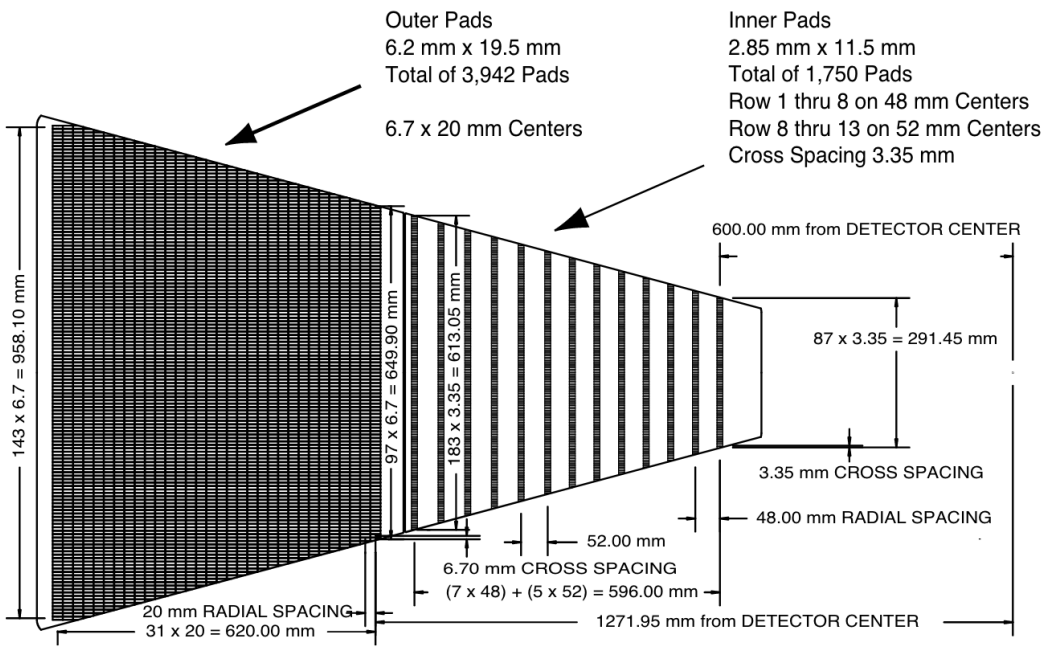

Figure 2.5 The anode pad plane, displaying a full sector, is organized with the inner subsector positioned on the right, featuring small pads arranged in rows that are widely spaced apart. Conversely, on the left side, the outer subsector is populated more densely with larger pads. Figure is taken from [122].

signal amplification. The ground grid, composed of 75 μm wires, not only terminates the electric field within the avalanche region but also offers additional RF shielding for the pads. This grid can be pulsed to facilitate the calibration of pad electronics, with a resistive divider ensuring 50 Ω termination for both the grid and the pulse driver. The gating grid, positioned 6 mm from the ground grid, acts as a dynamic barrier regulating electron entry from the TPC's drift volume into the MWPC and preventing positive ions generated in the MWPC from distorting the drift volume's electric field. The operational state of the gating grid alternates; it remains 'open' when wires are uniformly biased (typically at 110 V) and 'closed' with alternating voltages of ± 75 V from the base level, trapping positive ions during the closed phase and thus maintaining field integrity. To minimize data corruption upon gate opening, the driving voltages are finely tuned to cancel out induced signals on the pads. The alignment of gating wire planes across both subsectors and their potential matching with field cage cylinders are crucial for preserving the uniformity of the TPC's drift field, underscoring the sophisticated engineering behind maintaining optimal detection conditions.

The reconstruction of a primary particle's track within the TPC is accomplished by locating ionization clusters along the particle's trajectory, which are identified individually in 3D space—x, y, and z. Specifically, the local x-axis is aligned with the direction of the pad rows, the local y-axis extends outward from the beam line and is

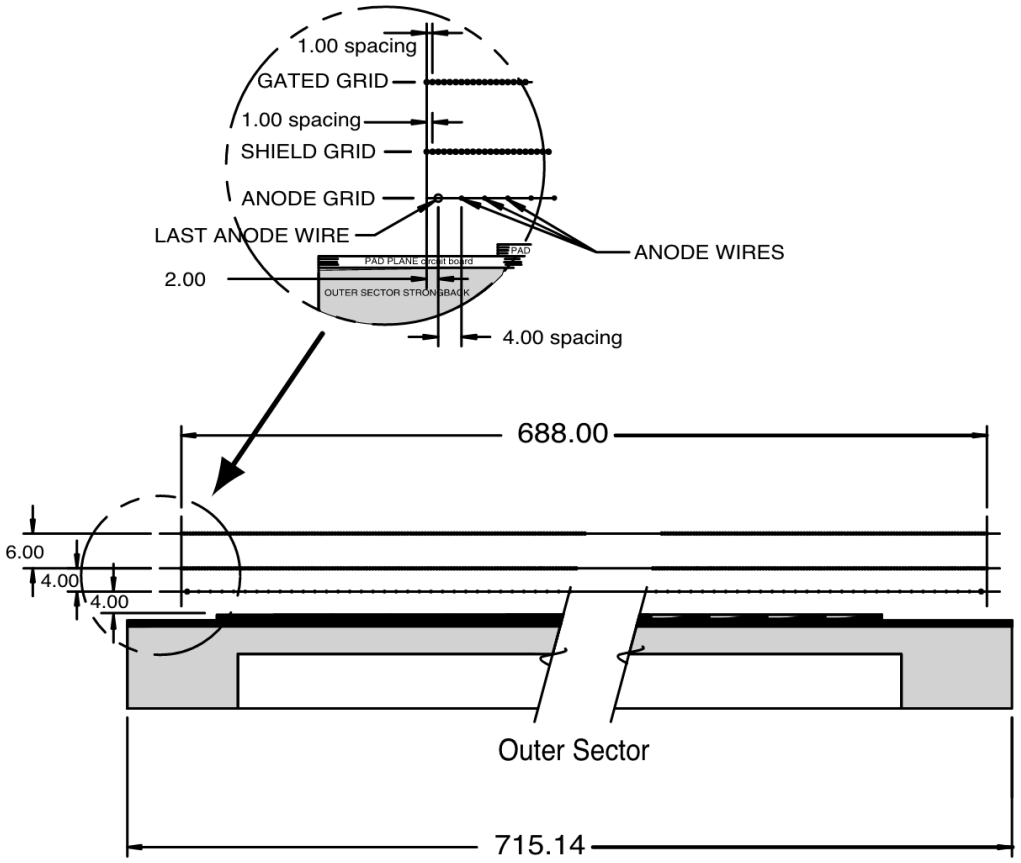

Figure 2.6 A sectional view of an outer subsector pad plane, executed along a radial trajectory from the TPC's center towards its outer field cage, placing the center of the detector to the right. A bubble diagram included offers further insight into the wire spacing specifics. All the dimensions mentioned are in millimeters. Figure is taken from [122].

perpendicular to the pad rows, and the local z-axis runs parallel to the beam line. For simple clusters, ionization energy from all pads is summed. When two tracks are close, clusters overlap and are split by an algorithm that detects peaks with valleys then divides ionization between tracks. Due to division uncertainty, these merged clusters are only used for tracking, not dE/dx determination. In central Au+Au events at 200 GeV, about 30% of clusters overlap. The x and y coordinates of each cluster are determined based on the charge collected on adjacent pads within a single row of pads. For the z coordinate, the time it takes for a cluster of secondary electrons to drift from their point of origin to the endcap anodes is measured and then converted into a spatial measurement using the average drift velocity. To accurately convert time measurements to spatial coordinates, the TPC's drift velocity must be determined with 0.1% precision. This involves two key steps: adjusting the cathode voltage to align the electric field with the drift velocity's optimal distribution peak, which is notably broad and stable against minor pressure fluctuations. Additionally, drift velocity is independently verified at regular intervals through artificial tracks generated by laser beams. Finally, the TPC hits

are reconstructed with the x, y, and z coordinates of these clusters.

Track trajectories within the STAR TPC are reconstructed from detected hits using a combination of Kalman filtering and track-finding algorithms, resulting in global tracks. The primary vertex determination involves aggregating all tracks that have been reconstructed in the TPC and extrapolating them to trace back to their point of origin, with the vertex position determined by a global average. The fitting of the primary vertex is refined by employing global tracks that register more than 10 hits. Furthermore, the Distance of Closest Approach (DCA)—which is the minimum distance between each track and the vertex—is calculated with precision. An iterative refinement process for fitting global tracks with a DCA less than 3 cm is employed until the vertex position converges, noting that the vertex resolution inversely correlates with the square root of the number of tracks involved. Achieving a resolution of 350 μm is possible with over 1000 tracks. Primary tracks are subsequently defined by reapplying the primary vertex to refit global tracks that have a DCA under 3 cm, which significantly enhances the momentum resolution. This refined fitting process, by leveraging the primary vertex, affords superior momentum accuracy for primary tracks as compared to global tracks, attributed to the more precise determination of track curvatures influenced by the magnetic field.

Energy loss (dE/dx) serves as a valuable method for identifying particle species. The dE/dx value is derived from energy loss data collected across up to 45 pad rows. However, the path length over which this energy loss is measured is insufficient to average out ionization fluctuations. Particles interacting with the gas medium undergo frequent collisions, typically releasing a few tens of eV, and occasionally, collisions result in the release of hundreds of eV. Consequently, it is impractical to obtain an accurate measure of the average dE/dx directly. To address this, the analysis focuses on determining the most probable energy loss by excluding the largest ionization clusters. A truncated mean approach, which discards a specified fraction (usually 30%) of the highest-signal clusters, effectively estimates the most probable dE/dx. Additionally, integrating the dE/dx distribution across all clusters associated with a track proves to be a more robust method, accommodating the variation in the most probable energy loss relative to the ionization sample length (dx). The resolution of dE/dx measurements is sensitive to the gas gain, which itself is influenced by the TPC's internal pressure. Maintained at a constant 2 mbar above atmospheric pressure, the TPC's internal pressure and consequently, the gas gain, fluctuate in response to external pressure changes. To mitigate local gas gain variations, a calibration process involves averaging the signal from a single pad row and assuming uniformity across all rows. This calibration is cru-

cial as the anode wires, positioned directly above the pad rows, span the full length of the pad row. Furthermore, the readout electronics introduce additional uncertainties in dE/dx readings due to potential variability in the response of individual pads, attributed to the disparate characteristics of each readout board. To ensure consistency across the pad response, calibration pulses are sent to both the ground and pad plane systems, maintaining the assumption of uniform response throughout the detector.

Figure 2.7 illustrates the energy loss of particles within the TPC as a function of their momentum. The mean rate of the energy loss of a charged particle is described by Bichsel function. This plot employs a 70% truncated mean for data correction, accounting for variations in signal and gain, set against a backdrop of a 0.25 T magnetic field. Under these conditions, the dE/dx resolution stands at 8% for tracks crossing 40 pad rows. Notably, an increase in the magnetic field to 0.5 T enhances the dE/dx resolution due to reduced transverse diffusion, thereby improving the signal-to-noise ratio for each cluster. The TPC is able to separate K/p up to $p \sim 1.1$ GeV/c and π/K up to $p \sim 0.7$ GeV/c.

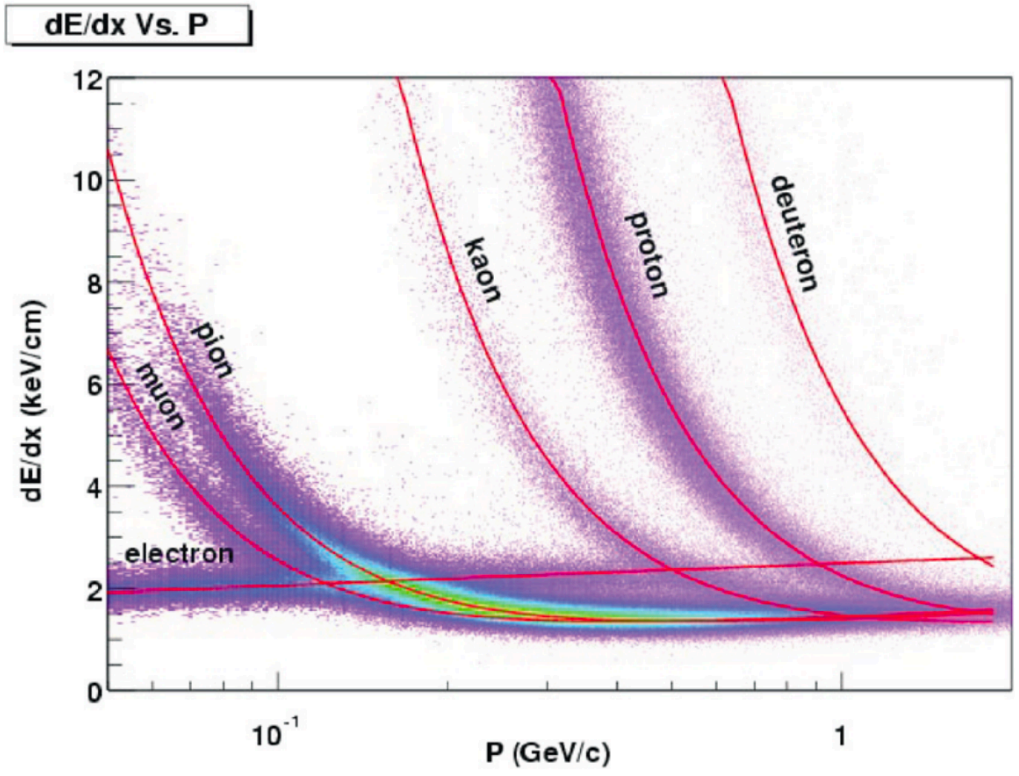

Figure 2.7 The p_{T} dependence of TPC energy loss for primary and secondary particles. The magnetic field is set at 0.25 Tesla. Figure is taken from [122].

2.4 Muon Telescope Detector

The Muon Telescope Detector (MTD) is based on the Multi-gap Resistive Plate Chambers (MRPC) technology, similar to the STAR Time-Of-Flight (TOF) system, yet features significantly larger MRPCs with elongated, double-ended readout strips known as Long-Strip Multi-Gap Resistive Plate Chambers (LMRPC). Located beyond the iron return bars of the STAR magnet, the MTD system extends across 45% of the total azimuthal coverage, positioned within a pseudo-rapidity range of $|\eta| < 0.5$. Initiated in 2011 and reaching completion in 2014, the development of the MTD system was preceded by an extensive prototype phase from 2007 to 2011, during which the detectors underwent rigorous testing with cosmic rays, in test beams, and within the STAR experiment across several RHIC runs. These evaluations demonstrated a timing resolution of up to 100 ps and an intrinsic spatial resolution of approximately 1 cm, both of which meet the requirements necessary to fulfill the system's physics objectives. Additionally, the MTD boasts a detection efficiency exceeding 95%, underscoring its effectiveness in muon identification and tracking within the complex environment of heavy-ion collisions.

The LMRPC modules were held in gastight aluminum boxes called "trays." Figure 2.8 offers a detailed schematic view of a LMRPC module[131], illustrating its construction with five gas gaps, each 250 μm wide, delineated by layers of float glass plates. These plates are held apart by nylon monofilament lines, with the inner and outer glass plates measuring 0.7 mm and 1.1 mm in thickness, respectively, and exhibiting a volume resistivity in the range of $10^{12} - 10^{13}\Omega$cm. The high voltage necessary for operation is supplied to the module's cathode and anode (HV electrodes) through a colloidal graphite paint applied to the outer glass surfaces, with copper tape ensuring the transmission of voltage along the module's edges. The active area of the module is 52 cm by 87 cm, and itis defined by the dimensions of the inner glass plates. Signal detection is enhanced through the arrangement of twelve pairs of readout strips, which are strategically placed both above and below the stack of glass, each strip being 3.8 cm wide and 87 cm long, spaced 0.6 cm apart. To ensure electrical isolation between the high voltage electrodes and the readout strips, Mylar layers 0.15 mm thick are placed in between, while the structural integrity and rigidity of the module are maintained by fiberglass-reinforced honeycomb plates.

The MTD system is installed behind the return bars, known as "backlegs", which is used as the hadron absorber with about 5 interaction lengths. A side view of this config-

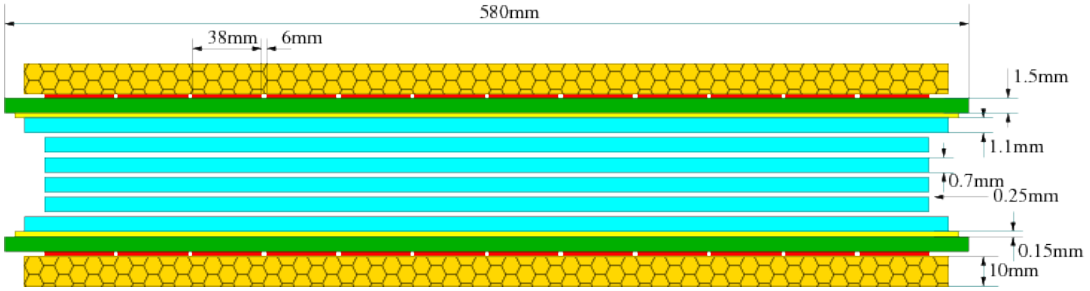

Figure 2.8 The LMRPC module of MTD, viewd in side. Figure is taken from[131].

uration is depicted in Fig. 2.9. The azimuthal plane is segmented into 30 backlegs, each covering 12 degrees. Starting at $\pi/2$ in the STAR global coordinate system, backleg numbering increases clockwise to 30. Within these divisions, the MTD's active detection area spans approximately 8 degrees, with the remaining 4 degrees allocated as gaps. The 3D schematic view of the MTD modules is shown in Fig. 2.10. Five MTD modules are installed on backlegs 1-8, 10-11, 21-22, and 24-30, providing a pseudo-rapidity coverage of $-0.6 < \eta < 0.6$. However, due to spatial constraints, only three modules are placed on backlegs 12-20, covering a narrower range of $-0.3 < \eta < 0.3$. Backlegs 9 and 23 are devoid of modules due to the physical constraints. In total, the system incorporates 122 modules across the 30 backlegs, providing an average azimuthal coverage of about 45% within a pseudo-rapidity range of $|\eta| < 0.5$.

Tracks are required to be matched MTD hits in order to be classified as muon candidates. This matching is achieved by projecting the tracks to the MTD radius, at which point the closest MTD hit to this projected location is identified as the matching hit. The searching window is quite loose for association, requiring that the extrapolated track position and the MTD hit reside within the same or neighboring backleg modules. When multiple tracks correspond to a single MTD hit, the track closest to the hit is selected, ensuring a straightforward one-to-one match. Subsequent to establishing a track-to-hit association, three Particle Identification (PID) variables, Δy, Δz, and Δtof, are computed. These variables quantify the discrepancies along the local y and z axes between MTD hits and the extrapolated track positions, alongside the difference in time of flight, respectively. The local y axis, aligned with the azimuthal direction, and the local z axis, parallel to the beam line, are pivotal in determining the positional and temporal dimensions of the hit. Specifically, the z-coordinate of an MTD hit is inferred from the temporal discrepancy between signals at either end of a readout strip. The time of flight difference, Δtof, contrasts the measured time of flight, derived from the VPD time (start) and the MTD time (end), against the expected flight duration based on track propagation.

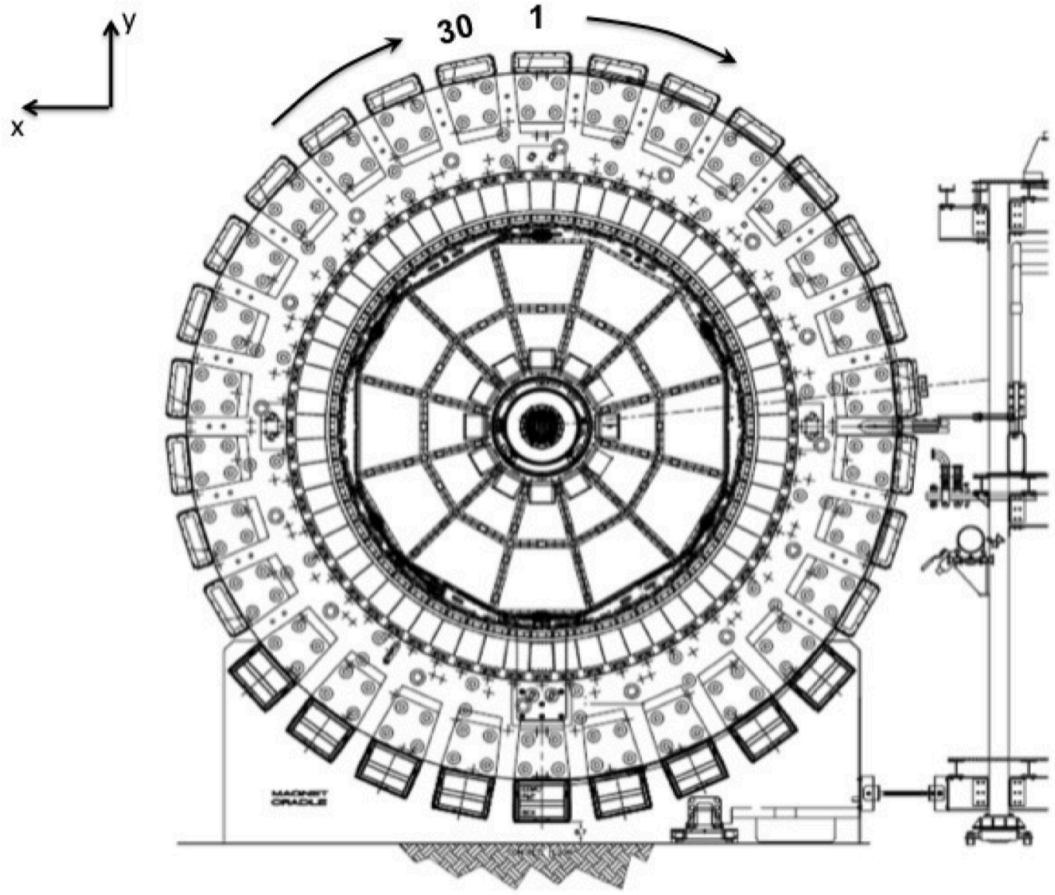

Figure 2.9 The STAR detector viewed from east. Backleg 1 is installed at an angle of $\pi/2$, with the subsequent backlegs arranged in a clockwise direction from this point. MTD system is installed outside of the magnet. Figure is taken from[132].

2.4.1 MTD performance

The MTD performance is calibrated using cosmic rays[131]. Spatial resolution measurements are based on tracks reconstructed in the STAR TPC and extrapolated to the MTD radius, measured in both the longitudinal (Z) direction, which aligns with the detector strips, and the azimuthal (ϕ) direction, which is perpendicular to the strips.

Figure 2.11 displays the differences between the extrapolated tracks from the TPC and the actual hit positions on the MTD in the Z direction, denoted as ΔZ, (on the left panel) and in the azimuthal angle ϕ direction, $\Delta\phi$, (on the right panel). For each hit registered on the MTD, the position in the ϕ direction is determined at the midpoint of the strip that records the largest signal. Meanwhile, the position along the Z axis is deduced from the difference in signal leading times between two readouts of the strip. The spatial precision in these directions, quantified by the standard deviations of the difference distributions, is measured to be 2.6 cm in Z and 0.006 radians in ϕ.

Figure 2.12 presents the spatial resolution along the Z and ϕ directions as a

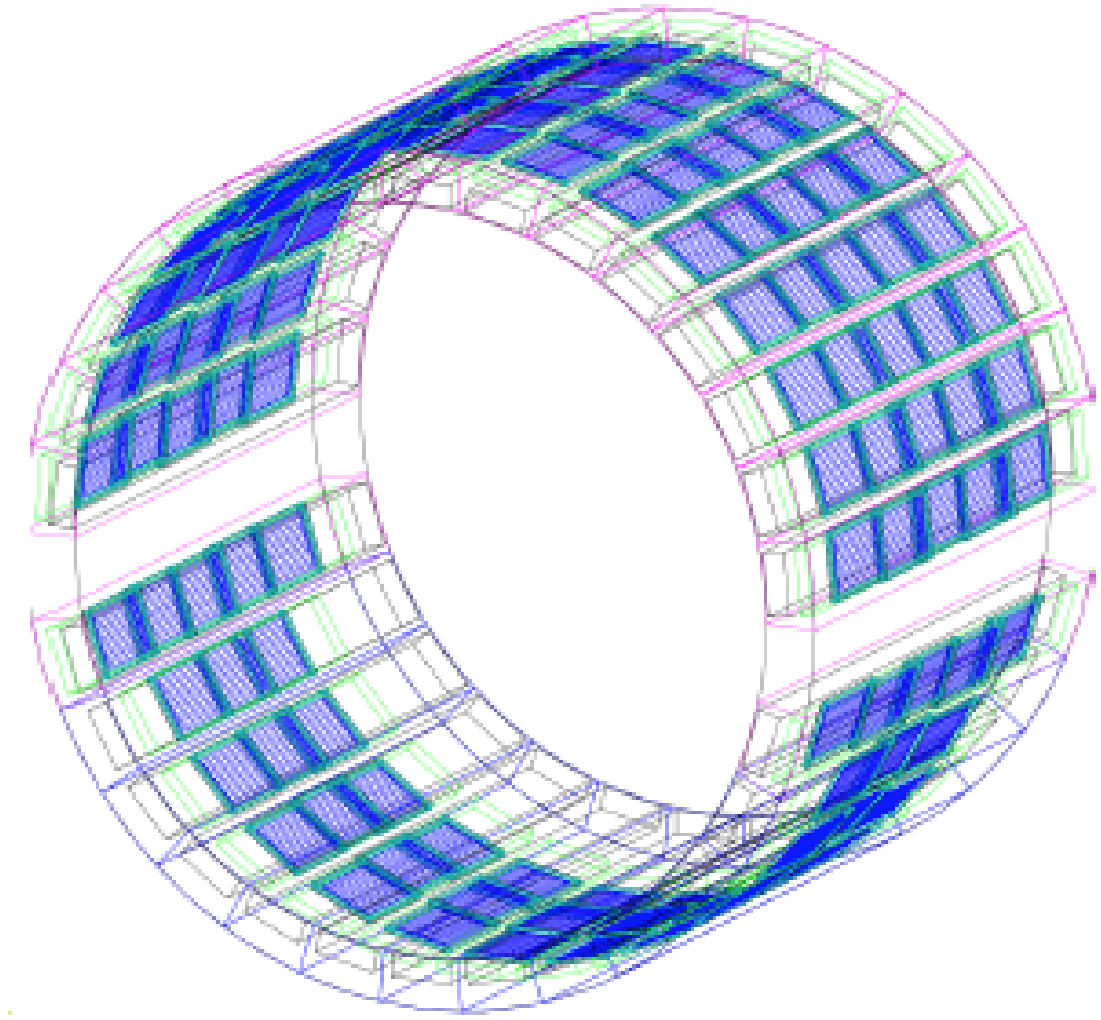

Figure 2.10 A sketch of the MTD system in 3D. Figure is taken from [132].

function of muon momentum. The observed data are fitted with a function $y = \sqrt{(p_0/x^2) + p_1}$, motivated by the expected influence of multiple scattering within the detector materials, where p_0 and p_1 are fitting parameters and x denotes the muon momentum. The spatial resolution of the MTD in the absence of multiple scattering in the detector materials, denoted by $\sqrt{p_1}$, yields resolutions of 0.8 cm in the Z direction and 2.2×10^{-3} rad in the ϕ direction. The ϕ resolution of 2.2×10^{-3} radians corresponds to a track resolution of 0.9 cm at the 400 cm radius where the MTD detectors are situated.

Fig. 2.13 presents a diagrammatic representation of a cosmic-ray event within the STAR detector. The times captured by the two TOF detectors and the MTD are indicated as tTOF1, tTOF2, and tMTD, respectively. The time of flight calculated between the two TOF detectors, determined from the path length and momentum (p) as measured by the TPC, is denoted as tTPC. Additionally, the time of flight from the MTD to the first TOF detector, denoted tSteel, is determined from the track's helical parameters, momentum p, and the 0.5 T magnetic field.

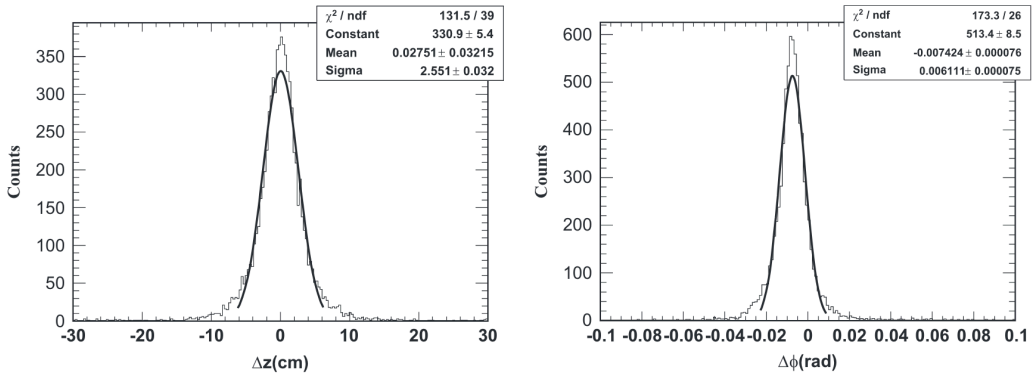

Figure 2.11 The distributions of ΔZ (the difference in the Z-direction) and $\Delta\phi$ (the difference in the azimuthal direction) for tracks reconstructed by the TPC and extrapolated to the MTD locations, compared with the actual hits measured by the MTD. The solid curves represent Gaussian fits to these distributions. Figure is taken from [131].

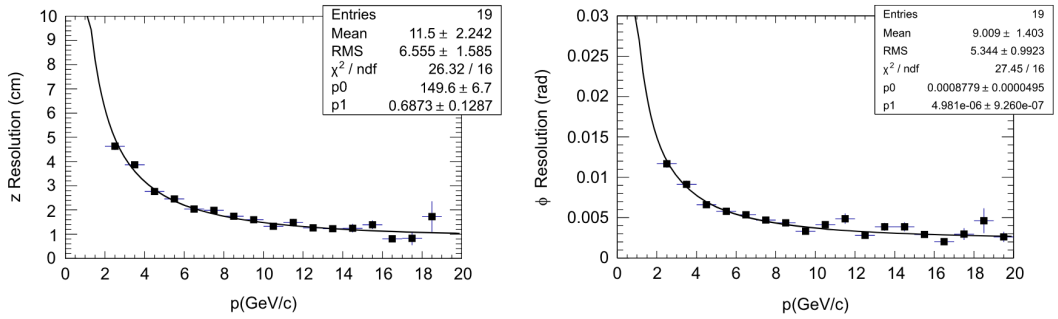

Figure 2.12 The spatial resolution along the Z direction (left panel) and the ϕ direction (right panel) is graphically as a function of muon momentum. The data is modeled with curves fitted using a function $y = \sqrt{(p_0/x^2) + p_1}$. Figure is taken from [131].

For calculating the time resolution, the focus is on the difference in time recorded by the MTD, tMTD, and the initial time from the TOF detectors, adjusted by the expected time-of-flight, tSteel, for cosmic muons traveling between the TOF and MTD detectors. This difference is represented as $\Delta T = (\text{tTOF2} - \text{tTPC} + \text{tTOF1})/2 - \text{tMTD} - \text{tSteel}$. The distributions of ΔT are meticulously logged for each separate MTD readout strip.

The ΔT distribution is characterized through fitting with a Gaussian function. The standard deviation derived from this fit is then utilized to determine the time resolution, as depicted for each strip in the left panel of Fig. 2.14. By compiling data from all the strips and conducting a Gaussian fit to this amalgamated ΔT distribution, shown in the right panel, an overall time resolution of 104 picoseconds (ps) is indicated. This figure includes the resolution of the start timing, calculated as 90 ps/2 = 45 ps, and the resolution's component attributed to multiple scattering for muons with an energy of 6 GeV/c, estimated to be 25 ps. Upon deducting these two factors quadratically, the deduced time resolution for the MTD is calculated to be 90 ps.

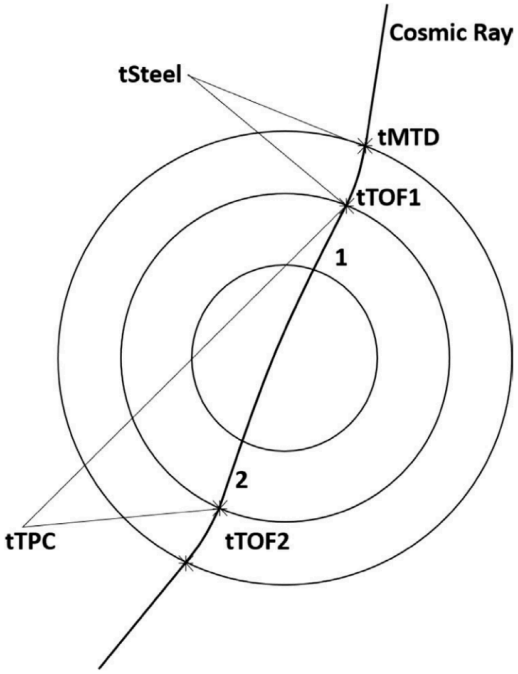

Figure 2.13 A schematic view of a cosmic-ray event in the STAR detector. Figure is taken from[131].

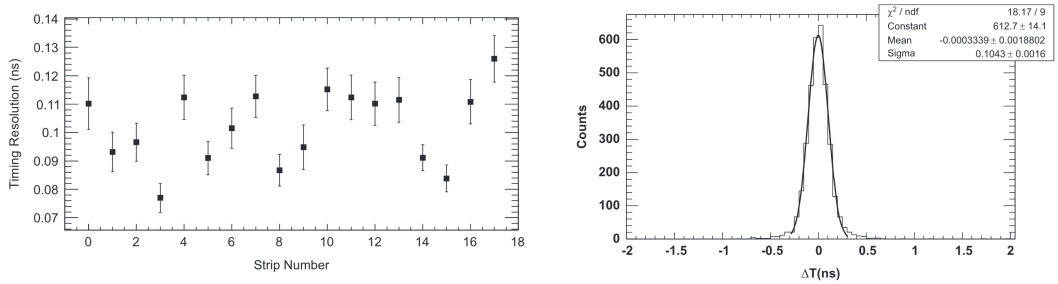

Figure 2.14 The left panel illustrates the variation in time resolution across different readout channels, while the right panel presents the distribution of ΔT across all strips, adjusted for slewing and offsets. A Gaussian curve is fitted to this distribution to calculate the combined timing resolution of the MTD and TOF systems. Figure is taken from[131].

2.5 Trigger System

MTD serves a crucial function in the triggering system as a fast detector, particularly for the dimuon trigger which is used in this analysis. Figure 2.15 presents a schematic representation of the MTD trigger system, with numbers 1 to 30 indicating the backleg numbers, and red numbers within boxes marking the module numbers. To streamline the number of trigger channels, MTD modules, varying from 2 to 5 at the same pseudo-rapidity (η), are aggregated to form a single trigger unit. This unit's signal is then directed to a single channel on a QT board. If multiple hits occur within one trigger unit, the signal with the fastest timing is prioritized for later stages. The dimuon trigger logic is outlined as follows:

- Given the MRPC's double-sided readout mechanism in the MTD, the two quickest

signals from each side of the 28 trigger units are dispatched to the four trigger boards.

- Each QT board comprises 8 channels. Within each channel, a minimal Threshold Amplitude Converter (TAC) cut is instituted to refine the signal quality. Subsequently, TAC signals from both sides are amalgamated, forming what is designated as "MtdTacSum". From this pool, the two fastest signals, identified by having the two greatest "MtdTacSum" values, are chosen and forwarded to the MT101 for further processing.
- In the MT101, as many as eight "MtdTacSum" signals are evaluated in comparison to the start time, known as "VpdTacSum", which is measured by the VPD. Signals meeting the online trigger window requirement based on "ΔTacSum = MtdTacSum - VpdTacSum" are recognized as muon candidates and moved to TF201. This implicitly necessitates valid VPD signals for all MTD-based triggers.
- The final decision regarding trigger activation resides with the TCU, taking inputs from TF201. Specifically, for the dimuon trigger to be activated, it is mandatory for two muon candidates to be identified within TF201, in addition to a ZDC coincidence.

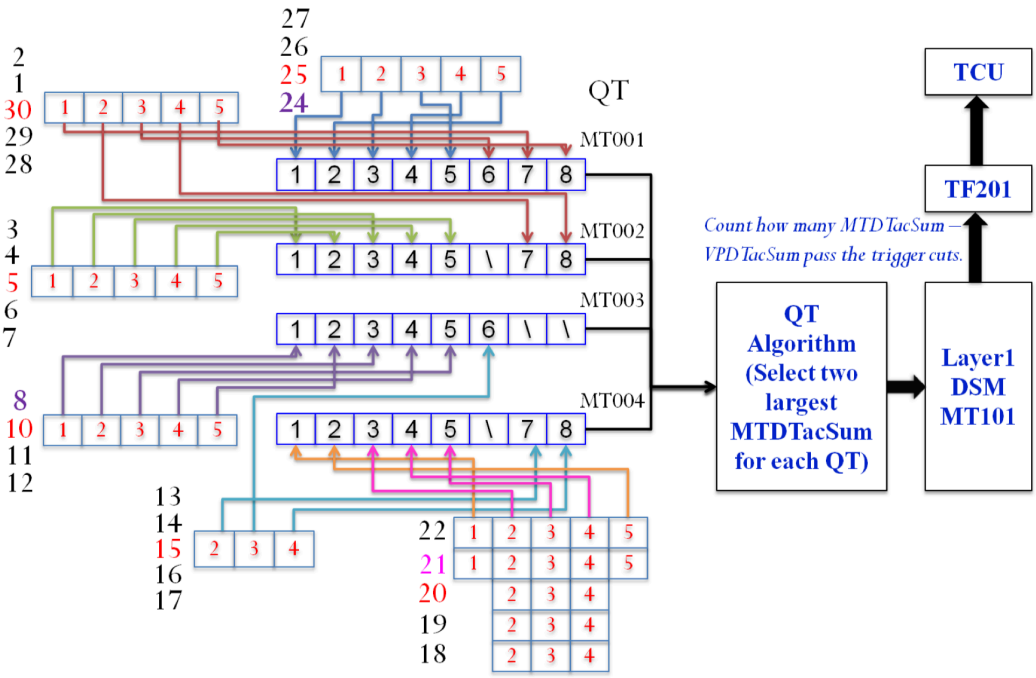

Figure 2.15 A sketch of the MTD trigger system. Figure is taken from [132].

The VPD is integral to the dimuon trigger system, serving as a critical component for timing and trigger initiation. Detailed previously in Sec. 2.2, the VPD's functional-

ity and structure are further explored here, with a schematic representation provided in Fig. 2.16. The VPD consists of two identical assemblies, each with 19 channels, located symmetrically on either side of the STAR detector. Figure 2.17 shows the VPD assemblies. The VPD can provide triggering information by the measurement of the arrival time of photons and the charged particles produced in a collision. To activate the online minimum-bias trigger for nucleus-nucleus collisions during data taking, a coincidence signal from both the east and west VPD is required. Specifically, for the dimuon trigger, the VPD's role extends to establishing the MTD's start time, with a single VPD tube boasting a timing resolution of approximately 100 ps. The event "start time" is meticulously derived by amalgamating signals across all VPD tubes, achieving a precision within tens of ps, and is governed by the equation:

$$T_{\text{start}} = \left(T_{\text{east}} + T_{\text{west}}\right)/2 - L/c. \tag{2.1}$$

Here, L denotes the distance between the center of STAR and the VPD detector. The timing resolution of the VPD is given by

$$\sigma_T = \sigma_0/\sqrt{N}, \tag{2.2}$$

where σ_0 is the intrinsic timing resolution of a single scintillator tube, and N represents the count of tubes that have fired. Additionally, the primary vertex location along the beam pipe, z_{vtx}, is ascertained through:

$$z_{vtx} = \left(T_{\text{east}} - T_{\text{west}}\right) c/2 \tag{2.3}$$

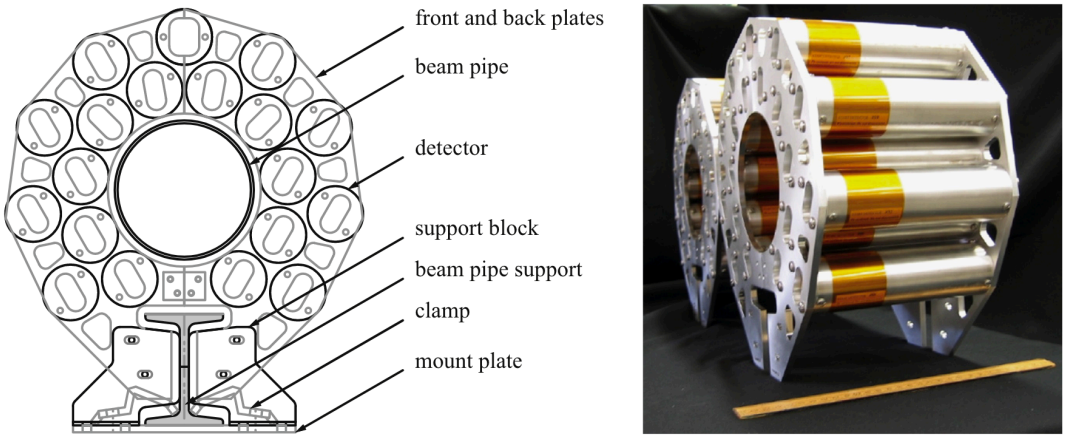

Figure 2.16 A schematic side view of VPD detector. Figure is taken from [129].

The primary task of the dimuon trigger is to selectively identify and trigger on pairs of muons originating from quarkonium decays, thereby facilitating the sampling of the full luminosity delivered through the data taking. The dimuon trigger requires

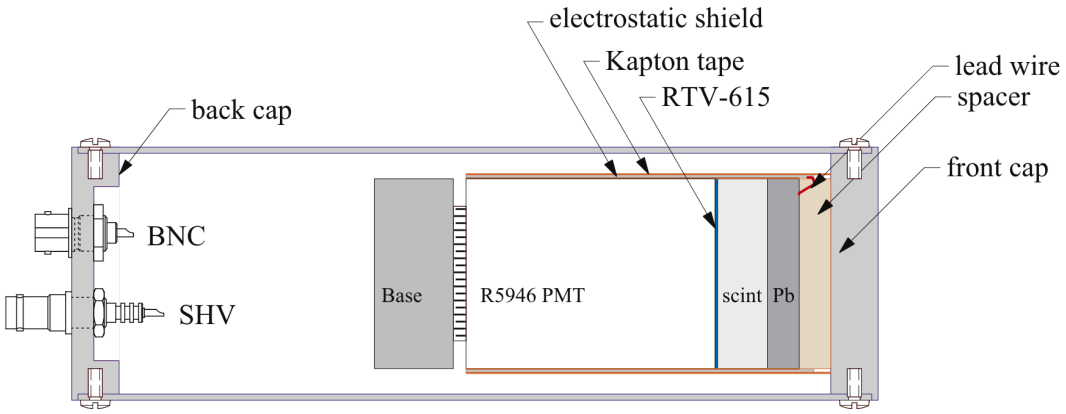

Figure 2.17 On the left is a schematic front view of a VPD assembly, and on the right is a photograph of the two VPD assemblies. A one foot long ruler is shown for scale on the right. Figure is taken from [129].

at least two MTD signals, which are then correlated with the collision's start time as determined by the VPD. The temporal discrepancies between these MTD signals and the start time must fall within a predefined trigger time window. The establishment of this window is crucial for minimizing background noise and managing the trigger rate effectively, ensuring that the dimuon trigger remains within the operational bandwidth. Additionally, a coincident signal from the ZDC is required.

Chapter 3 J/ψ Yield Measurement

This chapter details the methodology for analyzing J/ψ production in Au+Au collisions at $\sqrt{s_{\rm NN}} = 200$ GeV, which includes the raw signal extraction, efficiency correction and systematic uncertainty estimation. The datasets used in this analysis are collected in 2014 and 2016. The analysis techniques for both datasets are largely identical. The primary focus here will be on the analysis of one dataset, typically representing a year, with specific mention of any variations encountered in the analysis of the dataset from the other year.

3.1 Analysis setup

3.1.1 Dataset and trigger

The datasets used in this analysis were collected during 2014 (Run14) and 2016 (Run16) utilizing the dimuon trigger provided by the MTD. In terms of data volume, Run14 and Run16 sampled 14.2 nb^{-1} and 12.8 nb^{-1}, respectively. The dimuon trigger, as described in Sec. 2.5, requires at least two MTD signals in each event, ensuring the selection of events relevant for J/ψ analysis. In the STAR experiment, each trigger is uniquely identified by a trigger ID, a specific numerical code. These trigger IDs are crucial for distinguishing between different trigger configurations. Due to the need to adapt to different data-taking conditions, a single trigger type, such as the dimuon trigger, may be associated with several distinct trigger IDs. Table 3.1 lists the trigger IDs and the recorded number of events for the dimuon trigger for both Run14 and Run16.

Table 3.1 List of trigger IDs and recorded number of events for dimuon trigger used in Run14 & Run16

dataset	trigger ID	Nevents
Run16	520602, 520612, 520622	1.8B
Run14	450601, 450611, 450621, 450631, 450641	2.63B

3.1.2 Event selection

Offline event level cuts are applied to improve the quality of the events. To reject events without any reconstructed vertices, at least one of $|V_x^{TPC}|, |V_y^{TPC}|, |V_z^{TPC}|$ is required to larger than 10^{-5} cm. $|V_z^{TPC}|$ is required to be within 100 cm of the TPC center to ensure good TPC acceptance. To reject the events lacking correlation between $|V_z^{TPC}|$ and $|V_z^{VPD}|$, the difference between V_z of VPD and TPC is required to be less

than 3 cm, indicative of pile-up events or events with incorrect timing information in VPD. To reject the events from the beam hitting the beam pipe, the radial distance of the vertex should be less than 1.8 cm relative to the beam pipe center. All the event level cuts for the primary vertex are summarized in Tab. 3.2.

Figure 3.1 shows the distributions of V_y^{TPC} vs. V_x^{TPC}, V_z^{TPC} and $V_z^{TPC} - V_z^{VPD}$ before the vertex selection cuts in Run16. Notably, the V_z^{TPC} distribution exhibits two distinct peaks at approximately $\pm$60 cm. These peaks are attributed to the presence of satellite bunches.

Table 3.2 Event selection cut

Vertex cut
$!(\|V_x^{TPC}\| < 10^{-5} \&\& \|V_y^{TPC}\| < 10^{-5} \&\& \|V_z^{TPC}\| < 10^{-5}$ cm)
$\|V_z^{TPC}\| < 100$ cm
$\|V_z^{TPC} - V_z^{VPD}\| < 3$ cm
$\|V_r^{TPC}\| < 1.8$ cm

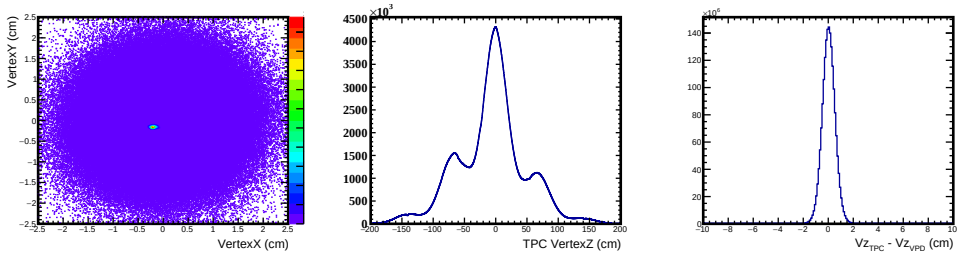

Figure 3.1 The distributions of V_y^{TPC} vs. V_x^{TPC}, V_z^{TPC} and $V_z^{TPC} - V_z^{VPD}$ distribution of selected primary vertex before the vertex selection cuts in Run16.

3.1.3 Centrality determination

Traditionally, centrality classes in the STAR experiment are determined based on the number of primary tracks, commonly referred to as refMult. During Run14 and Run16, the STAR experiment was augmented with the Heavy Flavor Tracker (HFT), a silicon detector designed to extend the measurement capabilities in open heavy flavor physics. The HFT, situated within the inner field cage of the STAR TPC, is used in the tracking along with the TPC. However, there exists a finite probability that TPC tracks may be incorrectly matched with HFT hits. Given the large weight assigned to HFT hits in the track reconstruction algorithm, such mismatches can significantly deviate the track from the primary vertex, adversely affecting track finding efficiency. To mitigate this issue and ensure accurate centrality determination, global tracks are employed. These tracks are reconstructed without incorporating the primary vertex information. The criteria for these global tracks include being within $|\eta| < 0.5$, having a minimum of 10 TPC hits used for track fitting, and maintaining a Distance of Closest Approach

(DCA) to the primary vertex of less than 3 cm. The new quantity based on the global tracks is referred to as gRefMult. Table 3.3 lists the kinematic and quality criteria used for gRefMult.

Table 3.3 gRefMult criteria

global tracks
$\|\eta\| < 0.5$
$nHitsFit \geq 3$ cm
$DCA < 3$ cm

3.1.4 Equivalent number of MB events

The normalization of event samples, particularly for datasets collected under specialized trigger conditions, is crucial for comparative analyses. The equivalent number of MB events serves as a normalization factor, adjusting observed event yields to a baseline expected under minimum bias triggering. Post-calibration for luminosity and vertex z position, the gRefMult distribution is shown in the left panel of Fig. 3.2 (red histogram), alongside a Monte Carlo (MC) Glauber model prediction (black histogram) for comparison. While both distributions align closely in higher gRefMult ranges, a notable divergence occurs in lower gRefMult areas, attributed to the VPD trigger's inefficiency in peripheral collisions. This discrepancy is addressed by fitting the Glauber model over data ratio of the gRefMult distributions, as shown in the right panel of Fig. 3.2, and applying the derived weight to each data event. This ensures a corrected classification of centrality.

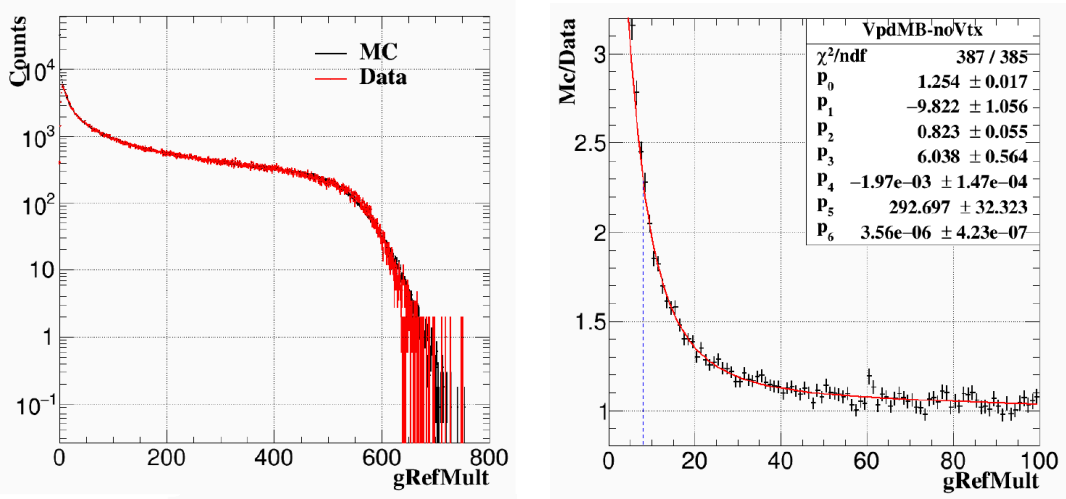

Figure 3.2 Left: gRefMult distribution from Run16 data (red histogram) and from the MC Glauber model (black histogram) after luminosity and vertex z calibrations. Right: Glauber model over data ratio of the gRefMult distributions in Run16.

Event weights, as a function of the corrected gRefMult, are illustrated in Fig. 3.3's

left panel, demonstrating a rapid increase towards lower gRefMult values, thereby correcting for the observed trigger inefficiency. The centrality distributions before and after the application of event weights are all shown for comparison are shown in the right panel of Fig. 3.3, which are MB events after vertex selection. Notably, the centrality distribution becomes nearly uniform after the application of the event weights, validating the effectiveness of the event weights.

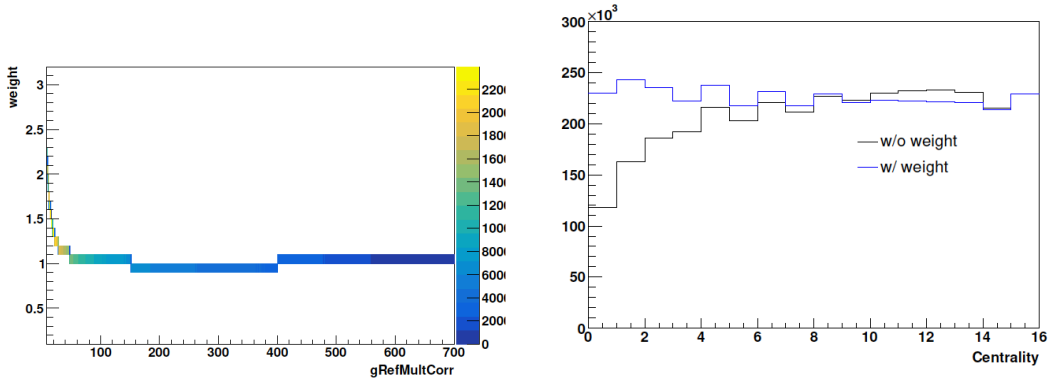

Figure 3.3 The event weight w.r.t the corrected gRefMult (left panel). The collision centrality distribution for the MB events after vertex selection before and after the application of the event weights (right panel).

The computation of equivalent MB events per centrality bin is formalized as follows:

$$N_{MB}^{cent} = \sum_{run} w_{gRefMult} \times N_{MB}^{cent,vtx} \times \frac{PS_{MB}}{PS_{dimuon}} \times \frac{livetime_{dimuon}}{livetime_{MB}} \tag{3.1}$$

where $w_{gRefMult}$ denotes the event weight, $N_{MB}^{cent,vtx}$ the count of MB events post-vertex cut per run, PS_{MB} and PS_{dimuon} the pre-scales, and $livetime_{dimuon}$ and $livetime_{MB}$ the live times for MB and dimuon trigger, respectively. Table 3.4 lists The equivalent number of MB events in each centrality class for the dimuon trigger used in this analysis.

Table 3.4 Equivalent number of MB events in both Run14 and Rn16 across various centrality class, calculated for the dimuon trigger.

Centrality	Run14 $N_{MB}^{Cent}(\times 10^9)$	Run16 $N_{MB}^{Cent}(\times 10^9)$
70-80%	8.37	6.8
60-70%	8.21	6.58
50-60%	8.1	6.54
40-50%	8.26	6.46
30-40%	8.11	6.46
20-30%	8.11	6.39
10-20%	8.14	6.34
0-10%	7.94	6.37

3.1.5 Embedding

The embedding technique is a crucial process in evaluating detector acceptance and the efficiency of various tracking and particle identification (PID) related cuts. As

a standard technique in the STAR experiment, this technique encompasses several key steps. Initially, Monte Carlo (MC) particles are sampled within an assigned kinematic range and positioned at the primary vertex of a real event. Utilizing GEANT3 simulation, the passage and energy loss of these MC particles within the TPC are simulated, allowing for the generation of MC TPC hits. These hits are processed through TPC response simulation to produce TPC electronic signals, which are subsequently mixed with real event TPC electronic signals. The standard reconstruction procedure is applied to these mixed TPC electronic signals to reconstruct TPC clusters/hits, followed by track fitting to reconstruct tracks. Through this embedding process, the efficiency in a real event environment is accurately reflected. For J/ψ analysis, embedding typically involves mixing generated J/ψ mesons decaying into two muons with real data. However, this analysis, focusing on very low p_{T} J/ψ production, adopts a modified approach. To enhance statistics in the low p_{T} region, the embedding sample is produced by separately mixing single muons, i.e., μ^+ and μ^-, with real data. The embedded single muons are generated with flat distributions over the ranges $0 < p_{\mathrm{T}} < 10$ GeV/c, $|\eta| < 0.8$, and $0 < \phi < 2\pi$. Figure 3.4 displays the p_{T}, η, and ϕ distributions for Monte Carlo (MC) muons in the Run16 embedding sample. To maintain a realistic TPC environment and accurately evaluate tracking efficiency, in each real events, there is a 10% limitation for the number of embedded single muons compared to the global track multiplicity.

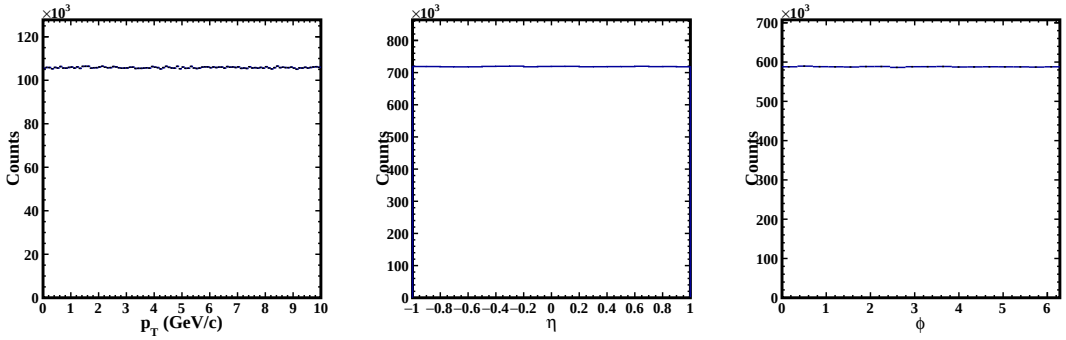

Figure 3.4 Distribution of p_{T}, and for input MC single muon in Run16 embedding sample.

The embedding process is conducted using the minimum bias (MB) sample, despite the analysis utilizing the dimuon sample. This decision is informed by previous STAR analysis of J/ψ production in the normal p_{T} range using Run14 data[56], where the MB sample was found to be more suitable. Initially, the dimuon sample was used for embedding, however, there is an inherent issue within this embedding sample. The TPC tracking efficiencies for muons above 2 GeV/c as a function of centrality in different luminosity ranges are shown in the left panel of Fig. 3.5. The tracking efficiency is expected to be affected by TPC occupancy, leading to decreased tracking efficiency at

increasing TPC occupancy. In this figure, at low luminosities, the efficiency follows the expectation, increases with a decrease in TPC occupancy as event multiplicity reduced from central to peripheral collisions. However, when luminosity exceeds the 50-60 kHz threshold, we observe a decline in efficiency from central to semi-central collisions, which contradicts what was anticipated. This atypical trend is probably due to a "leakage" phenomenon, where central events characterized by unusually low efficiency are misidentified as semi-central, thereby lowering the efficiency in semi-central categories in an artificial manner. As luminosity rises, increasing the level of activity within the TPC, this issue becomes more pronounced. Additionally, the utilization of the dimuon trigger sample for embedding exacerbates this problem, given that the dimuon trigger sample has a strong inclination towards central collisions due to the requirement of dimuon, as shown in the right panel of Fig. 3.5. To avoid this issue, the embedding process was subsequently conducted using the minimum bias (MB) sample. The monitor trigger "VPD-ZDC-novtx-mon" for Run14 and "VPD-ZDC-novtx" for Run16 have the same VPD and ZDC requirements as the dimuon trigger, were initially considered for embedding. However, due to their inclusion with high-rate triggers, extracting sufficient data for embedding was challenging. Consequently, in Run14, triggers VPDMB-5 and VPDMB-30 were used alongside the monitor trigger, while in Run16, VPDMB-5 and VPDMB-10 were selected. These triggers differ from the monitor triggers in that they include an additional requirement: the online VPD V_z must be within specific ranges (5 cm, 10 cm, or 30 cm). This additional criterion affects the vertex z distribution in the embedding sample, making it narrower compared to the distribution in the dimuon sample, as depicted in Fig. 3.6. To account for this, the J/ψ efficiencies across various V_z ranges were determined using the dimuon embedding sample, and the efficiency ratios relative to the scenario where $V_z < 100$ cm are depicted in Fig. 3.7. The efficiency variation for J/ψ within different V_z intervals remains below 4% across the p_{T} spectrum. Consequently, a 2% inefficiency correction is applied to the J/ψ efficiency derived from the MB embedding sample, with an accompanying 2% uncertainty attributed to account for this variation.

In addition to the considerations already discussed, there are other discrepancies between the real data and the embedding sample that require correction to ensure accurate analysis results. These include variations in luminosity, MTD acceptance loss and TPC occupancy, which are addressed as follows:

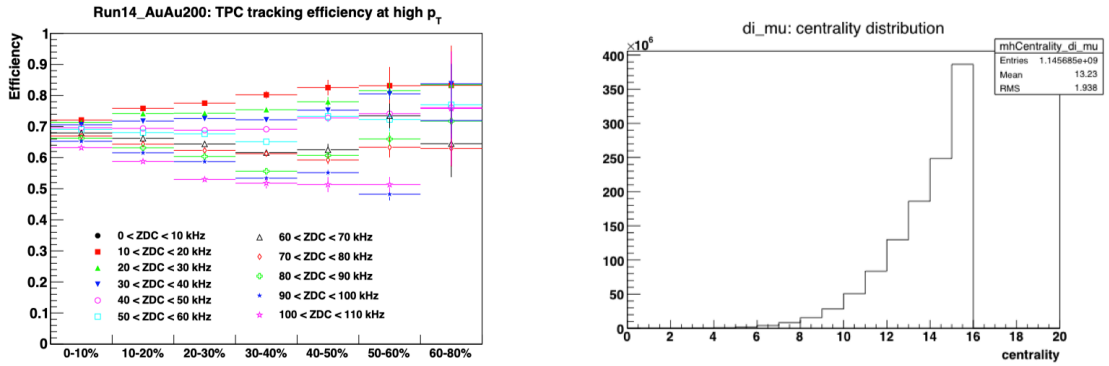

Figure 3.5 The centrality dependence of TPC tracking efficiency for muons with in p_{T} above 2 GeV/c in different luminosity ranges, from dimuon trigger embedding (left) and the centrality distribution of the dimuon trigger sample (right).

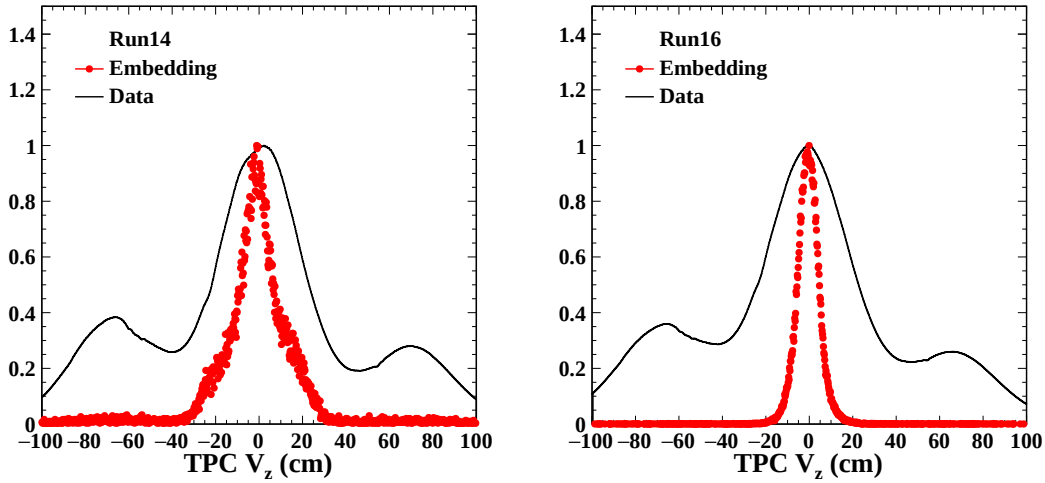

Figure 3.6 TPC V_z distributions from data (black) and embedding (red) in Run14 (left) and Run16 (right).

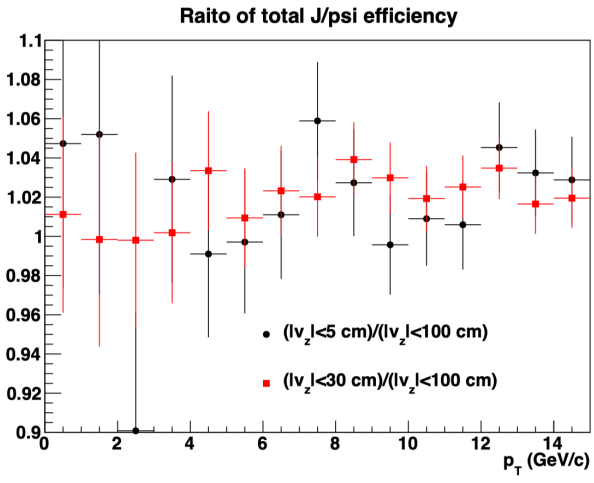

Figure 3.7 J/ψ efficiency ratios of different V_z ranges, estimated based on the dimuon embedding sample.

1. Luminosity and MTD acceptance loss correction

The TPC tracking efficiency is significantly influenced by luminosity, necessitating a correction in the embedding sample to align with the luminosity distribution of the real data. Additionally, it's possible for sections of the MTD backlegs to become unresponsive or lost due to hardware malfunctions during the data collection. This operational variance, corresponding to different run periods, is not reflected in the embedding process, which uses an ideal MTD geometry. The specific losses of MTD backlegs and modules for Run14 and Run16 are detailed in Tab. 3.5 and Tab. 3.6, respectively. For the majority of the data-taking period, only module 4 in backleg 15, denoted as "15-4", is missing due to a hardware failure. Additionally, two strips in each module of backleg 8 and 24 are masked out in the offline analysis. These strips are located in the gap of the magnet and therefore exposed to background. Figure 3.8 illustrates the MTD acceptances for Run16, as listed in Tab. 3.6. Therefore, the lost MTD backlegs need to be manually added to the embedding sample during efficiency estimation, and the run period distribution of the embedding sample requires correction to match the real data.

Table 3.5 List of lost MTD backlegs and modules during online data-taking for Run14. 15-4 stands for module 4 in backleg 15, while all other numbers stand for backleg.

Run period	Lost backlegs and modules
15074104-15078034	8, 15-4, 17, 19
15078035-15098066	8, 15-4, 19
15098067-15099003	8, 11, 12, 13, 14, 15-4
15099004-15106130	8, 15-4
15106131-15131036	15-4
15131037-15132019	15, 16, 17
15132020-15167014	15-4

Table 3.6 List of lost MTD backlegs and modules during online data-taking for Run16. 15-4 stands for module 4 in backleg 15, while all other numbers stand for backleg.

Run period	Lost backlegs and modules
17124035-17130013	15-4
17123053-17124034	15-4, 26, 27
17061018-17123052	15-4
17041001-17061017	1, 15-4, 30

A two-step weighting procedure is employed to address mismatches between the real data and the embedding sample in terms of luminosity profile and MTD acceptance loss.

First, event number distributions corresponding to run periods with different MTD

acceptance losses are compared, and their ratios are utilized as weights. This adjustment is depicted in Figs. 3.9 and 3.10 for Run14 and Run16, respectively. The left panels of these figures present the normalized run period distributions, while the right panels display the distribution ratios, subsequently applied as weights to the embedding events.

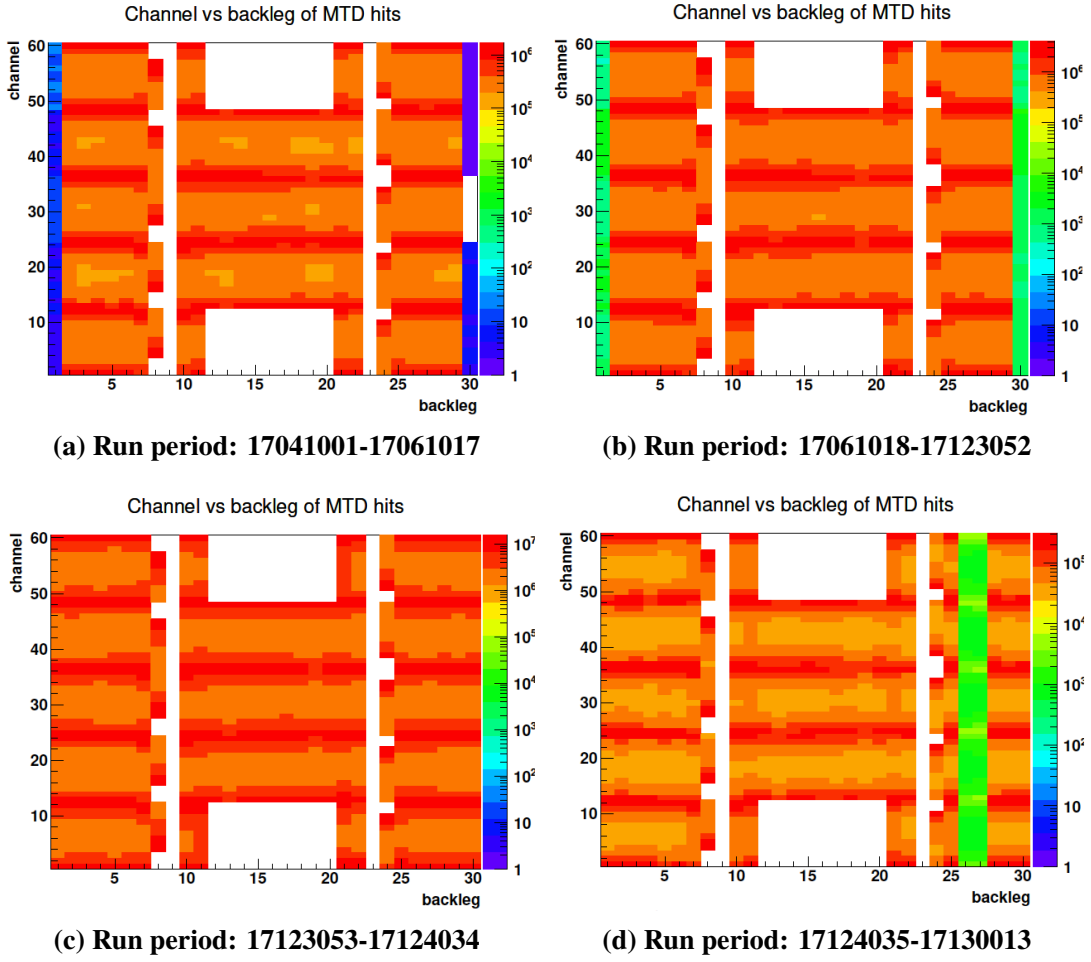

(a) Run period: 17041001-17061017 **(b) Run period: 17061018-17123052**

(c) Run period: 17123053-17124034 **(d) Run period: 17124035-17130013**

Figure 3.8 MTD hits distributions from Run16 data. Each panel represent a specific run period.

The second step compares the distributions of the ZDC coincidence rate after applying the run period weights. The ratios derived from this comparison are also used as weights for the embedding sample, with results presented in Figs. 3.11 and 3.12.

Post-weighting, a slight mismatch in run period distributions was observed, due to the correlation between run period and ZDC rate. To assess the impact of this mismatch, J/ψ efficiencies were evaluated for different run periods. The weighted efficiencies, calculated using run period distributions from both real data and the embedding sample (after the two-step weighting), showed a discrepancy of less than 0.1%, which was deemed negligible.

This two-step weighting process ensures that the embedding sample accurately reflects the real data's luminosity profile and MTD acceptance.

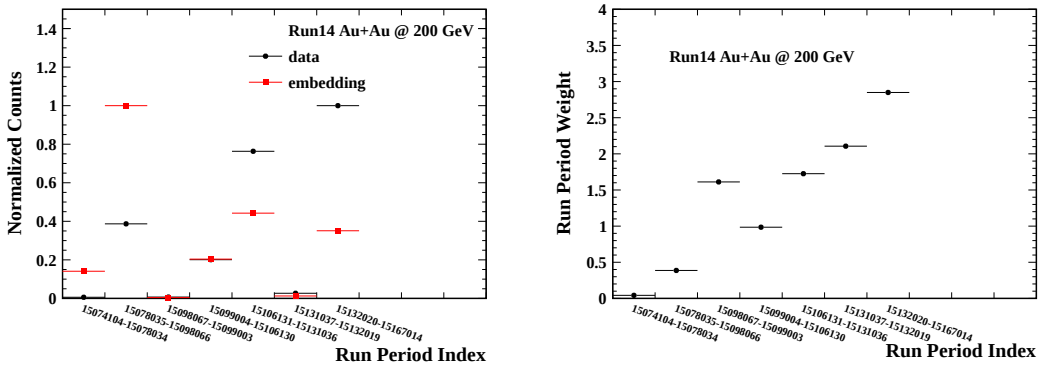

Figure 3.9 Left: normalized distributions of run periods corresponding to distinct MTD acceptances between data (black) and embedding (red) for Run14 analysis. Right: ratio of the two distributions from the left panel.

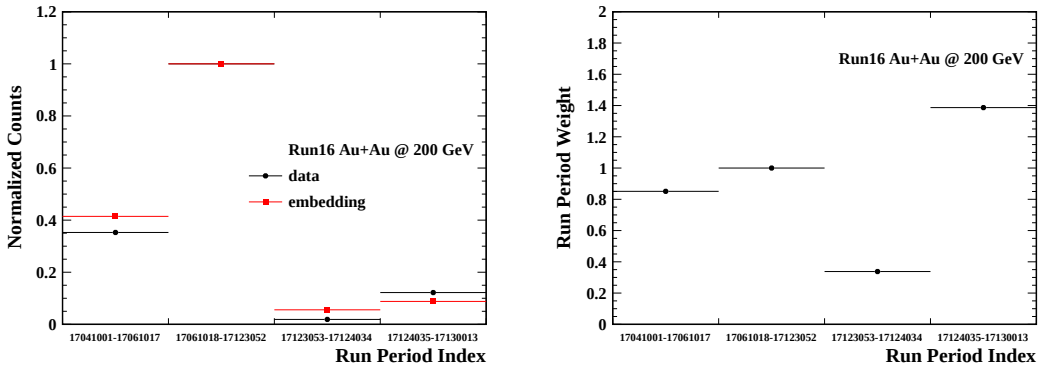

Figure 3.10 Left: normalized distributions of run periods corresponding to distinct MTD acceptances between data (black) and embedding (red) for Run16 analysis. Right: ratio of the two distributions from the left panel.

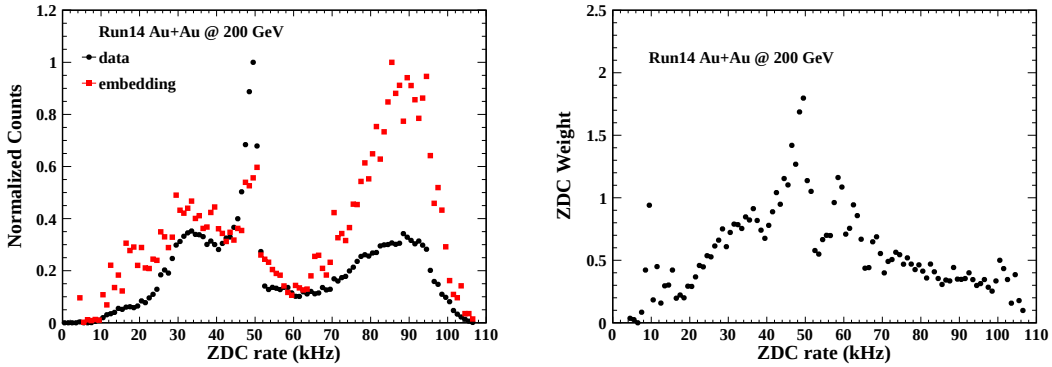

Figure 3.11 Left: normalized distributions of ZDC coincidence rate between data (black) and embedding (red) for Run14 analysis. Right: ratio of the two distributions from the left panel.

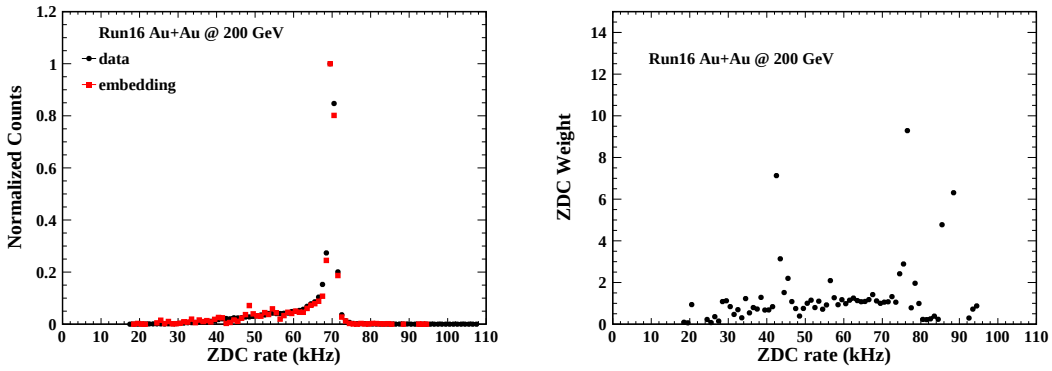

Figure 3.12 Left: normalized distributions of ZDC coincidence rate between data (black) and embedding (red) for Run16 analysis. Right: ratio of the two distributions from the left panel.

2. TPC occupancy correction

In Run16, the VPDMB-5-p-sst trigger was included in the embedding sample due to its significant representation in the overall event dataset, as illustrated in Figure 3.13. This figure shows the distributions of different triggers in a dataset of approximately 18,000 sampled events. The designation "p" signifies that this trigger includes TPC occupancy protection. During data acquisition, when the time between bunch crossings becomes comparable to or shorter than the TPC drift time, multiple events can be recorded during a single read-out, a phenomenon known as pile-up. The TPC occupancy protected triggers ensure an event is recorded only if no other event occurs within 40μs before or after it. Notably, the VPDMB-5 and VPDMB-5-p-sst triggers are not mutually exclusive; a low pile-up event can satisfy both conditions, leading to the inclusion of VPDMB-5-p-sst when VPDMB-5 is required.

The implementation of the VPDMB-5-p-sst trigger, with its TPC occupancy protection, means that the global tracks in these events are generally fewer, resulting in a lower TPC occupancy and, consequently, a higher TPC tracking efficiency compared to events triggered without such occupancy protection. To align the embedding sample with the real data, the number of reconstructed global tracks (NGlobalTracks) is utilized as a representative measure of TPC occupancy. Fig. 3.14 illustrates the single track efficiency as a function of NGlobalTracks for events both with and without TPC occupancy protection. The efficiencies under these two conditions demonstrate a decrease as NGlobalTracks increase, yet exhibit consistent efficiency at the same NGlobalTracks.

Figure 3.15 presents the distributions of NGlobalTracks for different triggers in Run16, including dimuon, VPDMB-5, VPDMB-10, VPD-ZDC-novtx and VPDMB-5-p-sst. To ensure a smooth correction process, centrality bins are segmented into 5% intervals, with examples from the most central (0-5%) to the most peripheral (75-80%)

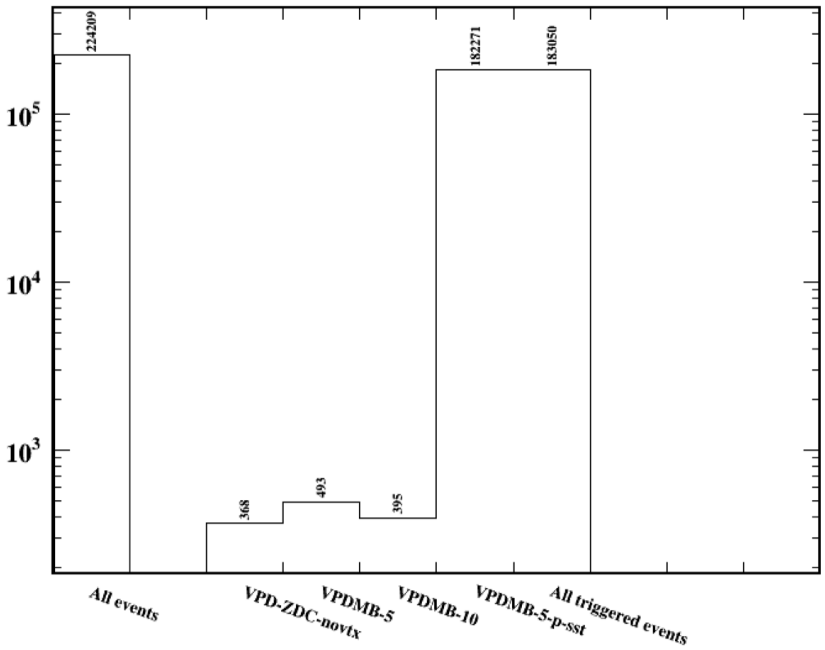

Figure 3.13 The distributions of different triggers in sampled data in Run16.

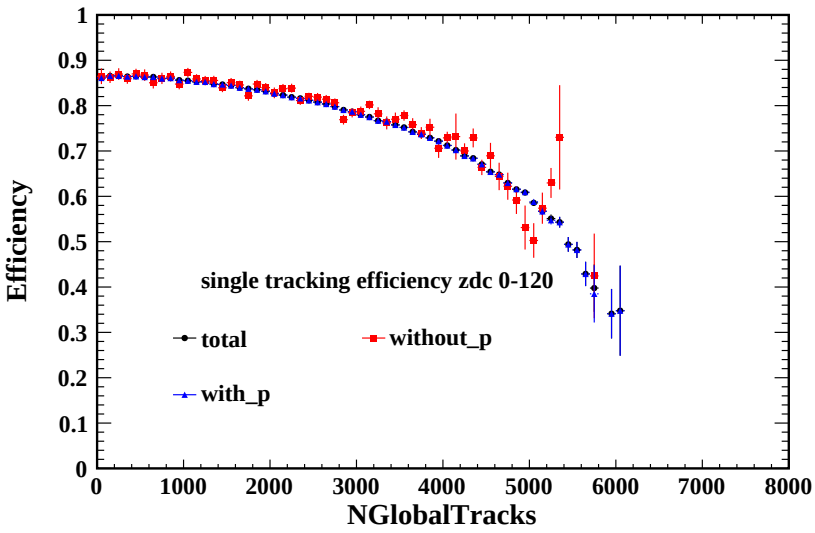

Figure 3.14 The NGlobalTracks dependence of TPC tracking efficiency in Run16.

classes illustrated. It is obvious that the VPDMB-5-p-sst trigger exhibits a higher frequency of events with lower NGlobalTracks. A comparison between the real data and the embedding sample, shown in Fig. 3.16, reveals that the global track number distribution from the embedding is lower at higher track counts, indicating a lower TPC occupancy and, consequently, a higher tracking efficiency. To correct this discrepancy and ensure accurate tracking efficiency in the embedding sample, the ratio of data over embedding is calculated and used as a weight, as depicted in Fig. 3.17. This weight is then applied to the embedding sample to align its tracking efficiency with that of the real data.

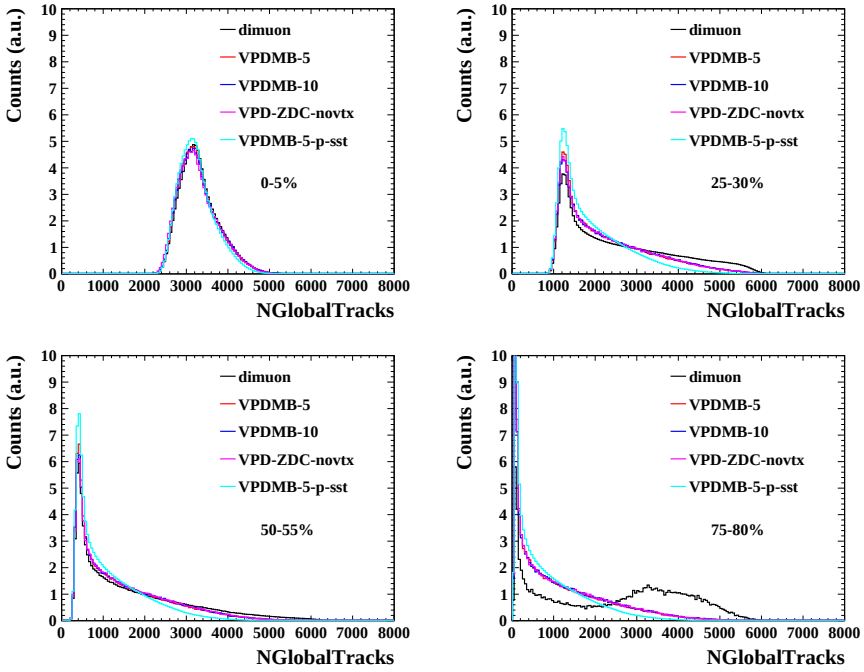

Figure 3.15 Distributions of global tracks numbers for different triggers in different centrality bins in Run16.

3.1.6 Muon selection

1. Track quality cuts

The tracks used for J/ψ reconstruction are required to be primary tracks, and satisfy the following track quality cuts. Due to the MTD's location behind the return bars, particles with low momenta are mostly absorbed by the material in front of the MTD. To guarantee that the track reaches the MTD, the transverse momentum, p_{T}, is required to be larger than 1.3 GeV/c. η is required to be less than 0.8 to ensure good detector acceptance. To reduce the tracks from secondary decays, DCA is required to be less than 1 cm. To ensure good momentum resolution, the number of TPC hits used for track fitting, nHitsFit, is required to be no less than 15. To reduce the split tracks, the ratio

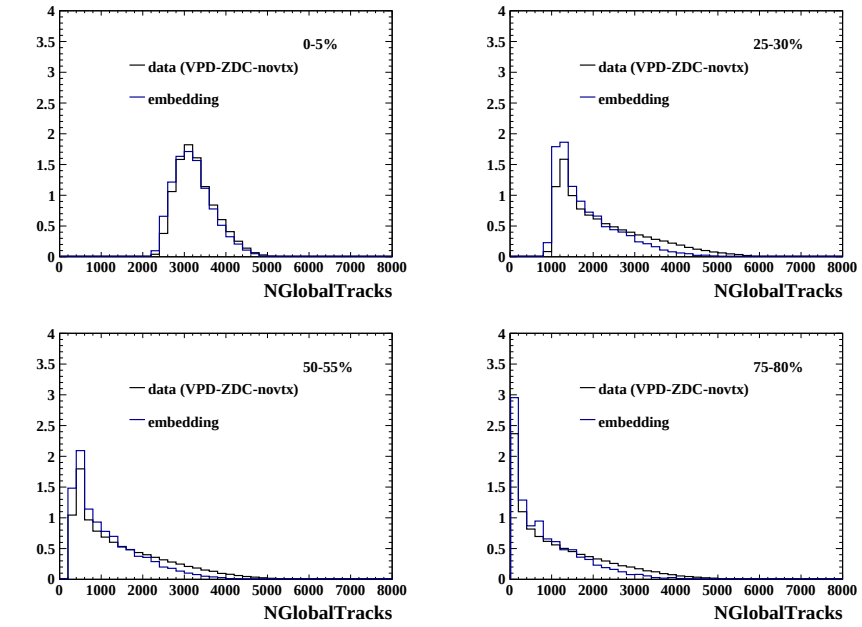

Figure 3.16 Distributions of global tracks numbers from data and embedding in Run16.

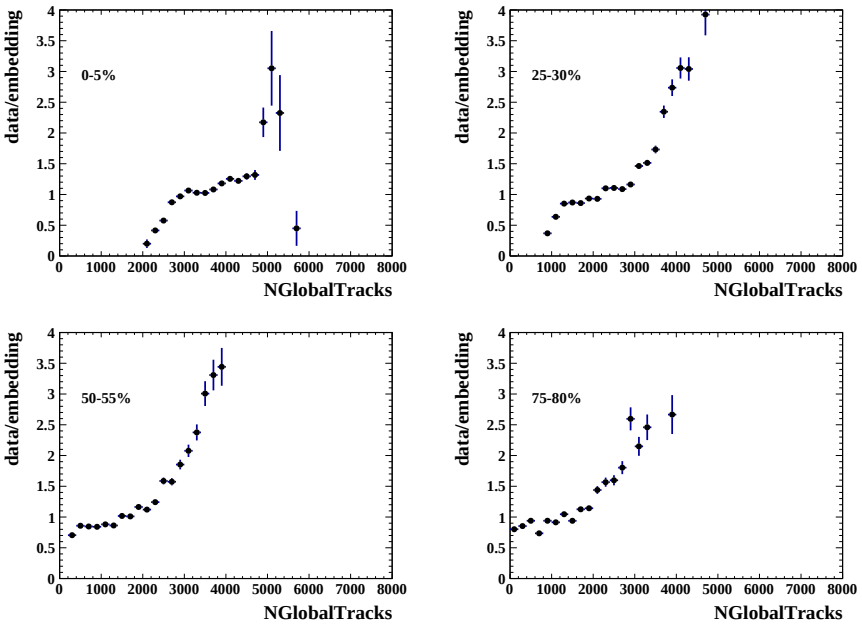

Figure 3.17 Weight of global tracks numbers in different centrality bins in Run16.

of nHitsFit over the number of maximum possible TPC hits (nHitsPoss), nHitsRatio, is required to be at least 0.52. To ensure good dE/dx resolution, the number of TPC hits used for dE/dx calculation, nHitsDedx, is required to be no less than 10. The track quality cuts are summarized in Tab. 3.7.

Table 3.7 Track quality cuts

Variables	Cut
Track type	Primary Track
p_{T}	> 1.3 GeV/c
η	< 0.8
nHitsFit	≥ 15
nHitsRatio	≥ 0.52
nHitsDedx	≥ 10
DCA	< 1 cm

2. Muon identification

The main subsystems utilized for muon identification in this analysis are TPC and MTD. In the TPC, ionization energy loss (dE/dx) is measured and used to select muon candidate tracks. Instead of using dE/dx directly, the normalized energy loss, $\mathrm{n}\sigma_\pi$, is employed, defined as:

$$\mathrm{n}\sigma_\pi = \frac{1}{\sigma}\log\frac{\langle \mathrm{dE/dx}\rangle^{Measured}}{\langle \mathrm{dE/dx}\rangle_\pi^{Theory}}, \tag{3.2}$$

where $\langle \mathrm{dE/dx}\rangle^{Measured}$ is the measured dE/dx, $\langle \mathrm{dE/dx}\rangle_\pi^{Theory}$ is the theoretical dE/dx for pions, and σ is the $\log\langle \mathrm{dE/dx}\rangle$ resolution. The $\mathrm{n}\sigma_\pi$ distribution should ideally follow a Gaussian distribution centered at 0 with a standard deviation of 1 for pions. Muons are expected to exhibit approximately 0.5 σ higher energy loss in the TPC compared to pions for high p_{T} tracks, as shown in Fig. 2.7. Consequently, a selection criterion of $-1 \leq \mathrm{n}\sigma_\pi \leq 3$ is applied to identify muon candidates.

To further enhance the rejection of background hadrons, muon candidate tracks in the TPC are required to match the hits in the MTD, and these hits must trigger the MTD dimuon trigger. This criterion is essential for evaluating trigger efficiency. The variables Δy, Δz, and Δtof, derived from matched TPC track and MTD hit pairs, are integral to the muon selection process. Δz and Δy represent the distance in the z (beam line) and y (azimuthal) directions, respectively, between the MTD hit and the extrapolated track position. The resolutions of Δy and Δz are dominantly influenced by the multiple Coulomb scattering in the absorber. It is expected to decrease with increasing p_{T}. Figures 3.18 and 3.19 compare the Δy and Δz distributions for muons from J/ψ decays in Run16 data with those from embedding, showing good agreement. Figure 3.20 shows the resolutions of Δy and Δz ($\sigma_{\Delta y}$ and $\sigma_{\Delta z}$) as a function of p_{T}. They are

extracted by fitting the Δy and Δz distributions from embedding with a Gaussian function. The resolutions are about 14 cm for Δy and 15 cm for Δz at p_{T} = 1.3 GeV/c and reach 2.5 cm at p_{T} = 10 GeV/c. This is significantly lower than the spatial resolution of LMRPC, which is better than 1 cm. The p_{T} dependence of Δy and Δz resolution is parameterized by the empirical function σ = a + b $\times$ exp(c/p_{T}) as shown in Fig. 3.20. For p_{T} less than 3 GeV/c the Δy and Δz values are required to be within 2σ, while for p_{T} greater than 3 GeV/c, they are required to be within 2.5σ.

Time of flight can be effectively utilized to suppress hadrons due to the relatively lower mass of muons compared to hadrons. Δtof is determined as $\mathrm{tof}_{\mathrm{hit}} - \mathrm{tof}_{\mathrm{track}}$, where tof denotes the time spent by particles flying from the primary vertex to the MTD. $\mathrm{tof}_{\mathrm{hit}}$ is determined using the VPD time (start) and the MTD time (end), while $\mathrm{tof}_{\mathrm{track}}$ is the expected flight time obtained through track propagation. In order to determine the optimal cut value for Δtof, a scan of different Δtof cuts is performed across various J/ψ p_{T} bins. Figure 3.21 illustrates such an analysis for 0 < p_{T} < 1 GeV/c in Run14, presenting the unlike-sign and like-sign invariant mass distributions for different Δtof cut values ranging from 1 ns (upper left) to 0 ns (lower middle). The bin-counting method determines the J/ψ signal significance by calculating the difference between unlike-sign and like-sign pairs under the J/ψ mass peak, i.e., [3.0, 3.2] GeV/c^2. The sideband regions, indicated by yellow bands in the figure, are utilized to determine scale factors for normalizing like-sign distributions. The lower right panel of Fig. 3.21 presents the extracted J/ψ significance for various Δtof cut values, revealing that the significance remains consistent across most values except for Δtof < 0 ns, which exhibits a significant efficiency drop. Figure 3.22 compares J/ψ signal significance across all relevant p_{T} bins for different Δtof cut values. For cut values above 0.25 ns, the resulting significances are notably similar. Considering the balance between signal efficiency and background rejection, while also aiming to reduce the risk of introducing artificial biases, the relatively large Δtof cut (< 0.75 ns) was selected. Furthermore, the relatively large Δtof cut is helpful in controlling the systematic uncertainty. A similar methodology is applied to Run16, selecting a Δtof < 1 ns cut. A summary of the muon particle identification (PID) cuts is listed in Tab. 3.8.

3.2 J/ψ Signal extraction

Following the muon identification criteria outlined previously, the focus is shifted to the reconstruction of the invariant mass distribution, and the next step is extract the

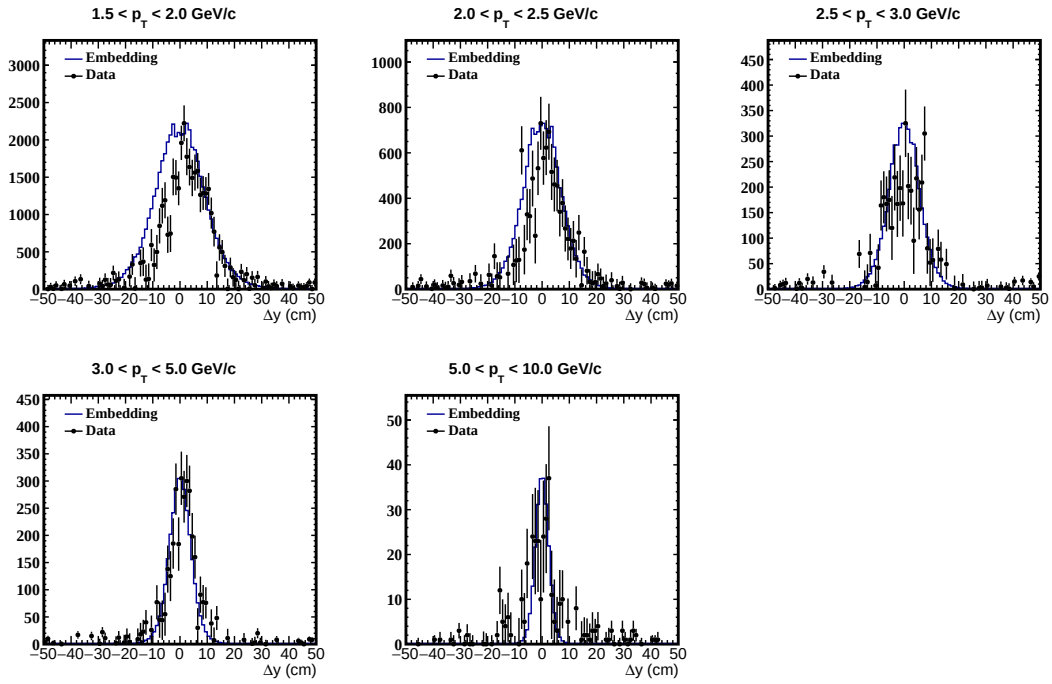

Figure 3.18 Δy **distributions from Run14 data and embedding across different muon** p_{T} **ranges.**

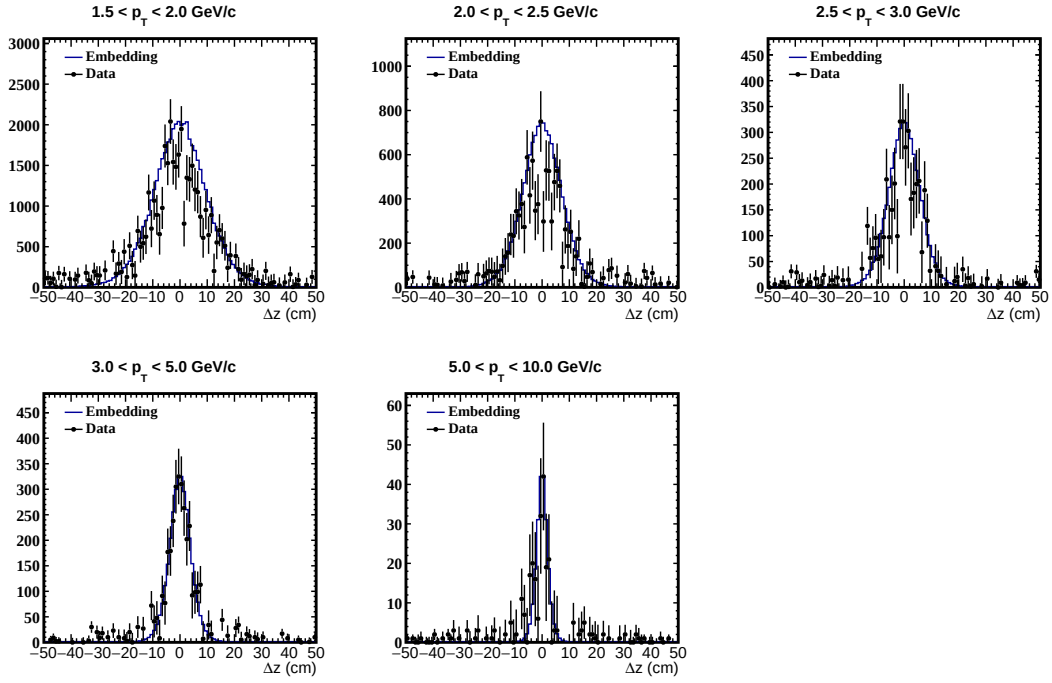

Figure 3.19 Δz **distributions from Run14 data and embedding across different muon** p_{T} **ranges.**

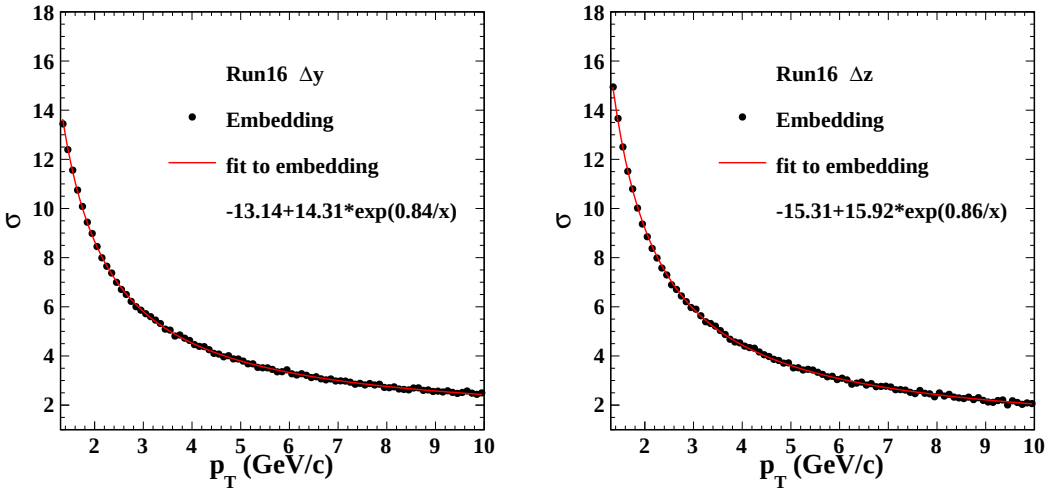

Figure 3.20 The muon p_{T} dependence of the resolution for Δy (left) and Δz (right). The red lines represent exponential fits to the distribution, which are used to determine the cut values on Δy and Δz.

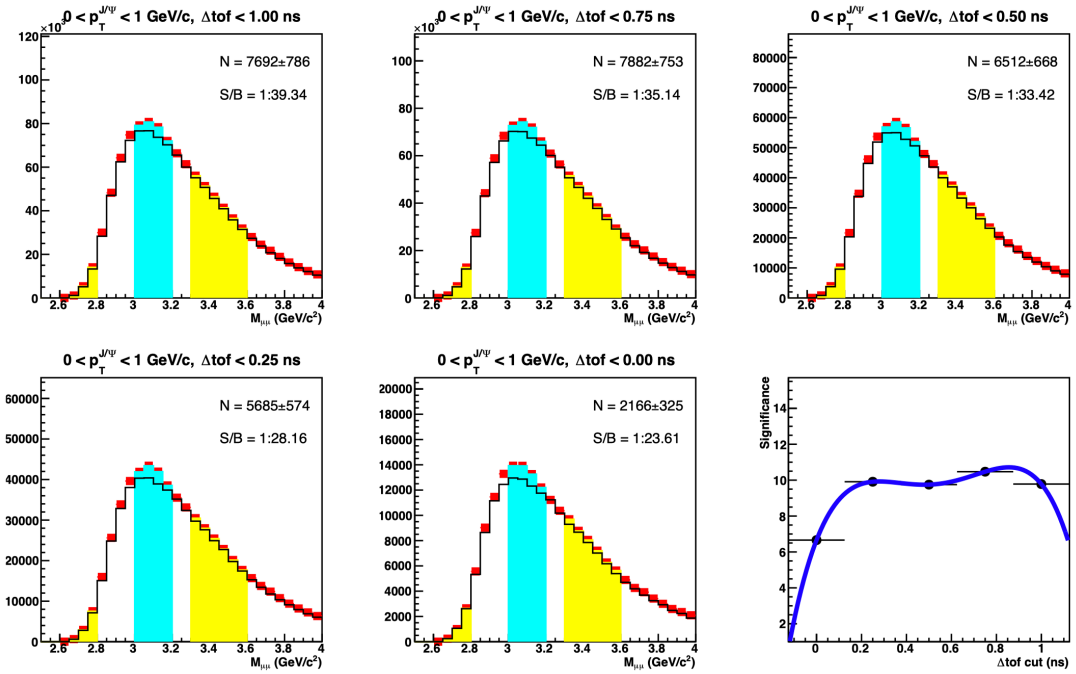

Figure 3.21 Distribution of unlike-sign (red square) and like-sign (black histogram) pairs for different Δtof cut values ranging from 1ns (upper left) to 0 ns (lower middle). The lower right panel shows the signal significance as a function of Δtof cut value.

Table 3.8 muon PID cuts

Variables	Cut
Track type	Primary Track
Trigger MTD	true
Δy and Δz	$\leq 2\sigma$ for $p_{\mathrm{T}} \leq 3$ GeV/$c$and $\leq 2.5\sigma$ for $p_{\mathrm{T}} \geq 3$ GeV/c
Δtof (ns)	≤ 0.75 (Run14) or ≤ 1.0 (Run16)
$n\sigma_{\pi}$	[-1,3]

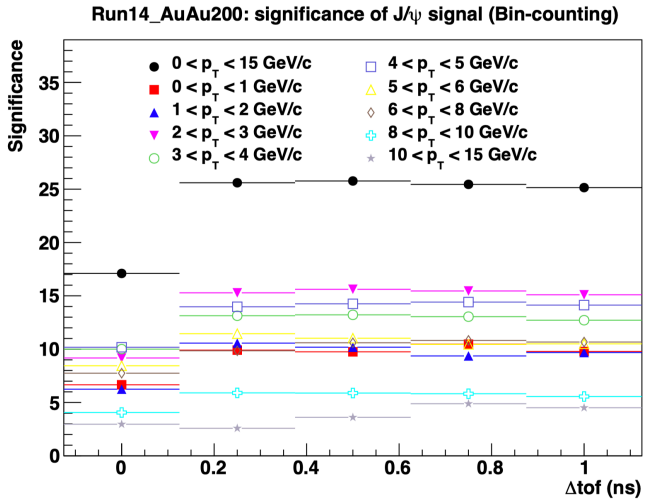

Figure 3.22 The scan of Δtof cut values to J/ψ signal significance for different J/ψ p_{T} bins.

J/ψ signal. This is achieved by analyzing muon pairs with opposite charge signs from the same event, referred to as same-event unlike-sign pairs. A key requirement for these pairs is that their rapidity falls within $|y| < 0.5$, ensuring that they are within the optimal acceptance range of detector. Figure 3.23 illustrates an example of the invariant mass distribution for $p_{\mathrm{T}} < 0.15$ GeV/c in the 40-60% centrality class of Run14. In this figure, the black points depict the distribution of same-event unlike-sign pairs. The J/ψ peak is clear around the mass of J/ψ, indicating the presence of the signal. However, this distribution encompasses not only the signal but also combinatorial and residual backgrounds. To accurately extract the J/ψ signal, it is essential to account for and subtract the background contributions. To estimate the combinatorial background, the distributions of same-event like-sign pairs and mixed-event unlike-sign pairs are utilized, represented in the figure by dashed and solid lines, respectively. The methodologies for background estimation will be discussed in subsequent sections.

3.2.1 Momentum smearing

For the extraction of the J/ψ yield from invariant mass distributions, the J/ψ signal is modeled with a Gaussian function, with the width determined from the embedding process. Nonetheless, it's observed that the momentum resolution of primary tracks in

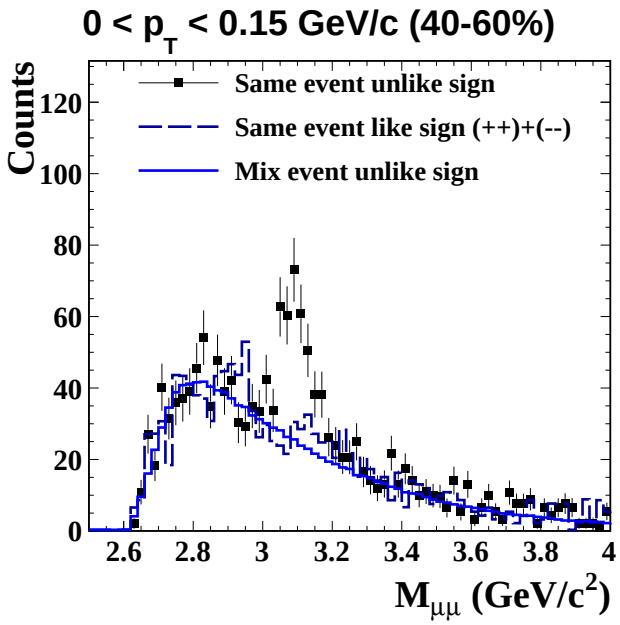

Figure 3.23 Invariant mass distribution for p_T < 0.15 GeV/c in 40-60% centrality in Run14.

the embedding tends to be better compared to that in real data. This discrepancy arises primarily due to two reasons: the imperfect simulation of real-world conditions; and the neglect of primary vertex resolution in the simulation. To rectify this, the momentum resolution within the embedding needs to be adjusted to align with the J/ψ signal width as a function of p_T in real data. This adjustment strategy was applied in the J/ψ R_{AA} analysis using data from Run14[56] and the same tuning procedure is applied in this analysis. Fig. 3.24 presents the mean and σ of the J/ψ peaks as a function of p_T, as extracted from published results. Although the mean value of J/ψ matches the PDG value across the entire p_T spectrum for all centrality bins, a noticeable increase in the σ value with p_T is observed, reflecting the degradation of primary track resolution with increasing p_T. Notably, the width of the J/ψ signal in the $60-80\%$ peripheral collisions appears systematically larger compared to those in more central collision categories. Consequently, the track momentum resolution is tuned separately for each centrality bin, based on the $\sigma(J/\psi)$.

To achieve this purpose, the Toy Monte Carlo (ToyMC) is applied. The ToyMC process involves sampling input J/ψ with uniform distributions across pseudorapidity, $|\eta| < 0.5$, and azimuthal angle, $0 < \varphi < 2\pi$. The p_T spectrum of the raw invariant yield of J/ψ is applied as input p_T spectrum, which is derived from published data within the $0-80\%$ centrality class, as shown in Fig. 3.25[56]. This distribution is fitted with an exponential function $e^{[0]+[1]\cdot p_T}$, subsequently fed into the ToyMC. The decay daughter muons from each J/ψ follow the standard two-body decay kinematics, and no

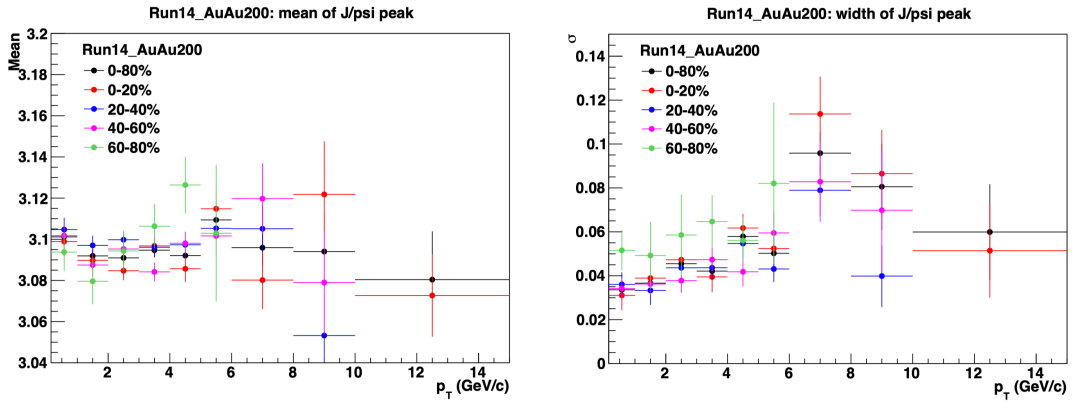

Figure 3.24 The p_{T} dependence of the mean value (left) and σ (right) of the J/ψ signal peaks across different centrality classes.

polarization is applied to the input J/ψ.

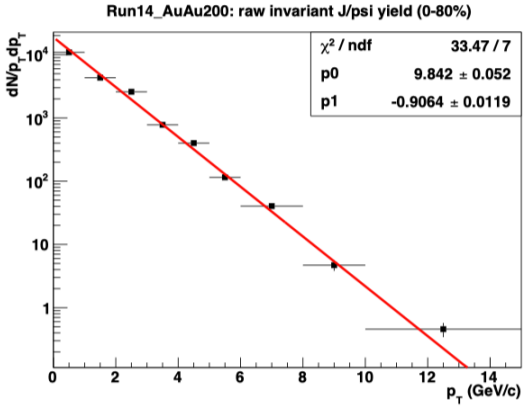

Figure 3.25 Raw invariant yield of J/ψ in 0-80% centrality bin. The exponential fit to the invariant yield is used for ToyMC input.

For every decayed muon, the reconstructed p_{T} is determined by sampling from the $\Delta p_{\mathrm{T}}/p_{\mathrm{T}}$ versus $p_{\mathrm{T,true}}$ distribution shown in Fig. 3.26, where $\Delta p_{\mathrm{T}} = p_{\mathrm{T,true}} - p_{\mathrm{T,reco}}$. For any specific true $p_{\mathrm{T,true}}$ of the muon post-decay, one can locate the corresponding x-axis bin in Fig. 3.26, project it onto the y-axis, and then draw from the resultant 1-D histogram to derive $p_{\mathrm{T,reco}}$, using the following equation:

$$p_{\mathrm{T,reco}} = p_{\mathrm{T,true}} - p_{\mathrm{T,true}} \times \frac{\Delta p_{\mathrm{T}}}{p_{\mathrm{T,true}}}. \tag{3.3}$$

This method ensures an accurate representation of the distribution tails as depicted in Fig. 3.26.

To execute the smearing process, it is imperative to initially derive the primary track p_{T} resolution as a function of p_{T} from the embedding. That in 0-80% centrality bin is depicted in Fig. 3.27 as an example. Observably, the track momentum resolution deteriorates rapidly with increasing p_{T}. The resolution curve is fitted using empirical

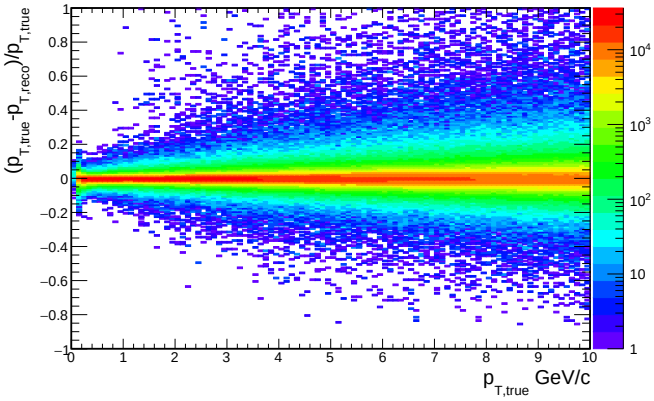

Figure 3.26 2-D distribution of $\Delta p_T/p_{T,\,\mathbf{true}}$ vs. $p_{T,\,\mathbf{true}}$ from Run14 embedding. The distribution is extracted in 0-80% centrality class.

formulas for TPC resolution:

$$\sigma\left(p_T\right) = \sqrt{a^2 p_T^2 + b^2} \tag{3.4}$$

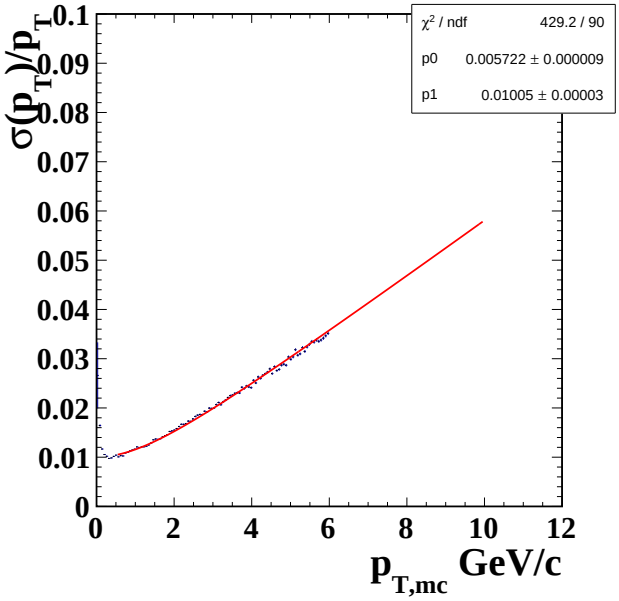

Figure 3.27 The p_T dependence of the track resolution in 0-80% centrality from Run14 embedding.

Given that the first term predominates in Eq. 3.4, smearing is performed by modifying a alone. For each adjusted parameter a', the momentum after smearing is given by:

$$p_{T,\,\text{smear}} = p_{T,\,\text{true}} - p_{T,\,\text{true}} \times \frac{\Delta p_T}{p_{T,\,\text{true}}} \times \frac{\sqrt{(a')^2\, p_{T,\,\text{true}}^2 + b^2}}{\sigma\left(p_{T,\,\text{true}}\right)} \tag{3.5}$$

After obtaining the reconstructed p_T, similar kinematic constraints to those applied in real data are enforced, specifically $p_T > 1.3\text{GeV}/c$ and $\left|\eta_\mu\right| < 0.8$. In the ToyMC simulation, the parameter a' is varied from 0 to 0.02. For each iteration, the width of

the J/ψ signal as a function of p_{T} is extracted. These results are displayed in the left panel of Fig. 3.28, alongside the corresponding distribution from real data and fits to the ToyMC distributions. To assess the congruence, a χ^2 calculation is performed as follows:

$$\chi^2 = \sum_i \frac{\sigma_i^{\mathrm{data}} - \sigma_i^{\mathrm{ToyMC}}}{Err\left(\sigma_i^{\mathrm{data}}\right)} \tag{3.6}$$

where $\sigma_i^{\mathrm{ToyMC}}$ is obtained from the fits. The right panel of Fig. 3.28 shows the χ^2 values as a function of the scanned parameter a'. To identify the parameter that minimizes χ^2, a 4th-order polynomial function is fitted to this distribution. The parameter is 0.007 for the $0-80\%$ centrality bin.

The uncertainty of a is calculated via a method that entails independently adjusting each data point within their individual statistical uncertainties, as shown in the left panel of Fig. 3.28. The process is carried out 500 times. This method is utilized to extract the optimal value of a that minimizes χ^2 for each iteration, resulting in a distribution of the parameter a. This process allows for a comprehensive assessment of the parameter's stability and the influence of statistical variations on its determination. For each centrality interval, the distribution obtained from this procedure is analyzed to quantify the uncertainty on a. The left panel of Fig. 35 illustrates one such distribution for the $0-80\%$ centrality interval, which is subsequently fitted with a Gaussian function. The standard deviation of this Gaussian fit provides a measure of the uncertainty on the smearing parameter a, ensuring a robust estimation of this critical parameter's variability due to statistical fluctuations in the data. The determined values of the smearing parameter a, inclusive of their uncertainties, are listed in Tab. 3.9 for each analyzed centrality interval.

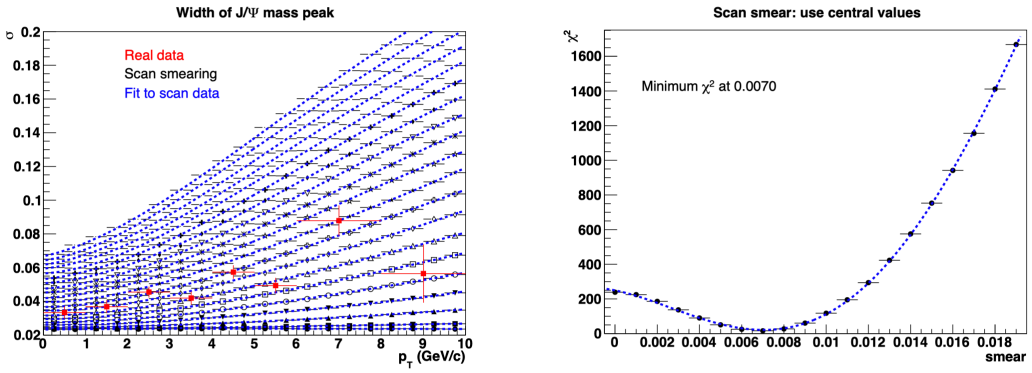

Figure 3.28 Left: The p_{T} dependence of J/ψ signal width distributions, the black points show the results from scanned parameters in ToyMC and red points show real data in Run14. Fits to the ToyMC are shown as blue dashed lines. Right: χ^2 between ToyMC and real data for all the scanned parameters.

After applied the best value for the smearing parameter a, the J/ψ width distribution as a function of transverse momentum (p_{T}) obtained from the Toy Monte Carlo (ToyMC) simulation is depicted in the right panel of Fig. 3.28. The simulated values of J/ψ width from ToyMC are shown as open black circles, and the magenta curves surrounding these points illustrate the uncertainty associated with the smearing parameter a. For comparison, the distribution derived from real data is also included in the figure, represented by filled red circles. This analysis procedure is consistently applied across different centrality intervals.

Furthermore, Fig. 3.29 showcases the J/ψ width as a function of p_{T} incorporating additional smearing based on the ToyMC simulation for various centrality intervals. The p_{T} binning adopted in this presentation matches that employed in the analysis of real data. The error bars attached to each data point reflect the systematic uncertainties stemming from the uncertainty in the smearing parameter a, thereby providing a comprehensive depiction of the J/ψ signal behavior across different centrality classes and p_{T} ranges.

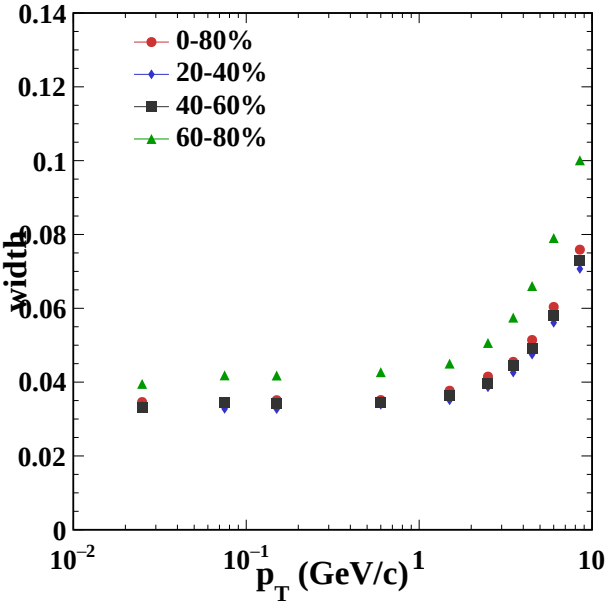

Figure 3.29 J/ψ width distribution as a function of p_{T} from ToyMC after applying the additional smearing in Run14.

3.2.2 Mixed event technique

The mixed-event technique is employed to estimate the combinatorial background in the dimuon invariant mass distributions. This method involves pairing muons from two distinct events, effectively eliminating any correlation between them. A key advantage of this method is the significant increase in statistics, as it allows for the mixing of

Table 3.9 Smeared a in different centrality

Centrality bin	a (10^{-3})
60-80%	9.7 ± 0.52
40-60%	6.7 ± 0.37
20-40%	6.39 ± 0.37
0-20%	7.58 ± 0.33
0-80%	7.01 ± 0.23

one muon from a particular event with muons from numerous other events. To ensure effective and appropriate mixing, events are selected for mixing only if they have similar global characteristics. Specifically, the events are categorized into 16 bins based on 0-80% centrality and 20 bins according to $|V_z|$ within 100 cm. An event buffer size of 20 is maintained to facilitate this process.

While the unlike-sign distribution from the mixed-event technique is utilized for background estimation, its normalization is typically determined by comparing the like-sign distributions from both mixed-event and same-event. Figure 3.30 illustrates the ratios of like-sign pair mass distributions from same-event and mixed-event for the 0-80% centrality range in Run14. To serve as examples, two p_{T} bins, specifically $0 < p_{\mathrm{T}} < 0.05$ GeV/c and $2 < p_{\mathrm{T}} < 3$ GeV/c, have been chosen. These ratios are fitted with a first-order polynomial function, depicted as red lines in the figure, to account for shape differences between same-event and mixed-event distributions. This fit is then used to normalize the unlike-sign distribution from the mixed-event.

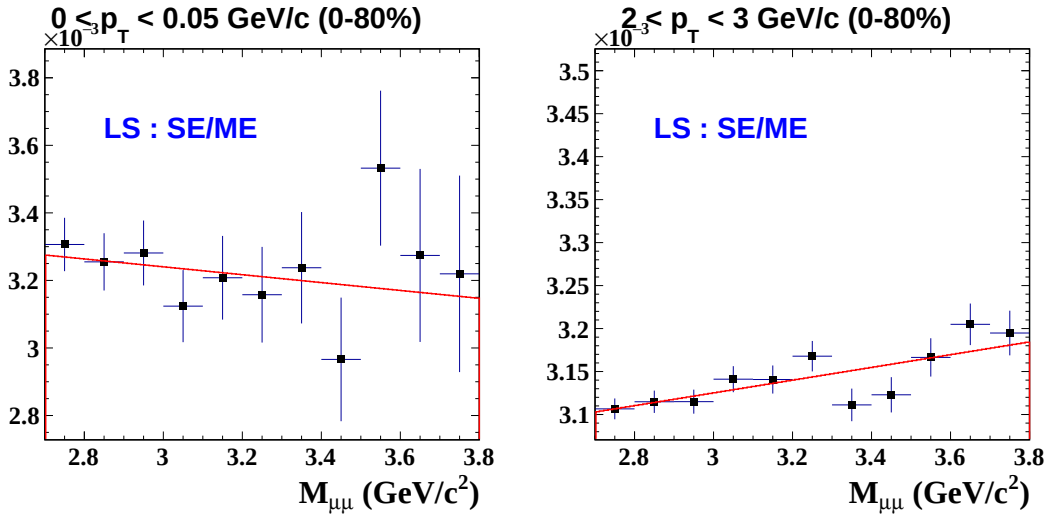

Figure 3.30 The ratios of like-sign distributions from same-event and mixed-event across two different J/ψ p_{T} bins for the 0-80% centrality range in Run14.

3.2.3 Signal extraction

The process of extracting the J/ψ signal counts from the same-event unlike-sign distributions encounters challenges related to statistical richness. In scenarios where

statistics are poor, the data tend to follow a Poisson distribution. Under these circumstances, the Maximum Likelihood (ML) method is more effective than the Least Squares fitting approach, providing better results. Moreover, the ML method remains comparable results when the statistics is good. Given these advantages, the extraction of the J/ψ signal in this analysis employs the Maximum Likelihood (ML) method, which integrates various components as elaborated in the preceding sections:

1. Signal: Modeled by a Gaussian distribution. The widths of these Gaussian functions are fixed based on the results from ToyMC simulations with additional smearing applied to account for track momentum resolution, as detailed in Section 3.2.1.
2. Combinatorial Background: Represented by the mixed-event unlike-sign distribution, scaled appropriately as described in Section 3.2.2.
3. Residual Background: Estimated using empirical functions. Specifically, an exponential function is applied to $p_{\mathrm{T}} < 0.15$ GeV/c in 40-60% and 60-80% centrality intervals, while a first-order polynomial function is used for other cases.

The left panel of Fig. 3.31 displays the invariant mass distribution of unlike-sign muon pairs within the 2 < pair p_{T} < 3 GeV/c range (depicted as open circles), along with the mixed-event background (illustrated in blue) and the combined fit (depicted as open circles) for the 60-80% centrality bin in Run14. The right panel demonstrates the distribution after the subtraction of the mixed-event background, showing fits to both the signal and residual background. Notably, for the p_{T} bins of 0-0.05 GeV/c and 0.05-0.1 GeV/c the fits include only the signal and residual background components due to the extremely low background in these bins, with the 0-0.05 GeV/c p_{T} bin also depicted as an instance in Fig. 3.32. The effectiveness of the fits across all p_{T} bins is well illustrated within these figures. There no signal is seen above 7 GeV/c in 60-80% centrality class. Additionally, J/ψ yields are extracted using the bin-counting method within $\pm 3\sigma$ of the signal peak, with the results presented in the figure. While the fit results are considered the default, the bin-counting method results are used to assess uncertainties. Similar evaluations are performed on unlike-sign invariant mass distributions across the 20-40% and 40-60% centrality classes for Run14, as well as these three centrality categories during Run16.

A similar extraction procedure for finer p_{T} bins in the 40-80% centrality class for both Run14 and Run16 is also taken. The finer p_{T} bins are used to obtain p_{T}^2 distribution. Two typical p_{T} bins are shown in Fig. 3.33 and Fig. 3.34 with in $p_{\mathrm{T}} < 0.03$ GeV/c and $0.09 < p_{\mathrm{T}} < 0.012$ GeV/c. In most cases, as in $0.09 < p_{\mathrm{T}} < 0.012$ GeV/cp_{T} bin, the

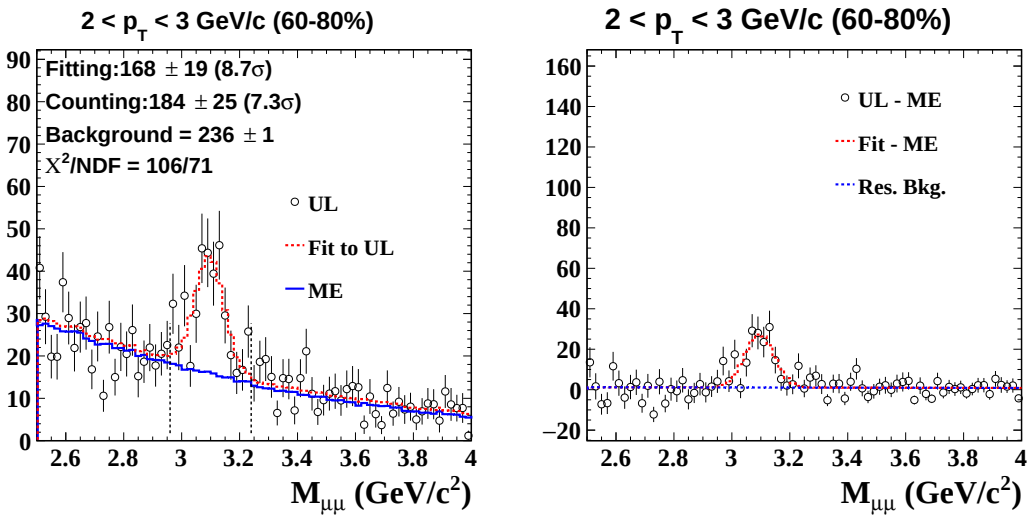

Figure 3.31 Unlike-sign muon pair distribution in 2 < p_T < 3 GeV/c (black) in 60-80% centrality bin in Run14. The blue histogram in the left panel indicates the mixed-event distributions for the combinatorial background, while the blue dashed line in the right panel represents fit to the residual background. The red curve indicates the combined fits of signal and background.

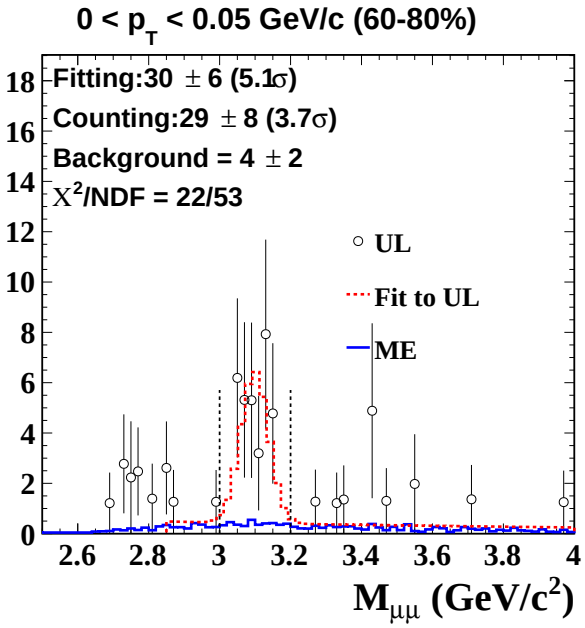

Figure 3.32 Unlike-sign muon pair distributions in pair p_T < 0.05 GeV/c (open circles) in 60-80% centrality bin in Run14. The blue histogram indicates the mixed-event distributions for combinatorial background. The red curves indicate the combined fits of signal and background.

invariant mass distributions of unlike-sign muon pairs are fitted using a Gaussian function to represent the signal, mixed-event distributions to account for the combinatorial background, and an exponential function for the residual background. The widths of these Gaussian functions are based on the ToyMC simulations. An exception is made for the 0-0.03 GeV/c and 0.03-0.05 GeV/c p_{T} bins, although the mixed-event technique is also applied in these bins, due to the limit contribution of combinatorial background, the fitting procedure is adjusted to include only the signal and residual background components, as shown in Fig. 3.34.

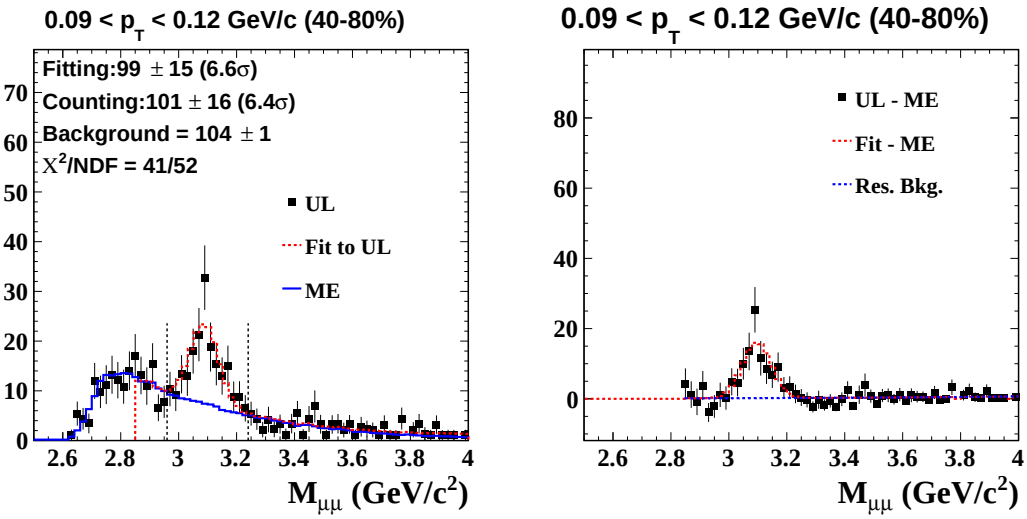

Figure 3.33 Unlike-sign muon pair distribution in 0.09 < p_{T} < 0.012 GeV/c (black) in 40-80% centrality bin in Run14. The blue histogram in the left panel indicates the mixed-event distributions for combinatorial background, while the blue dashed line in the right panel represents fit to residual background. The red curve indicates the combined fits of signal and background.

3.3 Efficiency Correction

The total J/ψ efficiency has the following main contributions:

$$\epsilon_{\mathrm{total}} = \epsilon_{\mathrm{TPC}} \times \epsilon_{\mathrm{match}} \times \epsilon_{\mathrm{PID}} \times \epsilon_{\mathrm{trigger}} \tag{3.7}$$

where the ϵ_{TPC} is the TPC tracking efficiency and acceptance, the $\epsilon_{\mathrm{match}}$ is the MTD matching efficiency, the ϵ_{PID} is the muon PID efficiency and the $\epsilon_{\mathrm{trigger}}$ is the MTD dimuon trigger efficiency.

The embedding sample is used to calculate the single track efficiency which includes ϵ_{TPC}, $\epsilon_{\mathrm{match}}$ and a portion of ϵ_{PID}. Efficiencies that cannot be evaluated using the embedding sample are determined through data-driven methods and manually applied to the embedding sample. The pair efficiency is evaluated by folding the single track efficiency using a Toy Monte-Carlo (ToyMC) approach.

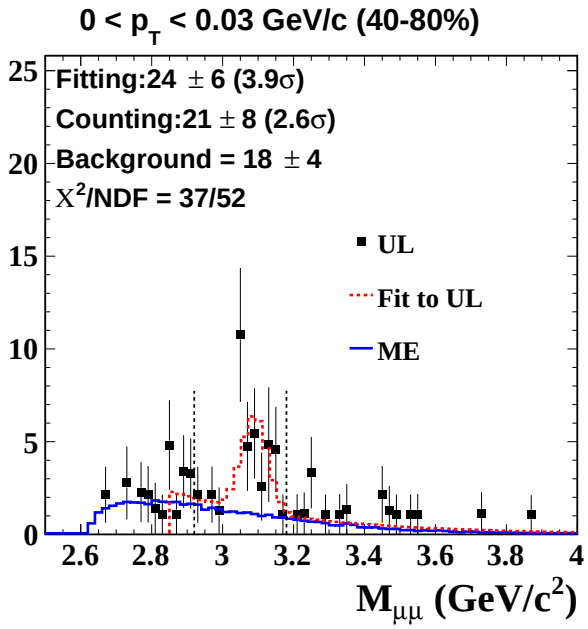

Figure 3.34 Unlike-sign muon pair distributions in p_T < 0.03 GeV/c(black) in 40-80% centrality bin in Run14. The blue histogram indicates the mixed-event distributions for combinatorial background. The red curve indicates the combined fits of signal and background.

3.3.1 TPC tracking efficiency

The TPC tracking efficiency as well as the TPC acceptance are evaluated as follows:

$$\epsilon_{\mathrm{TPC}} = \frac{N_{\mathrm{rec}}(\text{after track quality cuts})}{N_{\mathrm{emb}}} \tag{3.8}$$

where N_{rec} represents the number of reconstructed muon tracks that have passed the track quality cuts outlined in Sec. 3.1.6, and N_{emb} denotes the total number of Monte Carlo muon tracks generated for embedding.

The performance of the TPC in real data is not perfectly ideal, and the embedding process may not fully replicate this performance. Discrepancies are observed when comparing the η vs. ϕ distributions of reconstructed MC tracks in the embedding sample within $|V_z| < 30$ cm to those of charged tracks in the MB data sample within $|V_z| < 100$ cm, as shown in Fig. 3.35 for the 0-80% centrality class in Run16. The comparison necessitates the use of the MB sample due to biases in the dimuon sample. Notably, inefficiencies in some TPC sectors are visible in the data but are not reproduced in the embedding sample. Additionally, a decrease in the η distribution near η close to 1 in real data, which is absent in the embedding, is attributed to the narrower V_z distribution in the embedding. A dip in the $\eta < 0.05$ range in the embedding sample also does not match with real data.

To correct for the observed η and ϕ dependent TPC efficiency discrepancies in data, a two-step procedure is employed:

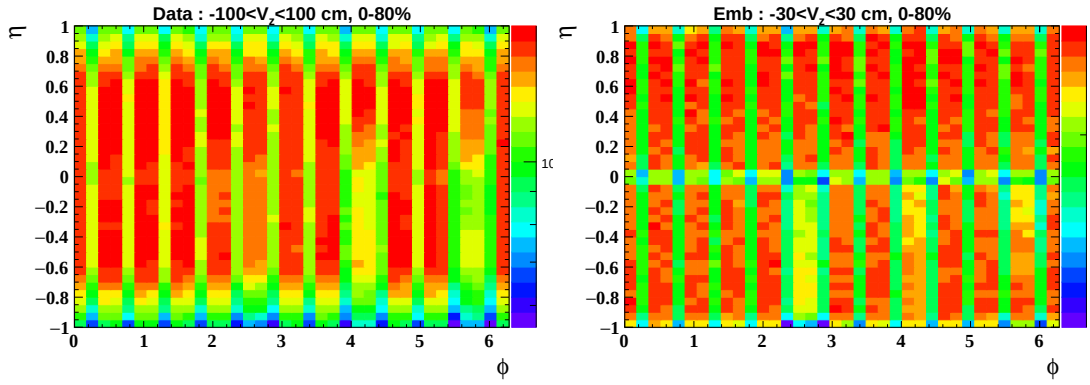

Figure 3.35 Left: η vs. ϕ distributions of reconstructed MC tracks in the embedding sample within $|V_z| < 30$ cm. Right: η vs. ϕ distribution of charged tracks in the MB data sample within $|V_z| < 100$ cm

- Step 1: The η distribution is corrected first. The η vs. ϕ distributions are projected onto the η distribution within $0 < \phi < 1.5$, a ϕ range not affected by TPC inefficiency. The ratio of data over embedding for the η distribution, depicted in the left panel of Fig. 3.36, is applied as a weight. The right panel of Fig. 3.36 shows the η vs. ϕ distributions of reconstructed MC tracks in the embedding sample within $|V_z| < 30$ cm after applying the η distribution weight.
- Step 2: TPC inefficiencies in specific sectors are addressed next. Track ϕ distributions for two distinct η ranges, $0.3 < \eta < 1.0$ and $-1.0 < \eta < 0.3$, are compared in Figs. 3.37 and 3.38, with distributions in various p_T bins for muon tracks from embedding and charged tracks from real data. Discrepancies in the ϕ distributions, particularly in the ranges of $1.9 < |\phi| < 2.3$, $4.0 < |\phi| < 4.5$, and $5.5 < |\phi| < 6.0$ within $-1.0 < \eta < 0.3$, are corrected by applying a factor to the embedding sample to match the data, as shown in Fig. 3.39. This correction factor, dependent on track p_T and $|\phi|$, is specifically applied within the $-1.0 < \eta < 0.3$ range. To avoid statistical fluctuations in the highest track p_T bin, the correction factor derived for $3 < p_T < 5$ GeV/c is extended to tracks with p_T above 5 GeV/c, ensuring a consistent correction across all relevant p_T ranges.

Figure 3.40 shows the TPC tracking efficiency as a function of p_{T} for run16 in different centralities. A similar procedure is applied to run14 to estimate the TPC tracking efficiency.

3.3.2 MTD matching efficiency

As previously discussed in Section 3.1.5, the MTD acceptance is artificially introduced in the embedding and the acceptance efficiency is evaluated through the embedding.

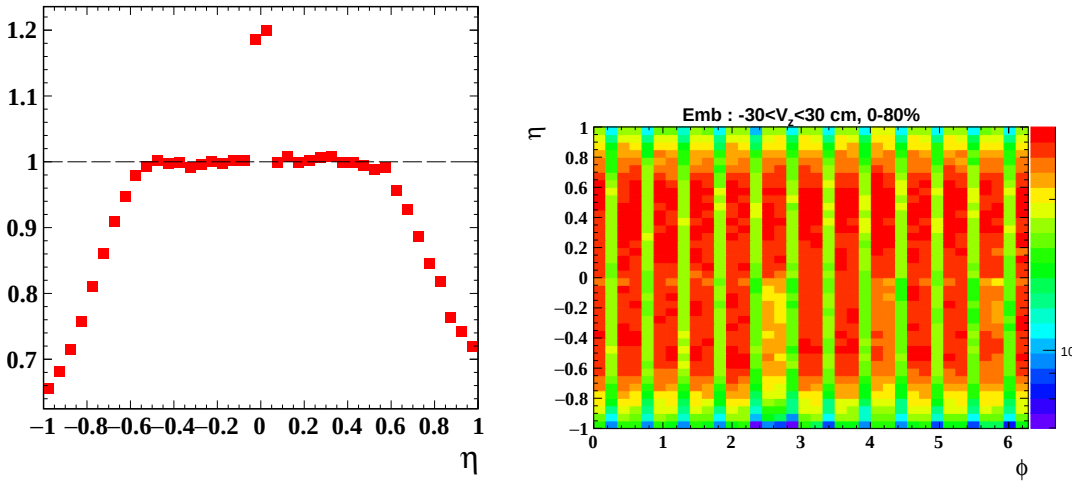

Figure 3.36 Left: Ratio of η distribution for muon tracks from data over embedding within $0 < \phi < 1.5$. Right: The η vs. ϕ distributions of reconstructed MC tracks in the embedding sample within $|V_z| < 30$ cm after applying the η distribution weight.

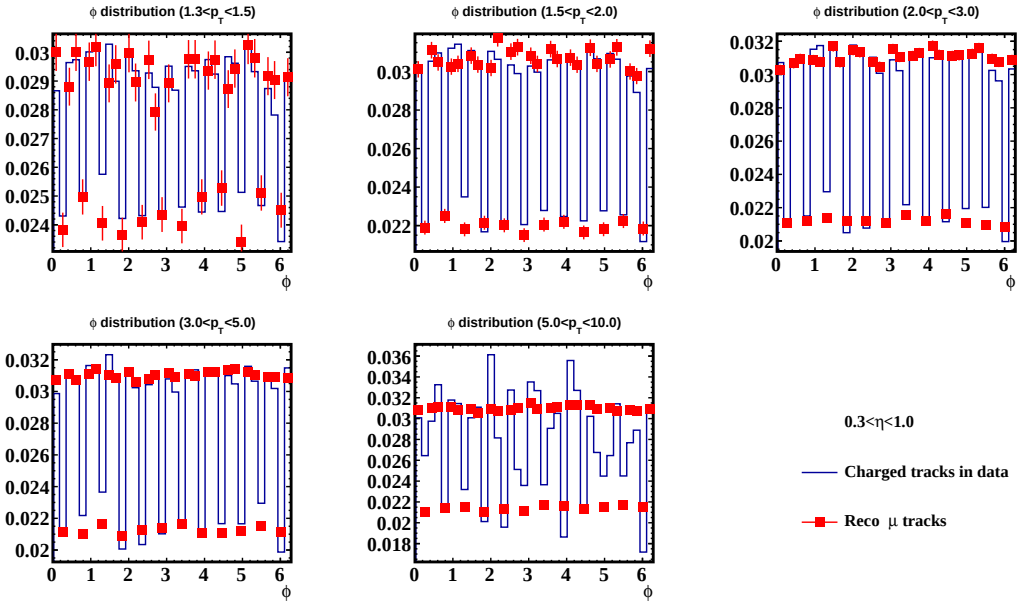

Figure 3.37 ϕ distributions for muon tracks from embedding and charged tracks from data within $0.3 < \eta < 1.0$. Different panels correspond to different track p_{T} ranges.

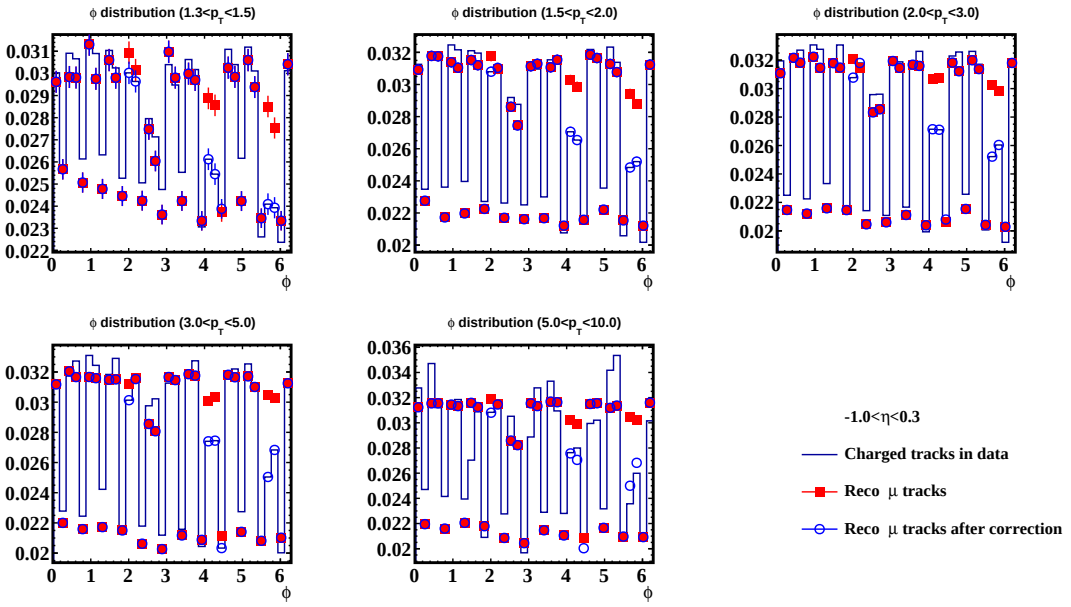

Figure 3.38 **ϕ distributions for muon tracks from embedding and charged tracks from data within -1.0 < η < 0.3. Muon track distributions from embedding after correction are shown as open blue squares. Different panels correspond to different track p_{T} ranges.**

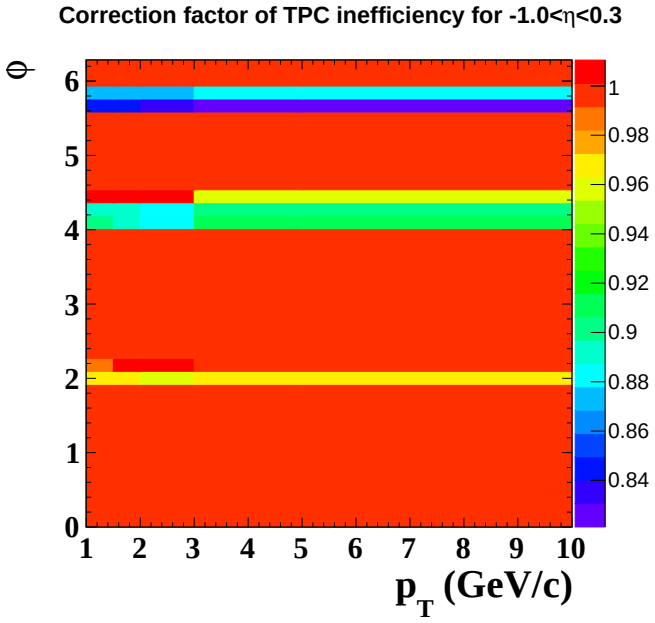

Figure 3.39 **Additional correction factor corresponding to the inefficiency of TPC as a function of track p_{T} and ϕ in Run16.**

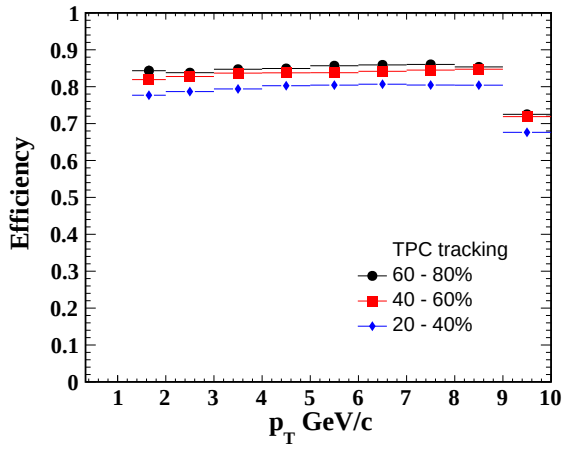

Figure 3.40 Efficiencies of TPC tracking as a function of muon p_{T} in different centrality classes in Run16.

The estimation of MTD response efficiency involves the extrapolation of tracks to the MTD detectors utilizing cosmic ray data, followed by determining the fraction of these tracks that produce detectable hits within the MTD's active zones. This process of efficiency evaluation is similarly undertaken during the embedding procedure, as depicted in Figure 3.41, under the assumption that the MTD response operates flawlessly. Discrepancies observed between the cosmic ray data and embedding outcomes, illustrated in Figure 3.42, are subsequently applied to adjust the embedding sample's efficiency.

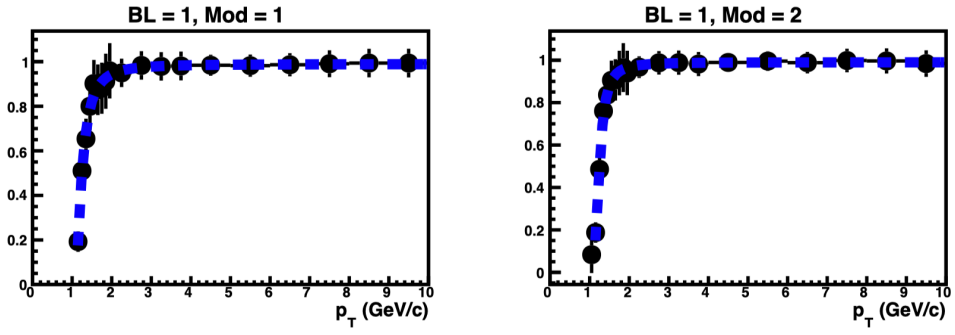

Figure 3.41 The p_{T} dependence of MTD response efficiency for two MTD modules from embedding.

The MTD trigger efficiency comprises both the efficiency of MTD trigger electronics and the efficiency of the online trigger time window cut. The MTD trigger efficiency applied in this analysis is derived from the STAR published results using the Run14 and Run16 datasets[56,133]. The left panel of Fig. 3.43 shows the MTD trigger electronics efficiency as a function of muon p_{T}, while the right panel shows the MTD online trigger time window cut efficiency as a function of muon p_{T}.

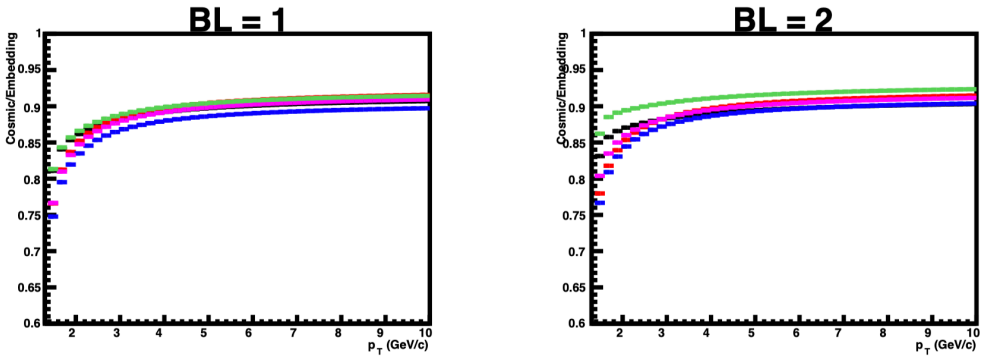

Figure 3.42 The cosmic ray data over embedding ratios of MTD responses efficiency across different backlegs.

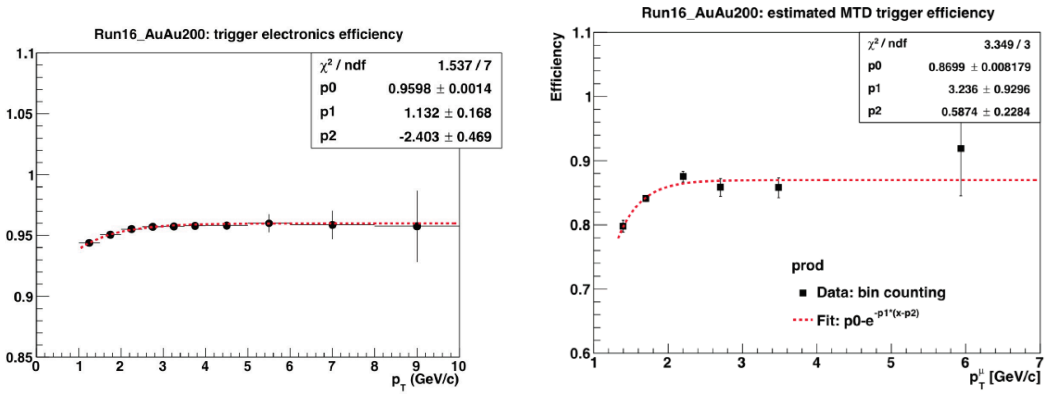

Figure 3.43 Displayed as a function of muon p_T in Run16: the MTD trigger electronics efficiency (left) and the MTD online trigger time window cut efficiency(right).

3.3.3 Muon PID efficiency

The muon PID cuts are detailed in Sec. 3.1.6. Efficiencies for Δy and Δz are estimated within the embedding sample, aligning closely with real data distributions.

Due to the absence of simulated timing information for VPD and MTD, a data-driven tag-and-probe method estimates the Δtof cut efficiency. The Tag and Probe method relies on the decay of known resonances in particle pairs. In this technique, decaying muons are classified according to specific criteria. A Tag Muon is a well-identified, triggered muon that adheres to tight selection criteria. Conversely, a Probe Muon comprises a broad set of muon candidates subjected to very loose selection criteria. These muons are assessed to determine whether they meet or fail the criteria for which the efficiency is being measured. Tag muons are used to trigger the presence of a resonance decay, while probe muons, paired with tag muons, are employed to measure efficiency due to their unbiased characteristic. The efficiency is determined by the fraction of probe muons that satisfy a specific criterion. This can be expressed as:

$$\varepsilon = \frac{\text{Number of probe muons passing the criterion}}{\text{Total}} \tag{3.9}$$

Here, the denominator represents the total number of J/ψ candidates (tag + probe pairs) reconstructed within the dataset, while the numerator is the subset of these candidates for which the probe muon successfully meets the criterion. The PID criteria for tagged and probed muons are listed in Tab. 3.10. Notably, the Δtof cut for tagged muons in Run16 is more stringent than in Run14, reflecting a shift in the Δtof mean value towards the negative in Run16, as depicted in Fig. 3.44. Conversely, the probed muon's PID cuts mirror the standard analysis, excluding the Δtof cut to determine its efficiency.

Table 3.10 List of muon PID cuts for tag and probe muons

	Tag muon	Probe muon
$n\sigma_\pi$	$[0, 3]$	$[-1, 3]$
Δy	$\leq 2(2.5)\sigma$ for $p_T \leq(\geq)$ 3 GeV/c	$\leq 2(2.5)\sigma$ for $p_T \leq(\geq)$ 3 GeV/c
Δz	$\leq 2(2.5)\sigma$ for $p_T \leq(\geq)$ 3 GeV/c	$\leq 2(2.5)\sigma$ for $p_T \leq(\geq)$ 3 GeV/c
Δtof	≤ 0 (Run16) or ≤ 0.2 (Run14)	no Δtof cut

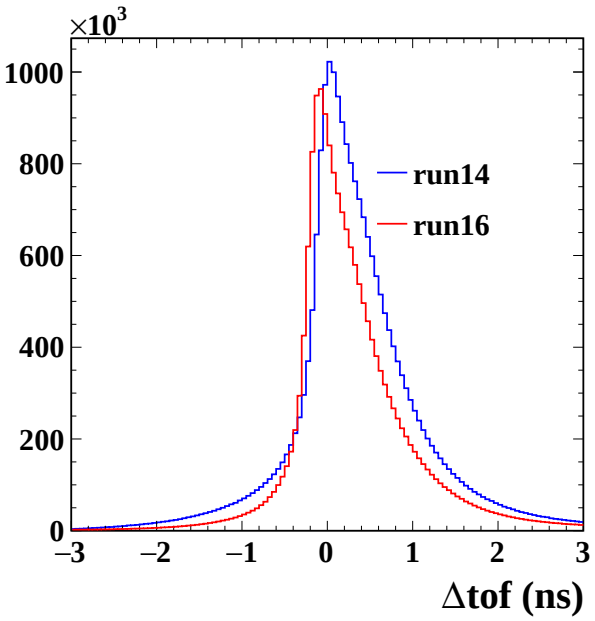

Figure 3.44 Δtof distribution for J/ψ decayed muons from Run14 (blue) and Run16 (red).

Figure 3.45 illustrates the invariant mass distributions of unlike-sign muon pairs across different pair p_T bins in Run16, exempting the probed muon from the Δtof cut. These distributions are fitted with a Gaussian function for the signal, fixed at the PDG value of the J/ψ meson (3.096 GeV/c^2), and a third-order polynomial for background, shown as red and blue dashed lines respectively in Fig. 3.45. Applying a 1.0 ns Δtof cut to the probed muon, Figure 3.46 presents the resulting invariant mass distributions. The J/ψ yields are extracted with fixed Gaussian widths from Fig. 3.45. The extracted J/ψ counts for the case of no Δtof cut and a Δtof < 1.0 ns cut are plotted in the left panel of Fig. 3.47 as a function of J/ψ p_T. The Δtof cut efficiency, shown in the right

panel of Fig. 3.47, increases from approximately 94% at the lowest p_{T} to about 96.5% at higher p_{T}, fitted with the function:

$$f(x) = [0] - e^{-[1]\cdot(x-[2])}. \tag{3.10}$$

Also shown in the right panel are the systematic uncertainties for the Δtof cut efficiency (dashed lines) as estimated in Sec. 3.4.3.

The $\mathrm{n}\sigma_{\pi}$ distributions for muons from J/ψ decays in Run16 data, compared to embedding simulations, are shown in Fig. 3.48. As anticipated, the data's $\mathrm{n}\sigma_{\pi}$ distributions peak around 0.5. However, it is observed that the $\mathrm{n}\sigma_{\pi}$ values in embedding are systematically higher than in the data, likely due to insufficient simulation tuning. Consequently, the embedding sample is deemed unsuitable for calculating the $\mathrm{n}\sigma_{\pi}$ cut efficiency. In contrast, the $\mathrm{n}\sigma_{\pi}$ distributions between data and embedding for Run14 align well, as illustrated in Fig. 3.49, thus the efficiency is extracted from embedding for Run14. The data-driven method, similar to that applied for the Δtof cut efficiency, is therefore employed to calculate the $\mathrm{n}\sigma_{\pi}$ cut efficiency for Run16, the result $\mathrm{n}\sigma_{\pi}$ cut efficiency is depicted in Fig. 3.50.

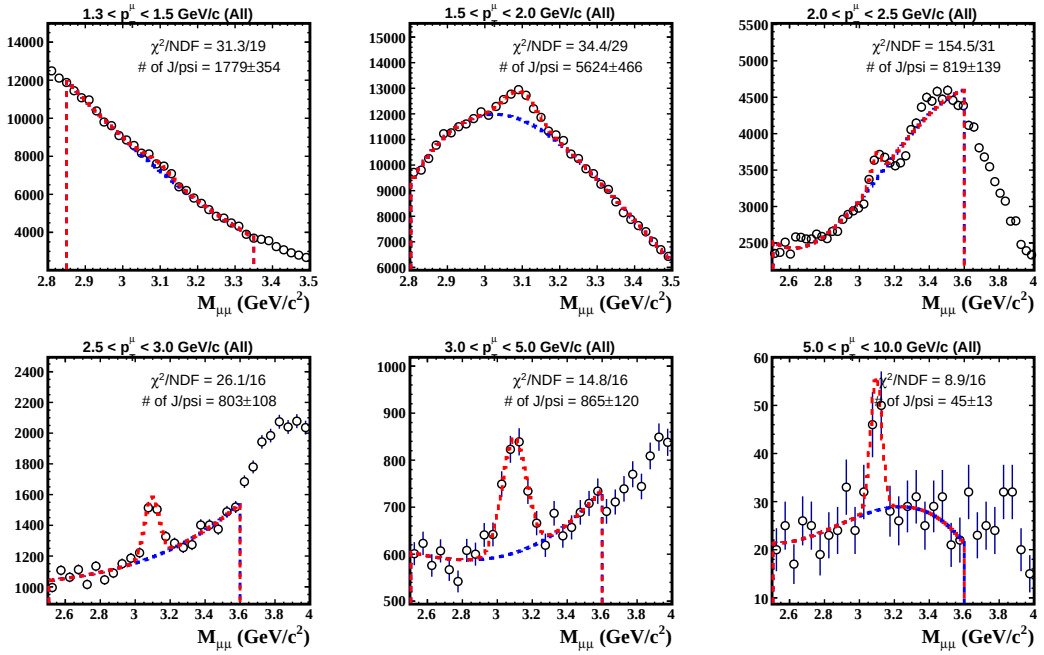

Figure 3.45 Unlike-sign muon pairs mass distributions in different pair p_{T} bins, where no Δtof cut is applied to the probed muon. The red dashed lines are combined fits to the signal and the background while the blue dashed lines indicate the background component of the fit.

3.3.4 Total efficiency

The single track efficiencies are estimated and enable the evaluation of J/ψ pair efficiency. This analysis employs a ToyMC simulation to fold single track efficiencies

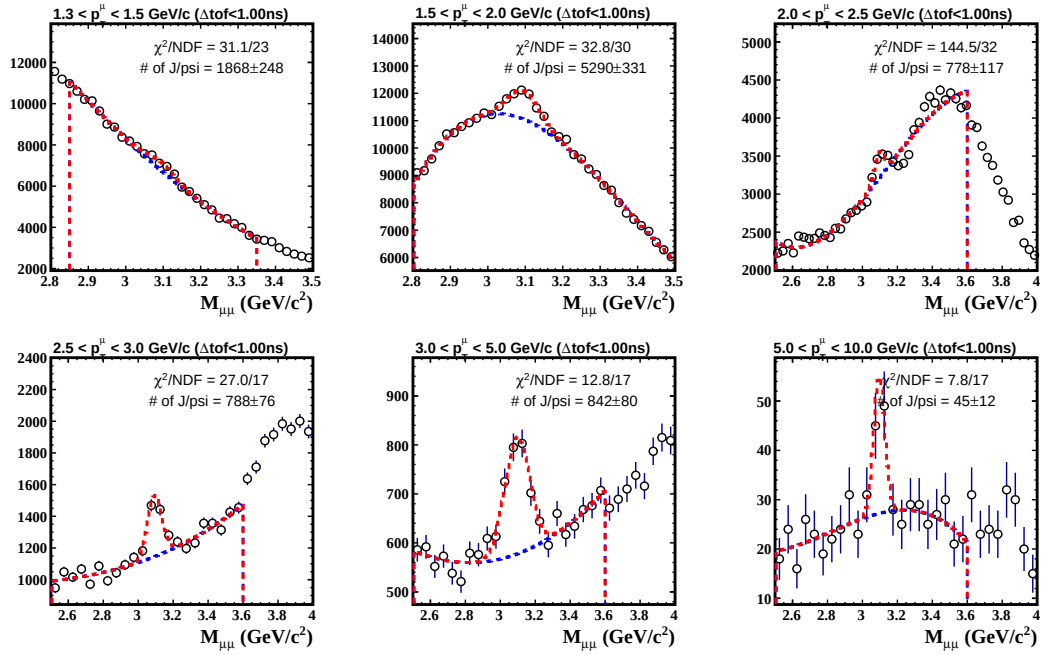

Figure 3.46 Invariant mass distributions of unlike-sign muon pairs in different pair p_{T} bins, where Δtof < 1.0 ns cut is applied to the probed muon. The red dashed lines are combined fits to the signal and the background while the blue dashed lines indicate the background component of the fit.

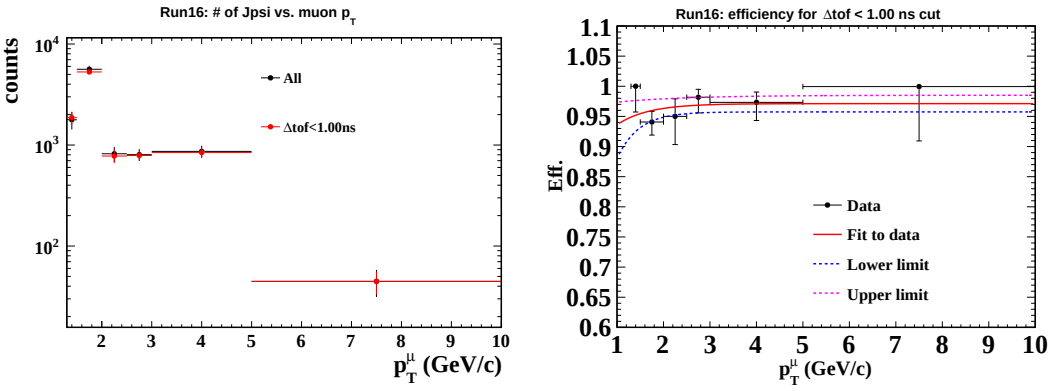

Figure 3.47 Left: Extracted J/ψ counts for probed muons without a Δtof cut (black) and with a Δtof < 1.0 ns cut (red). Right: efficiency of the Δtof cut, derived from the ratio of the distributions shown on the left. The efficiency fit is represented by the red curve.

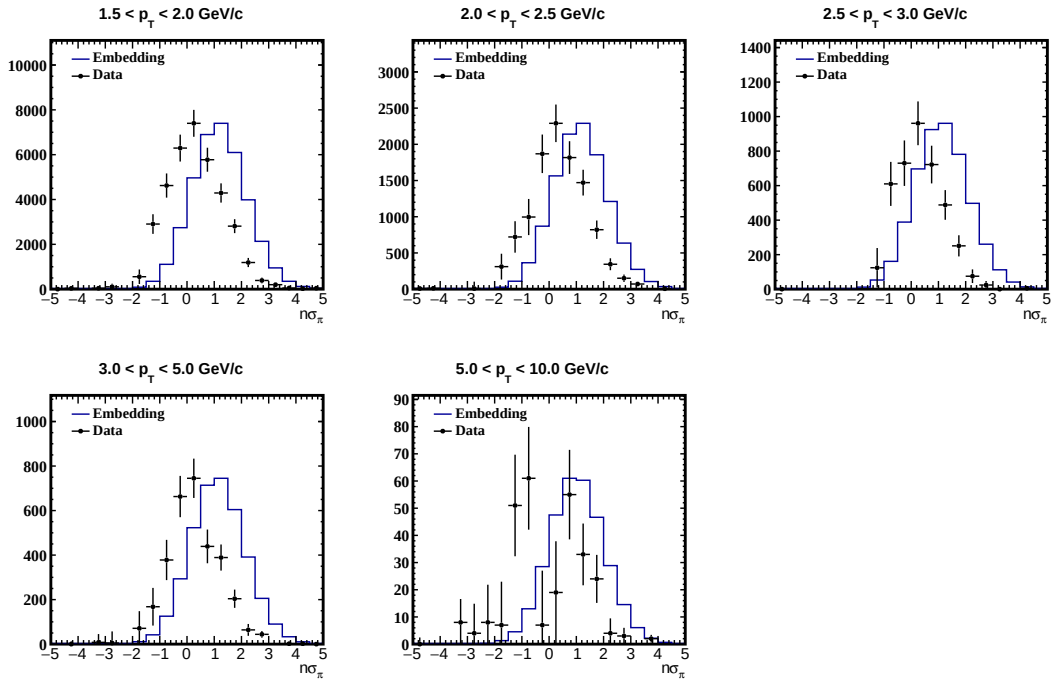

Figure 3.48 $n\sigma_\pi$ **distributions from Run16 data and embedding across different muon** p_T **ranges.**

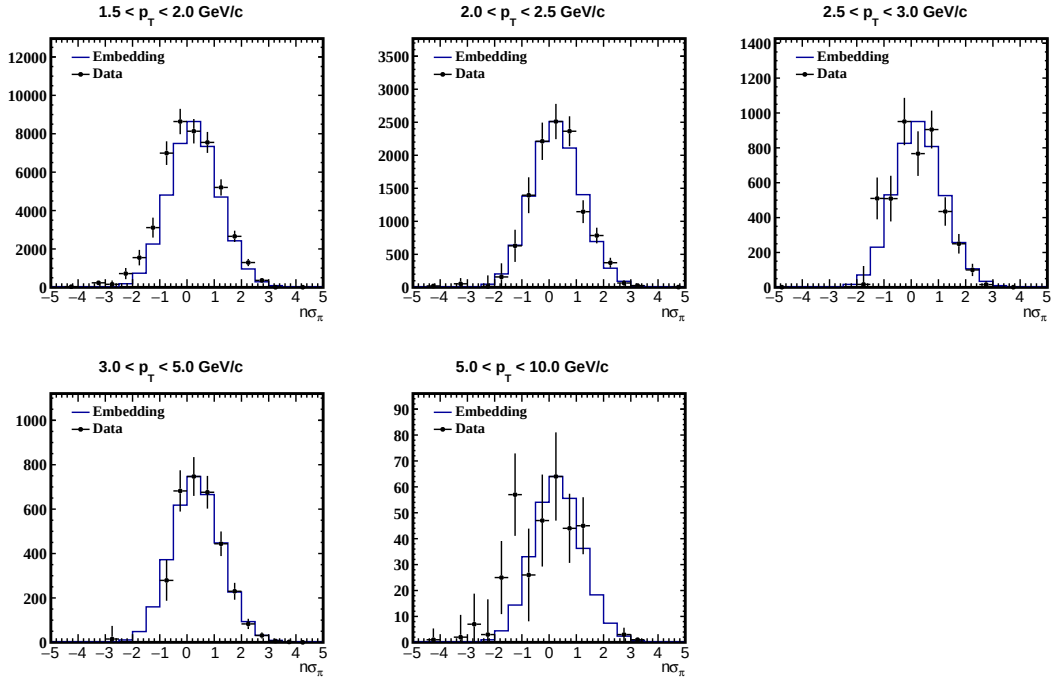

Figure 3.49 $n\sigma_\pi$ **distributions from Run14 data and embedding across different muon** p_T **ranges.**

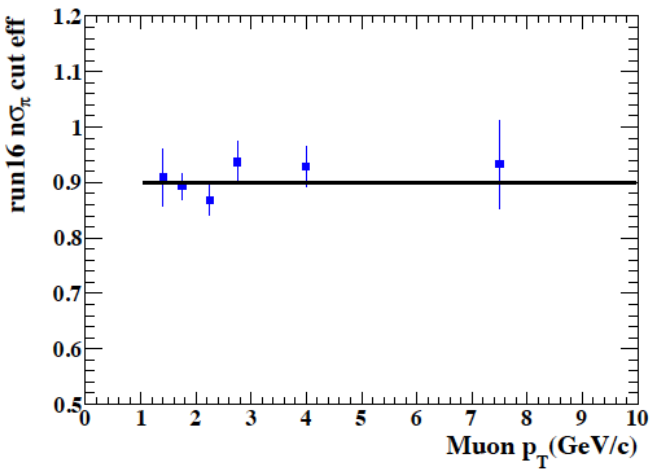

Figure 3.50 $n\sigma_\pi$ **cut efficiency in Run16 as a function of muon** p_T**. The black curve represents the fit to the** $n\sigma_\pi$ **cut efficiency.**

into pair efficiency, incorporating the following features:

- Input J/ψ distribution: A p_T distribution modeled by the Tsallis Blast Wave function, with a uniform distribution in $|y| < 0.5$ and $0 < \phi < 2\pi$.
- Decay of input J/ψ into two muons is modeled following two-body decay kinematics.For J/ψ with p_T lower than 0.2 GeV, this p_T range is expected to be dominated by coherent production. Accordingly, the J/ψ in this range are set to be transversely polarized to align with the characteristics of coherent production. The $cos\theta$ of decayed muons is sampled according to:

$$p(cos\theta) = 1 + cos^2\theta. \tag{3.11}$$

Single track efficiencies are defined in 3-D momentum space (p_T, η, ϕ), segmented into 10 bins in $|\eta| < 1.0$ and 18 bins in $0 < \phi < 2\pi$. Figure 3.51 shows the single muon efficiency as a function of p_T in 6 individual $\eta - \phi$ bins as an example. This approach allows for the calculation of pair efficiency by taking the ratio of the number of J/ψ pairs before and after applying single track efficiency weighting. Given the TPC tracking efficiency's strong centrality dependence, as illustrated in Fig. 3.40, the following formula estimates efficiency across a broad centrality range:

$$\epsilon_{\text{total}} = \frac{N^{\text{reco},J/\psi}}{N^{\text{true},J/\psi}} = \frac{\sum_i N_i^{\text{reco},J/\psi}}{\sum_i N_i^{\text{true},J/\psi}} = \frac{\sum_i N_i^{\text{true},J/\psi} \times \epsilon_{\text{total}}^i}{\sum_i N_i^{\text{true},J/\psi}} = \sum_i w_i \epsilon_{\text{total}}^i, \tag{3.12}$$

where i represents fine centrality intervals, $\epsilon_{\text{total}}^i$ is the total efficiency in each interval, and $w_i = N_i^{\text{true},J/\psi} / \sum_i N_i^{\text{true},J/\psi}$ is the weight for interval i. This analysis utilizes 16 centrality bins from 0 to 80%.

The "true" number of J/ψ in each centrality interval is unknown. As described in Sec. 1.5.4, the nuclear modification factor R_{AA} is defined as the yield in nucleus-nucleus

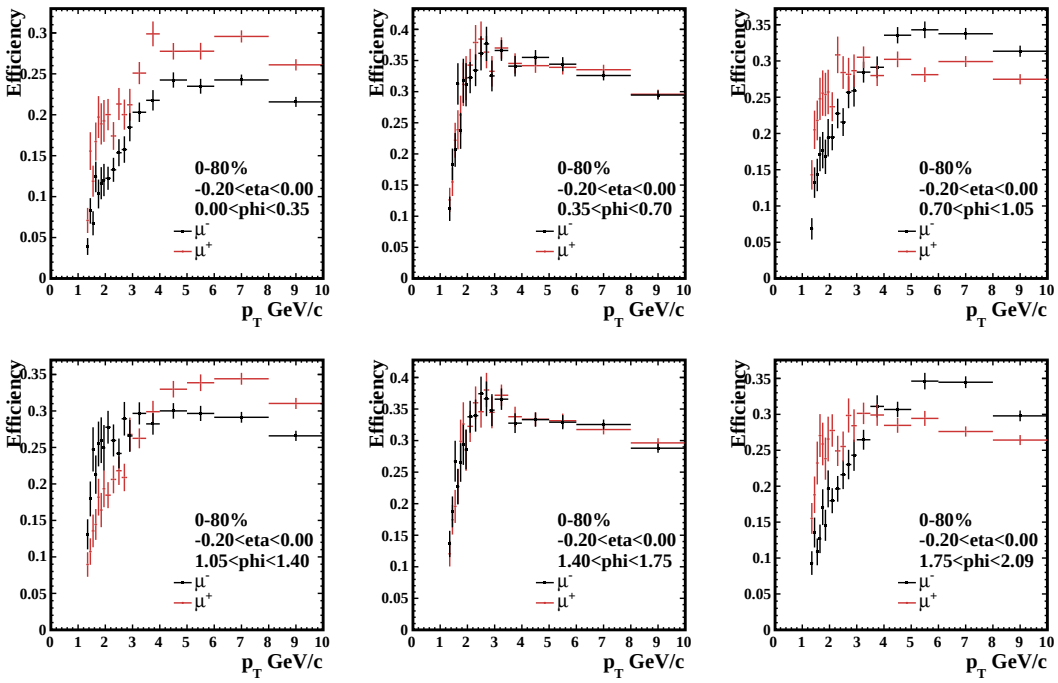

Figure 3.51 Single muon efficiency as a function of p_T in 6 individual $\eta - \phi$ bins in 0-80% centrality.

collisions divided by the yield in p+p collisions, scaled by $N_{\rm coll}$. Since the yield in p+p collisions serves as the baseline, and $R_{\rm AA}$ has model predictions, the "true" number of J/ψ can be estimated by $N_{\rm coll}$ and $R_{\rm AA}$. Additionally, to accommodate this dimuon trigger analysis, the equivalent number of MB events, as described in Sec. 3.1.4, also needs to be considered. Hence, the "true" number of J/ψ is estimated as:

$$N_i^{\rm true,J/\psi} \propto N_{\rm MB,i}^{\rm cent} \times N_{\rm coll} \times R_{\rm AA}^{J/\psi} \tag{3.13}$$

where $N_{\rm MB,i}^{\rm cent}$ is the number of equivalent MB events in interval i. The mean values of $N_{\rm coll}$ in 16 centrality bins, calculated from M"C Glauber models, are summarized in Tab. 3.11. The transport model calculation from Tsinghua is used for $R_{\rm AA}^{J/\psi}$ [111]. For coherent J/ψ (i.e., p_T lower than 0.2 GeV/c), the production is expected to exhibit no centrality dependence. Consequently, the "true" number of J/ψ is estimated as:

$$N_i^{\rm true,J/\psi} \propto N_{\rm MB,i}^{\rm cent}, \tag{3.14}$$

to ensure proper normalization from MB events to dimuon trigger events. The resulting weights in different centrality bins are shown in Fig. 3.52 for p_T above and below 0.2 GeV/c respectively. For p_T above 0.2 GeV/c, the weights decrease from central to peripheral collisions, reflecting the higher J/ψ yield in central collisions. Conversely, for p_T below 0.2 GeV/c, the weights remain relatively constant across centrality intervals, attributable to the similar number of equivalent MB events in each centrality class.

Table 3.11 Number of collisions for Au+Au 200 GeV/c.

Centrality	$\langle N_{coll} \rangle$
0-5%	1048.11
5-10%	838.41
10-15%	663.04
15-20%	524.31
20-25%	411.86
25-30%	320.78
30-35%	246.95
35-40%	186.69
40-45%	138.71
45-50%	101.51
50-55%	72.79
55-60%	51.62
60-65%	35.64
65-70%	23.96
70-75%	15.98
75-80%	10.54

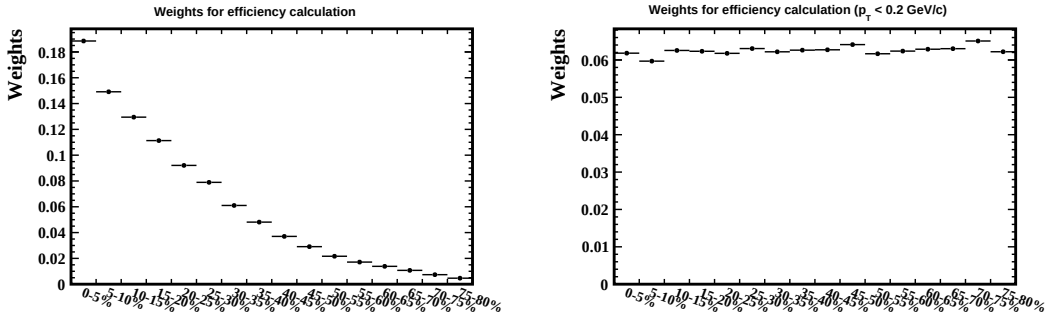

Figure 3.52 Event weights for J/ψ efficiency calculation estimated based on equivalent number of MB events. Left: p_{T} > 0.2 GeV/c. Right: p_{T} < 0.2 GeV/c.

The total J/ψ efficiency also needs to be evaluated for fine centrality intervals, i.e. $\epsilon^{i}_{\mathrm{total}}$ in Eq. 3.7. However, the statistics in the embedding sample are not sufficient to determine such an efficiency, especially for peripheral events. To deduce the total J/ψ efficiency for each centrality interval, the overall embedding sample efficiency ($\epsilon_{\mathrm{total}}$) is adjusted for the difference in TPC tracking efficiencies:

$$\epsilon^{i}_{\mathrm{total}} = \epsilon^{all}_{\mathrm{total}} \times \frac{\epsilon^{i}_{\mathrm{TPC}}}{\epsilon^{all}_{\mathrm{TPC}}} \tag{3.15}$$

where $\epsilon^{i}_{\mathrm{TPC}}$ is the TPC tracking efficiency in interval i, and $\epsilon^{\mathrm{all}}_{\mathrm{TPC}}$ is derived from the inclusive embedding sample. To minimize statistical fluctuations, $\epsilon^{i}_{\mathrm{TPC}}$ is also obtained from ToyMC but with TPC tracking efficiency of single track in 1-D momentum space (p_{T}).

Fig. 3.53 shows the total J/ψ efficiencies as a function of J/ψ p_{T} across various centrality bins in Run14 and Run16, respectively.

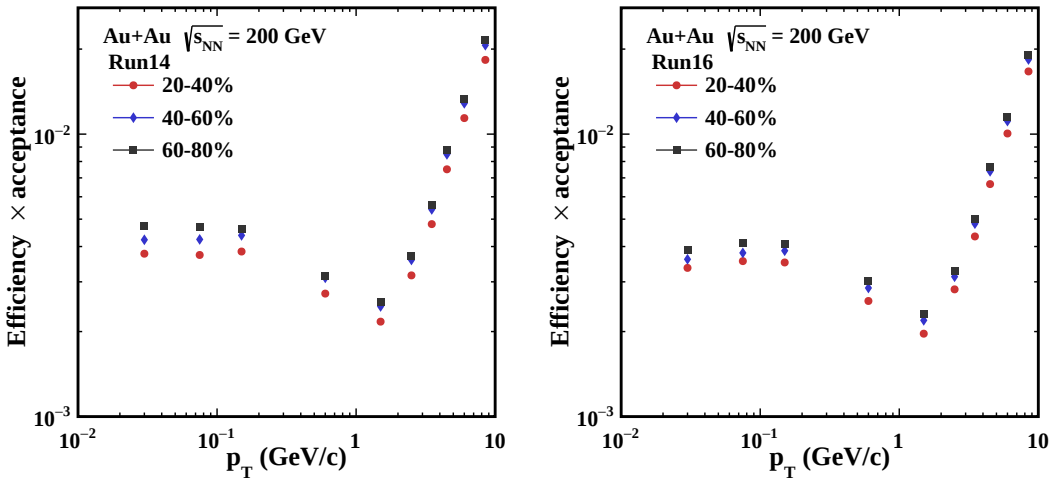

Figure 3.53 p_T **dependence of Total** J/ψ **efficiency in various centrality bins in Run14 and Run16.**

3.4 Systematic Uncertainty

The systematic uncertainties in this analysis come from signal extraction and efficiency correction. This section provides a detailed discussion of these sources of uncertainty.

3.4.1 Signal extraction

The process of extracting the J/ψ signal involves several steps, each subject to specific choices that can introduce systematic uncertainties. To evaluate these uncertainties, various aspects of the signal extraction procedure are systematically varied:

- The fit range for determining the normalization factor of the mixed-event background is adjusted from the default $[2.7, 3.8]$ GeV/c^2 to alternative ranges of $[2.5, 4.0]$ GeV/c^2 or $[2.8, 3.7]$ GeV/c^2.
- The functional form used to fit the ratio of like-sign distributions between same events and mixed events is varied from a first-order polynomial to a constant line. This adjustment occasionally results in a non-flat residual background, necessitating the use of higher-order polynomials for adequate representation.
- The default bin width for invariant mass distributions, set at 40 MeV/c^2, is varied to 20 MeV/c^2 to assess the impact of binning on the signal extraction.
- For J/ψ with $p_T < 0.2$ GeV/c, the default exponential form for modeling the residual background is alternated with a second-order polynomial function. For J/ψ with $p_T > 0.2$ GeV/c, the default first-order polynomial is varied by ± 1 order.
- The fitting range for signal extraction, typically $[2.5, 4.0]$ GeV/c^2, is varied to $[2.3, 4.2]$ GeV/c^2 or $[2.6, 3.8]$ GeV/c^2For the low J/ψ p_T bins ($p_T < 1$ GeV/c),

which start from 2.7 GeV/c^2 due to kinematic constraints, the fitting range is adjusted from [2.85, 4.0] GeV/c^2 to either [2.8, 4.2] or [2.82, 3.8] GeV/c^2.

- The fitting range for signal extraction is adjusted from [2.5, 4.0] GeV/c^2 to either [2.3, 4.2] or [2.6, 3.8] GeV/c^2. Due to kinematic limitations, the invariant mass distributions for J/ψ p_{T} bins less than 1 GeV/c begin at 2.7 GeV/c^2 or higher. Consequently, their fitting ranges are varied from [2.85, 4.0] GeV/c^2 to either [2.8, 4.2] or [2.82, 3.8] GeV/c^2.
- The widths of the J/ψ signals are varied within the uncertainties of the additional smearing parameters to account for resolution effects.
- The bin-counting method, with the residual background subtracted, is also considered as an alternative approach.

These variations are illustrated in Fig. 3.54, showcasing the different variations over default case ratios of raw J/ψ counts across various centrality classes. The red dashed line show the maximum deviation to the default case. The relative root mean square (RMS) of these distributions, taken as the measure of uncertainty, is depicted in Fig. 3.55 with blue dashed lines.

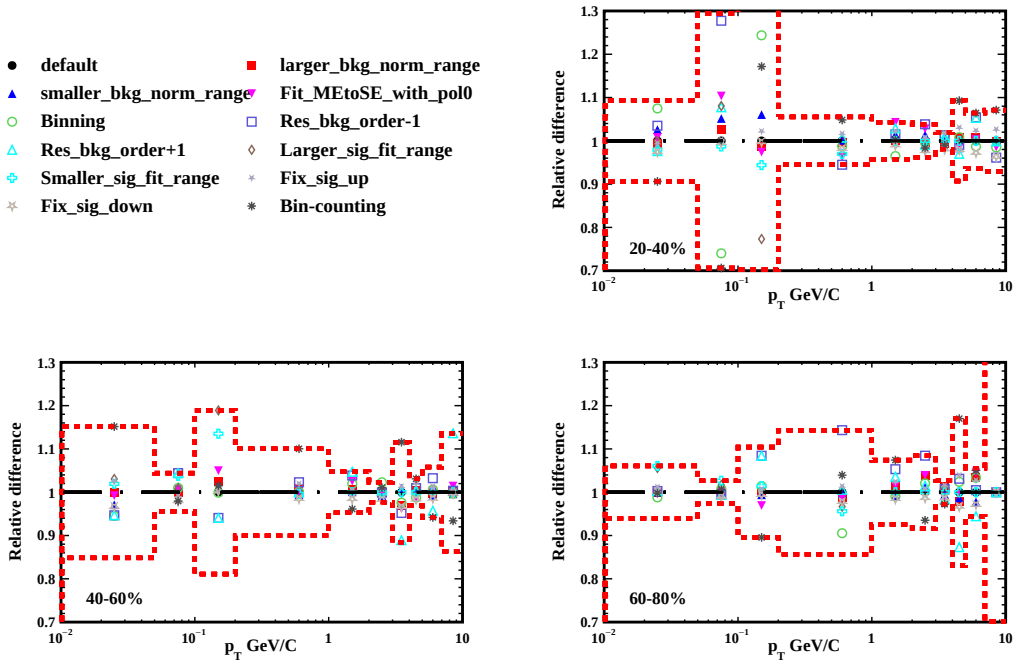

Figure 3.54 Ratios of the corrected J/ψ yields as a function of p_{T} for different variations from signal extraction procedure to the default case. The dashed lines indicate the maximum deviations in each p_{T} bin.

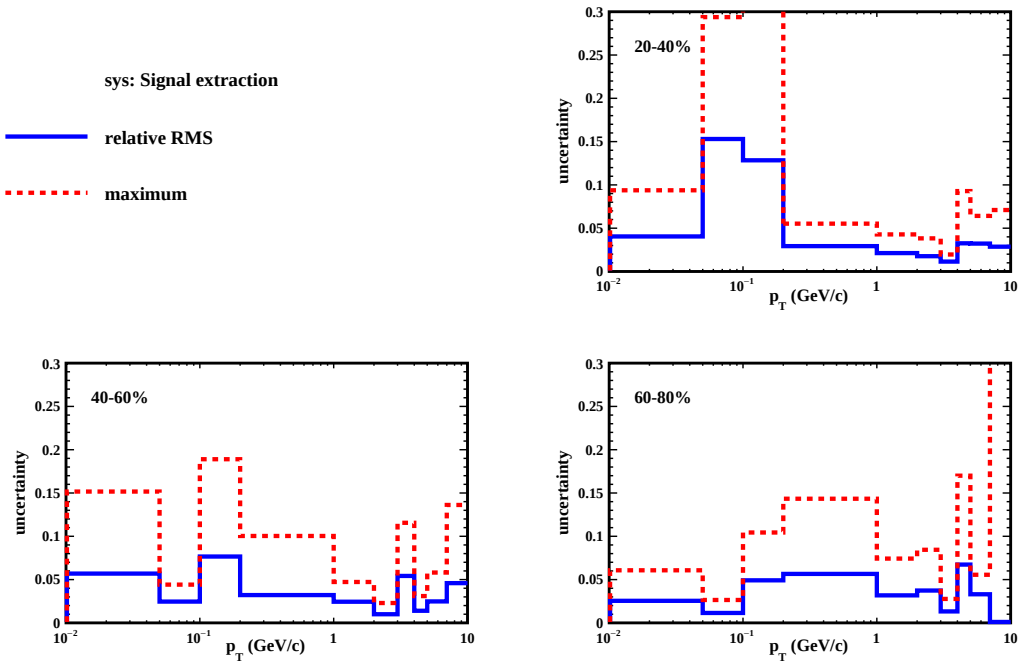

Figure 3.55 The maximum deviation from the default signal extraction case (red dashed line) and the calculated relative root mean square (RMS) of systematic variations (blue line) across different centrality bins for Run16.

3.4.2 TPC tracking

To evaluate the systematic uncertainties associated with TPC tracking, track quality cuts were simultaneously varied in both real data and embedding. The variations are listed in Tab. 3.12.

Table 3.12 List of variations to the track quality cuts in evaluating the uncertainties associated with the TPC tracking.

Track quality cut	Default	Variation
DCA	1 cm	0.8 or 1.5 cm
NHitsFit, NHitsDedx	15,10	20,15

The variations in raw J/ψ counts as a function of p_{T} across different collision centrality bins, resulting from adjustments to the set of quality cut variations for Run16, are shown in Fig. 3.56. Furthermore, Fig. 3.57 presents the changes in TPC tracking efficiency for J/ψ attributable to these quality cut modifications in Run16. These efficiencies are calculated by applying TPC tracking efficiencies for single muons from various cases to J/ψ efficiencies using the 3-D method outlined in Sec. 3.3.4. Similar to the approach in the signal extraction section, the relative root mean square (RMS) of all sources is considered as the measure of uncertainty.

Given the potential correlation in TPC tracking systematic uncertainties between the two runs, a direct estimation of the RMS using the combined J/ψ yield is employed

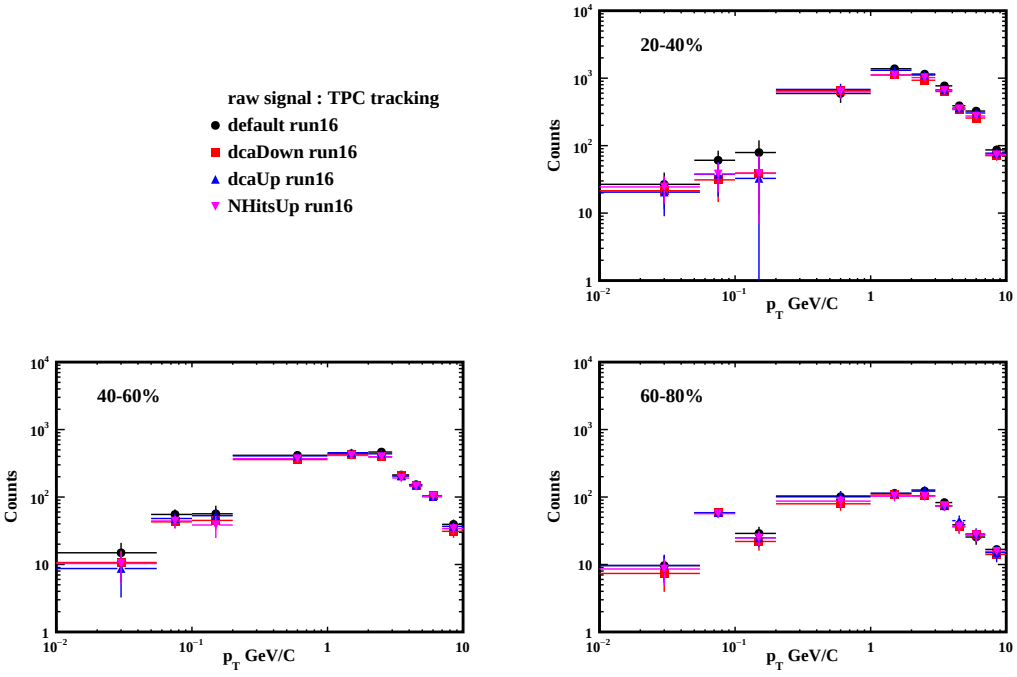

Figure 3.56 Raw J/ψ counts as a function of p_{T} in different centrality classes for all the variations of the track quality cuts in Run16.

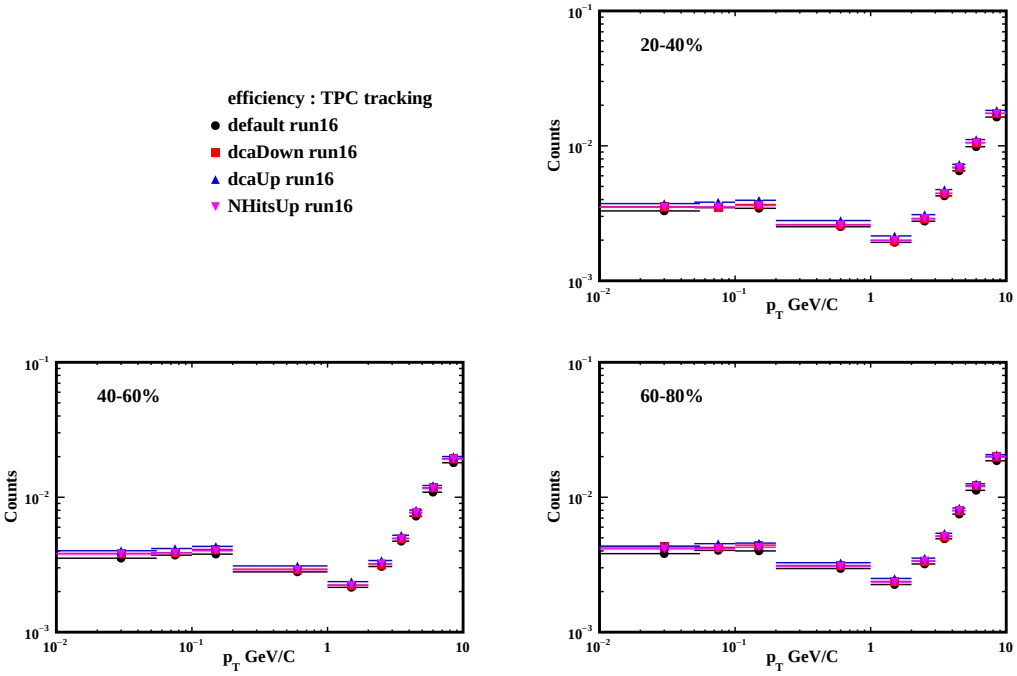

Figure 3.57 p_{T} dependence of TPC tracking efficiency in different centrality classes for all the variations of the track quality cuts in Run16.

rather than estimating it separately for each run and then combining it. The calculation of the combined J/ψ yield is as follows:

$$\text{yield}_{\text{combine}} = \text{weight}_{\text{run14}} \times \text{yield}_{\text{run14}} + \text{weight}_{\text{run16}} \times \text{yield}_{\text{run16}} \quad (3.16)$$

Here, the yield refers to the corrected J/ψ yield, and the weights are derived from their statistical uncertainties, which will be discussed in detail in Sec. 4. For a specific variation i corresponding to a quality cut in, for example, Run14, the modified combined yield is expressed as:

$$\text{yield}_{\text{combine},i} = \text{weight}_{\text{run14}} \times \text{yield}_{\text{run14},i} + \text{weight}_{\text{run16}} \times \text{yield}_{\text{run16}} \quad (3.17)$$

Weights remain consistent with the default case, and $\text{yield}_{\text{run14},i}$ represents the corrected J/ψ yield, accounting for both variations in raw J/ψ counts and the corresponding TPC tracking efficiency adjustments. The changes in the corrected combined J/ψ yield are shown in Fig. 3.58. The red lines indicate the maximum deviations in each p_{T} bin. The relative RMS of these distributions are calculated and shown in Fig. 3.59 as blue dashed lines. This figure also includes a comparison of the maximum deviations, represented by red dashed lines.

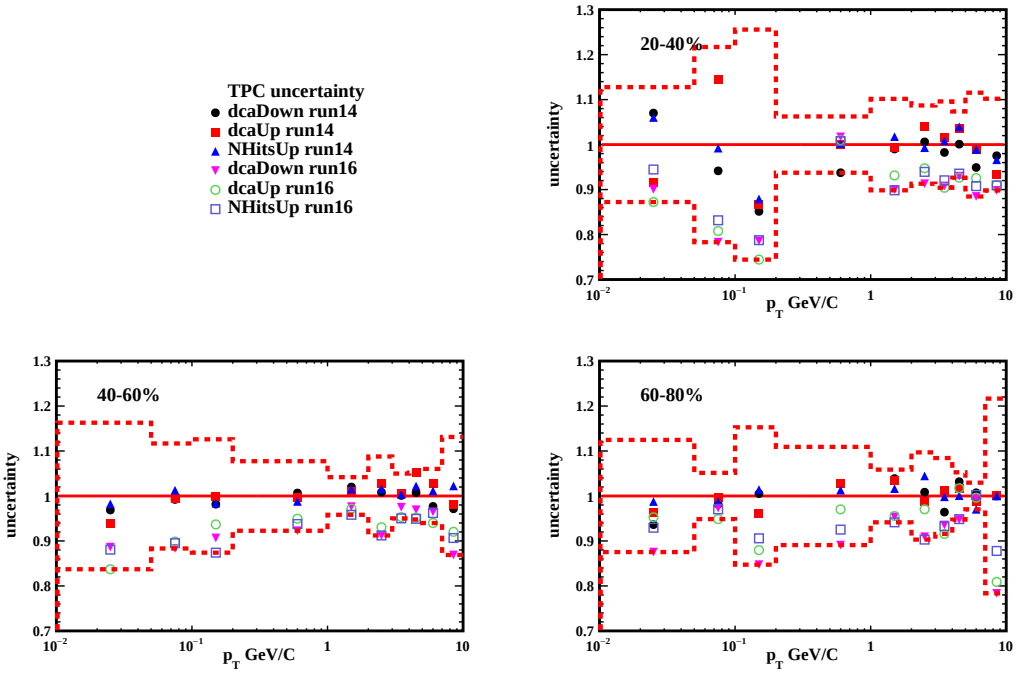

Figure 3.58 Ratios of the corrected combined J/ψ yields as a function of p_{T} for different variations from track quality cuts to the default case. The red lines indicate the maximum deviations in each p_{T} bin.

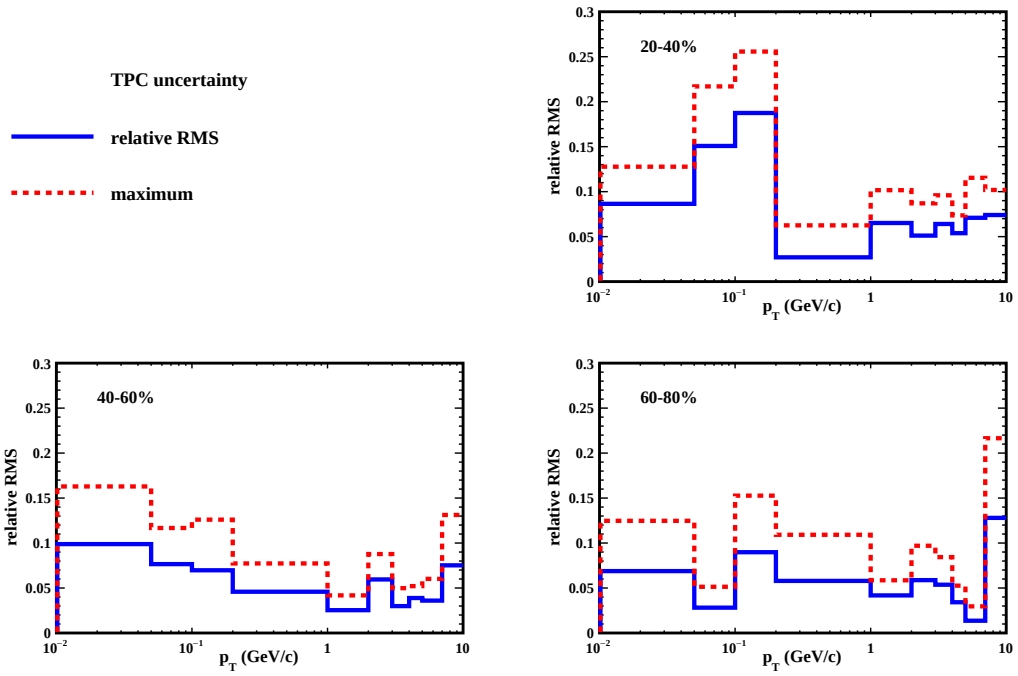

Figure 3.59 The maximum deviation from the default track quality cut case (red dashed line) and the calculated relative root mean square (RMS) of systematic variations (blue line) across different centrality bins.

3.4.3 Muon PID

The uncertainties related to the Δy, Δz and Run14's n$\sigma_\pi$cuts are estimated using the same procedure as for the TPC tracking efficiency. The variations applied to these PID cuts are detailed in Table 3.13.

Table 3.13 List of variations to the Muon PID cuts.

Muon PID cut	Default	Variation
nσ_π (only for Run14)	$[-1, 3]$	$[-1.25, 3.25]$ or $[-0.75, 2.75]$
Δy	$\leq 2(2.5)\sigma$ for $p_T \leq(\geq)$ 3 GeV/c	$\leq 1.75(2.25)\sigma$ or $\leq 2.25(2.75)\sigma$
Δz	$\leq 2(2.5)\sigma$ for $p_T \leq(\geq)$ 3 GeV/c	$\leq 1.75(2.25)\sigma$ or $\leq 2.25(2.75)\sigma$

After simultaneously varying these cuts in both real data and embedding, the resulting uncertainties are shown in Fig. 3.60, where the data points are the ratios of the corrected combined J/ψ yields for different muon PID cut variations to the default case. The red lines indicate the maximum deviations in each p_T bin. Fig. 3.61 compares these maximum deviations and the calculated relative RMS across different centrality bins, adopting the relative RMS as the systematic uncertainty measure.

As discussed in Sec. 3.3.3, the Δtof cut efficiency and Run16's nσ_π cut efficiency are estimated using a tag-and-probe technique. For Δtof cut efficiency, since it is a data-driven approach, only statistical uncertainties on the data points (illustrated in the right panel of Fig. 3.47) are considered as the source of uncertainty. This uncertainty is quan-

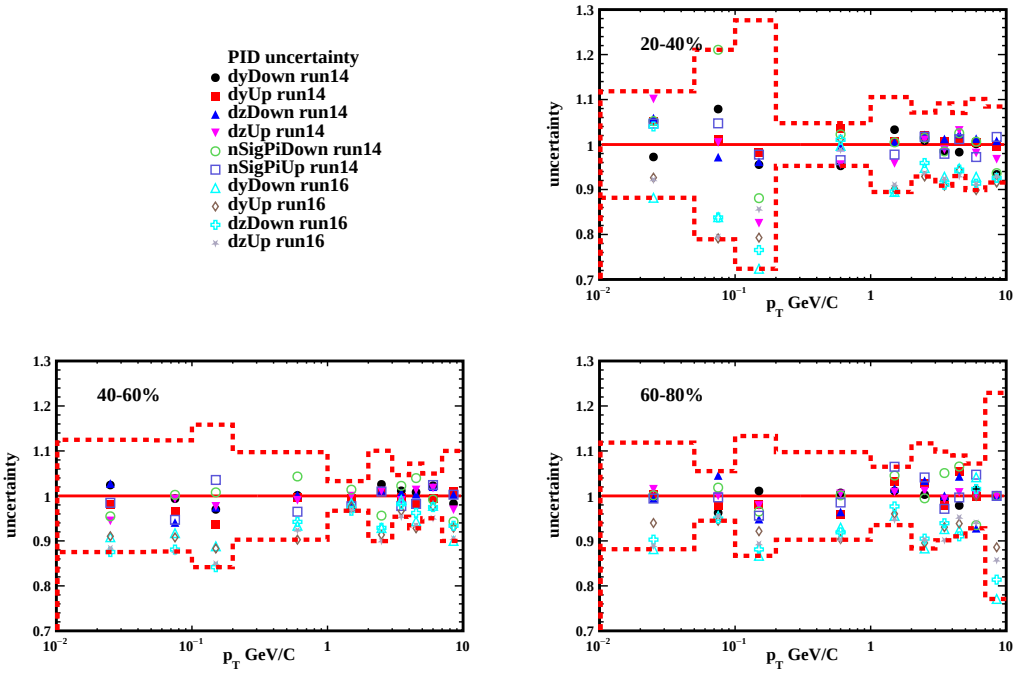

Figure 3.60 Ratios of the corrected combined J/ψ yields as a function of p_{T} for different variations from track quality cuts to the default case. The red lines indicate the maximum deviations in each p_{T} bin.

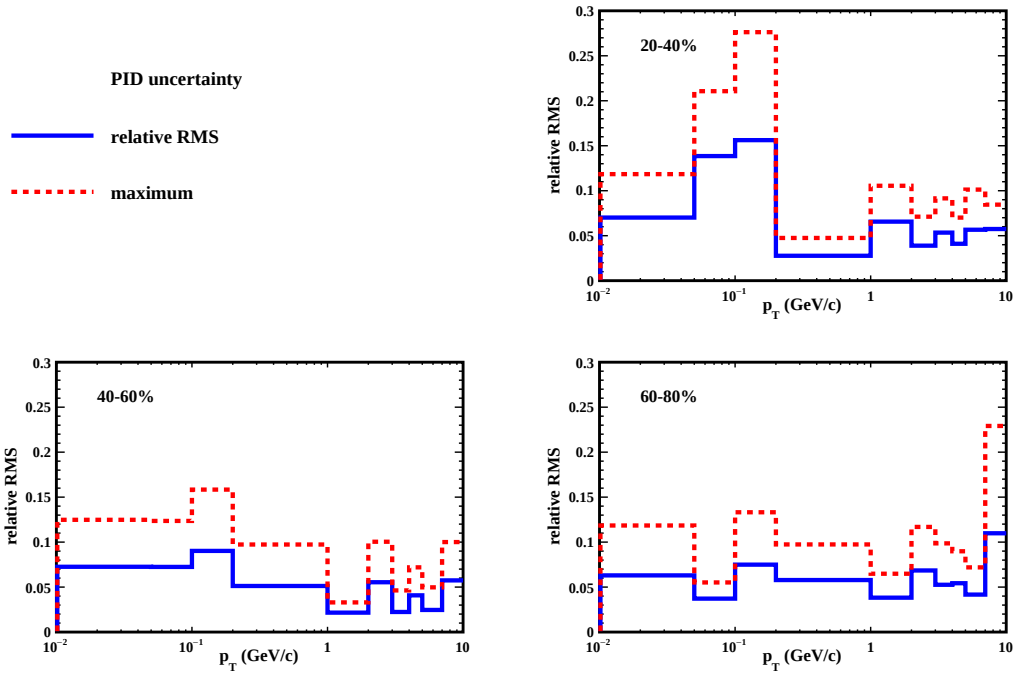

Figure 3.61 The maximum deviation from the default track quality cut case (red dashed line) and the calculated relative root mean square (RMS) of systematic variations (blue line) across different centrality bins.

tified by independently randomizing each data point within its statistical uncertainties 1000 times, followed by re-evaluating the Δtof cut efficiency after each randomization, which are shown as red dashed lines in Fig. 3.62. The efficiency distributions for 12 muon p_{T} bins, along with Gaussian fits, are presented in Fig. 3.63, with the RMS of each distribution closely matching the widths of the Gaussian fits. In the end, the RMS of these efficiency distributions, depicted as magenta and blue circles in Fig. 3.62, are adopted as the uncertainty estimates. The same functional form used for the original Δtof cut efficiency fit is applied to the upper and lower limits, illustrated as magenta and blue dashed lines in the figure as well as in the right panel of Fig. 3.47. The uncertainty on single muons is transformed to the uncertainty on J/ψ utilizing a ToyMC, taking into account the decay kinematics. The changes in the corrected combined J/ψ yield are shown in Fig. 3.64. Here, for the corrected J/ψ yield, raw counts are consistent with the default case, with only the efficiencies adjusted. The systematic uncertainty, represented by the relative RMS and compared with the maximum deviation, is detailed in Fig. 3.65.

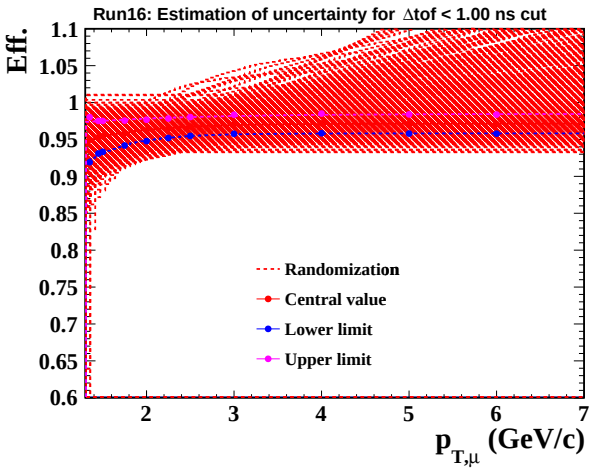

Figure 3.62 The p_{T} dependence of Δtof efficiencies extracted from randomized data points, shown as red dashed lines.

Similar procedure is applied to Run16's $n\sigma_{\pi}$ cut, shown in Figs. 3.66, 3.67 and 3.68.

3.4.4 3-D method

As described in Sec. 3.3.4, the calculation of pair efficiency from single track efficiencies employs a 3-D method. This approach intricately folds the single track efficiency into the pair efficiency, accounting for variations across different p_{T}, η and ϕ bins. Fig. 3.51 shows the single track efficiency as a function of p_{T} across various $\eta - \phi$ bins. The standard procedure involves folding the central value of each p_{T} bin to derive the

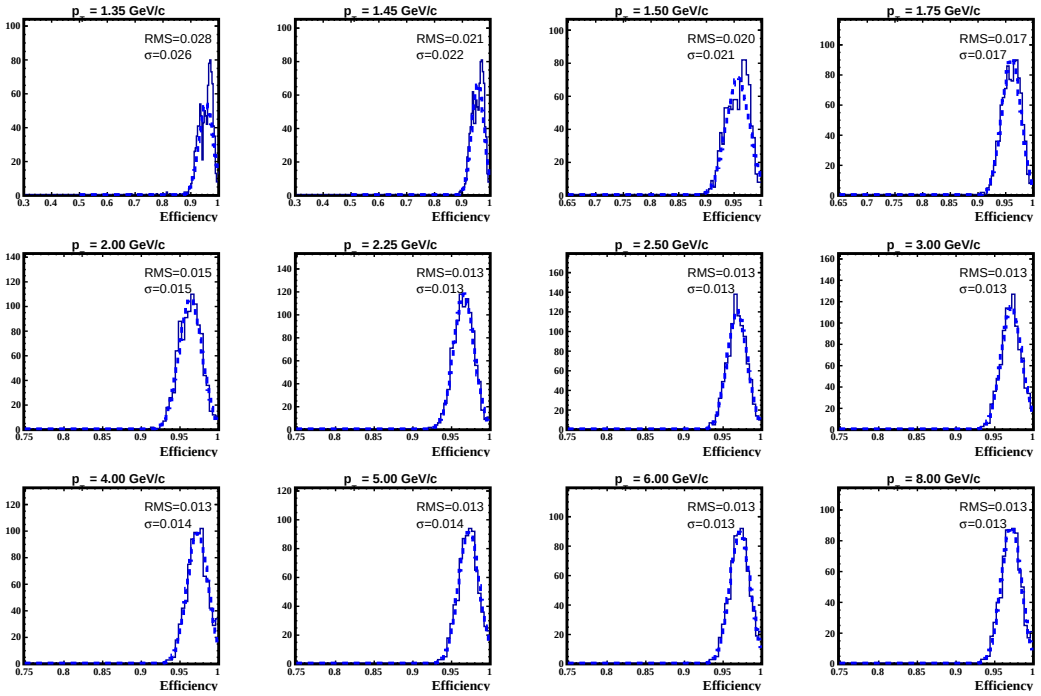

Figure 3.63 Distributions of the Δtof efficiency from 1000 randomization exercises. Different panel represents different p_{T} range. The blue dashed lines are Gaussian fits to the distributions.

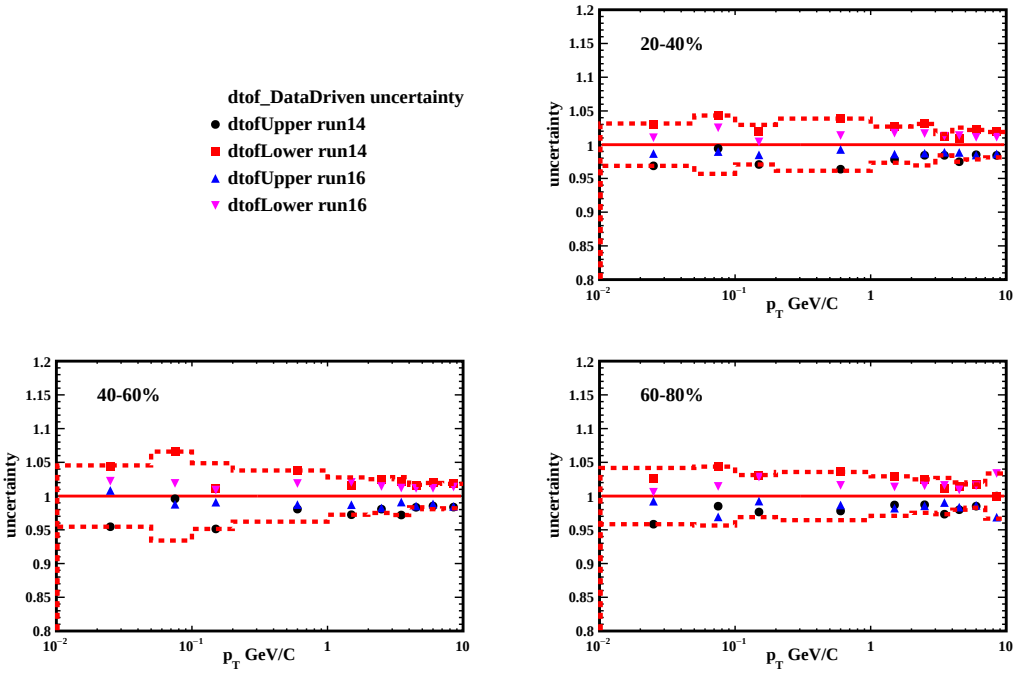

Figure 3.64 Ratios of the corrected combined J/ψ yields as a function of p_{T} for different variations from Δtof cuts to the default case. The red lines indicate the maximum deviations in each p_{T} bin.

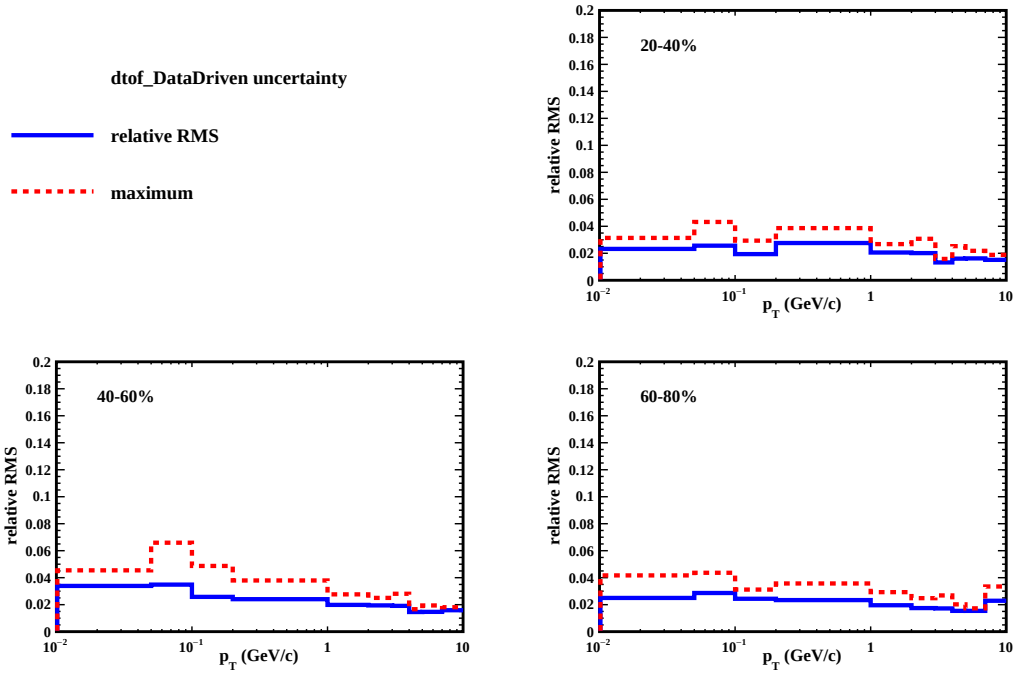

Figure 3.65 The maximum deviation from the default case (red dashed line) and the calculated relative root mean square (RMS) of Δtof cut efficiency variations (blue line) across different centrality bins.

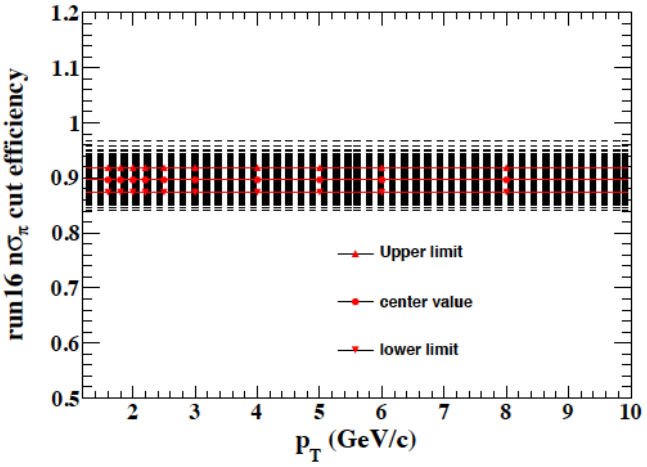

Figure 3.66 The muon p_T dependence of nσ_π cut efficiencies in Run16 from randomization, shown as black dashed lines.

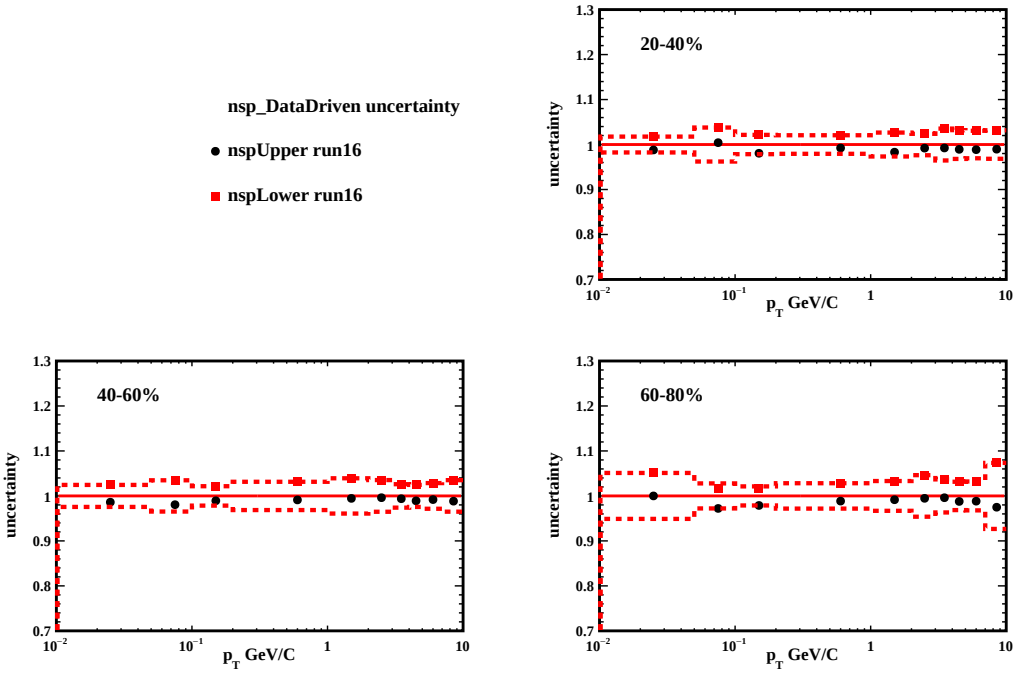

Figure 3.67 Ratios of the corrected combined J/ψ yields as a function of p_{T} for different variations from $\mathrm{n}\sigma_{\pi}$ cuts to the default case. The red lines indicate the maximum deviations in each p_{T} bin.

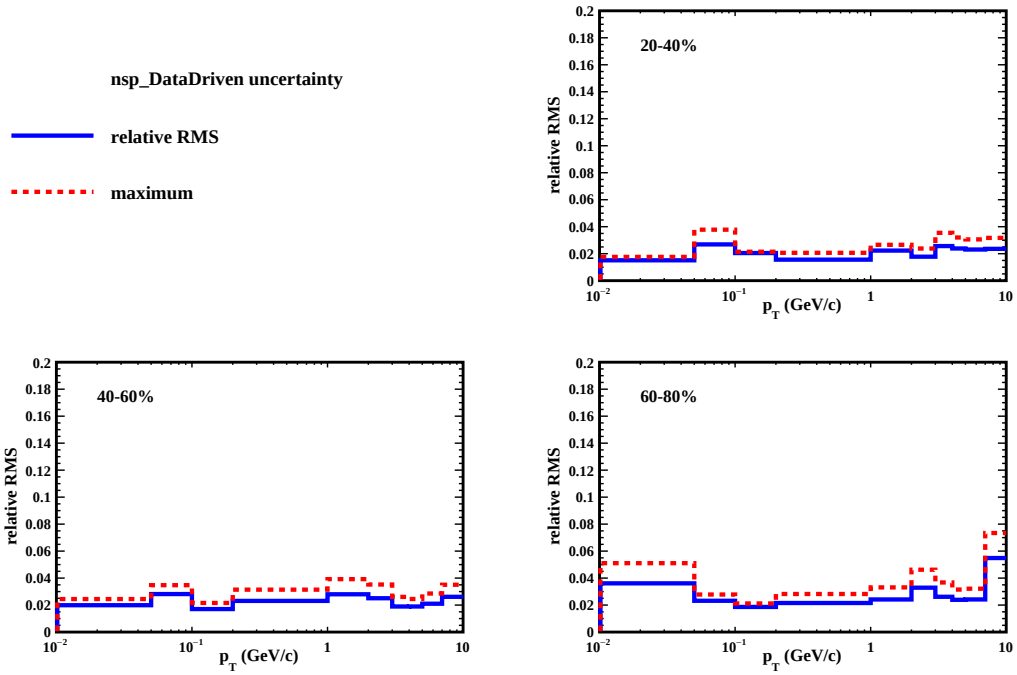

Figure 3.68 The maximum deviation from the default case (red dashed line) and the calculated relative root mean square (RMS) of $\mathrm{n}\sigma_{\pi}$ cut efficiency variations (blue line) across different centrality bins.

pair efficiency. To estimate the systematic uncertainty inherent in this method, each bin is varied within its statistical uncertainty margin, with this process being independently repeated 100 times. This iterative approach facilitates the generation of a modified single track efficiency distribution for each variation and fold to pair efficiency, as shown in Fig. 3.69. The RMS of the result pair efficiency distributions, depicted in Fig. 3.70, serves as a measure of the systematic uncertainty associated with this method.

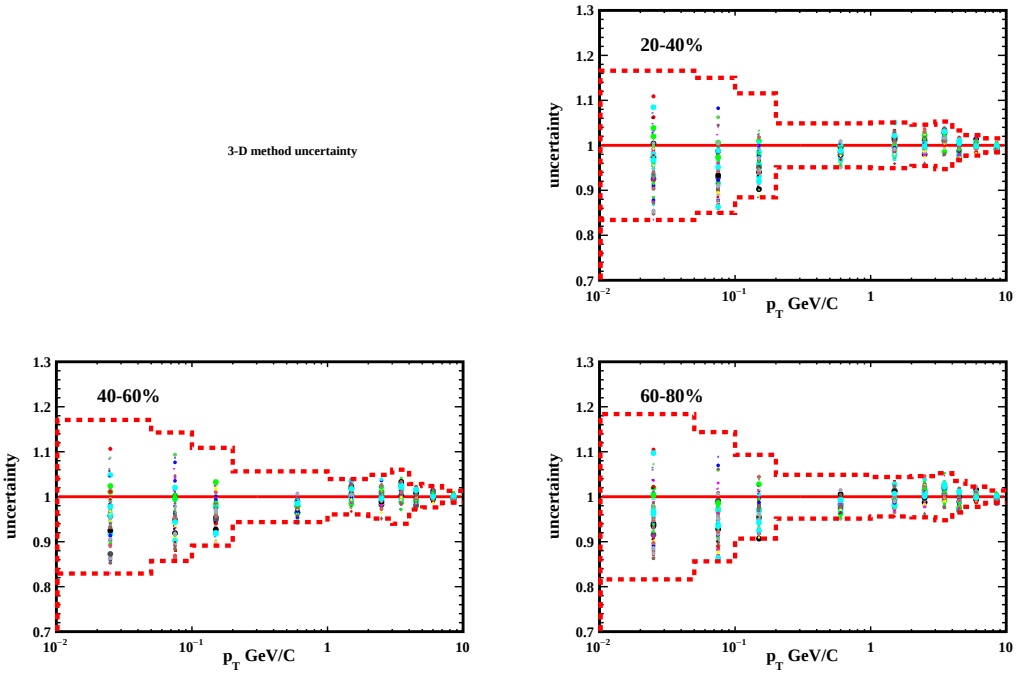

Figure 3.69 Ratios of the pair efficiency distributions as a function of p_{T} for different variations from 3-D method. The red lines indicate the maximum deviations in each p_{T} bin.

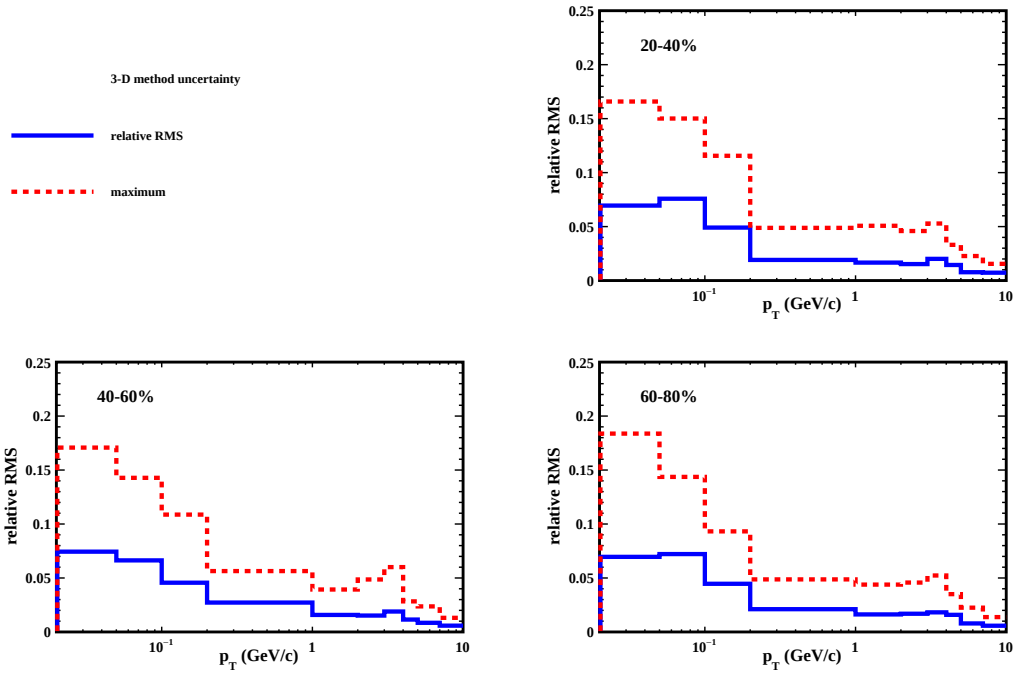

Figure 3.70 The maximum deviation from the default case (red dashed line) and the calculated relative root mean square (RMS) of 3-D method variations (blue line) across different centrality bins.

Chapter 4 Results and Discussions

Following the extraction of the raw counts through the maximum-likelihood method and subsequent correction by the reconstruction efficiency, the p_{T} spectra, p_{T}^2 spectra and excess yields of J/ψ as a function of N_{part} for J/ψ are obtained in Au + Au collisions at $\sqrt{s_{\mathrm{NN}}}$ = 200 GeV. These measurements incorporate data from both 2014 and 2016 RHIC running, and the results from both runs are consistent with each other, and therefore are averaged to enhance precision. To combine the results from the two runs, they were treated as independent measurements and averaged using weights equal to the inverse of their statistical uncertainties squared. Specifically, the weights are calculated as:

$$w_i = \frac{1/\left(\sigma^i_{\mathrm{stat}}\right)^2}{\sum_i 1/\left(\sigma^i_{\mathrm{stat}}\right)^2}, \tag{4.1}$$

where i stands for either 2014 or 2016 results, and σ^i_{stat} denotes the statistical uncertainty for each run. The combined result and it statistical uncertainty are computed as follows:

$$y_{\mathrm{combine}} = \sum_i w_i \times y^i \tag{4.2}$$

$$\sigma_{\mathrm{stat.combine}} = \sqrt{\sum_i (w_i \times \sigma^i_{\mathrm{stat}})^2} \tag{4.3}$$

where y^i represents the results from 2014 or 2016, y_{combine} and $\sigma_{\mathrm{stat.combine}}$ are the combined yield and its corresponding statistical uncertainty, respectively. Regarding systematic uncertainties, as elaborated in Sec. 3.4, those arising from efficiency corrections are evaluated directly for the combined results. For systematic uncertainties associated with the signal extraction process, they are determined separately for each run, and combined, assumed to be uncorrelated, according to:

$$\sigma_{\mathrm{sys.signal.combine}} = \sqrt{\sum_i (w_i \times \sigma^i_{\mathrm{sys.signal}})^2} \tag{4.4}$$

where $\sigma^i_{\mathrm{sys.signal}}$ is the systematic uncertainty from the signal extraction process for 2014 or 2016 results, and $\sigma_{\mathrm{sys.signal.combine}}$ represents the systematic uncertainty for the combined results. The total systematic uncertainties are subsequently derived by summing these individual sources in quadrature.

4.1 The invariant yield spectra

The invariant yield of J/ψ is calculated as follows:

$$B_{J/\psi\to\mu\mu}\frac{d^2N_{J/\psi}}{2\pi p_{\mathrm{T}}dp_{\mathrm{T}}dy} = \frac{\Delta N_{J/\psi}}{2\pi p_{\mathrm{T}}\Delta p_{\mathrm{T}}\Delta y N_{\mathrm{MB}}\epsilon_{\mathrm{total}}}, \tag{4.5}$$

where $\mathbf{B}_{J/\psi\to\mu\mu}$ is the branching ratio for a J/ψ decaying into two muons, $\Delta N_{J/\psi}$ is the raw number of J/ψ in a specific p_{T} bin of the interested centrality, Δp_{T} is the p_{T} bin width, Δy is the pseudo-rapidity coverage of the measurement, *i.e.*, $\Delta y = 1$, N_{MB} represents the equivalent number of MB events in the interested centrality bin as detailed in Sec. 3.1.4, and $\epsilon_{\mathrm{total}}$ is the total J/ψ reconstructed efficiency.

The measured J/ψ yield in each p_{T} bin reflects the average yield within the bin, which is not necessarily the same as the yield at the bin center. Therefore, positioning the data point at the center of the p_{T} bin could be misleading, especially for bins with a large bin width. To address this potential confusion, the p_{T} position for data points is determined according to[134]:

$$f(p_{\mathrm{T}}^{\mathrm{pos}}) = \frac{\int_{p_{\mathrm{T}}^{\mathrm{min}}}^{p_{\mathrm{T}}^{\mathrm{max}}} f(p_{\mathrm{T}})dp_{\mathrm{T}}}{p_{\mathrm{T}}^{\mathrm{max}} - p_{\mathrm{T}}^{\mathrm{min}}}, \tag{4.6}$$

where $f(p_{\mathrm{T}})$ is a function used to parameterize the J/ψ p_{T} distribution, $p_{\mathrm{T}}^{\mathrm{pos}}$ is the p_{T} position whose yield is same as the measured average yield of the bin, and $p_{\mathrm{T}}^{\mathrm{min}}$ and $p_{\mathrm{T}}^{\mathrm{max}}$ being the lower and upper limits of the bin, respectively. The functional form is taken as the Tsallis function[135-136]:

$$f(p_{\mathrm{T}}) = \frac{1}{2\pi}\frac{dN}{dy}\frac{(n-1)(n-2)}{nC\left(nC + m_0(n-2)\right)}\left(1 + \frac{m_{\mathrm{T}} - m_0}{nC}\right)^{-n}, \tag{4.7}$$

with $m_{\mathrm{T}} = \sqrt{p_T^2 + m_0^2}$ and m_0 representing the transverse mass and rest mass of J/ψ, respectively, while n and C are free parameters. The fitting is done to the corrected J/ψ yields as a function of p_{T} above $p_{\mathrm{T}} > 0.2$ GeV/c, as shown in Fig. 4.1, for three different centrality classes (20-40%, 40-60%, and 60-80%). Given the quite narrow bin widths for $p_{\mathrm{T}} < 0.2$ GeV/c the p_{T} position for bins below 0.2 GeV/c is designated as the center of each bin. The fitting process is carried out iteratively, adjusting the p_{T} positions of data points based on the fitting outcome of the preceding iteration in accordance with Eq. 4.6. The iterative fit results, illustrated by dashed lines in Fig. 4.1, stabilizes after three iterations.

The resulting p_{T} positions for each bin are exhibited in Fig. 4.2, where a diagonal dashed line is also plotted for visual guidance. The estimated p_{T} positions are consistent

across all three centrality intervals analyzed except for the 1-2 GeV/c bin due to the spectra turning over in this range, making the fit less stable. In the end, the averaged p_{T} positions (green points) across the three centrality classes are adopted as the final p_{T} positioning. Notably, these estimated positions closely align with the bin centers, attributed to the relatively narrow bin widths, except for the highest p_{T} bin ($5 < p_{\mathrm{T}} < 7$ GeV/c), where the bin width is large and the spectrum falls steeply.

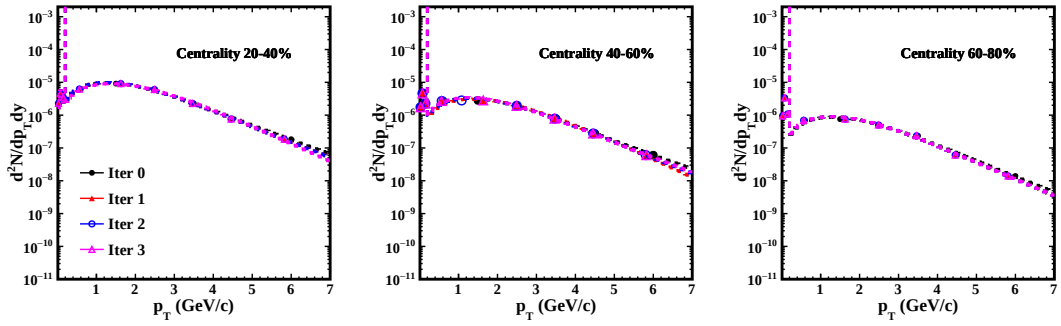

Figure 4.1 Iterative fitting to the corrected J/ψ yield as a function of p_{T} in different centrality bins.

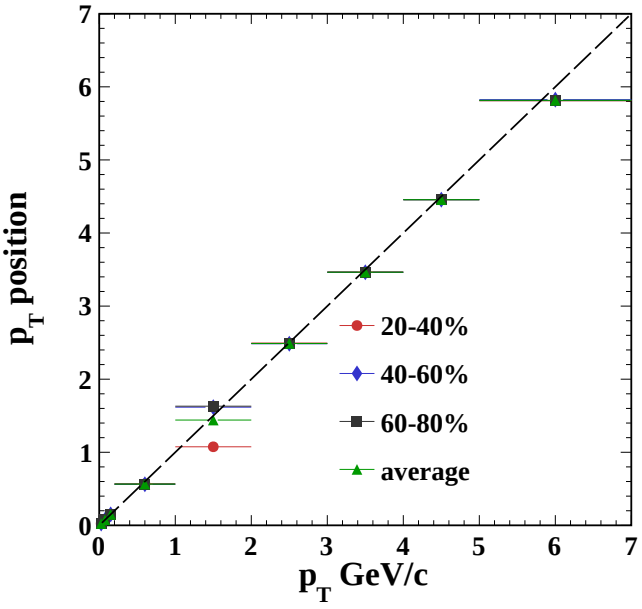

Figure 4.2 Estimated p_{T} position for each p_{T} bin. The dashed line along diagonal represents the bin center.

Figure 4.3 shows the invariant yield of J/ψ as a function of p_{T} within $|y| < 0.5$ in Au+Au collisions at $\sqrt{s_{\mathrm{NN}}} = 200$ GeV. Data points are placed as the positions according to Fig. 4.2. Solid markers denote the results from the current analysis for centrality classes of 60-80%, 40-60%, and 20-40%, while open markers depict results from published measurements of J/ψ production via the dimuon decay channel for $p_{\mathrm{T}} > 0.15$ GeV/c by STAR[56], utilizing the 2014 dataset for the same centrality classes. Statis-

tical uncertainties are indicated by the error bars, and the systematic uncertainties are illustrated with boxes. Good consistency is seen between new and published results. The solid lines are the Tsallis fit to the current results in the range of $p_T > 0.2$ GeV/c, while the dashed lines are the extrapolations of the fits down to 0.01 GeV/c. The fits can describe the data very well within $p_T > 0.2$ GeV/c. Significant enhancements at $p_T < 0.2$ GeV/c are observed with respect to the extrapolation of the fit, which are expected from the contribution of coherent photon-nucleus interactions in this very low p_T region.

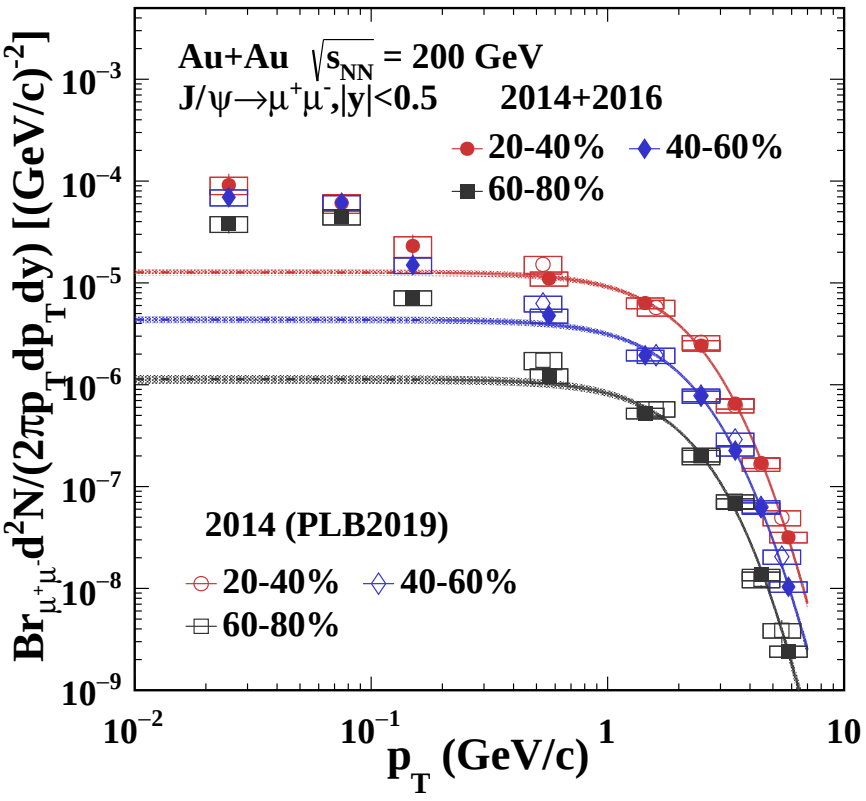

Figure 4.3 Invariant yields of J/ψ as a function of p_T for different centralities within $|y| < 0.5$, in comparison with published results for $p_T > 0.15$ GeV/c [56]. The solid lines are the fits to the new results within the range of $p_T > 0.2$ GeV/c, while the dashed lines represent the fits extrapolated down to very low p_T. The bands show fit uncertainties.

4.2 Nuclear modification factor (R_{AA})

To quantify the modifications of J/ψ yield in heavy-ion collisions with respect to that in p+p collisions, the nuclear modification factor, R_{AA}, is utilized. It is defined as:

$$R_{AA} = \frac{1}{N_{coll}} \times \frac{\left(dN_{J/\psi}/dp_T\right)_{Au+Au}}{\left(dN_{J/\psi}/dp_T\right)_{p+p}}, \tag{4.8}$$

where $N_{\rm coll}$ is the average nucleon-nucleon binary collisions for a given centrality class as listed in Tab. 3.11, $\left(dN_{J/\psi}/dp_{\rm T}\right)_{\rm Au+Au}$ is the J/ψ invariant yield in Au+Au collisions and $\left(dN_{J/\psi}/dp_{\rm T}\right)_{p+p}$ is the J/ψ invariant yield in p+p collisions. The J/ψ distribution in p+p collisions at $\sqrt{s}$ = 200 GeV is obtained by combining STAR and PHENIX measurements[137-138].

Figure 4.4 presents the J/ψ $R_{\rm AA}$ as a function of $p_{\rm T}$ in various centrality classes of Au+Au collisions at $\sqrt{s_{\rm NN}}$ = 200 GeV. Solid markers denote the results from the current analysis, while open markers show results from published measurements of J/ψ production via dielectron channel by STAR[101]. The new results are consistent with the published ones within uncertainties. A suppression pattern of J/ψ production for $p_{\rm T}$ > 0.2 GeV/c across all collision centrality classes is seen, which can be well described by transport models that incorporate both cold and hot medium effects[68,111]. Notably, a significant enhancement in J/ψ yield is observed at lower $p_{\rm T}$ (below 0.2 GeV/c) in peripheral collisions relative to p+p collisions. Within this $p_{\rm T}$ range, both color screening and CNM effects suppress the J/ψ production, while the regeneration effect, which can enhance the J/ψ production, is expected to be very small in these peripheral collisions. Therefore, the observed enhancement is attributed to coherent J/ψ production from photon-nucleus interactions.

The enhancement of the $R_{\rm AA}$ value reaches 15 ± 3 (stat.) ± 3 (syst.) and 18 ± 3 ± 4 for 0 < $p_{\rm T}$ < 0.05 and 0.05 < $p_{\rm T}$ < 0.1 GeV/c in the 60-80% centrality class, which are comparable to the published dielectron channel results of 24 ± 5 ± 9 and 18 ± 2 ± 2 in same $p_{\rm T}$ range and centrality class. The coherent photon-nucleus cross section is expected to be proportional to the photon flux and, thus, to the square of the nuclear charge, Z^2, which does not depend on centrality, it is not directly related to $N_{\rm coll}$, which decreases towards peripheral collisions and used for calculating $R_{\rm AA}$. Consequently, the $R_{\rm AA}$ value in peripheral collisions is expected to be larger than those for semi-central collisions, as observed in Fig. 4.4

4.3 $p_{\rm T}^2$ distribution of excess yield

The differential cross section $d\sigma/dt$ of coherent J/ψ production, with t representing the negative momentum transfer squared ($-t \sim p_T^2$), encodes information about the distribution of interaction sites on the transverse plane, which can be used to deduce the gluon distribution within the nucleus. To isolate the excess J/ψ yield, contributions from hadronic interactions—approximated with the extrapolation of Tsallis function fits

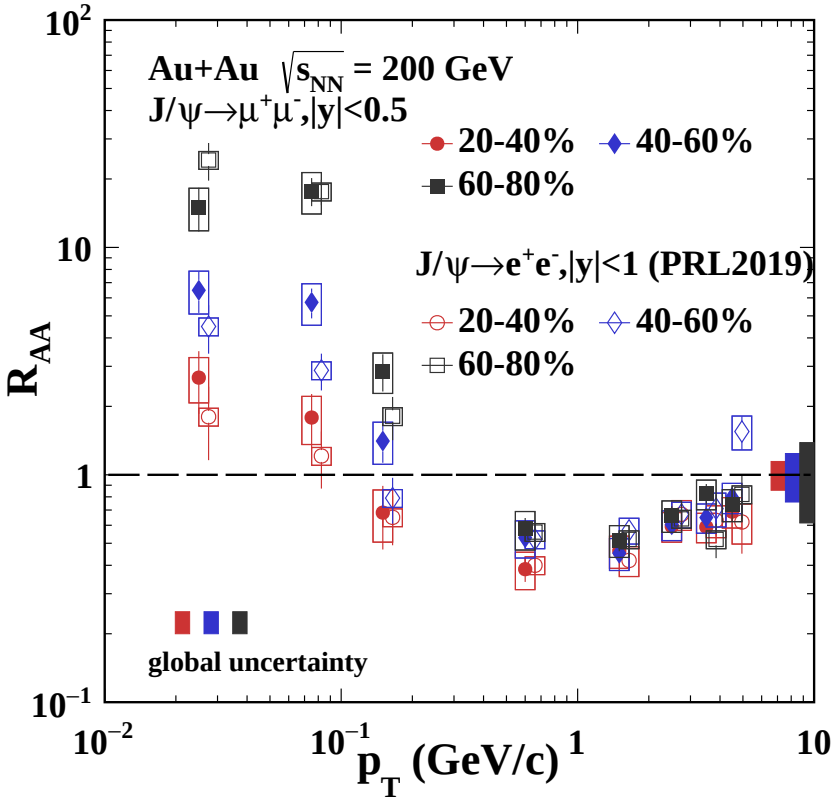

Figure 4.4 The J/ψ R_{AA} as a function of p_T in 200 GeV Au+Au collisions compared to similar measurements via the dielectron decay channel. Data points have been horizontally shifted for clarity. The shaded bands at unity show the global uncertainties, which include the 10% uncertainty on $p+p$ reference and the N_{coll} uncertainties.

(dashed lines in Fig. 4.3)—are subtracted from the observed yield. Figure 4.5 shows the excess yield of J/ψ as a function of p_T^2 for the $40-80\%$ centrality class. Here, the centrality classes are combined to increase statistics. The results from the current analysis are depicted with blue markers, while open black circles represent published STAR resutls through the dielectron decay channel[101]. The new and published results agree with each within uncertainties, and thus they are combined using weights equal to the inverse of their statistical uncertainties squared. The combined results are shown as red diamonds.

The $-t$ distribution features a distinct peak and a tail, resembling the structure observed for J/ψ in Au+Au UPC at $\sqrt{s_{NN}}$ = 200 GeV[139]. The peak at $p_T^2 < 0.015$ $(\text{GeV}/c)^2$ suggests coherent photon-nucleus production, whereas the tail beyond this range may arise from incoherent production. Exponential fits to the p_T^2 distribution within the $0.002 < p_T^2 < 0.015$ $(\text{GeV}/c)^2$ range are used to extract the slope parameter, which is related to the interaction region's size within the target nucleus. The obtained slope parameters from this analyzsis, from previously published dielectron results, as well as from combined results are summarized in Tab. 4.1. A good consistency is seen

between this analysis and previous publication. It is worth noting that the extracted slope parameters seem to be systematically lower than that anticipated for an Au nucleus theoretically [199 $(\mathrm{GeV}/c)^{-2}$][94,103,140]. This potential discrepancy could hint that, in peripheral collisions where nuclei overlap, the interaction may not involve the entire target nucleus.

A notable suppression in the lowest p_T^2 range, more evident in the averaged results reaching a significance of 5.5σ away from the extrapolation of the exponential fit, could arise from the interference effects, as previously seen in UPCs for ρ^0 mesons by STAR[104].

The model calculation[141] for the coherent component and incoherent component of photoproduced J/ψ is also shown in this plot, which can describe data very well.

Additionally, identifying the expected incoherent tail could enable the study of incoherent photon-nucleus production, which is directly related to the fluctuations in the nucleus and can also potentially used for exploring nuclear deformation[142]. However, the precision of the current analysis, even after being combined with published dielectron results, is insufficient for a detailed investigation of the incoherent component.

Table 4.1 List of the slope parameters from current analysis, published dielectron channel results and the average of the two.

	Slope parameter
dimuon channel	135 ± 31
dielectron channel[101]	177 ± 23
averaged	161 ± 24

4.4 Centrality dependence of excess yield

Figure 4.6 depicts the excess J/ψ yields integrated over $p_{\mathrm{T}} < 0.1$ GeV/c as a function of N_{part}. The expected hadronic contributions are subtracted. The results from this thesis are shown with blue markers, while open black circles represent published results through the dielectron decay channel[101], and red markers denote the combined results of the two. These yields are determined for centrality classes in increments of 10% within the 30-80% centrality range. Remarkably, the measured excess yields demonstrate no significant centrality dependence for the measured centrality classes within the uncertainties. A theoretical calculation, based on the EPA approach, for Au+Au collisions is also shown for comparison[110]. The model calculations, which posit coherent photoproduction for J/ψ with one entire nucleus acting as the photon emitter and the entire nucleus or only spectator nucleons in the other colliding nucleus serving

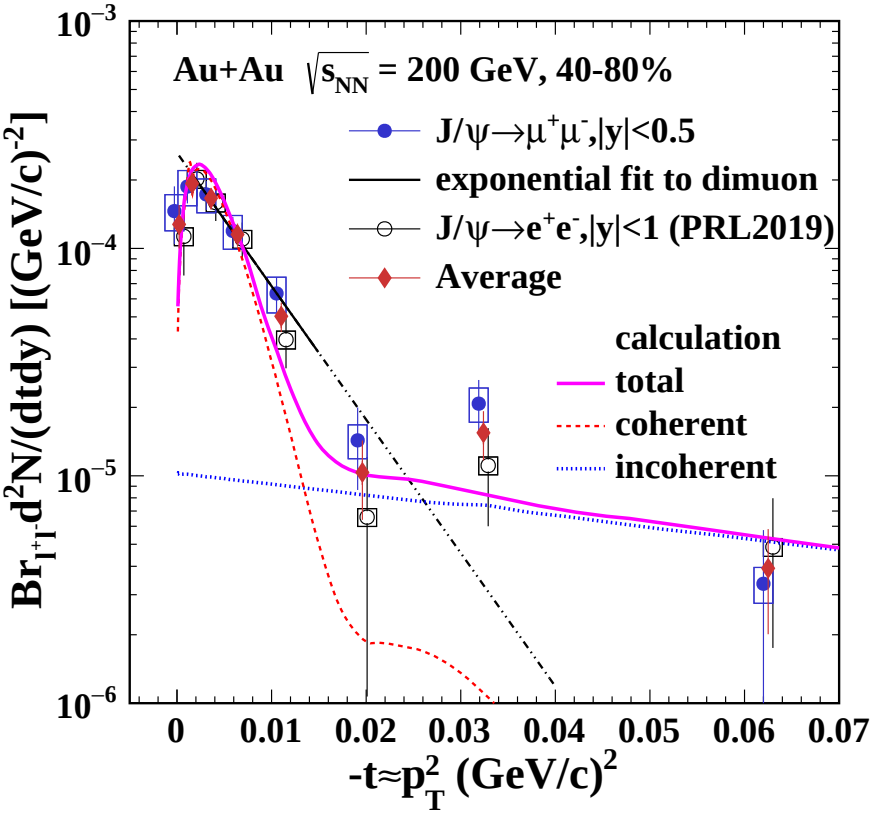

Figure 4.5 The coherent J/ψ excess yield as a function of the negative momentum transfer squared $-t\,(\approx p_T^2)$ for the $40-80\%$ centrality class in Au+Au collisions, in comparison with previous dielectron measurements. Data points are displaced horizontally for clarify. The black solid line is an exponential fit to the dimuon resutls. The dashed black line is an extrapolation of the fit.

as the Pomeron emitter, align closely with the observed excess yields within the measured centrality range. However, the Nucleus+Spectator calculation seems to favor the data. This model incorporates the shadowing effect in nPDF that is consistent with the UPC results at RHIC kinematics[96]. However, it does not account for any potential hot medium effects, such as dissociation. It is worth noting that this model predicts a significant decrease of the coherent J/ψ yield towards central collisions due to the decreasing number of spectator nucleons for emitting Pomeron. Future measurements in more central collisions, beyond what has been achieved in current results, could provide stringent tests to this picture.

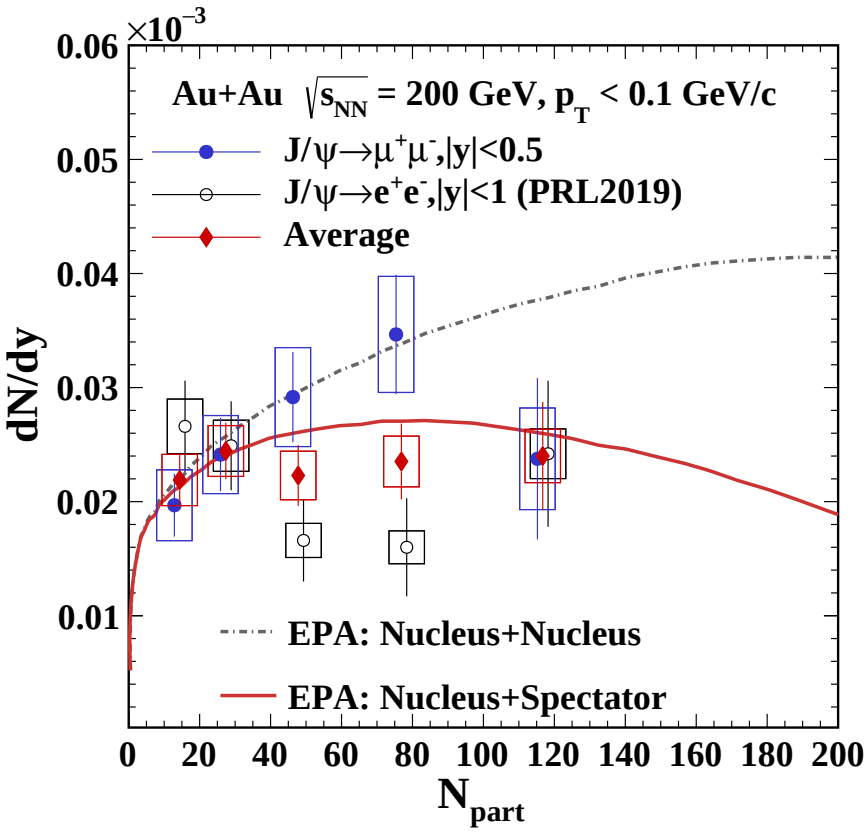

Figure 4.6 The N_{part} dependence of p_T-integrated excess J/ψ yield (p_T < 0.1 GeV/c) in comparison with previous dielectron channel measurement and a model calculation. Data points have been horizontally shifted for clarity.

Chapter 5 Summary and Outlook

In summary, this thesis presents the measurements of coherent photo-induced J/ψ production in 30-80% Au+Au collisions at $\sqrt{s_{\rm NN}}$ = 200 GeV, utilizing data collected in 2014 and 2016 by the STAR experiment. The MTD system, which is designed for muon identification and triggering, facilitates the measurement of J/ψ production via the dimuon channel. This is for the first time that STAR has measured very low $p_{\rm T}$ J/ψ production via the dimuon channel. The results provide insights into the properties of very low $p_{\rm T}$ J/ψ produced through photo-induced processes, thanks to the intense electromagnetic fields generated in ultra-relativistic heavy-ion collisions. The measurements include the J/ψ invariant yield and nuclear modification factor as a function of $p_{\rm T}$ in the range of $0.02 < p_{\rm T} < 6$ GeV/c, as well as $p_{\rm T}^2$ and centrality dependence of the excess yield for very low $p_{\rm T}$ J/ψ beyond hadronic production contribution. These measurements are seen to be consistent with published results through the dielectron channel[101], and thus they are combined to improve the measurement precision.

The J/ψ invariant yields as a function of $p_{\rm T}$ are measured in 20-40%, 40-60% and 60-80% centrality classes. The yields are fitted with the Tsallis function for $p_{\rm T} >$ 0.2 GeV/c, and the extrapolations of the fits below 0.2 GeV/c are treated as estimates of the contributions from hadronic interactions. The $p_{\rm T}$ distributions reveal significant enhancement within $p_{\rm T} < 0.2$ GeV/c with respect to the expected hadronic contribution in all three centrality classes, especially for 60-80% interval. Based on the yields, the nuclear modification factor $R_{\rm AA}$ is calculated as a function of $p_{\rm T}$ for the same centrality classes. Suppression of $R_{\rm AA}$ for $p_{\rm T} > 0.2$ GeV/c is observed, aligning with the combined cold and hot medium effects, due to the present of the QGP in these nuclear collisions. Notably, an enhancement above unity in 60-80% centrality class is observed, with values reaching 15 ± 3 (stat.) $\pm$ 3 (syst.) and $17 \pm 4 \pm 4$ for $0 < p_{\rm T} < 0.05$ and $0.05 < p_{\rm T} < 0.1$ GeV/c. The enhancements seen in the J/ψ yield at very low $p_{\rm T}$ beyond the expected hadronic contribution, and in $R_{\rm AA}$ with respect to the p+p reference, strongly suggest that photon-induced production is also present in hadronic peripheral heavy-ion collisions, and constitute the dominant production mechanism for very low $p_{\rm T}$ J/ψ.

We also present coherent J/ψ yield as a function of $-t$ ($\sim p_{\rm T}^2$) in 40-80% peripheral Au+Au collisions. This differential cross section is considered a golden channel for measuring gluon distribution in the nucleus. The $p_{\rm T}^2$ distribution shows a similar structure to that observed in UPCs, and an exponential fit to the distribution results in

a slope parameter of 161 ± 24 $(\mathrm{GeV}/c)^{-2}$. The extracted slope parameters from this analysis, from previously published dielectron results, as well as from combined results seem to be systematically lower than that anticipated for an Au nucleus theoretically [199 $(\mathrm{GeV}/c)^{-2}$]. Maybe a hint that the interaction may not involve the entire target nucleus in peripheral collisions. Furthermore, we've measured the p_{T} integrated coherent J/ψ yield as a function of collision centrality. No significant centrality dependence is seen within the large uncertainties for the measured centrality range. These results are compared with a EPA calculation of J/ψ production from coherent photon-nuclear interactions, which treats the entire projectile nucleus as the photon emitter and only the spectator nucleons in the target nucleus as Pomeron emitters. This model accounts for the nPDF effects, such as the nuclear shadowing, but no potential hot medium effects from the QGP is included. Data and the model calculation are seen to agree with each other within uncertainties, which further supports the conclusion that the observed J/ψ yield enhancement beyond hadronic contribution at very low p_{T} originate from photon-induced interactions.

The exploration of photon-nucleus interactions, the initial EM fields, and the QGP properties present a complex and multifaceted challenge. The statistical limitations of dimuon channel results highlight an urgent need for precision measurements in forthcoming studies. Moreover, the expansion of measured observables is essential to deepen our understanding of these phenomena.

The RHIC running of Au+Au collisions at $\sqrt{s_{\mathrm{NN}}}$ = 200 GeV in 2023 and 2025 promises significantly larger datasets than what's currently available. Notably, the iTPC upgrade, installed in 2019, has greatly enhanced TPC's efficiency and resolution, both of which are beneficial for low-p_{T} J/ψ measurement. The minimum bias events expected from these two years are projected to be 20 times that of 2014, with an anticipated sampled luminosity of 37 nb^{-1}. This substantial increase in data volume is set to markedly improve the analysis of coherent J/ψ production.

Additionally, the quasi-real photons generated by the initial intense EM fields in heavy-ion collisions are linearly polarized. This linear polarization is inherited by vector mesons produced in coherent photon-nucleus interactions, leading to a preferential alignment of their decay products along the polarization direction. This results in an azimuthal $\cos 2\phi$ modulation in the momentum distribution with respect to the polarization direction, where ϕ is the angle between the momentum of the vector meson and one of the decay daughters. The nature of coherent photon-nucleus interactions blurs the distinction between the photon-emitting nucleus and the target, introducing interfer-

ence that makes this angular modulation observable and significant. Such modulations provide insights into the gluon distribution within the nucleus, and have been observed in the $\rho^0 \to \pi^+\pi^-$ process by the STAR collaboration[143]. Compared to the ρ^0 meson, the J/ψ meson has a longer lifetime, and its decay products (electrons or muons) are spin-1/2 fermions, adding a relationship between the angular modulation of J/ψ and the level of interference. Moreover, investigating the cos2ϕ modulation of J/ψ in the overlap region could enhance our understanding of possible medium effects and how they vary with impact parameters. Although attempts to measure the cos2ϕ modulation of daughter muons from J/ψ decays in peripheral collisions have been made using the current dataset as shown in the left panel of Fig. 5.1 for p_T < 0.1 GeV/c in the 60-80% centrality class, large statistical uncertainties preclude any firm conclusions on the existence of such a modulation. The projected statistical uncertainty for $A_{2\phi}$ measurement based on 2023 and 2025 statistics is shown in the right panel of Fig. 5.1, suggesting a significantly reduced uncertainty compared to the current result, and potentially a 3σ measurement assuming the same central value as measured in this thesis.

Furthermore, the increased statistics from future runs present an opportunity to isolate the incoherent contribution, enabling detailed studies of fluctuations in nucleus. Moreover, measuring coherent production in more central collisions could provide a rigorous test of EPA calculation. With sufficiently precise data, it might become possible to tease out possible hot medium effects, assuming a comprehensive understanding of the QED baseline.

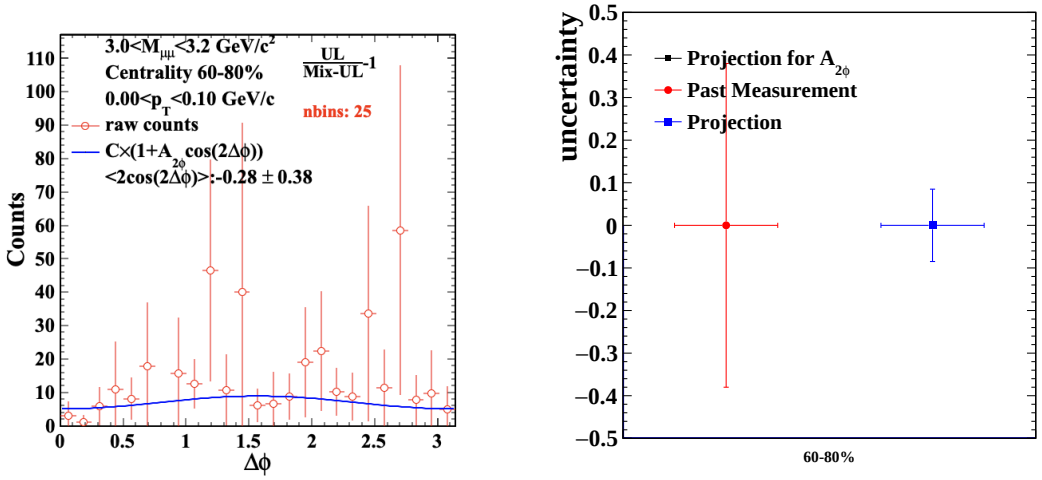

Figure 5.1 Left: The $\Delta\phi$ disbribution of dimuon pair within J/ψ mass range (3.0-3.2 GeV/c^2) in p_T < 0.1 GeV for 60-80% centrality. Right: The projection of the statistical uncertainty of $A_{2\phi}$ for future statistics in 2023 and 2025.

Bibliography

[1] GAILLARD M K, GRANNIS P D, SCIULLI F J. The Standard model of particle physics [J/OL]. Rev. Mod. Phys., 1999, 71: S96-S111. DOI: 10.1103/RevModPhys.71.S96.

[2] WIKI. Standard Model - Wikipedia — en.wikipedia.org[EB/OL]. https://en.wikipedia.org/wiki/Standard_Model.

[3] AAD G, et al. Observation of a new particle in the search for the Standard Model Higgs boson with the ATLAS detector at the LHC[J/OL]. Phys. Lett. B, 2012, 716: 1-29. DOI: 10.1016/j.physletb.2012.08.020.

[4] FRITZSCH H, GELL-MANN M. Current algebra: Quarks and what else?[J]. eConf, 1972, C720906V2: 135-165.

[5] SALAM G P. Elements of QCD for hadron colliders[J/OL]. CERN Yellow Rep. School Proc., 2020, 5: 1-56. DOI: 10.23730/CYRSP-2020-005.1.

[6] SKANDS P. Introduction to QCD[C/OL]//Theoretical Advanced Study Institute in Elementary Particle Physics: Searching for New Physics at Small and Large Scales. 2013: 341-420. DOI: 10.1142/9789814525220_0008.

[7] WORKMAN R L, et al. Review of Particle Physics[J/OL]. PTEP, 2022, 2022: 083C01. DOI: 10.1093/ptep/ptac097.

[8] DUKE D W, ROBERTS R G. Deep Inelastic Scattering and Asymptotic Freedom: A Detailed Analysis and Confrontation[J/OL]. Nucl. Phys. B, 1980, 166: 243-283. DOI: 10.1016/0550-3213(80)90227-8.

[9] WILSON K G. Confinement of Quarks[J/OL]. Phys. Rev. D, 1974, 10: 2445-2459. DOI: 10.1103/PhysRevD.10.2445.

[10] JACOB M, TRAN THANH VAN J. QUARK MATTER FORMATION AND HEAVY ION COLLISIONS[J/OL]. Phys. Rept., 1982, 88: 325-413. DOI: 10.1016/0370-1573(82)90083-7.

[11] BUSZA W, RAJAGOPAL K, VAN DER SCHEE W. Heavy Ion Collisions: The Big Picture, and the Big Questions[J/OL]. Ann. Rev. Nucl. Part. Sci., 2018, 68: 339-376. DOI: 10.1146/annurev-nucl-101917-020852.

[12] KARSCH F, LAERMANN E, PEIKERT A. The Pressure in two flavor, (2+1)-flavor and three flavor QCD[J/OL]. Phys. Lett. B, 2000, 478: 447-455. DOI: 10.1016/S0370-2693(00)00292-6.

[13] RUAN L. Bulk physics: critical point search[J/OL]. Quark Matter 2023, 2023. https://indico.cern.ch/event/1139644/contributions/5372774/.

[14] FODOR Z, KATZ S D. Critical point of QCD at finite T and mu, lattice results for physical quark masses[J/OL]. JHEP, 2004, 04: 050. DOI: 10.1088/1126-6708/2004/04/050.

[15] BAZAVOV A, et al. The QCD Equation of State to $\mathcal{O}(\mu_B^6)$ from Lattice QCD[J/OL]. Phys. Rev. D, 2017, 95(5): 054504. DOI: 10.1103/PhysRevD.95.054504.

[16] LEE T D, WICK G C. Vacuum Stability and Vacuum Excitation in a Spin 0 Field Theory [J/OL]. Phys. Rev. D, 1974, 9: 2291-2316. DOI: 10.1103/PhysRevD.9.2291.

[17] MATTIA. Evolution of collisions and qgp[EB/OL]. https://particlesandfriends.wordpress.com/2016/10/14/evolution-of-collisions-and-qgp.

[18] TOIA A. Participants and spectators at the heavy-ion fireball – CERN Courier — cerncourier.com[EB/OL]. 2023. https://cerncourier.com/a/participants-and-spectators-at-the-heavy-ion-fireball/.

[19] MILLER M L, REYGERS K, SANDERS S J, et al. Glauber modeling in high energy nuclear collisions[J/OL]. Ann. Rev. Nucl. Part. Sci., 2007, 57: 205-243. DOI: 10.1146/annurev.nucl.57.090506.123020.

[20] AUGUSTIN J E, et al. Discovery of a Narrow Resonance in e^+e^- Annihilation[J/OL]. Phys. Rev. Lett., 1974, 33: 1406-1408. DOI: 10.1103/PhysRevLett.33.1406.

[21] AUBERT J J, et al. Experimental Observation of a Heavy Particle J[J/OL]. Phys. Rev. Lett., 1974, 33: 1404-1406. DOI: 10.1103/PhysRevLett.33.1404.

[22] ABRAMS G S, et al. The Discovery of a Second Narrow Resonance in e+ e- Annihilation [J/OL]. Phys. Rev. Lett., 1974, 33: 1453-1455. DOI: 10.1103/PhysRevLett.33.1453.

[23] GOLDHABER G, et al. Observation in e+ e- Annihilation of a Narrow State at 1865-MeV/c**2 Decaying to K pi and K pi pi pi[J/OL]. Phys. Rev. Lett., 1976, 37: 255-259. DOI: 10.1103/PhysRevLett.37.255.

[24] KNAPP B, et al. Observation of a Narrow anti-Baryon State at 2.26-GeV/c**2[J/OL]. Phys. Rev. Lett., 1976, 37: 882. DOI: 10.1103/PhysRevLett.37.882.

[25] HERB S W, et al. Observation of a Dimuon Resonance at 9.5-GeV in 400-GeV Proton-Nucleus Collisions[J/OL]. Phys. Rev. Lett., 1977, 39: 252-255. DOI: 10.1103/PhysRevLett.39.252.

[26] INNES W R, et al. Observation of Structure in the Υ Region[J/OL]. Phys. Rev. Lett., 1977, 39: 1240-1242. DOI: 10.1103/PhysRevLett.39.1240.

[27] UENO K, et al. Evidence for the Υ'' and a Search for New Narrow Resonances[J/OL]. Phys. Rev. Lett., 1979, 42: 486-489. DOI: 10.1103/PhysRevLett.42.486.

[28] BEBEK C, et al. Evidence for New Flavor Production at the Upsilon (4S)[J/OL]. Phys. Rev. Lett., 1981, 46: 84. DOI: 10.1103/PhysRevLett.46.84.

[29] BASILE M, et al. Evidence for a New Particle With Naked 'Beauty' and for Its Associated

Production in High-energy (pp) Interactions[J/OL]. Lett. Nuovo Cim., 1981, 31: 97. DOI: 10.1007/BF02822406.

[30] ABE F, et al. Evidence for top quark production in $\bar{p}p$ collisions at $\sqrt{s} = 1.8$ TeV[J/OL]. Phys. Rev. Lett., 1994, 73: 225-231. DOI: 10.1103/PhysRevLett.73.225.

[31] TANABASHI M, et al. Review of Particle Physics[J/OL]. Phys. Rev. D, 2018, 98(3): 030001. DOI: 10.1103/PhysRevD.98.030001.

[32] DIGAL S, PETRECZKY P, SATZ H. Quarkonium feed down and sequential suppression [J/OL]. Phys. Rev. D, 2001, 64: 094015. DOI: 10.1103/PhysRevD.64.094015.

[33] FRITZSCH H. Producing Heavy Quark Flavors in Hadronic Collisions: A Test of Quantum Chromodynamics[J/OL]. Phys. Lett. B, 1977, 67: 217-221. DOI: 10.1016/0370-2693(77)90108-3.

[34] GLUCK M, OWENS J F, REYA E. Gluon Contribution to Hadronic J/psi Production[J/OL]. Phys. Rev. D, 1978, 17: 2324. DOI: 10.1103/PhysRevD.17.2324.

[35] BARGER V D, KEUNG W Y, PHILLIPS R J N. On psi and Upsilon Production via Gluons [J/OL]. Phys. Lett. B, 1980, 91: 253-258. DOI: 10.1016/0370-2693(80)90444-X.

[36] ADARE A, et al. Ground and excited charmonium state production in $p + p$ collisions at $\sqrt{s} = 200$ GeV[J/OL]. Phys. Rev. D, 2012, 85: 092004. DOI: 10.1103/PhysRevD.85.092004.

[37] AAIJ R, et al. Measurement of $\psi(2S)$ meson production in pp collisions at $\sqrt{s}$=7 TeV[J/OL]. Eur. Phys. J. C, 2012, 72: 2100. DOI: 10.1140/epjc/s10052-012-2100-4.

[38] MA Y Q, VOGT R. Quarkonium Production in an Improved Color Evaporation Model[J/OL]. Phys. Rev. D, 2016, 94(11): 114029. DOI: 10.1103/PhysRevD.94.114029.

[39] CHEUNG V, VOGT R. Production and polarization of prompt $\Upsilon(n\mathrm{S})$ in the improved color evaporation model using the k_T-factorization approach[J/OL]. Phys. Rev. D, 2019, 99(3): 034007. DOI: 10.1103/PhysRevD.99.034007.

[40] ABE F, et al. J/ψ and $\psi(2S)$ production in $p\bar{p}$ collisions at $\sqrt{s} = 1.8$ TeV[J/OL]. Phys. Rev. Lett., 1997, 79: 572-577. DOI: 10.1103/PhysRevLett.79.572.

[41] ARTOISENET P, LANSBERG J P, MALTONI F. Hadroproduction of J/ψ and Υ in association with a heavy-quark pair[J/OL]. Phys. Lett. B, 2007, 653: 60-66. DOI: 10.1016/j.physletb.2007.04.031.

[42] CAMPBELL J M, MALTONI F, TRAMONTANO F. QCD corrections to J/psi and Upsilon production at hadron colliders[J/OL]. Phys. Rev. Lett., 2007, 98: 252002. DOI: 10.1103/PhysRevLett.98.252002.

[43] ARTOISENET P, CAMPBELL J M, LANSBERG J P, et al. Υ Production at Fermilab Tevatron and LHC Energies[J/OL]. Phys. Rev. Lett., 2008, 101: 152001. DOI: 10.1103/PhysRevLett.101.152001.

[44] BODWIN G T, BRAATEN E, YUAN T C, et al. P wave charmonium production in B meson decays[J/OL]. Phys. Rev. D, 1992, 46: R3703-R3707. DOI: 10.1103/PhysRevD.46.R3703.

[45] NAYAK G C, QIU J W, STERMAN G F. NRQCD Factorization and Velocity-dependence of NNLO Poles in Heavy Quarkonium Production[J/OL]. Phys. Rev. D, 2006, 74: 074007. DOI: 10.1103/PhysRevD.74.074007.

[46] ZHANG P, MENG C, MA Y Q, et al. Gluon fragmentation into ${}^3P_J^{[1,8]}$ quark pair and test of NRQCD factorization at two-loop level[J/OL]. JHEP, 2021, 08: 111. DOI: 10.1007/JHEP08 (2021)111.

[47] MANGANO M L, PETRELLI A. NLO quarkonium production in hadronic collisions[J/OL]. Int. J. Mod. Phys. A, 1997, 12: 3887-3897. DOI: 10.1142/S0217751X97002048.

[48] CHEN A P, MA Y Q, ZHANG H. A Short Theoretical Review of Charmonium Production [J/OL]. Adv. High Energy Phys., 2022, 2022: 7475923. DOI: 10.1155/2022/7475923.

[49] MA Y Q, CHAO K T. New factorization theory for heavy quarkonium production and decay [J/OL]. Phys. Rev. D, 2019, 100(9): 094007. DOI: 10.1103/PhysRevD.100.094007.

[50] CHEN A P, MA Y Q. Theory for quarkonium: from NRQCD factorization to soft gluon factorization[J/OL]. Chin. Phys. C, 2021, 45(1): 013118. DOI: 10.1088/1674-1137/abc683.

[51] TANG Z, TANG Z B, ZHA W, et al. An experimental review of open heavy flavor and quarkonium production at RHIC[J/OL]. Nucl. Sci. Tech., 2020, 31(8): 81. DOI: 10.1007/s41365-020-00785-8.

[52] MATSUI T, SATZ H. J/ψ Suppression by Quark-Gluon Plasma Formation[J/OL]. Phys. Lett. B, 1986, 178: 416-422. DOI: 10.1016/0370-2693(86)91404-8.

[53] SATZ H. Quarkonium Binding and Dissociation: The Spectral Analysis of the QGP[J/OL]. Nucl. Phys. A, 2007, 783: 249-260. DOI: 10.1016/j.nuclphysa.2006.11.026.

[54] CHEN S, HE M. Gluo-dissociation of heavy quarkonium in the quark-gluon plasma reexamined[J/OL]. Phys. Rev. C, 2017, 96(3): 034901. DOI: 10.1103/PhysRevC.96.034901.

[55] LAINE M, PHILIPSEN O, ROMATSCHKE P, et al. Real-time static potential in hot QCD [J/OL]. JHEP, 2007, 03: 054. DOI: 10.1088/1126-6708/2007/03/054.

[56] ADAM J, et al. Measurement of inclusive J/ψ suppression in Au+Au collisions at $\sqrt{s_{NN}}$ = 200 GeV through the dimuon channel at STAR[J/OL]. Phys. Lett. B, 2019, 797: 134917. DOI: 10.1016/j.physletb.2019.134917.

[57] KHACHATRYAN V, et al. Suppression and azimuthal anisotropy of prompt and nonprompt J/ψ production in PbPb collisions at $\sqrt{s_{\rm NN}} = 2.76$ TeV[J/OL]. Eur. Phys. J. C, 2017, 77(4): 252. DOI: 10.1140/epjc/s10052-017-4781-1.

[58] ESKOLA K J, PAAKKINEN P, PAUKKUNEN H, et al. EPPS21: a global QCD analysis of nuclear PDFs[J/OL]. Eur. Phys. J. C, 2022, 82(5): 413. DOI: 10.1140/epjc/s10052-022-10

359-0.

[59] ARLEO F, KOLEVATOV R, PEIGNÉ S, et al. Centrality and pT dependence of J/psi suppression in proton-nucleus collisions from parton energy loss[J/OL]. JHEP, 2013, 05: 155. DOI: 10.1007/JHEP05(2013)155.

[60] ARLEO F, PEIGNE S. Heavy-quarkonium suppression in p-A collisions from parton energy loss in cold QCD matter[J/OL]. JHEP, 2013, 03: 122. DOI: 10.1007/JHEP03(2013)122.

[61] VITEV I. Non-Abelian energy loss in cold nuclear matter[J/OL]. Phys. Rev. C, 2007, 75: 064906. DOI: 10.1103/PhysRevC.75.064906.

[62] VITEV I, GOLDMAN J T, JOHNSON M B, et al. Open charm tomography of cold nuclear matter[J/OL]. Phys. Rev. D, 2006, 74: 054010. DOI: 10.1103/PhysRevD.74.054010.

[63] ARLEO F, PEIGNE S, SAMI T. Revisiting scaling properties of medium-induced gluon radiation[J/OL]. Phys. Rev. D, 2011, 83: 114036. DOI: 10.1103/PhysRevD.83.114036.

[64] VOGT R. Are the J/ψ and chi(c) A dependencies the same?[J/OL]. Nucl. Phys. A, 2002, 700: 539-554. DOI: 10.1016/S0375-9474(01)01313-6.

[65] ARMESTO N, CAPELLA A, FERREIRO E G, et al. J / psi suppression at SPS and RHIC in the comovers approach[J/OL]. Nucl. Phys. A, 2002, 698: 583-586. DOI: 10.1016/S0375-94 74(01)01433-6.

[66] CAPELLA A, FERREIRO E G. J/ psi suppression at s**(1/2) = 200-GeV in the comovers interaction model[J/OL]. Eur. Phys. J. C, 2005, 42: 419-424. DOI: 10.1140/epjc/s2005-023 48-0.

[67] ADAMCZYK L, et al. Energy dependence of J/ψ production in Au+Au collisions at $\sqrt{s_{NN}}$ = 39, 62.4 and 200 GeV[J/OL]. Phys. Lett. B, 2017, 771: 13-20. DOI: 10.1016/j.physletb.201 7.04.078.

[68] ZHAO X, RAPP R. Charmonium in Medium: From Correlators to Experiment[J/OL]. Phys. Rev. C, 2010, 82: 064905. DOI: 10.1103/PhysRevC.82.064905.

[69] HUANG X G. Electromagnetic fields and anomalous transports in heavy-ion collisions — A pedagogical review[J/OL]. Rept. Prog. Phys., 2016, 79(7): 076302. DOI: 10.1088/0034-488 5/79/7/076302.

[70] OLAUSEN S A, KASPI V M. The McGill Magnetar Catalog[J/OL]. Astrophys. J. Suppl., 2014, 212: 6. DOI: 10.1088/0067-0049/212/1/6.

[71] TUROLLA R, ZANE S, WATTS A. Magnetars: the physics behind observations. A review [J/OL]. Rept. Prog. Phys., 2015, 78(11): 116901. DOI: 10.1088/0034-4885/78/11/116901.

[72] BZDAK A, SKOKOV V. Event-by-event fluctuations of magnetic and electric fields in heavy ion collisions[J/OL]. Phys. Lett. B, 2012, 710: 171-174. DOI: 10.1016/j.physletb.2012.02.0 65.

[73] DENG W T, HUANG X G. Event-by-event generation of electromagnetic fields in heavy-ion collisions[J/OL]. Phys. Rev. C, 2012, 85: 044907. DOI: 10.1103/PhysRevC.85.044907.

[74] BLOCZYNSKI J, HUANG X G, ZHANG X, et al. Azimuthally fluctuating magnetic field and its impacts on observables in heavy-ion collisions[J/OL]. Phys. Lett. B, 2013, 718: 1529-1535. DOI: 10.1016/j.physletb.2012.12.030.

[75] CHERNODUB M N. Superconductivity of QCD vacuum in strong magnetic field[J/OL]. Phys. Rev. D, 2010, 82: 085011. DOI: 10.1103/PhysRevD.82.085011.

[76] CHERNODUB M N. Spontaneous electromagnetic superconductivity of vacuum in strong magnetic field: evidence from the Nambu–Jona-Lasinio model[J/OL]. Phys. Rev. Lett., 2011, 106: 142003. DOI: 10.1103/PhysRevLett.106.142003.

[77] LIU Y C, HUANG X G. Anomalous chiral transports and spin polarization in heavy-ion collisions[J/OL]. Nucl. Sci. Tech., 2020, 31(6): 56. DOI: 10.1007/s41365-020-00764-z.

[78] HATTORI K, HUANG X G. Novel quantum phenomena induced by strong magnetic fields in heavy-ion collisions[J/OL]. Nucl. Sci. Tech., 2017, 28(2): 26. DOI: 10.1007/s41365-016-0178-3.

[79] KHARZEEV D E. The Chiral Magnetic Effect and Anomaly-Induced Transport[J/OL]. Prog. Part. Nucl. Phys., 2014, 75: 133-151. DOI: 10.1016/j.ppnp.2014.01.002.

[80] KHARZEEV D E, LIAO J, VOLOSHIN S A, et al. Chiral magnetic and vortical effects in high-energy nuclear collisions—A status report[J/OL]. Prog. Part. Nucl. Phys., 2016, 88: 1-28. DOI: 10.1016/j.ppnp.2016.01.001.

[81] LI W, WANG G. Chiral Magnetic Effects in Nuclear Collisions[J/OL]. Ann. Rev. Nucl. Part. Sci., 2020, 70: 293-321. DOI: 10.1146/annurev-nucl-030220-065203.

[82] XIN-LI Z, GUO-LIANG M, YU-GANG M, et al. Electromagnetic field effects and anomalous chiral phenomena in heavy-ion collisions at intermediate and high energy[J/OL]. Acta Phys. Sin., 2023, 72(11): 112502. DOI: 10.7498/aps.72.20230245.

[83] GUO X, SHI S, XU N, et al. Magnetic Field Effect on Charmonium Production in High Energy Nuclear Collisions[J/OL]. Phys. Lett. B, 2015, 751: 215-219. DOI: 10.1016/j.physletb.2015.10.038.

[84] GUO Y, SHI S, FENG S, et al. Magnetic Field Induced Polarization Difference between Hyperons and Anti-hyperons[J/OL]. Phys. Lett. B, 2019, 798: 134929. DOI: 10.1016/j.physletb.2019.134929.

[85] GUO X, LIAO J, WANG E. Spin Hydrodynamic Generation in the Charged Subatomic Swirl [J/OL]. Sci. Rep., 2020, 10(1): 2196. DOI: 10.1038/s41598-020-59129-6.

[86] FERMI E. On the Theory of the impact between atoms and electrically charged particles [J/OL]. Z. Phys., 1924, 29: 315-327. DOI: 10.1007/BF03184853.

[87] VON WEIZSACKER C F. Radiation emitted in collisions of very fast electrons[J/OL]. Z. Phys., 1934, 88: 612-625. DOI: 10.1007/BF01333110.

[88] WILLIAMS E J. Nature of the high-energy particles of penetrating radiation and status of ionization and radiation formulae[J/OL]. Phys. Rev., 1934, 45: 729-730. DOI: 10.1103/Phys Rev.45.729.

[89] BAUR G, HENCKEN K, TRAUTMANN D, et al. Coherent gamma gamma and gamma-A interactions in very peripheral collisions at relativistic ion colliders[J/OL]. Phys. Rept., 2002, 364: 359-450. DOI: 10.1016/S0370-1573(01)00101-6.

[90] BERTULANI C A, KLEIN S R, NYSTRAND J. Physics of ultra-peripheral nuclear collisions [J/OL]. Ann. Rev. Nucl. Part. Sci., 2005, 55: 271-310. DOI: 10.1146/annurev.nucl.55.0907 04.151526.

[91] BALTZ A J. The Physics of Ultraperipheral Collisions at the LHC[J/OL]. Phys. Rept., 2008, 458: 1-171. DOI: 10.1016/j.physrep.2007.12.001.

[92] BREIT G, WHEELER J A. Collision of two light quanta[J/OL]. Phys. Rev., 1934, 46(12): 1087-1091. DOI: 10.1103/PhysRev.46.1087.

[93] BERTULANI C A, NAVARRA F. Two photon and three photon fusion in relativistic heavy ion collisions[J/OL]. Nucl. Phys. A, 2002, 703: 861-875. DOI: 10.1016/S0375-9474(01)0 1666-9.

[94] KLEIN S, NYSTRAND J. Exclusive vector meson production in relativistic heavy ion collisions[J/OL]. Phys. Rev. C, 1999, 60: 014903. DOI: 10.1103/PhysRevC.60.014903.

[95] LANSBERG J P, SZYMANOWSKI L, WAGNER J. Lepton-pair production in ultraperipheral collisions at AFTER@LHC[J/OL]. JHEP, 2015, 09: 087. DOI: 10.1007/JHEP09(20 15)087.

[96] AFANASIEV S, et al. Photoproduction of J/psi and of high mass e+e- in ultra-peripheral Au+Au collisions at s**(1/2) = 200-GeV[J/OL]. Phys. Lett. B, 2009, 679: 321-329. DOI: 10.1016/j.physletb.2009.07.061.

[97] ABELEV B, et al. Coherent J/ψ photoproduction in ultra-peripheral Pb-Pb collisions at $\sqrt{s_{NN}} = 2.76$ TeV[J/OL]. Phys. Lett. B, 2013, 718: 1273-1283. DOI: 10.1016/j.physletb.2 012.11.059.

[98] ABBAS E, et al. Charmonium and e^+e^- pair photoproduction at mid-rapidity in ultra-peripheral Pb-Pb collisions at $\sqrt{s_{\rm NN}}$=2.76 TeV[J/OL]. Eur. Phys. J. C, 2013, 73(11): 2617. DOI: 10.1140/epjc/s10052-013-2617-1.

[99] ADAM J, et al. Measurement of an excess in the yield of J/ψ at very low $p_{\rm T}$ in Pb-Pb collisions at $\sqrt{s_{\rm NN}}$ = 2.76 TeV[J/OL]. Phys. Rev. Lett., 2016, 116(22): 222301. DOI: 10.1103/PhysRe vLett.116.222301.

[100] ZHA W. Excess of J/ψ yield at very low transverse momenta in Au+Au collisions at $\sqrt{s_{NN}}$ and U+U at $\sqrt{s_{NN}}$ with STAR[J/OL]. J. Phys. Conf. Ser., 2017, 779(1): 012039. DOI: 10.1088/1742-6596/779/1/012039.

[101] ADAM J, et al. Observation of excess J/ψ yield at very low transverse momenta in Au+Au collisions at $\sqrt{s_{\mathrm{NN}}}$ = 200 GeV and U+U collisions at $\sqrt{s_{\mathrm{NN}}}$ = 193 GeV[J/OL]. Phys. Rev. Lett., 2019, 123(13): 132302. DOI: 10.1103/PhysRevLett.123.132302.

[102] ZHA W, KLEIN S R, MA R, et al. Coherent J/ψ photoproduction in hadronic heavy-ion collisions[J/OL]. Phys. Rev. C, 2018, 97(4): 044910. DOI: 10.1103/PhysRevC.97.044910.

[103] KLEIN S R, NYSTRAND J. Interference in exclusive vector meson production in heavy ion collisions[J/OL]. Phys. Rev. Lett., 2000, 84: 2330-2333. DOI: 10.1103/PhysRevLett.84.2330.

[104] ABELEV B I, et al. Observation of Two-source Interference in the Photoproduction Reaction Au Au —> Au Au rho0[J/OL]. Phys. Rev. Lett., 2009, 102: 112301. DOI: 10.1103/PhysRevLett.102.112301.

[105] ACHARYA S, et al. Photoproduction of low-p_{T} J/ψ from peripheral to central Pb−Pb collisions at 5.02 TeV[J/OL]. Phys. Lett. B, 2023, 846: 137467. DOI: 10.1016/j.physletb.2022.137467.

[106] SHI W, ZHA W, CHEN B. Charmonium Coherent Photoproduction and Hadroproduction with Effects of Quark Gluon Plasma[J/OL]. Phys. Lett. B, 2018, 777: 399-405. DOI: 10.1016/j.physletb.2017.12.055.

[107] CEPILA J, CONTRERAS J G, KRELINA M. Coherent and incoherent J/ψ photonuclear production in an energy-dependent hot-spot model[J/OL]. Phys. Rev. C, 2018, 97(2): 024901. DOI: 10.1103/PhysRevC.97.024901.

[108] KŁUSEK-GAWENDA M, RAPP R, SCHÄFER W, et al. Dilepton Radiation in Heavy-Ion Collisions at Small Transverse Momentum[J/OL]. Phys. Lett. B, 2019, 790: 339-344. DOI: 10.1016/j.physletb.2019.01.035.

[109] GAY DUCATI M B, MARTINS S. Heavy meson photoproduction in peripheral AA collisions [J/OL]. Phys. Rev. D, 2018, 97(11): 116013. DOI: 10.1103/PhysRevD.97.116013.

[110] ZHA W, RUAN L, TANG Z, et al. Double-slit experiment at fermi scale: coherent photoproduction in heavy-ion collisions[J/OL]. Phys. Rev. C, 2019, 99(6): 061901. DOI: 10.1103/PhysRevC.99.061901.

[111] LIU Y P, QU Z, XU N, et al. J/psi Transverse Momentum Distribution in High Energy Nuclear Collisions at RHIC[J/OL]. Phys. Lett. B, 2009, 678: 72-76. DOI: 10.1016/j.physletb.2009.06.006.

[112] ABELEV B I, et al. ρ^0 photoproduction in ultraperipheral relativistic heavy ion collisions at

$\sqrt{s_{NN}}$ = 200 GeV[J/OL]. Phys. Rev. C, 2008, 77: 034910. DOI: 10.1103/PhysRevC.77.034910.

[113] AAIJ R, et al. J/ψ photoproduction in Pb-Pb peripheral collisions at $\sqrt{s_{NN}}$= 5 TeV[J/OL]. Phys. Rev. C, 2022, 105(3): L032201. DOI: 10.1103/PhysRevC.105.L032201.

[114] HARRISON M, LUDLAM T, OZAKI S. RHIC project overview[J/OL]. Nucl. Instrum. Meth. A, 2003, 499: 235-244. DOI: 10.1016/S0168-9002(02)01937-X.

[115] HARRISON M, PEGGS S G, ROSER T. The RHIC accelerator[J/OL]. Ann. Rev. Nucl. Part. Sci., 2002, 52: 425-469. DOI: 10.1146/annurev.nucl.52.050102.090650.

[116] BAZILEVSKY A. The RHIC Spin Program Overview[J/OL]. J. Phys. Conf. Ser., 2016, 678 (1): 012059. DOI: 10.1088/1742-6596/678/1/012059.

[117] DEAN C. The sPHENIX experiment at RHIC[J/OL]. PoS, 2021, ICHEP2020: 731. DOI: 10.22323/1.390.0731.

[118] HAHN H, et al. The RHIC design overview[J/OL]. Nucl. Instrum. Meth. A, 2003, 499: 245-263. DOI: 10.1016/S0168-9002(02)01938-1.

[119] CHRISTIE W B. Overview and Status of the Star Detector at RHIC[C/OL]//15th Winter Workshop on Nuclear Dynamics. Springer, 1999: 321-328. DOI: 10.1007/978-1-4615-4719-8_33.

[120] ACKERMANN K H, et al. STAR detector overview[J/OL]. Nucl. Instrum. Meth. A, 2003, 499: 624-632. DOI: 10.1016/S0168-9002(02)01960-5.

[121] WIEMAN H, et al. STAR TPC at RHIC[J/OL]. IEEE Trans. Nucl. Sci., 1997, 44: 671-678. DOI: 10.1109/23.603731.

[122] ANDERSON M, et al. The Star time projection chamber: A Unique tool for studying high multiplicity events at RHIC[J/OL]. Nucl. Instrum. Meth. A, 2003, 499: 659-678. DOI: 10.1016/S0168-9002(02)01964-2.

[123] CONTIN G. The STAR Heavy Flavor Tracker and Upgrade Plan[J/OL]. Nucl. Phys. A, 2016, 956: 858-861. DOI: 10.1016/j.nuclphysa.2016.02.064.

[124] LLOPE W J. The large-area time-of-flight (TOF) upgrade for the STAR detector[J/OL]. AIP Conf. Proc., 2009, 1099(1): 778-781. DOI: 10.1063/1.3120153.

[125] BEDDO M, et al. The STAR barrel electromagnetic calorimeter[J/OL]. Nucl. Instrum. Meth. A, 2003, 499: 725-739. DOI: 10.1016/S0168-9002(02)01970-8.

[126] RUAN L, et al. Perspectives of a Midrapidity Dimuon Program at RHIC: A Novel and Compact Muon Telescope Detector[J/OL]. J. Phys. G, 2009, 36: 095001. DOI: 10.1088/0954-3899/36/9/095001.

[127] ADLER C, DENISOV A, GARCIA E, et al. The RHIC zero degree calorimeter[J/OL]. Nucl. Instrum. Meth. A, 2001, 470: 488-499. DOI: 10.1016/S0168-9002(01)00627-1.

[128] WHITTEN C A. The beam-beam counter: A local polarimeter at STAR[J/OL]. AIP Conf. Proc., 2008, 980(1): 390-396. DOI: 10.1063/1.2888113.

[129] LLOPE W J, et al. The STAR Vertex Position Detector[J/OL]. Nucl. Instrum. Meth. A, 2014, 759: 23-28. DOI: 10.1016/j.nima.2014.04.080.

[130] SHEN F, WANG S, KONG F, et al. MWPC prototyping and performance test for the STAR inner TPC upgrade[J/OL]. Nucl. Instrum. Meth. A, 2018, 896: 90-95. DOI: 10.1016/j.nima .2018.04.019.

[131] YANG C, et al. Calibration and performance of the STAR Muon Telescope Detector using cosmic rays[J/OL]. Nucl. Instrum. Meth. A, 2014, 762: 1-6. DOI: 10.1016/j.nima.2014.05.0 75.

[132] STAR MTD web[EB/OL]. https://drupal.star.bnl.gov/STAR/subsys/mtd.

[133] ABOONA B, et al. Observation of sequential Υ suppression in Au+Au collisions at $\sqrt{s_{\rm NN}}$ = 200 GeV with the STAR experiment[J/OL]. Phys. Rev. Lett., 2023, 130(11): 112301. DOI: 10.1103/PhysRevLett.130.112301.

[134] LAFFERTY G D, WYATT T R. Where to stick your data points: The treatment of measurements within wide bins[J/OL]. Nucl. Instrum. Meth. A, 1995, 355: 541-547. DOI: 10.1016/0168-9002(94)01112-5.

[135] TSALLIS C. Possible Generalization of Boltzmann-Gibbs Statistics[J/OL]. J. Statist. Phys., 1988, 52: 479-487. DOI: 10.1007/BF01016429.

[136] ABELEV B I, et al. Strange particle production in p+p collisions at s**(1/2) = 200-GeV [J/OL]. Phys. Rev. C, 2007, 75: 064901. DOI: 10.1103/PhysRevC.75.064901.

[137] ADAM J, et al. J/ψ production cross section and its dependence on charged-particle multiplicity in $p + p$ collisions at $\sqrt{s}$ = 200 GeV[J/OL]. Phys. Lett. B, 2018, 786: 87-93. DOI: 10.1016/j.physletb.2018.09.029.

[138] ADARE A, et al. Transverse momentum dependence of J/psi polarization at midrapidity in p+p collisions at s**(1/2) = 200-GeV[J/OL]. Phys. Rev. D, 2010, 82: 012001. DOI: 10.1103/PhysRevD.82.012001.

[139] Exclusive J/ψ, $\psi(2s)$, and e^+e^- pair production in Au+Au ultra-peripheral collisions at RHIC [A]. 2023. arXiv: 2311.13632.

[140] KLEIN S R, NYSTRAND J, SEGER J, et al. STARlight: A Monte Carlo simulation program for ultra-peripheral collisions of relativistic ions[J/OL]. Comput. Phys. Commun., 2017, 212: 258-268. DOI: 10.1016/j.cpc.2016.10.016.

[141] WANG P, WU X, ZHA W, et al. Calculations of differential momentum transfer spectra for J/ψ photoproduction in heavy-ion collisions[J/OL]. Chin. Phys. C, 2022, 46(7): 074103. DOI: 10.1088/1674-1137/ac5db8.

[142] MÄNTYSAARI H, SALAZAR F, SCHENKE B, et al. Effects of nuclear structure and quantum interference on diffractive vector meson production in ultraperipheral nuclear collisions [J/OL]. Phys. Rev. C, 2024, 109(2): 024908. DOI: 10.1103/PhysRevC.109.024908.

[143] ABDALLAH M, et al. Tomography of ultrarelativistic nuclei with polarized photon-gluon collisions[J/OL]. Sci. Adv., 2023, 9(1): eabq3903. DOI: 10.1126/sciadv.abq3903.

Acknowledgements

在科大读研究生的这些年，太多的人给了我帮助和支持。在他们的帮助和支持下，我才能完成这篇博士论文。在论文的最后，我想对他们表达诚挚的谢意。

首先我要感谢我的导师，唐泽波教授。他丰富的专业知识，耐心细致的指导，引领我从茫然于初跨专业状态，进入高能物理的专业领域。在数据分析工作以及论文撰写过程中，他能以洞见的眼光发现问题的存在，指出可能的改善空间。在和唐老师的讨论过程中，我不断丰富着自己的知识，也学到了很多解决问题的方法。我要感谢查王妹副教授，这篇文章的完成也离不开他的激励，很多工作得到了他的帮助和指导，与他的讨论让我获益匪浅。另外我还要感谢李澄教授、张一飞教授、邵明教授、孙勇杰副教授在平时的科研工作中，尤其是每周的组会中给予的帮助和指导。还要感谢张云龙教授，在他的实验室的经历虽然短暂，但是是我进入粒子物理与原子核物理学科的开始。

感谢 STAR 国际合作组提供了数据分析工作的平台，感谢 STAR-MTD 小组的成员，每周的讨论让我积极发现问题并解决问题。特别感谢 BNL 的马荣荣研究员，每周组织这个讨论组，在数据分析工作中给了我很多帮助，也帮助我修改了很多学术报告。不仅在工作上，在我去 BNL 交流的半年，异国他乡，他也在生活上提供了很多帮助。感谢科大高能物理实验组的各位同学，在科研上我们互相讨论学术问题，提高自己，在生活上我们组织各项活动，丰富业余生活。感谢刘圳师姐、王鹏飞师兄对我数据分析工作的讨论和帮助。也感谢赵晓坤师兄、江琨师兄对我初入实验室时硬件工作的指导。

感谢我的好朋友韩冰、刘葭妍、汪逸凡、黄兴萌，以及我的其他朋友们。虽然我们不一定在同一个专业，但是他们对我的倾听和建议，朋友之间的小聚带来的欢乐也成为我坚持科研工作的动力和活力。

感谢我的父母，感谢他们三十年来的养育，无微不至的关怀，感谢他们支持我的每一个决定，让我成为现在这样的人，他们是我研究生以来最坚实的后盾。

最后，感谢科大，从本科生到博士生，科大给我提供的平台让我受益良多。

Publications

Publications

1. B. Aboona *et al.* [STAR], "Observation of sequential Υ suppression in Au+Au collisions at $\sqrt{s_{\rm NN}}$ = 200 GeV with the STAR experiment," Phys. Rev. Lett. **130**, no.11, 112301 (2023)
2. Ziyang Li, Wangmei Zha and Zebo Tang, "Rescattering effect on the measurement of K*0 spin alignment in heavy-ion collisions," Phys. Rev. C **106**, no.6, 064908 (2022)
3. Ziyang Li, "Very low-p_T di-muon production in peripheral Au+Au collision at $\sqrt{s}_{NN}$ = 200 GeV at STAR," PoS **ICHEP2022**, 498

Presentations

1. Dimuon production at low transverse momentum in peripheral Au+Au collisions at 200 GeV at STAR (talk), International workshop on the physics of Ultra Peripheral Collisions (UPC 2023), 10-15 Dec. 2023, Playa del Carmen, Mexico
2. Very low-$p_{\rm T}$ J/ψ production in Au+Au collisions at $\sqrt{s_{\rm NN}}$ = 200 GeV and U+U collisions at $\sqrt{s_{\rm NN}}$= 193 GeV at STAR (talk), UPC physics 2023, 26-28 May 2023, Fudan University, Shanghai, China
3. Dimuon production at low transverse momentum in peripheral Au+Au collisions at 200 GeV at STAR (poster), The 9th Asian Triangle Heavy-Ion Conference (ATHIC 2023), 23-27 Apr. 2023, JMS Aster Plaza, Hiroshima, Japan
4. Very low-$p_{\rm T}$ dimuon production in peripheral Au+Au collision at 200 GeV at STAR (talk), The 41st International Conference on High Energy Physics (ICHEP 2022), 6-13 July 2022, Bologna, Italy, Online
5. Very low-$p_{\rm T}$ J/ψ production in Au+Au collision at $\sqrt{s_{\rm NN}}$= 200 GeV at STAR (poster), the XXIXth International Conference on Ultra-relativistic Nucleus-Nucleus Collisions (Quark Matter 2022), 4-10 Apr. 2022, Krakow, Poland (Virtual Meeting)
6. Rescattering effect on the measurement of K* spin alignment in heavy-ion collisions with UrQMD model (talk), The 13th workshop in the series of workshops on QCD phase transition and relativistic heavy-ion physics (QPT 2019), 16-20 Aug. 2019